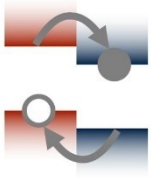
Imperial College London



TRANSIENT OPTOELECTRONIC ANALYSIS OF EVAPORATED AND SOLUTION PROCESSED ORGANIC SOLAR CELLS

Richard Adam Pacalaj

Plastic Electronics Centre for Doctoral Training

Department of Chemistry

Imperial College London

Submitted for the Degree of Doctor of Philosophy

London, February 2024

Abstract

This thesis focusses on performance limitations in vapour- and solution-processed organic solar cells (OSCs), particularly on the analysis of non-geminate recombination kinetics and voltage losses by means of transient optoelectronic techniques. Following an assessment of the climate mitigating potential of OSCs, the theoretical background and methodology employed in this thesis are introduced. The results section will be separated into two parts focusing on vapour- and solution-processed OSCs, respectively.

In the first part, the morphology-function-relationship in a state-of-the-art evaporated OSCs is systematically investigated. It is further divided into two sub-chapters focusing on the influence of the active layer morphology on the collection efficiency and strategies to increase the open circuit voltage, respectively, two key bottlenecks of evaporated OSCs. Varying the substrate temperature during deposition can significantly enhance the performance of evaporated OSCs. Morphological, optical and optoelectronic characterisations demonstrate that increased domain size and purity lead to better charge transport explaining the observed performance increases. However, comparison with solution-processed OSCs suggests that transport is a key limitation of evaporated OSCs. The second study on evaporated OSCs focusses on the voltage losses in planar and bulk heterojunctions (PHJs/BHJs) and the trade-off with charge generation and collection.

The second part addresses voltage losses in solution-processed PHJ and BHJ OSCs using different non-fullerene acceptors including sub-chapters on IT-4F and Y6. While IT-4F shows similar qualitative voltage trends to the evaporated BHJs/PHJs, Y6 shows additional orientation dependent electrostatic effects on the photovoltage. Despite the potential for reduced voltage losses, the studied PHJs remained limited by poor charge generation or extraction. In the final sub-chapter, charge generation in neat Y6 is assessed. Bias dependent photoluminescence measurements suggest efficient charge generation but only at reverse bias. Optoelectronic characterisations show that non-geminate recombination is not the limiting factor behind the poor OSC performance neat Y6 contrary to previous reports.

Keywords: vacuum-processed, evaporated organic solar cell, non-fullerene acceptor, planar heterojunction, single component organic solar cell, non-geminate recombination

Declaration of Originality

The work presented in this thesis was carried out as part of the Plastic Electronics Centre for Doctoral Training (PE-CDT), a collaboration across the Departments of Chemistry, Materials and Physics at Imperial College London, under the supervision of Prof. James Durrant and Prof. Ji-Seon Kim, between October 2019 and March 2023. Except where the contributions of others have been specifically referenced, the material presented within this thesis is the result of my own work. This thesis has not been submitted in whole or in part for a degree at this or any other university.

Richard Adam Pacalaj, London, 2024

Copyright Declaration

The copyright of this thesis rests with the author. Unless otherwise indicated, its contents are licensed under a Creative Commons Attribution-Non Commercial 4.0 International Licence (CC BY-NC). Under this licence, you may copy and redistribute the material in any medium or format. You may also create and distribute modified versions of the work. This is on the condition that: you credit the author and do not use it, or any derivative works, for a commercial purpose. When reusing or sharing this work, ensure you make the licence terms clear to others by naming the licence and linking to the licence text. Where a work has been adapted, you should indicate that the work has been changed and describe those changes. Please seek permission from the copyright holder for uses of this work that are not included in this licence or permitted under UK

Acknowledgements

There are many people who have been an important part of this journey. First and foremost, I would like to thank Ann-Sophie and Olafur Arnalds – without the care by *Ann-Sophie* and the music by *Olafur Arnalds* I could not have stayed alive or sane during the last stages of writing up this thesis.

Thank you to my supervisors, *James Robert Durrant* and *Ji-Seon Kim*, as well as my thesis assessors *Safa Shoaee* and *Jenny Nelson*. Thank you to all the Durrantites, JSK group members, Plastic Electronics CDT members and other colleagues at Imperial – especially *Li, Pabitra, Lucy, Yifan, Ben, Jiaying, Scot, Michael, Tack-Ho, Weidong, Eva, Hyojung, Keren, Helen, Andy, Soyeong, Tian, Lin, Nicola, Aniket, Joel, Charlie, Katie, Flurin…* and many more! Thank you to *Lisa Bushby* and *Lisa O'Donnel* and all administrative staff in Imperial Chemistry for having kept it all together! The Centre for Processable/Plastic Electronics not only provided a scientifically nurturing environment to study organic photovoltaics with many collaborators right next door but also provided a particularly good social atmosphere. Many of the people surrounding me at Imperial were not only scientific role models but also showed great kindness to the people surrounding them despite their immense workload and responsibilities – particularly *James*! Thank you to the collaborators outside of Imperial in Swansea, Durham, Dresden, Chemnitz, Gwangju, Guangzhou, Oxford… Thank you to *Martin Pfeiffer* and *Ivan Ramirez*! 감사합니다, 산성과 기영! Thank you for all the opportunities to travel and meet researchers around the world.

Long before my time at Imperial, there are many people in my life who put me on the path culminating at this point: starting with my mother, *Cornelia,* and my grandfather, *Paul Schneider*, who first gave me the chance to discover London and fostered my wish to study abroad long before starting university; my father, *Anton*, sitting through the early physics and maths homework with me; the teachers that have influenced me throughout my time in school (*Frau Taubner, Herr Henschel, Herr Schmöker, Frau Höppner-Dörnfeld, Frau Reuter, Herr Ensslen, Herr Schade, Frau Tschiedel and many more*) and who have encouraged me in my earliest science ambitions and fostered my curiosity. Thank you!

Especially the learning environment and opportunities for early scientific projects provided at Carl-Zeiss-Gymnasium in Jena have been an immense privilege. It was at the Leibniz-Institute

of Photonic Technologies in Jena that I built my first ever solar cell and read *Brian O'Regan*'s 1991 paper as part of my final year high school project. I went on to make my first organic solar cell steps at Merck surrounded by amazing colleagues and friends (*Graham, Nico, Stephane, Ignasi, Kornel, Luca Michal, Ollie, Delphine, Dorothee etc.*). *OPV, OPV, OPV*!

And finally, this led me to Imperial – to meet *James* and *Ji-Seon*, to learn about TPV and to realise I would spend my PhD with a setup built by *Brian O'Regan*! Following my viva, I was lucky enough to be able to thank *Brian* in person out on a hike in California. Full circle. It has been a great journey and I am deeply grateful to everyone who has been part of it.

Thank you also to everyone for their patience when listening to me going on and on and on about organic solar cells and the joy/pain of the PhD journey. Thank you to *Kiasmos, Kollektiv Turmstrasse, Solumun, Christian Löffler, HVOB, Bonobo, Rival Consoles, WhoMadeWho, The Blaze, David August, Moderat, Meute, Modeselektor, Above and Beyond, Grandbrothers, (Dr) Pöbel MC* and many more for providing a productive soundtrack!

Publications

Lee, T. H.; Rao, R. R.; **Pacalaj, R. A.**; Wilson, A. A.; Durrant, J. R. A Dual Functional Polymer Interlayer Enables Near-Infrared Absorbing Organic Photoanodes for Solar Water Oxidation. *Advanced Energy Materials* **2022**, *12* (18), 2103698. https://doi.org/10.1002/aenm.202103698.

Xu, W.; Du, T.; Sachs, M.; Macdonald, T. J.; Min, G.; Mohan, L.; Stewart, K.; Lin, C.-T.; Wu, J.; **Pacalaj, R.**; Haque, S. A.; McLachlan, M. A.; Durrant, J. R. Asymmetric Charge Carrier Transfer and Transport in Planar Lead Halide Perovskite Solar Cells. *Cell Reports Physical Science* **2022**, *3* (5), 100890. https://doi.org/10.1016/j.xcrp.2022.100890.

Lee, T. H.; Dong, Y.; **Pacalaj, R. A.**; Park, S. Y.; Xu, W.; Kim, J.-S.; Durrant, J. R. Organic Planar Heterojunction Solar Cells and Photodetectors Tailored to the Exciton Diffusion Length Scale of a Non-Fullerene Acceptor. *Advanced Functional Materials* **2022**, *32* (51), 2208001. https://doi.org/10.1002/adfm.202208001.

Fu, Y.; Lee, T. H.; Chin, Y.-C.; **Pacalaj, R. A.**; Labanti, C.; Park, S. Y.; Dong, Y.; Cho, H. W.; Kim, J. Y.; Minami, D.; Durrant, J. R.; Kim, J.-S. Molecular Orientation-Dependent Energetic Shifts in Solution-Processed Non-Fullerene Acceptors and Their Impact on Organic Photovoltaic Performance. *Nature Communications* **2023**, *14* (1), 1870. https://doi.org/10.1038/s41467-023-37234-0.

Xu, W.; Hart, L. J. F.; Moss, B.; Caprioglio, P.; Macdonald, T. J.; Furlan, F.; Panidi, J.; Oliver, R. D. J.; **Pacalaj, R. A.**; Heeney, M.; Gasparini, N.; Snaith, H. J.; Barnes, P. R. F.; Durrant, J. R. Impact of Interface Energetic Alignment and Mobile Ions on Charge Carrier Accumulation and Extraction in P-i-n Perovskite Solar Cells. *Advanced Energy Materials* **2023**, *13* (36), 2301102. https://doi.org/10.1002/aenm.202301102.

Park, S. Y.; Labanti, C.; **Pacalaj, R. A.**; Lee, T. H.; Dong, Y.; Chin, Y.-C.; Luke, J.; Ryu, G.; Minami, D.; Yun, S.; Park, J.-I.; Fang, F.; Park, K.-B.; Durrant, J. R.; Kim, J.-S. The State-of-the-Art Solution-Processed Single Component Organic Photodetectors Achieved by Strong Quenching of Intermolecular Emissive State and High Quadrupole Moment in Non-Fullerene Acceptors. *Advanced Materials* **2023**, *35* (49), 2306655. https://doi.org/10.1002/adma.202306655.

Hußner, M.; **Pacalaj, R. A.**; Olaf Müller-Dieckert, G.; Liu, C.; Zhou, Z.; Majeed, N.; Greedy, S.; Ramirez, I.; Li, N.; Hosseini, S. M.; Uhrich, C.; Brabec, C. J.; Durrant, J. R.; Deibel, C.; MacKenzie, R. C. I. Machine Learning for Ultra High Throughput Screening of Organic Solar Cells: Solving the Needle in the Haystack Problem. *Advanced Energy Materials* **2024**, *14* (3), 2303000. https://doi.org/10.1002/aenm.202303000.

Mazzolini, E.; **Pacalaj, R. A.**; Fu, Y.; Patil, B.; Patidar, R; Lu, X.; Watson, T. M.; Durrant, J. R.; Li, Z.; Gasparini, N. Pathways to upscaling highly efficient organic solar cells using green solvents: a study on device photophysics in the transition from Lab-to-Fab. *Advanced Science* **2024**, *11*, 2402637. https://doi.org/10.1002/advs.202402637.

Li, Y.*; **Pacalaj, R. A.***; Luo, Y.; Ai, K.; Hai, Y.; Liang, S.; Fan, K.; Sergeev, A. A.; Ma, R.; Dela Peña, T. A.; Müller, J. S.; Jin, Z.; Tuladhar, P S.; Jia, T.; Wang, J.; Li, G.; Wong, K. S.; Li, W.; Durrant, J. R.; Wu, J. Molecular Control of the Donor/Acceptor Interface Suppresses Charge Recombination Enabling High-Efficiency Single-Component Organic Solar Cells. *Advanced Materials* **2024**, 2409212. https://doi.org/10.1002/adma.202409212.

Pacalaj, R. A.; Dong, Y.; Mackenzie R. I.; Ramirez, I.; Wu, J; Hosseini, S. M.; Levichkova, M.; Bittrich, E.; Heger, J. E.; Müller-Buschbaum, P; Kaienburg, P.; Riede, M.; Mukherjee, S; Ade, H.; Pfeiffer, M.; Durrant, J. R. From Generation to Collection – Impact of Deposition Temperature on Charge Carrier Dynamics of High Performance Evaporated Organic Solar Cells. (manuscript accepted in *Energy and Environmental Science*)

Pacalaj, R. A.; Hart, L.; Dong, Y.; Eisner, F.; Hosseini, S. M.; Pfeiffer, M.; Durrant, J. R. Charge Carrier Dynamics in Vacuum-Deposited Planar and Bulk Heterojunction Organic Solar Cells. (in preparation)

Table of Contents

Abstract 3

Declaration of Originality 4

Copyright Declaration 4

Acknowledgements 5

Publications 7

Table of Contents 9

Table of Figures 14

List of Parameters and Abbreviations 28

1. Introduction 33

1.1. Change, Crisis, Catastrophe – Climate Communication 33

1.2. Status Quo and Climate Mitigation Scenarios 35

1.3. The Future Global Energy Mix 37

1.4. Photovoltaics and How They Became Cheap 39

1.5. The Case for Second and Third Generation Photovoltaics 40

References 43

2. Fundamentals of Organic Photovoltaics 50

2.1. Solar Cell Operation 50

2.2. Organic Semiconductors 51

2.2.1. The Origin of Semiconductivity in Organic Materials 51

2.2.2. Bandgap Engineering 53

2.2.3. Processing of Organic Semiconductors 53

2.2.4. Disorder in Organic Semiconductors 55

2.2.5. Aggregation Dependent Effects on Energetic Levels 57

2.2.6. Charge Transport in Organic Semiconductors 57

2.3. Device Structure of Organic Solar Cells 58

2.3.1. Single Material Devices....58
2.3.2. Organic Planar Heterojunction....58
2.3.3. Organic Bulk Heterojunction....59
2.3.4. Interlayers and Electrodes....61
2.4. Device Operation of Organic Solar Cells....62
2.4.1. Current-Voltage Characteristics of Solar Cells....62
2.4.2. Simple Electrical Model of Organic Solar Cells....64
2.5. Performance Limiting Factors in Organic Solar Cells....66
2.5.1. The Choice of Bandgap....66
2.5.2. Limitations of the Short Circuit Current Density....66
2.5.3. Open Circuit Voltage and the Charge Carrier Density....67
2.5.4. Non-Geminate Recombination....69
2.5.5. Limitations of the Fill Factor....71
2.6. Research Question and Thesis Outline....71
2.6.1. Vapour-Processed versus Solution-Processed Organic Solar Cells....72
2.6.2. Limitations of Vapour-Processed Organic Solar Cells....73
2.6.3. Solution-Processed Bilayer and Single Component OSCs....75
References....77
3. Experimental Methods....91
3.1. Device Fabrication....91
3.1.1. Organic Semiconductor Materials....91
3.1.2. Vapour-Processed Organic Solar Cells....91
3.1.3. Solution-Processed Organic Solar Cells....93
3.2. *J*-*V*-Characterisation & External Quantum Efficiency....94
3.3. Light Intensity Dependent *J*-*V*-Measurements....94
3.4. Transient Optoelectronic Techniques....95
3.4.1. Charge Extraction....96

3.4.2. Transient Photovoltage 97
3.4.3. Transient Photocurrent and Differential Charging 99
3.4.4. Loss Current & Open Circuit Voltage Reconstruction 101
3.4.5. Note on the Meaning of TPV Lifetime Analysis 101
3.4.6. Experimental Determination of Energetic Disorder 102
3.4.7. Charge Extraction at Short Circuit 103
References 105
4. Limitations of State-of-the-Art Evaporated Organic Solar Cells 110
4.1. Introduction 110
4.2. Charge Carrier Dynamics of Vapour-Processed Organic Solar Cells – The Impact of Morphology 112
4.2.1. Background 112
4.2.2. Contributions 114
4.2.3. Materials, Device Architecture & Performance 115
4.2.4. Light Intensity Dependent JV-Curves 116
4.2.5. Morphology Analysis 118
4.2.6. Absorption & Free Charge Generation 121
4.2.7. Disorder, Non-Geminate Recombination & Transport 125
4.2.8. Discussion 130
4.2.9. Conclusions and Outlook 142
4.3. Analysing Energetics & Kinetics in Evaporated Bulk & Planar Heterojunctions 144
4.3.1. Background 144
4.3.2. Contributions 147
4.3.3. Device Structure and Performance 148
4.3.4. External Quantum Efficiency & the Photovoltaic Gap 149
4.3.5. Analysing Emission Spectra 151
4.3.6. Summary of Photovoltaic Gap and Emission Spectra 153

4.3.7. Non-Geminate Recombination....155
4.3.8. Interpretation of Energetic and Kinetic Results....163
4.3.9. Potential for Multi-Junction Performance Increases....165
4.3.10. Conclusion....168
Appendix....169
4.4. Summary of Results for DCV-V-Fu-Ind-Fu-V:C_{60}....179
References....180
5. Blends, Bilayers, Single Component: Solution-Processed Devices....193
5.1. Introduction....193
5.2. Planar Heterojunctions Tailored to the Exciton Diffusion Length of IT-4F....197
5.2.1. Background....197
5.2.2. Contributions....198
5.2.3. Device Structure and Performance....198
5.2.4. Hole Transfer Kinetics and the Short Circuit Current Density....199
5.2.5. Field Dependence of Photocurrent and the Fill Factor....201
5.2.6. Non-Geminate Recombination Kinetics and Open Circuit Voltage....204
5.2.7. Electroluminescence and Photoluminescence Emission Spectra....207
5.2.8. Conclusion....209
5.3. Orientation-Dependent Electrostatic Effects in PM6/Y6 Planar and Bulk Heterojunctions....210
5.3.1. Background....210
5.3.2. Contributions....211
5.3.3. Orientation Dependent Energetic Shift in Neat Acceptor Films....212
5.3.4. Bilayers and Planar Heterojunction Devices....214
5.3.5. Planar Heterojunction: Charge Carrier Kinetics....217
5.3.6. Interpretation of Non-Geminate Recombination Analysis....219
5.3.7. Effect of Acceptor Quadrupole on Blend Energetics....221

5.3.8. Bulk Heterojunction Device Characterisation 223
5.3.9. Bulk Heterojunction: Charge Carrier Kinetics 225
5.3.10. Comparison of Planar versus Bulk Heterojunction Systems 227
5.3.11. Conclusion 229
5.4. Charge Generation in Neat Non-Fullerene Acceptors 230
5.4.1. Background 230
5.4.2. Contributions 231
5.4.3. Materials and Absorption Spectra 231
5.4.4. Bias Dependent Photocurrent and Photoluminescence Quenching 232
5.4.5. Light Intensity Dependence of the Photo-Response 234
5.4.6. Determination of the Bimolecular Recombination Coefficient 236
5.4.7. Photophysical Experiments to Elucidate Differences in Charge Generation 240
5.4.8. Conclusion 241
5.5. Concluding Remarks: Bulk versus Planar Heterojunctions 242
References 245
6. Conclusions and Outlook 260

Table of Figures

Figure 1.2.1. Projected scenarios of energy and process related CO_2 emissions between 2010 and 2050 and the increase of global temperature relative to the pre-industrial age in 2100 for the different scenarios. Obtained from the World Energy Outlook 2022 published by the International Energy Agency. 37

Figure 1.3.1. Total global primary energy supply by source in the NZE scenario between 2010 and 2050. Note that fossil fuels listed under the low-emissions sources include carbon capture and storage. Obtained from the World Energy Outlook 2022 published by the International Energy Agency. 38

Figure 1.5.1. Learning curve of inflation-corrected Euros/(Watt peak capacity) versus cumulative installed capacity for silicon and cadmium-telluride (CdTe) photovoltaics up to 2018. Obtained from Hart (2020).[49].....41

Figure 2.2.1. (a) The linear combination of atomic $2p_z$ orbitals leads to the formation of a bonding and antibonding π-molecular orbital. **(b)** Illustration of the formation of a band like structure upon extending the length of an alternating alkene chain. The asymmetric contraction and elongation of bonds resulting in Peierls distortion is also shown. Image obtained from the thesis by Scot Wheeler.[4].....52

Figure 2.2.2. Chemical structure of semiconducting materials for organic solar cells manufactured by evaporation **(top)** and solution processing **(bottom).** The highlighted aliphatic chains are added to aid the solubility of the materials in organic solvents. Blue and green highlighted groups signify the electron accepting and donating groups, respectively. The names of the trivial names of the compounds are DCV-V-Fu-Ind-Fu-V **(top left)** and C_{60}-fullerene **(top right)**, PM6 **(bottom left)** and Y6 **(bottom right).** A comparison of the photovoltaic properties of these compounds will be provided in **Chapter 4**. 55

Figure 2.2.3. Visualisation of the effect of static disorder in organic semiconductors. The bandgap (E_g) changes when moving from an isolated, straight, conjugated alkene, to a bent chain, to mixing several chains and eventually a solid film consisting of many polymer chains with the emergence of a band of tailstates inside the gap of valence and conduction band (E_V and E_C, respectively). 56

Figure 2.3.1. Schematic representation of the planar and bulk heterojunction device structure (left and right, respectively). The dimensions of the donor and acceptor phases are referenced to the exciton diffusion length (L_D). In the bulk heterojunction the pathway of the

exciton diffusion to the donor/acceptor interface leading to charge transfer is depicted. Following that, the charge transfer state must be separated which is followed by extraction of the free charges to the respective transport layers as indicated by arrows. Additionally, the interlayers and electrodes in the inverted structure are shown, as discussed later in the text. 60

Figure 2.3.2. Exemplary energy band diagram depicting the energy level offsets of photoactive layer, interlayers and electrodes. Note that, in a BHJ, the donor and acceptor are also in contact with the opposite transport layer. 62

Figure 2.4.1. Current Density – Voltage Curve of an organic solar cell under light and in the dark. Various points of interest are marked and the fill factor is visualised as the ratio of the light and dark squares' area. The right axis shows the power output of the solar cell as a function of voltage. 63

Figure 2.4.2. Simple energy level diagram to describe OSC operation. **(a)** Visualisation of the effective medium approach: the BHJ is treated as a single medium with the band gap defined by the acceptor LUMO and the donor HOMO (labelled here as the acceptor electron affinity $E_{A,acceptor}$ and the donor ionisation potential $I_{P,donor}$, respectively). **(b)** Band diagram in dark equilibrium conditions. **(c)** Visualisation of V_{OC} conditions and the quasi-Fermi level splitting. **(d)** Band diagram at an applied voltage close to *MPP*. Image obtained from the thesis by Scot Wheeler.[4] 65

Figure 2.6.1 Development of the record power conversion efficiency of organic solar cells over time. 72

Figure 3.1.1. Chemical structure of active layer components and the organic hole transporting material BPAPF used in **Chapter 4**: **(a)** DCV-V-Fu-Ind-Fu-V (2,2'-((2E,2'E)-((1H-indole-4,7-diyl)bis(furan-5,2-diyl))bis(prop-2-en-3-yl-1-ylidene))dimalononitrile) **(b)** C_{60} – fullerene **(c)** BTR (5,5'-[[4,8-bis[5-(2-ethylhexyl)-4-hexyl-2-thienyl]benzo[1,2-b:4,5-b']dithiophene-2,6-diyl]bis [(3',3''-dihexyl[2,2':5',2''-terthiophene]-5'',5-diyl)methylidyne]] bis[3-hexyl-2-thioxo-4-thiazolidinone]) **(d)** $PC_{70}BM$ ([6,6]-Phenyl-C71-butyric acid methyl ester) **(e)** PM6 (Poly[(2,6-(4,8-bis(5-(2-ethylhexyl-3-fluoro)thiophen-2-yl)-benzo[1,2-b:4,5-b']dithiophene))-alt-(5,5-(1',3'-di-2-thienyl-5',7'-bis(2-ethylhexyl)benzo[1',2'-c:4',5'-c']dithiophene-4,8-dione)]) **(f)** Y6 (2,2'-((2Z,2'Z)-((12,13-bis(2-ethylhexyl)-3,9-diundecyl-12,13-dihydro-[1,2,5]thiadiazolo[3,4-e]thieno[2'',3'':4',5']thieno[2',3':4,5]pyrrolo[3,2-g]thieno [2',3':4,5] thieno[3,2-b]indole-2,10-diyl)bis(methanylylidene))bis(5,6-difluoro-3-

oxo-2,3-dihydro-1H-indene-2,1-diylidene)) dimalononitrile) **(g)** BPAPF (9,9-Bis[4-(N,N-bis-biphenyl-4-yl-amino) phenyl]-9H-fluorene).....92

Figure 3.4.1. Schematic illustrating the basic setup of commonly used transient optoelectronic systems. The MOSFETS are labelled BS and CS denoting cell switch and bias switch, respectively. PS stands for power supply. R_m is a measurement resistor. Figure obtained from the thesis of Scot Wheeler.[1] 95

Figure 4.2.1. (a) Chemical structure of the donor molecule DCV-V-Fu-Ind-Fu-V and the acceptor C_{60}. **(b)** Schematic of the energy level alignment of the active layer and interlayers. Note that the relative energetic alignment is deduced from a combination of literature and experimental values as described in the main text. **(c)** *JV*-curve of the devices with 50 nm active layer thickness used for the analysis herein. **(d)** Corresponding dark *JV*-curves and J_{SC} vs V_{OC} graphs.....115

Figure 4.2.2 (left) *JV*-curves of evaporated OSCs and solution processed reference OSCs. The legend shows the active layer thickness. Note that these *JV*-curves were obtained using an LED light source calibrated to the same J_{SC} value. **(right)** *JV*-parameters of the OSCs.....116

Figure 4.2.3. (a), (b), (c) Normalised *JV*-curves of DCV-V-Fu-Ind-Fu-V : C_{60} (RT and 50C, blue and red, respectively), BTR : PCBM and PM6 : Y6, respectively, for the range of 3 % to 300 % of 1 sun equivalent light intensity. **(d), (e), (f)** Light intensity dependence of power conversion efficiency, fill factor and linearity of the short circuit current density, respectively. See **(f)** for the legend. 117

Figure 4.2.4. (a), **(b)** 2D-GIWAXS diffraction patterns for *RT* and *50C* films, respectively. The sharp reflection in **(a)** is due to specular reflection from the edged Si substrate (see **Figure 4.2.5 (a)**). **(c)** 1D diffraction patterns obtained from out-of-plane cake cuts of the RT and 50C film, respectively. The Gaussian fits are shown in solid lines together with the corresponding FWHM values used to calculate the coherence length in the main text. **(d)** RSoXS data at resonance on a log-log scale for samples deposited at different substrate temperatures. The stack is SiN/C_{60} (10 nm)/BHJ (50 nm, D:A 3:2 wt%)/BPAPF(10 nm). The *40C* sample was 30 nm and its intensity scaled accordingly. The table indicates the long period *L* and integrated scattering intensity *ISI* normalized to the *60C* sample. GIWAXS measurements and analysis were carried out by Julian E. Heger and Eva Bittrich. Pascal Kaienburg provided the RSoXS results with support from Subhrangsu Mukherjee. 119

Figure 4.2.5. (a) 2D-GIWAXS diffraction pattern of the edged Si substrate showing a similar specular reflection as observed for the *RT* diffraction pattern shown in the main text. This

demonstrates that this feature arises from the Si substrate rather than the organic layers as would be expected for such a sharp feature. **(b)**, **(e)** Pole figures obtained from azimuthal tube cuts of the (100) and (010) reflexes, respectively. The Gaussian fits are shown in solid lines. GIWAXS measurements and analysis were carried out by Julian E. Heger and Eva Bittrich. 120

Figure 4.2.6. (a) Absorption spectra of the neat donor DCV-V-Fu-Ind-Fu-V, acceptor C_{60} and blend films deposited at 50˚C and room temperature. **(b)** Field-dependent external quantum efficiency (EQE) spectra of the *50C* and *RT* devices. Also shown is the relative charge separation efficiency (CSE) that was calculated as the ratio of the EQE at 0V and -3V. **(c)** Donor photoluminescence spectra of the neat donor, *RT* and *50C* blends normalized by their absorption. 122

Figure 4.2.7. (a), (b) Transient absorption spectra of *RT* and *50C* films, respectively, after selectively pumping the donor at 600 nm with a fluence of 48 μJ cm^{-2}. **(c)** Time evolution of the exciton signal between 900 and 920 nm together with fits of the exciton decay with lifetimes of 0.9 and 2.9 ps for *RT* and *50C*, respectively. TAS spectra were measured by Yifan Dong. 123

Figure 4.2.8. (a), (b) Fluence dependent decay of the exciton signal between 900 and 920 nm for the 50C and RT film, respectively. **(c), (d)** Fluence dependent decay of the signal assigned to the hole polaron between 1050 and 1070 nm for the 50C and RT film, respectively. Bimolecular fits to these spectra were used to calculate k_{bi} together with the charge carrier density estimated from the pump power and the film absorbance. **(e)** Ultrafast TAS spectra of the neat donor film recorded under identical conditions as the BHJ films. A pump fluence of 2 μJ cm^{-2} was chosen to minimize exciton-exciton annihilation effects. The amplitude weighted biexponential lifetimes were used to calculate an exciton lifetime of approximately 53 ps. TAS measurements were carried out by Yifan Dong. 124

Figure 4.2.9. (a) Differential capacitance vs open circuit voltage (as measured and corrected for geometric capacitance) together with the respective fits for the *RT* and *50C* device. **(b)** Charge carrier density vs the open circuit voltage rescaled by the open circuit voltage at 2 sun equivalent illumination to enable a better comparison of the slopes. Exponential fits of the form $n0\exp qVoc2Ech$ and the bandtail of an ideal semiconductor are shown. **(c)** Charge carrier lifetime determined by TPV versus the spatially averaged charge carrier density determined from CE measurements. **(d**) Effective mobility and effective bimolecular

recombination coefficient vs charge carrier density. Both axes scaled proportionally to each other to reveal the proportionality of the charge carrier dependence of mobility and recombination coefficient. 126
Figure 4.2.10. (a) Open circuit voltage as a function of light intensity. **(b), (c), (d)** Measured and reconstructed open circuit voltage of the respective devices. The right axis shows the residual of the reconstructed value subtracted from the measured value. 128
Figure 4.2.11. (a) Charge extraction transients of VP-OSCs and SP-OSC references recorded upon switching from steady-state 1 sun equivalent illumination to dark while the device is kept under short circuit conditions. **(b)** Normalised high-resolution photocurrent transients following laser excitation. Additionally shown are the current transients simulated using OghmaNano following a global fit of a large set of optoelectronic data as discussed below. The global fir was carried out by Roderick MacKenzie. The simulated transients correspond to values of E_{ch} of 121 and 89 meV for the *RT* and *50C* device, respectively. 129
Figure 4.2.12. Charge extraction transients upon switching off the LED illumination at short circuit conditions that were used to characterise the effective mobility. Normalised transients recorded following different levels of LED illumination from 5% to 600% 1 sun equivalent illumination on a linear and logarithmic scale for the 50C (**(a)** and **(b)**, respectively) and RT device (**(c)** and **(d)**, respectively).....130
Figure 4.2.13. (a), (b) Light intensity dependence of the Langevin reduction factor and electronic quality, respectively. The electronic quality Q was determined from JV-curves (Q_{JV}) and optoelectronic measurements (Q_{Exp}). The results demonstrate that quoting a single value for the Langevin reduction factor without reference of the charge carrier density may be less comparable across different devices. The discrepancies between the values of Q determined by the different methods may have a variety of reasons such as the oversimplification of equating the generation current and J_{SC}, especially at high light intensity. To calculate $Q_{Exp.}$ the charge carrier density at MPP was estimated by assuming the difference of J_{SC} and J_{MPP} to be a reasonable measure for the bimolecular loss current. By applying the recombination kinetics determined from TPV and DC measurements, an estimate of the charge carrier density corresponding to the loss current is possible when assuming a simple zero-dimensional model. μ_{eff} and k_{bi} are taken at this value of n_{MPP} to calculate γ and $Q_{Exp.}$. 133
Figure 4.2.14. Bimolecular recombination coefficients of PM6:Y6, the *RT* and *50C* device measured by transient photovoltage/differential capacitance and transient absorption spectroscopy. For PM6:Y6 the dashed line is a guide to the eye demonstrating the good

agreement of the values obtained with both methods. For the *RT* and *50C* device, the dashed lines are based on OghmaNano simulations with an additional recombination coefficient for free electron to free hole recombination set to match the k_{BI} value obtained from the transient absorption measurements. 135

Figure 4.2.15. Global fit of experimental data using simulation software OghmaNano for the RT device. **(a)** 1 sun JV-curve. **(b)** V_{OC} vs. light intensity. **(c)** J_{SC} vs. light intensity. **(d), (e), (f)** Photocurrent transients recorded at -1V, 0V and 0.5V, respectively. Photocurrent transients were recorded as outlined by Street.[63] **(g)** 1 sun TPV transient. **(h)** Charge vs. light intensity. The global fitting was carried out by Roderick MacKenzie. 136

Figure 4.2.16. Global fit of experimental data using simulation software OghmaNano for the RT device. **(a)** 1 sun JV-curve. **(b)** V_{OC} vs. light intensity. **(c)** J_{SC} vs. light intensity. **(d), (e), (f)** Photocurrent transients recorded at -1V, 0V and 0.5V, respectively. Photocurrent transients were recorded as outlined by Street.[63] **(g)** 1 sun TPV transient. **(h)** Charge vs. light intensity. The global fitting was carried out by Roderick MacKenzie. 137

Figure 4.2.17. Comparison of experimental data with simulated data obtained from global fit parameters shown in SI Table 1 for the RT and 50C device. **(a)** Experimental obtained from TPV and simulated spatially averaged charge carrier lifetime. **(b)** Experimental effective mobility obtained from charge extraction measurements and simulated effective mobility. Note that in the case of 50C, the tailslopes and free mobility values for holes and electrons were assumed to be near identical leading to identical effective mobilities at different levels of trap filling. For RT the tailslopes were not identical and therefore the effective electron and hole mobility are shown as well as their geometric mean. The geometric mean was chosen following work by Heiber et al.[73] 139

Figure 4.2.18. Normalised charge extraction current transients recorded upon switching from 1 sun equivalent LED illumination to dark at short circuit conditions. The device thickness of the 1:2 and 2:1 D/A ratio samples differs slightly from that of the *RT* sample. 140

Figure 4.2.19. (a) Simulated fitted JV-curves of the *RT* and *50C* device. Additionally shown are the *JV*-curves for the *RT* device with iteratively changing the generation current (*J*gen), the trap symmetry and density (n_{trap}), and the mobility of carriers at the band edge (μ_{free}) and the capture cross-section of the charge carriers ($r_{capture}$) to the values obtained from the global fit of the *50C* device. **(b)** Simulated *JV*-curves visualising the effect of adjusting E_{ch}, free mobility, trap density and active layer thickness to achieve 10 % PCE. **(c)** *PCE* corresponding

to the simulated *JV*-curves in **(a)** and **(b)**. The full list of modelling parameters can be found in **Table 4.2.2**. 141

Figure 4.2.20. (a) Absorption profile calculated using transfer-matrix simulations built-in to OghmaNano with n, k data obtained by Heliatek GmbH. Note that the interlayer configuration was not changed and the thickness of doped transport layers that can act as optical spacers was not optimised. **(b)** Maximum achievable generation current as calculated from the integrated absorption profiles. 142

Figure 4.3.1. (a), (b) Device architecture of the BHJ and PHJ devices, respectively. The molecular structures have been shown in **Chapter 3**. The intrinsic HTL and the molecular dopants are proprietary materials of Heliatek GmbH. **(c)** *JV*-curve of the BHJ and PHJ devices at 1 sun light intensity. 148

Figure 4.3.2. (a) External quantum efficiency spectra for the BHJ and PHJ devices. The BHJs exhibit a moderate field dependence of the EQE. **(b)** Normalised EQE spectra. **, (c)** Derivative of the EQE with respect to energy illustrating the blueshift of the absorption onset for the 5 nm PHJ and 1:2 BHJ devices. **(d)** Normalised EQE on a log-scale with fitted Urbach tails.....150

Figure 4.3.3. (a) Electroluminescence spectra of the PHJ and BHJ devices recorded at 28 mA/cm^2 (BHJs), 70 mA/cm^2 (15 nm PHJ) and 141 mA/cm^2 (5 nm PHJ). These values correspond to the lowest injection currents that a spectrum could be resolved at. **(b)** Photoluminescence spectra. **(c), (d)** Fitting of the PHJ spectra to resolve the low energy emission peak.....152

Figure 4.3.4. Comparison of the photovoltaic gap determined from the derivative of the EQE, EL peak energy and V_{OC} for the 2:1 BHJ, 1:2 BHJ, 5 nm PHJ and 15 nm PHJ. The quantities were chosen for the comparison due to the uncertainty in fitting the EL and EQE_{PV} spectra to determine the radiative limit. Additionally, the values obtained from the *RT* and *50C* devices studied in **Subchapter 4.2** are shown. Note that due to the difficulties in fitting the low intensity EL peaks, the values listed below correspond to EL peak energies rather than Marcus fits of the CT energy. 154

Figure 4.3.5. (a) J_{SC} (left scale) and J_{SC} linearity (right scale) versus light intensity. **(b)** J_{SC} linearity versus J_{SC} illustrating the effect of the reduced generation current of the PHJ on the onset of the linearity drop.....156

Figure 4.3.6. V_{OC} (left scale) and light ideality factor n_{id} (right scale) versus light intensity. 157

Figure 4.3.7. (a), (b) Total differential capacitance (C_{total}) and active layer capacitance (C_{AL}) determined by subtracting the geometric capacitance (C_{geo}) for the PHJ and BHJ devices, respectively. The fitted ideality factors of the devices were determined to be 10.1 V^{-1}, 11.0 V^{-1} and 10.2 V^{-1} for the PHJ, 2:1 and 1:2 device respectively.....159

Figure 4.3.8. (a) Charge extraction results of the 15nm PHJ device illustrating the correction for the linear geometric charge term. Also shown is the result from differential capacitance measurements with a significantly different slope parameter and overall charge. **(b)** Charge extraction results for the PHJ and BHJ devices including the corrected charge. The ideality factors of the charge vs V_{OC} were determined to be 5.7 V^{-1}, 10.7 V^{-1} and 9.8 V^{-1} for the PHJ, 2:1 and 1:2 device, respectively. 160

Figure 4.3.9 (a) Side-by-side comparison of the spatially averaged charge carrier density determined from charge extraction and differential capacitance measurements. The fitted ideality factors of the devices were determined to be 10.1 V^{-1}, 11.0 V^{-1} and 10.2 V^{-1} for the PHJ, 2:1 and 1:2 device respectively. **(b)** TPV lifetime and active layer lifetime value calculated as previously shown[118]. The fitted exponentials were used for the V_{OC} reconstruction. The fitted ideality factors of the devices were determined to be 22.6 V^{-1} and 23.6 V^{-1} for the PHJ and BHJs, respectively.....160

Figure 4.3.10. (a) Comparison of the calculated loss current and J_{SC} at varying light intensity. The bars on the right axis show the percentage deviation between the two values. 161

Figure 4.3.11. (a) Spatially averaged charge carrier density versus V_{OC} determined from DC measurements. The arrows signify changes relative to the 2:1 device. **(b)** Equivalent data plot with the x-axis rescaled by the position of the EL emission peak to illustrate the changes of the effective electronic bandgap relative to the change in the photovoltaic bandgap and the EL emission (both shifted by ~50-60 meV from 2:1 to 1:2).....163

Figure 4.3.12. (a) Small perturbation lifetime determined from TPV versus the open circuit voltage. **(b)** Charge carrier lifetime versus the spatially averaged charge carrier density. The arrows in both plots signify changes relative to the 2:1 device discussed in the main text. .163

Figure 4.3.13. **(a)** Total EQE and corresponding integrated current density of different hypothetical multi-junction combinations. **(b)** Fill factor as a function of light intensity for the BHJ devices. **(c), (d)** Light Intensity dependent JV-curves of the 1:2 and 2:1 device, respectively. 167

Figure 4.3.14: Dark JV-curves of the PHJ and BHJ devices illustrating that the large gradient in the PHJ light JV-curves cannot be explained by an excessive leakage current..169
Figure 4.3.15: Fitting of the 5 nm PHJ electroluminescence emission spectrum recorded at 70 mA/cm^2. The raw data was fitted yielding an emission peak of 1.254 eV and a width of the emission peak of 0.116 eV (corresponding to a values of E_{CT} = 1.50 eV and λ_{CT} = 0.25 eV) 170
Figure 4.3.16: Normalised reduced EL and EQE_{PV} spectra (**(a)** and **(b)**) and PL and EQE_{PV} spectra (**(c)** and **(d)**) of the 2:1 and 1:2 BHJ, respectively. **(a)** shows the 2:1 EL obtained at injection currents of 14 and 35 mA/cm^2. Due to the reduced noise, the EL is fitted to the higher injection current. Note the fitting of the PL emission being focused on the high energy tail. The PL spectra are well described by a weighted sum of this high energy tail and the EL emission for both BHJs. 171
Figure 4.3.17: Alternative fitting assuming similar E_{CT} in the 1:2 BHJ as determined for 2:1 above with a changing reorganisation energy to illustrate the difficulty in determining the fitting parameters reliably. Here a larger weighting is given to the high energy tail of the CT emission justified by the poor background correction. 172
Figure 4.3.18. Normalised electroluminescence and photoluminescence emission spectra for the BHJ and PHJ devices studied in this chapter as well as the BHJ devices studied in **Chapter 3** (RT and 50C). The dashed lines are a guide to the eye marking the position of the low injection current EL and PL emission peaks as well as their shift relative to the 2:1 40C BHJ device (for the 1:2 BHJ and 5 nm PHJ). 175
Figure 4.3.19. (a) Shift of the electroluminescence peak position as a function of injection current (equivalent to current densities of 28 to 422 mA/cm^2) together with the position of the photoluminescence emission peak. **(b)** Normalised EL quantum yield versus the injection current. The values were calculated by integrating the EL emission peaks and normalising by the value obtained at the highest measured injection current. 176
Figure 4.3.20. Charge extraction transients recorded upon switching off the LED light source while the device is kept at short circuit. The transients were recorded at different short circuit current density values of roughly 0.8, 3.5, 14 and 45 mA/cm^2 (**(a)**, **(b), (c)** and **(d)**, respectively). Fits representing biexponential decays are shown in dashed lines. 177
Figure 4.3.21. Extracted charge in the slow and fast phase of the current transients shown above for the 2:1 and 1:2 BHJ. The dashed line signifies a proportionality between the extracted charge and the short circuit current density (equivalent to a power law exponent of

1). The charge extracted from the slow phase exhibits a reduced power law exponent indicative of a charge carrier density dependent mobility related to the filling of tailstates.....178
Figure 4.4.1 Schematic depiction of the morphological characteristics and their relation to device functionality.....179
Figure 5.2.1. (a) Absorption spectra of neat films used for the preparation of PHJ solar cells. **(b)** Transfer matrix modelling of the exciton generation rate under 1 sun illumination for different IT-4F thicknesses. Note that in the used inverted architecture the device is illuminated from the left-hand side. **(c**) JV-curves of the PHJs and BHJ reference. **(d)** Corresponding JV-parameters. Absorption spectra were measured by Tack-Ho Lee.....199
Figure 5.2.2. (a) PM6 ground state bleach (GSB) signal (pump: 775 nm, probe: 560-570 nm) of neat IT-4F, IT-4F/PM6 bilayer and BHJ films. The probe wavelength was chosen to avoid overlap with IT-4F GSB signals. **(b)** Schematic illustration of the hole transfer (HT) process in the IT-4F/PM6 bilayer. **(c)** EQE spectra of the PHJ and BHJ devices. **(d)** Comparison of the trends of the maximum change in absorption (ΔA), EQE and J_{SC} as well as the trend in V_{OC} for the PHJ and BHJ devices. TAS and EQE measurements carried out by Tack Ho Lee. 200
Figure 5.2.3. (a) Light intensity dependent JV-curves of neat IT-4F, 40 nm PHJ and BHJ devices divided by the light intensity in % sun. The data of the neat film is taken from **Section 6.4**. **(b)** JV-curve of the neat IT-4F and 40 nm PHJ device at 1 sun. Additionally shown are the photocurrent of the BHJ device at 0.38 sun equivalent illumination. Subtracting this from the PHJ JV-curve yields the green dashed line. This represents a hypothetical scenario to explain the observed inflection point and field dependence of the JV-curve. **(c), (d)** Field dependent photoluminescence spectra of the 40 nm PHJ and the BHJ, respectively, recorded at an externally biased varying from -3 to 0 V. PL measurements carried out by Tack Ho Lee and Weidong Xu. 202
Figure 5.2.4. (a) J_{SC} and responsivity at short circuit versus the light intensity in units of sun equivalent illumination density. The dashed lines are power law fits over the range shown here. Fitted exponents α for BHJ and PHJ are shown in brackets. **(b)** V_{OC} and light ideality factor versus the light intensity. Circles are measured values and crosses show the values of V_{OC} reconstructed from optoelectronic measurements to validate the experimental results. 205
Figure 5.2.5. (a), (b) Charge carrier density and TPV lifetime versus the open circuit voltage. **(c)** Charge carrier lifetime versus charge carrier density. **(d)** Charge carrier lifetime

versus generation current density. The generation current density was calculated from the J_{SC} data assuming that any deviation from a power law exponent of 1 is caused by non-geminate recombination.....206

Figure 5.2.6. (a) Electroluminescence spectra of the BHJ and PHJ at an injection current density of 19 mA/cm^2. **(b)** Quantum yield of the electroluminescent emission versus the injected current density. **(c), (d)** Normalised PL and EL spectra of the PHJ and BHJ, respectively, for a range of injected current densities from ~19 to 180 mA/cm^2. The coloured lines are the EL spectra and the arrows indicate increasing current density. Additionally shown is the PL of neat IT-4F films. EL and PL measurements carried out by Tack Ho Lee and Weidong Xu. 208

Figure 5.3.1. (a) Chemical structure of Y6 and schematic representation of the Y6 orientation and packing in films spin-coated from CF or CB. **(b)** Absorption spectra of the Y6 films deposited from CF and CB. **(c)** Fermi and HOMO energy level measurements as determined from Kelvin probe and APS measurements, respectively. **(d)** Simulated HOMO and LUMO energy levels obtained from molecular dynamics simulations of face-on and edge-on oriented Y6 clusters with alternate and eclipsed packing structure, respectively. Absorption spectra were measured by Yuang Fu. Measured and simulated energetics provided by Yuang Fu and Daiki Minami, respectively.....213

Figure 5.3.2. (a) HOMO energy level of neat PM6 compared to thin layers of PM6 deposited on top of Y6 CF and Y6 CB. Additionally, the HOMO energy level of the Y6 layers deposited from both solvents following thermal annealing are shown. This is consistent with the processing conditions used for the preparation of the PHJ devices. **(b)** EQE and absorption spectra of the full PHJ devices and bilayers, respectively. **(c)** JV-curve of the PHJ devices. **(d)** Light intensity dependence of the V_{OC} and normalised responsivity. The latter was calculated by dividing the J_{SC} by the corresponding light intensity. The crosses signify the values of the reconstructed V_{OC} determined from the transient optoelectronic measurements discussed later. Energetic and EQE measurements carried out by Yuang Fu and Tack-Ho Lee, respectively. 216

Figure 5.3.3. (a) Differential capacitance of the PHJ devices with exponential fits of the chemical capacitance. The shaded area under the exponential signifies the active layer charge. At the bottom also the charge stored on the electrodes is shown. **(b)** Charge carrier lifetime versus the charge per unit cell area. 218

Figure 5.3.4. Schematic representation of the effect of the charge-quadrupole interactions on the band bending at the Y6/PM6 interface. The additional band bending in the Y6 CB layer leads to additional charge accumulation away from the interface which slows down the effective non-geminate recombination rate thereby partially compensating for the energetic penalty on the V_{OC}. Image obtained from the original publication.[52].....221

Figure 5.3.5. (a) Molecular quadrupole moment Q_{π} in π-π-stacking direction for a range of NFAs including ITIC and its derivatives IT-2M and IT-4F, IDIC and Y6. The values were calculated by DFT simulation for isolated molecules. **(b), (c)** Change in polymer HOMO level ΔE_{HOMO} upon blending with the NFAs for PM6 and PBDB-T, respectively. Calculated quadrupole moments provided by Yi-Chun Chin. Energetics measured by Chiara Labanti. 222

Figure 5.3.6. (a) JV-curves of the BHJ devices deposited from CB and CF. **(b)** EQE and absorption spectra of BHJ devices and films, respectively. Note that the films were of a similar thickness. **(c)** Effective mobility determined from charge extraction at short circuit measurements as previously described.[106] **(d)** V_{OC} and normalised responsivity calculated from the J_{SC} normalised by the light intensity versus the light intensity in units of sun equivalent illumination levels. The crosses show the reconstructed V_{OC} from lifetime and charge carrier density measurements. EQE and absorption measurements by Tack-Ho Lee. 224

Figure 5.3.7. (a) Charge carrier density versus V_{OC} for the BHJ devices. Additionally, the charge carrier density for the PHJs is shown which was calculated by spatially averaging over the entire active layer. The values were collected for up to a 6 sun equivalent illumination using DC. For CF the CE results are shown that were in generally good agreement with DC but yielded less outliers during the collection. The arrow corresponds to the potential shift at the 1 sun point of the CF BHJ. **(b)** Charge carrier lifetime versus the spatially averaged charge carrier density for the BHJ and PHJ devices.....226

Figure 5.3.8. Charge carrier lifetime determined from transient photovoltage measurements for different material systems in planar and bulk heterojunction configuration. The arrows indicate an apparent shift along the voltage axis when moving from BHJ to PHJ architecture in PM6:IT-4F and DCV-V-Fu-Ind-Fu-V:C_{60} (abbreviated as D:C_{60} in the legend). While the arrow for Y6 devices signifies a shift along a similar functional dependence on the V_{OC} for different solvents and device architectures (PHJ vs BHJ and CB vs CF).....228

Figure 5.4.1. (a) Molecular structures of the four NFA materials used: IDIC, Y6, IT-4F, O-IDFBR. **(b)** Energy badn diagram of the single component devices. HOMO levels of the NFAs were determined by APS. LUMO levels were calculated by adding the optical gap to the measured HOMO level. **(c)** Absorption coefficient as a funtion of wavelength of the neat NFA films. Energy level measurements carried out by Yi-Chun Chin. Absorption spectra measured by Chiara Labanti.....232

Figure 5.4.2. (a) Bias-dependent EQE spectra of a Y6 single component device. **(b)** Peak value of the EQE spectra versus the applied bias for O-IDFBR, IDIC, IT-4F and Y6. The legend shows the wavelength at which the EQE spectra reach their maximum. **(c)** Bias-dependent PL spectra of a Y6 single component device. **(d)** PL quenching efficiency as a function of bias for all four NFAs. The calculation of the PLQE is described in the text. Measurements carried out by Song Yi Park and Chiara Labanti. 233

Figure 5.4.3. (a) Normalised photocurrent of Y6 versus applied bias at 56 light intensity levels logarithmically spaced from 0.028 to 655 mW/cm^2 (equivalent to % sun intensity). The LED light intensity was calibrated to reproduce the integrated EQE at 1 sun AM1.5 illumination at -5 V reverse bias. On the right axis, the laser induced charge extracted in transient photocurrent measurements. **(b)** Total extracted current and corrected photocurrent of Y6 at -5 and -1 V illustrating the lower bound of the linear dynamic range at high reverse bias where the dark current increases. The measurements were obtained from the JV-curves. **(c)** Corrected photocurrent of Y6 versus light intensity at short circuit and reverse bias conditions. **(d)** Responsivity calculated from the corrected photocurrent divided by the light intensity in mW/cm^2 (or % sun equivalent). Not that small discontinuities arise where neutral density filters were inserted (around 8% sun) to access light intensity levels otherwise inaccessible with the LED setup due to the unreliable low power output.....235

Figure 5.4.4. (a), (b) Extracted charge carrier density versus the LED background light intensity and the steady-state current density, respectively. Dashed lines in **(a)** are fits with a power law exponent of 0.84. The solid line in **(b)** signifies proportionality between the charge carrier density and extracted current density. **(c)** Photocurrent transients recorded with varying background light intensity recorded at -5 V. **(d)** Extracted charge induced by small perturbation laser pulses versus the background charge carrier density induced by LED illumination for different bias conditions.....237

Figure 5.4.5. (a) Photocurrent transients without background illumination at different biases. **(b)** Normalised laser induced charge versus the LED induced steady-state charge

carrier density. The grey area signifies the range of values of k_2 encompassing the measurements at all bias conditions. 239

Figure 5.4.6. External quantum efficiency spectrum of devices prepared from chloroform and chlorobenzene resulting in a mostly face-on and mixed orientation, respectively. EQE measurements performed by Song Yi Park. 241

List of Parameters and Abbreviations

Parameters	Description
A	Device area defined by the area of overlap of top and bottom electrode
C	Capacitance
d	Active layer thickness
e	Elementary charge
E_A	Electron affinity used here often interchangeably with the E_{LUMO}
E_c / E_v	Energy of the conduction / valence band
E	Electric field
E_{ch}	Characteristic energy of the exponential bandtail
E_f / E_{fn} / E_{fp}	Fermi energy level / electron fermi level / hole fermi level
E_g	Energy of the bandgap i.e. effective photovoltaic gap from absorption onset
FF	Fill factor
G	Generation rate per unit density
I_P	Ionisation potential used here often interchangeably with the E_{HOMO}
J_{dark}	Dark current density
J_{Light}	Light current density
J_{gen}	Generation current density
J_{rec}	Recombination current density
J_0	Dark saturation current density
J_{loss}	Loss current density due to non-geminate recombination
J_{ph}	Photocurrent density
J_{sc}	Short circuit current density
k_0	Charge carrier density independent recombination rate constant
k_B	Boltzmann constant
k_{bi} / k_2	Bimolecular recombination rate constant
$k_{Langevin}$	Langevin recombination rate constant
n	Charge carrier density
n_0	Equilibrium charge carrier density
N_C / N_V	Conduction / valence band density of states
n_{id}	Ideality factor
P	Power density

q	Elementary charge
R	Recombination rate
r	distance
R_s	Series resistance
R_{sh}	Shunt resistance
T	Temperature
t	Time
V	Voltage
V_{BI}	Built-in potential
V_{OC}	Open circuit voltage
β	Slope of parameter of the exponential decrease of $\tau_{\Delta n}$ (V_{OC})
γ	Slope of parameter of the exponential decrease of n (V_{OC})
δ	Empirical reaction order
ε_r	Relative permittivity
ε_0	Permittivity of free space
τ	Charge carrier lifetime
$\tau_{\Delta n}$	Small perturbation TPV lifetime
τ_0	Equilibrium carrier lifetime

Abbreviation	**Description**
Ag	Silver
Al	Aluminium
BHJ	Bulk heterojunction
CdTe	Cadmium telluride
CE	Charge extraction
CIGS	Copper indium gallium selenide
CT	Charge transfer state
DC	Differential charging
DoS	Density of states
EL	Electroluminescence
HOMO	Highest occupied molecular orbital
ITO	Indium tin oxide

MoO_3	Molybdenum oxide
MOSFET	Metal oxide semiconductor field effect transistor
MPP	Maximum power point
OLED	Organic light emitting diode
OPV / OSC	Organic photovoltaics / solar cell
PCE	Power conversion efficiency
PET	Polyethylene terephthalate
PHJ	Planar Heterojunction
PL	Photoluminescence
PV	Photovoltaics
QFLS	Quasi-Fermi level splitting
SCLC	Space charge limited photocurrent
SP-OSC	Solution-processed organic solar cell
TAS	Transient absorption spectroscopy
TPC	Transient photocurrent
TPV	Transient photovoltage
VP-OSC	Vacuum processed organic solar cell

“The philosophers have hitherto only interpreted the world in various ways. The point, however, is to change it.”

- Karl Marx

“The man who will do something great must learn, as Goethe says, to limit himself. The man who, on the contrary, would do everything, really would do nothing, and fails. There is a host of interesting things in the world: Spanish poetry, chemistry, politics, and music are all very interesting, and if anyone takes an interest in them we need not find fault. But for a person in a given situation to accomplish anything, he must stick to one definite point, and not dissipate his forces in many directions.”

- Georg W. F. Hegel

“Science is like sex: sometimes something useful comes out, but that is not the reason we are doing it.”

- Richard P. Feynman

1

INTRODUCTION

1. Introduction

The climate and energy crisis humanity is facing right here and now are providing motivation for many who enter the field of renewable energy research. However, it is often difficult to keep an eye on this bigger picture when solving interesting scientific problems such as explaining the non-geminate recombination rate in non-fullerene acceptor single component devices or the reduction in the photoluminescence quenching efficiency in evaporated bulk heterojunction solar cells. The following pages are intended to serve as a reminder to myself and others of what the bigger picture is, before diving into the joy of finding answers to scientific questions.

1.1. Change, Crisis, Catastrophe – Climate Communication

Wallace S. Broecker coined the phrases "global warming" to refer to a carbon dioxide emissions induced *climate change* in 1975.[1] As the discipline of climate science formed in the following decades, the scientific evidence for climate change and its grave consequences became more and more clear. It took 40 years, until the Paris Agreement in 2015,[2] for the international community to agree on the common goal of limiting the global warming to 1.5 °C – a limit deemed safe to prevent the most catastrophic changes to the global climate.[3] One reason behind the delay in political action is the aggressive lobbying by fossil fuel companies like Exxon against the evidence on climate science that has emerged in the last decades and is scientific consensus.[4] This is despite the fact that their own research had made surprisingly accurate predictions on the effects of fossil fuel combustion on the climate.[5] To stay with the example of Exxon and their denial of human made climate change, a recent peer-reviewed study on Exxon-funded research concluded that the company was aware of the consequences of CO_2 emissions on the climate as early as 1975 and their own predictions were surprisingly accurate in hindsight.[6] These above mentioned studies now serve as evidence against Exxon in *climate change* related litigation for knowingly deceiving the public and causing delays to climate action.[7]

While today there is scientific and often even political consensus on the urgency of decisive climate action, how to communicate this urgency to the different involved stakeholders (from consumers to corporations to policy makers) and make real political changes is still debated intensely - with additional crossfire by those who benefit from business as usual. Leaving the latter aside, the question is how to best advocate for decisive climate action. This is also a

relevant question for scientists in the broad field of green energy as it affects how we communicate our motivation, our findings and the impact of our work not just within the scientific community but also beyond.

> "It is, I promise, worse than you think. If your anxiety about global warming is dominated by fears of sea-level rise, you are barely scratching the surface of what terrors are possible, even within the lifetime of a teenager today."
> - David Wallace-Wells

This is the opening sentence of David Wallace-Wells' 2017 article "The Uninhabitable Earth" published in New York Magazine.[8] Combining scientific reports and dozens of interviews with researchers of various disciplines Wallace-Wells describes the effect global warming will have on various aspects of our habitat - from the increase of the likelihood of heat related deaths and the occurrence of pandemics to food insecurity. His article paints a truly harrowing picture of the apocalyptic future that awaits without decisive action, changes that remain abstract when talking about 1.5˚C or 580 $GtCO_2$ (the CO_2 budget left to limit global warming to within 1.5˚C with 50% confidence as of 2018). Despite the Paris Agreement, not enough had been done in terms of real policy change at that point.

The article – dubbed alarmist by some – resonated with the readership.[9] Within days it became one of the most read articles of the New York Magazine to date.[8] The increased frequency of extreme weather events further contributed to the change in attitude.[10–14] In 2018, Fridays for Future was initiated after Greta Thunberg and other young activists had started their school strikes.[15] A public that had been dormant, started to wake up to the *climate crisis* almost four decades after the first studies on fossil fuel related man-made *climate change*.

Re-framing the *climate change* from an inevitable global temperature change to a human-made *climate crisis* causing palpable threats in the here and now was – and still is – necessary to create traction for change. And the mobilisation and activism were in part successful in creating public pressure to enact change. The heightened awareness of the *climate crisis* also leads to the phenomenon of “climate anxiety”. Studies found that almost 60% of young people globally reported to be very or extremely worried about climate change and government inaction.[16] Paradoxically, anxiety about *climate catastrophe* and the so called climate “doomerism” increasingly replace climate change denial as the cause for inaction.[17] Promoting

such “doomerism” has also been found to benefit fossil fuel companies along with an increased focus on individual consumption (“carbon footprint”) to deflect from fossil fuel responsibility and regulation.[18–20] In the face of scientific consensus on the origins and consequences of the global temperature rise, fossil fuel companies changed media strategies to instead overpromote their green initiatives[21,22] or delay action on climate mitigation in favour of future technologies (e.g. nuclear fusion, large scale air capture of CO_2) promising business as usual.[23]

But change is not only necessary now but also possible. Today, 90% of global GDP are subject to net carbon zero pledges and the world is likely on track for 2 to 3˚C warming instead of 4 ˚C by the end of the century.[3] This is a success and yet far off the goal of limiting global warming to 1.5˚C that “conventional wisdom has dictated [...] could allow for some continuing normal”.[24] In his 2022 article “Beyond Catastrophe - A New Climate Reality Is Coming Into View” David Wallace-Wells writes that neither the most terrifying predictions of “The Uninhabitable Earth” nor the most optimistic scenarios of a global warming limited to 1.5˚C will come true.[24] This is on one hand due to pledges since the Paris Agreement and tragic delay of action on the other.

> “It’s not the end of the world, but it’s the end of the world as we’ve known it.”
>
> - Alex Steffen

Somewhere in-between “doomerism” and the optimism that through future technological advancements we can keep doing business as usual (in the “global north”) lies a middle way. It is what Alex Steffen calls “transapocalypse”.[25] The realisation that change is possible is key to hold the commercial and political stakeholders accountable. But our lives will change. It is therefore necessary for scientists working on technologies for climate mitigation to be transparent about the potential these solutions offer and on what time scale. Because the climate mitigation scenarios based on proven technologies and political/social change already exist and need to be implemented without further delay.[26]

1.2. Status Quo and Climate Mitigation Scenarios

The existence of anthropogenic climate change caused by the burning of fossil fuels and the graveness of its consequences are scientific consensus.[27] According to the intergovernmental panel on climate change (IPCC), the global surface temperature over the period from 2011-

2020 increased by 1.1˚C compared to 1850-1900. In 2015, the international community agreed to the ambitious target of limiting global warming to well below 2 ˚C and pursue efforts to limit it to 1.5˚C compared to the pre-industrial age in order to minimise negative effects for human health, food production and global eco-systems.[2] The latter goal was reaffirmed at COP26 in Glasgow.[28] This requires the ambitious achievement of net zero emissions (NZE) by 2050 according to the International Energy Agency (IEA).[29] Current projections predict that the 1.5˚C "milestone" will be reached already in the early 2030s.[3] Recent data by the Copernicus Program revealed that over the last 12 months (February 2023 to January 2024) the global mean temperature already exceeded that of the pre-industrial age by 1.52˚C.[30]

Most realistic scenarios - even those with ambitious reduction targets for carbon dioxide emissions like the announced pledges scenario (APS) - expect the temperature rise to approach 2˚C by the end of the century that would still result in strong negative consequences for societies around the world, generally increasing inequities and hitting the most vulnerable hardest.[31] The stated policy scenario (STEPS), i.e. the scenario based on current policies, is projected to result in a temperature rise above 2.5˚C. **Figure 1.2.1** shows the projected emissions and temperature rise under the different scenarios and illustrates how far current policies and policy pledges are from the goals the international community has set to avoid the most catastrophic consequences of climate change. The NZE scenario does not only require a reduction of the CO_2 emissions to zero by 2050, but also a 75% reduction in methane emissions (often a consequence of fossil fuel production).[29]

According to the IEA, one of the main requirements to reach "net zero" is the rapid electrification of the global energy system. The share of electricity in the final energy consumption (including transport, heating etc.) is projected to increase from 20% today to 52% by 2050 in the NZE scenario. Together with the increasing electricity demand driven mainly by the countries of the so-called “global south” this leads to a projected 150% growth of the global electricity demand. This NZE scenario would also fulfil the United Nations' (UN) Sustainable Development Goal 7 (SDG7) targets of providing universal access to electricity and clean cooking which are currently not met by 113 and 128 countries, respectively.[29] The increased electricity demand will of course need to be met by a rapid increase in low-emissions energy sources in order to achieve net zero.

Reports by international organisations such as the UN's IPCC, the IEA or the World Bank, and non-governmental organisations such as Green Peace collate results from a large range of climate science and economic models that produce a very clear outlook of what is needed.[3,29,32] Bar any phenomenon not included in these models - such as the possible release of methane from a thawing permafrost - we know how to achieve net zero. In theory.

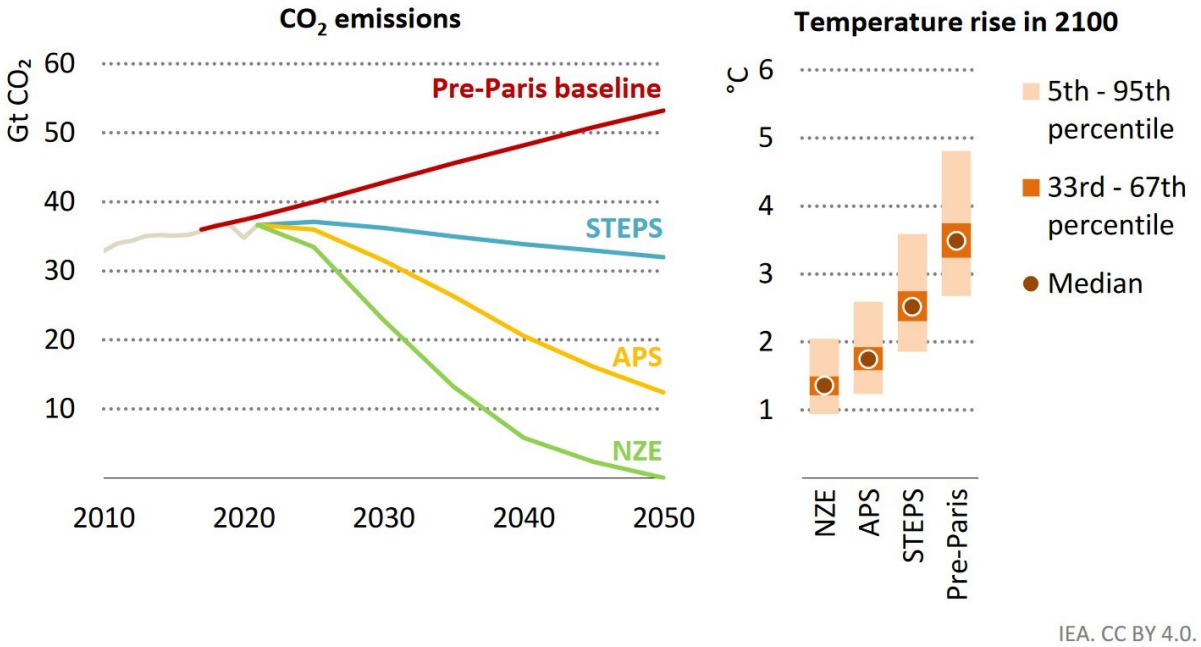


Figure 1.2.1. Projected scenarios of energy and process related CO_2 emissions between 2010 and 2050 and the increase of global temperature relative to the pre-industrial age in 2100 for the different scenarios. Obtained from the World Energy Outlook 2022 published by the International Energy Agency.

1.3. The Future Global Energy Mix

Global electricity production currently relies to 60% on fossil fuels (coal, oil, gas) while the remaining 40% are split up between nuclear (10%) and renewable energy (30%). To reach net zero the combined contribution of wind and solar will need to reach 70% of the total electricity generation by 2050 according to the IEA.[29] The needed electrification of other sectors and increased energy demand see the total electricity generation rise by 150% in the same scenario. This is better reflected when considering the current total primary energy consumption, where the fossil fuel share is even more dominant. **Figure 1.3.1** shows the change of the contribution of different energy sources to primary energy generation in the IEA's NZE scenario between 2010 and 2050.[29] The way to net zero requires the near complete phaseout of unabated fossil fuel use not only in electricity generation but also in heating, industry and

transport. The IEA projects photovoltaics (PV) to provide the largest share of primary energy in the NZE scenario followed by biomass and wind power.[29] Nuclear, as another low emissions technology, is projected to take only a minor role due to the associated environmental and financial risks and the high external costs of that are often not included when quoting operating costs.[3,33,34] It should be noted that while the exact mix in primary energy generation differs between the 1.5˚C compatible scenarios of the IPCC and the IEA, photovoltaics take on a dominant role in both.[3,29] Reasons for this divergence are mainly different assumptions made on the availability of biomass by the two reports that the IEA forecasts to be more limited warranting a higher proportion of wind and photovoltaics.

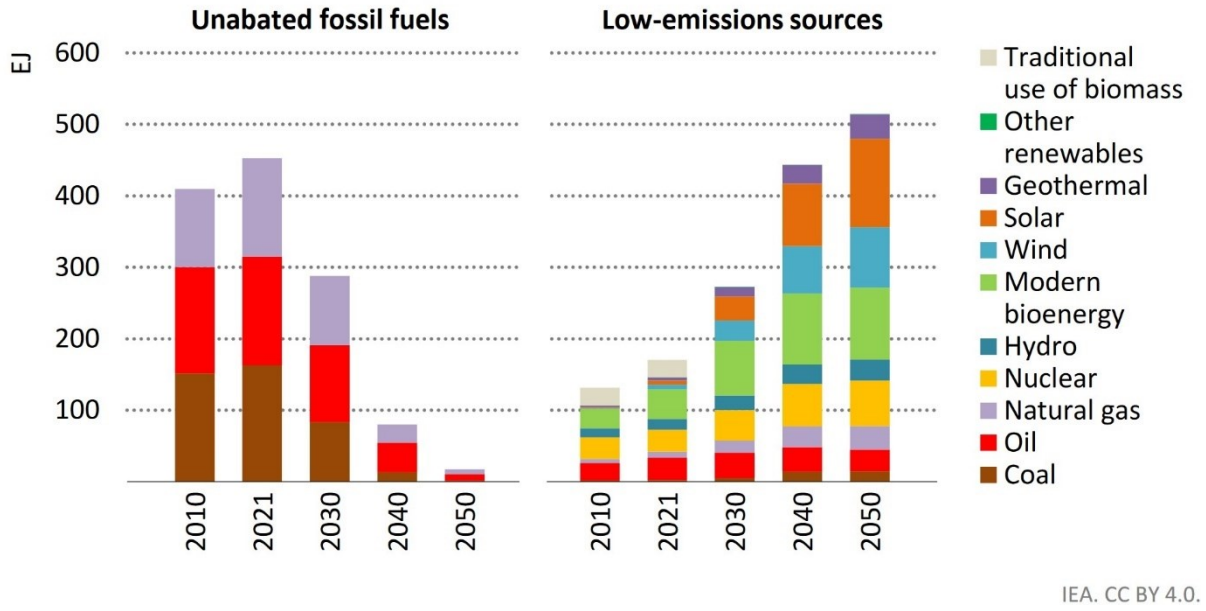


Figure 1.3.1. Total global primary energy supply by source in the NZE scenario between 2010 and 2050. Note that fossil fuels listed under the low-emissions sources include carbon capture and storage. Obtained from the World Energy Outlook 2022 published by the International Energy Agency.

While these scenarios are currently still far from what has been pledged by governments (APS) and businesses around the world, the mere fact that such a scenario exists and is realistic given the political will is reason for optimism. That solar plays a key role in it is astonishing given that photovoltaics were taunted to be one of the most expensive and unviable means of electricity generation as little as two decades ago.[35] Today PV is one of the cheapest forms of electricity generation.[36–38] Their price advantage is even more pronounced when taking the external cost of fossil energy sources into account.[39,40]

1.4. Photovoltaics and How They Became Cheap

Photovoltaics (PV) or solar cells are electronic components that directly convert sun light into electricity. They constitute the main form of what is colloquially dubbed as "solar energy". Other forms of solar energy include photothermal electricity generation that makes use of solar irradiation to heat a medium to power engines or turbines.

It has been a long way from the first discovery of the photovoltaic effect by Edmond Becquerel in 1839,[41] the observation of photoconductivity in selenium by Willoughby Smith in 1873,[42] the demonstration of the first rooftop photovoltaic installation based on a selenium/copper junction by Charles Fritts in 1884[43], to the first modern PV cell based on silicon built at Bell Labs.[44] Wafer based mono- or multi-crystalline solar cells based on the original innovation by Bell Labs are often referred to as "first generation PV".

At the time, solar energy was not cost competitive with conventional energy sources but soon found applications in remote powering of radio stations and – ironically – oil rigs. Satellites were the first major application as the reduced weight made PV more competitive with earlier battery powered solutions. The main reason for the high cost was the energy intensive process of producing defect free silicon ingots that are the base for silicon PV.

Throughout their further development, the high price of first-generation PV remained a motivating factor for the market entry of alternative PV technologies such as second generation thin-film technologies (amorphous silicon, CdTE, CIGS) and later on novel third generation technologies (dye-sensitized, organic and perovskite solar cells). However, to this day, first generation silicon PV dominates the global PV market with about 95% market share due to its impressive price decline by a factor of 10 000 since they were first commercialised.[45,46] This proves that the factors that caused the high initial cost of silicon PV were in fact extrinsic and could be reduced through technical innovation and the economics of scale. Many publications address the history of silicon PV from its invention to large scale cost-competitive applications.[35,43,46–49]

With "How Solar Became Cheap", Gregory Nemet published a very comprehensive and complete overview over the critical steps it needed for this process to occur and most importantly draws conclusions for future low-carbon innovation (such as future generations of PV).[46] He identifies six crucial steps in the development of PV:

1. Scientific discovery, USA, 1954
2. Federal technology push, USA, 1973 – 1981
3. Niche markets in consumer electronics and rooftop program, Japan, 1980s and 1990s, respectively
4. Demand-pull subsidy, Germany, 2000 – 2012
5. Scale-up of manufacturing by engineers trained in Australia, China, from 2001 onwards
6. Reduction of installation cost globally through local learning, from 2010 onwards

Besides the technological innovations, first in the USA and later driven by research led by Martin Green in Australia among others, the creation of markets through the demand-pull subsidies by Germany, Spain and other countries was vital to the observed price decline. It provided the incentive for aggressive upscaling of PV production capacities in China that soon dominated global PV markets with upwards of 70% market share in all parts of the PV production chain.[46] As Hal Harvey told the New York Times in 2014 "The Germans were not really buying power – they were buying a price decline."[50]

In a country that was sceptical of nuclear (especially after Chernobyl) and in the face of climate change, this was partly by design and partly based on a miscalculation about the competitiveness of the domestic solar industry at the time.[46] Hermann Scheer, former member of the German Parliament and one of the drivers behind the German feed-in tariff subsidies, said in 2000 that "We are responsible for this problem [of climate change] and should not shrug this responsibility by only thinking of ourselves."[51] Globally, it can be seen as a success as it enabled the unprecedented price decline that makes solar a viable option today for large scale replacement of fossil fuel resources.

1.5. The Case for Second and Third Generation Photovoltaics

Some have pointed out that, while positive for the climate, the advantage of silicon PV due to the impressive learning curve over the past decades stifles PV innovation of second or third generation PV technologies today. Second generation technologies like CdTe have the potential to provide cheaper solar energy than silicon PV if a similar learning curve is assumed yet cannot compete with the market might of silicon PV.[49] This is illustrated below by direct comparison of the two learning curves in **Figure 1.5.1**.

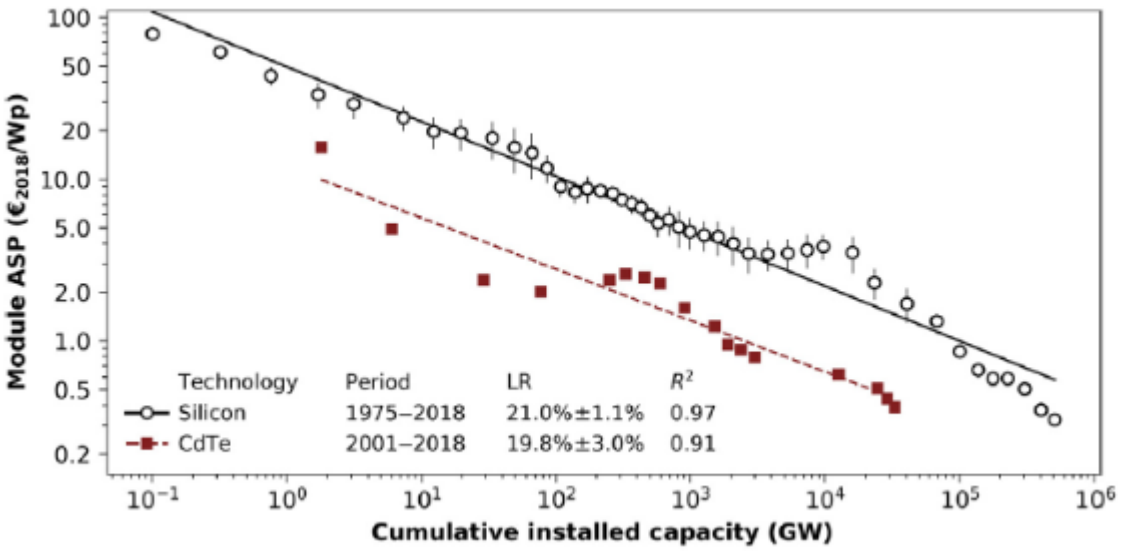


Figure 1.5.1. Learning curve of inflation-corrected Euros/(Watt peak capacity) versus cumulative installed capacity for silicon and cadmium-telluride (CdTe) photovoltaics up to 2018. Obtained from Hart (2020).[49]

Similar issues would arise for third generation photovoltaics when trying to compete with silicon PV for utility scale applications. These technologies include most prominently dye-sensitized and organic solar cells that properly emerged in the early 1990s[52–54] as well as perovskite solar cells that emerged around 2009.[55] Ease of fabrication through high-throughput, low-cost solution-processing (or roll-to-roll evaporation) was the main driving force behind the research into these technologies. Research efforts were focused on increasing the efficiency to compete with silicon PV. Today, as lab-scale efficiencies of solution-processed organic solar cells exceed impressive 19%, large scale commercialisation legs behind with the highest certified submodule efficiency at 14.5% (compared to 26.8% for the record crystalline silicon modules).[56,57]

Over time, competitiveness with silicon PV in terms of price, efficiency and stability became unlikely as it had embarked on its journey down a steep learning curve following the built-up of mass production in the early 2000s. Therefore, third generation photovoltaics, especially organic solar cells, increasingly target niche markets (façade integration,[58,59] agrivoltaics,[60–64] low-light indoor applications[65–67]) accessible due to their properties such as the potential for lightweight, flexible, semi-transparent, colour tunable and free-form devices.[68] Additionally, perovskite solar cells offer the possibility of being commercialised in tandem architectures with silicon PV.[69] Policies encouraging the uptake of organic solar cells for these niche

applications (e.g. for façade integration which may otherwise remain untapped solar energy potential) may provide the needed demand-pull that enabled the price decreases of silicon PV.

While the scope of the potential for organic solar cells has changed since their infancy, advantages like the short energy payback times, the lowest carbon footprint of any energy conversion technology and the potential for large scale applications in the built environment[68] hold important climate mitigation potential[68] – in addition to the significantly larger contribution that will be made by silicon PV. Beyond that also consumer applications to power internet-of-things sensors (low-light application conditions) remain a promising market.

To unlock the potential organic solar cells may have, an increased research focus on addressing the obstacles to commercialisation is necessary. Evaporated organic solar cells currently offer the highest potential for commercialisation as they can rely on proven OLED technology for industrial scale production.[68] However, they remain under-researched in the academic community and suffer from their lower performance relative to their solution processed counterparts. Therefore, the first part of this thesis will address the performance limitations in a state-of-the-art evaporated material system.

In solution processed organic solar cells, the morphological stability remains an issue. Alternative device structures like planar heterojunction solar cells may offer a solution to this but suffer from reduced the reduced performance. In addition, such systems offer valuable insights into the working principles of organic solar cells. Comparative studies on solution processed planar and bulk heterojunction will form the second part of this thesis. The final small chapter will address observations regarding the charge generation in single component devices.

References

(1) Broecker, W. S. Climatic Change: Are We on the Brink of a Pronounced Global Warming? *Science* **1975**, *189* (4201), 460–463. https://doi.org/10.1126/science.189.4201.460.

(2) *The Paris Agreement | UNFCCC*. https://unfccc.int/process-and-meetings/the-paris-agreement (accessed 2024-02-14).

(3) Calvin, K.; Dasgupta, D.; Krinner, G.; Mukherji, A.; Thorne, P. W.; Trisos, C.; Romero, J.; Aldunce, P.; Barrett, K.; Blanco, G.; Cheung, W. W. L.; Connors, S.; Denton, F.; Diongue-Niang, A.; Dodman, D.; Garschagen, M.; Geden, O.; Hayward, B.; Jones, C.; Jotzo, F.; Krug, T.; Lasco, R.; Lee, Y.-Y.; Masson-Delmotte, V.; Meinshausen, M.; Mintenbeck, K.; Mokssit, A.; Otto, F. E. L.; Pathak, M.; Pirani, A.; Poloczanska, E.; Pörtner, H.-O.; Revi, A.; Roberts, D. C.; Roy, J.; Ruane, A. C.; Skea, J.; Shukla, P. R.; Slade, R.; Slangen, A.; Sokona, Y.; Sörensson, A. A.; Tignor, M.; Van Vuuren, D.; Wei, Y.-M.; Winkler, H.; Zhai, P.; Zommers, Z.; Hourcade, J.-C.; Johnson, F. X.; Pachauri, S.; Simpson, N. P.; Singh, C.; Thomas, A.; Totin, E.; Arias, P.; Bustamante, M.; Elgizouli, I.; Flato, G.; Howden, M.; Méndez-Vallejo, C.; Pereira, J. J.; Pichs-Madruga, R.; Rose, S. K.; Saheb, Y.; Sánchez Rodríguez, R.; Ürge-Vorsatz, D.; Xiao, C.; Yassaa, N.; Alegría, A.; Armour, K.; Bednar-Friedl, B.; Blok, K.; Cissé, G.; Dentener, F.; Eriksen, S.; Fischer, E.; Garner, G.; Guivarch, C.; Haasnoot, M.; Hansen, G.; Hauser, M.; Hawkins, E.; Hermans, T.; Kopp, R.; Leprince-Ringuet, N.; Lewis, J.; Ley, D.; Ludden, C.; Niamir, L.; Nicholls, Z.; Some, S.; Szopa, S.; Trewin, B.; Van Der Wijst, K.-I.; Winter, G.; Witting, M.; Birt, A.; Ha, M.; Romero, J.; Kim, J.; Haites, E. F.; Jung, Y.; Stavins, R.; Birt, A.; Ha, M.; Orendain, D. J. A.; Ignon, L.; Park, S.; Park, Y.; Reisinger, A.; Cammaramo, D.; Fischlin, A.; Fuglestvedt, J. S.; Hansen, G.; Ludden, C.; Masson-Delmotte, V.; Matthews, J. B. R.; Mintenbeck, K.; Pirani, A.; Poloczanska, E.; Leprince-Ringuet, N.; Péan, C. *IPCC, 2023: Climate Change 2023: Synthesis Report. Contribution of Working Groups I, II and III to the Sixth Assessment Report of the Intergovernmental Panel on Climate Change [Core Writing Team, H. Lee and J. Romero (Eds.)]. IPCC, Geneva, Switzerland.*, First.; Intergovernmental Panel on Climate Change (IPCC), 2023. https://doi.org/10.59327/IPCC/AR6-9789291691647.

(4) Supran, G.; Oreskes, N. Assessing ExxonMobil's Climate Change Communications (1977–2014). *Environ. Res. Lett.* **2017**, *12* (8), 084019. https://doi.org/10.1088/1748-9326/aa815f.

(5) Milman, O. Revealed: Exxon Made 'Breathtakingly' Accurate Climate Predictions in 1970s and 80s. *The Guardian*. January 12, 2023. https://www.theguardian.com/business/2023/jan/12/exxon-climate-change-global-warming-research (accessed 2023-09-27).

(6) Supran, G.; Rahmstorf, S.; Oreskes, N. Assessing ExxonMobil's Global Warming Projections. *Science* **2023**, *379* (6628), eabk0063. https://doi.org/10.1126/science.abk0063.

(7) Gelles, D. California Sues Giant Oil Companies, Citing Decades of Deception. *The New York Times*. September 16, 2023. https://www.nytimes.com/2023/09/15/business/california-oil-lawsuit-newsom.html (accessed 2024-02-14).

(8) Wallace-Wells, D. *The Uninhabitable Earth, Annotated Edition*. Intelligencer. https://nymag.com/intelligencer/2017/07/climate-change-earth-too-hot-for-humans-annotated.html (accessed 2023-09-25).
(9) Watts, J. David Wallace-Wells on Climate: 'People Should Be Scared – I'm Scared.' *The Guardian*. February 3, 2019. https://www.theguardian.com/environment/2019/feb/03/david-wallace-wells-on-climate-people-should-be-scared-im-scared (accessed 2024-02-14).
(10) Myers, T. A.; Maibach, E. W.; Roser-Renouf, C.; Akerlof, K.; Leiserowitz, A. A. The Relationship between Personal Experience and Belief in the Reality of Global Warming. *Nature Clim Change* **2013**, *3* (4), 343–347. https://doi.org/10.1038/nclimate1754.
(11) Konisky, D. M.; Hughes, L.; Kaylor, C. H. Extreme Weather Events and Climate Change Concern. *Climatic Change* **2016**, *134* (4), 533–547. https://doi.org/10.1007/s10584-015-1555-3.
(12) Sisco, M. R.; Bosetti, V.; Weber, E. U. When Do Extreme Weather Events Generate Attention to Climate Change? *Climatic Change* **2017**, *143* (1), 227–241. https://doi.org/10.1007/s10584-017-1984-2.
(13) Saunders, C.; Grasso, M. T.; Hedges, C. Attention to Climate Change in British Newspapers in Three Attention Cycles (1997–2017). *Geoforum* **2018**, *94*, 94–102. https://doi.org/10.1016/j.geoforum.2018.05.024.
(14) Crellin, C.; MacNeil, R. Extreme Weather Events and Public Attention to Climate Change in Australia. *Climatic Change* **2023**, *176* (9), 121. https://doi.org/10.1007/s10584-023-03601-5.
(15) *Fridays For Future is an international climate movement active in most countries and our website offers information on who we are and what you can do*. Fridays For Future. https://fridaysforfuture.org/ (accessed 2024-02-14).
(16) Hickman, C.; Marks, E.; Pihkala, P.; Clayton, S.; Lewandowski, R. E.; Mayall, E. E.; Wray, B.; Mellor, C.; Susteren, L. van. Climate Anxiety in Children and Young People and Their Beliefs about Government Responses to Climate Change: A Global Survey. *The Lancet Planetary Health* **2021**, *5* (12), e863–e873. https://doi.org/10.1016/S2542-5196(21)00278-3.
(17) Osaka, S. Why Climate 'Doomers' Are Replacing Climate 'Deniers.' *Washington Post*. March 27, 2023. https://www.washingtonpost.com/climate-environment/2023/03/24/climate-doomers-ipcc-un-report/ (accessed 2024-02-14).
(18) Nuttall, P. *Don't listen to the climate doomists*. New Statesman. https://www.newstatesman.com/environment/2022/08/climate-doomism-dont-listen-toxic-narrative (accessed 2024-02-14).
(19) Supran, G.; Oreskes, N. Rhetoric and Frame Analysis of ExxonMobil's Climate Change Communications. *One Earth* **2021**, *4* (5), 696–719. https://doi.org/10.1016/j.oneear.2021.04.014.
(20) Mann, M. E. *The New Climate War: The Fight to Take Back Our Planet*, 1st edition.; Scribe UK: Melbourne London, 2021.

(21) Doyle, J. Where Has All the Oil Gone? BP Branding and the Discursive Elimination of Climate Change Risk. In *Culture, environment and ecopolitics*; Heffernan, N., Wragg, D. A., Eds.; Cambridge Scholars Publishing: Newcastle upon Tyne, UK, 2011; pp 200–225.
(22) Li, M.; Trencher, G.; Asuka, J. The Clean Energy Claims of BP, Chevron, ExxonMobil and Shell: A Mismatch between Discourse, Actions and Investments. *PLOS ONE* **2022**, *17* (2), e0263596. https://doi.org/10.1371/journal.pone.0263596.
(23) Jakob, C. Gegen Das Untergangsdenken. *Blätter für deutsche und internationale Politik*. September 2023, pp 47–56.
(24) Wallace-Wells, D. Beyond Catastrophe: A New Climate Reality Is Coming Into View. *The New York Times*. October 26, 2022. https://www.nytimes.com/interactive/2022/10/26/magazine/climate-change-warming-world.html (accessed 2023-09-25).
(25) Steffen, A. *The Transapocalyptic Now*. The Snap Forward. https://alexsteffen.substack.com/p/the-transapocalyptic-now (accessed 2023-09-25).
(26) Ipcc. *Global Warming of 1.5°C: IPCC Special Report on Impacts of Global Warming of 1.5°C above Pre-Industrial Levels in Context of Strengthening Response to Climate Change, Sustainable Development, and Efforts to Eradicate Poverty*, 1st ed.; Cambridge University Press, 2022. https://doi.org/10.1017/9781009157940.
(27) Oreskes, N. Beyond the Ivory Tower. The Scientific Consensus on Climate Change. *Science* **2004**, *306* (5702), 1686. https://doi.org/10.1126/science.1103618.
(28) *The Glasgow Climate Pact*. UN Climate Change Conference (COP26) at the SEC – Glasgow 2021. https://webarchive.nationalarchives.gov.uk/ukgwa/20230418183423mp_/https://ukcop26.org/the-glasgow-climate-pact/ (accessed 2024-02-14).
(29) Birol, D. F. World Energy Outlook 2022.
(30) *Copernicus: In 2024, the world experienced the warmest January on record | Copernicus*. https://climate.copernicus.eu/copernicus-2024-world-experienced-warmest-january-record (accessed 2024-02-14).
(31) Mahesh, L., Maria,Sperling, Frank,Liptow, Holger,Mausolf, Elisabeth,Verheyen, Roda,Agrawala, Shardul,Caspary, Georg,Paris, Ramy,Kashyap, Arun,Sharma, Arun,Abeygunawardena, Piya,Vyas, Yogesh,Knill, Philipp,Foy, Tim,Harrold, Melissa,Steele, Paul,Tanner, Thomas,Hirsch, Danielle,Oosterman, Maresa,Rooimans, Jaap,Mathur, Ajay,Debois, Marc,Sharma. *Poverty and Climate Change : Reducing the Vulnerability of the Poor through Adaptation*; Working Paper 52176; World Bank Group, 2009. https://documents.worldbank.org/en/publication/documents-reports/documentdetail/534871468155709473/Poverty-and-climate-change-reducing-the-vulnerability-of-the-poor-through-adaptation (accessed 2024-08-02).
(32) *Country Climate and Development Reports (CCDRs)*. World Bank. https://www.worldbank.org/en/publication/country-climate-development-reports (accessed 2024-02-14).
(33) Wirth, D. H.; Ise, F. Recent Facts about Photovoltaics in Germany.
(34) Schrems, I.; Fiedler, S. Gesellschaftliche Kosten Der Atomenergie in Deutschland, 2020. https://www.google.com/url?sa=t&rct=j&q=&esrc=s&source=web&cd=&cad=rja&uact

=8&ved=2ahUKEwj509KJp62EAxWcZEEAHX0LA1cQFnoECA4QAQ&url=https%3A%2F%2Ffoes.de%2Fpublikationen%2F2020%2F2020-09_FOES_Kosten_Atomenergie.pdf&usg=AOvVaw1O3ovrb_deiBJ9u8gwCCxr&opi=89978449.

(35) Nemet, G. F. Beyond the Learning Curve: Factors Influencing Cost Reductions in Photovoltaics. *Energy Policy* **2006**, *34* (17), 3218–3232. https://doi.org/10.1016/j.enpol.2005.06.020.

(36) Ray, D. Lazard's Levelized Cost of Energy Analysis—Version 15.0. **2021**.

(37) Levelized Costs of New Generation Resources in the Annual Energy Outlook 2022. **2022**.

(38) Kost, C.; Shammugam, S.; Fluri, V.; Peper, D.; Davoodi Memar, A.; Schlegl, T. Stromgestehungskosten Erneuerbare Energien. **2021**.

(39) Wronski, R. WAS BRAUNKOHLESTROM WIRKLICH KOSTET. **2018**.

(40) Parry, I. W. H.; Black, S.; Vernon, N. Still Not Getting Energy Prices Right: A Global and Country Update of Fossil Fuel Subsidies, 2021. https://www.imf.org/en/Publications/WP/Issues/2021/09/23/Still-Not-Getting-Energy-Prices-Right-A-Global-and-Country-Update-of-Fossil-Fuel-Subsidies-466004 (accessed 2023-09-26).

(41) *Becquerel: Mémoire sur les effets électriques produits... - Google Scholar*. https://scholar.google.com/scholar?cluster=5130257220201923997&hl=de&as_sdt=2005&sciodt=0,5&as_ylo=2015 (accessed 2016-02-11).

(42) Effect of Light on Selenium During the Passage of An Electric Current *. *Nature* **1873**, *7* (173), 303–303. https://doi.org/10.1038/007303e0.

(43) Perlin, J. *From Space to Earth: The Story of Solar Electricity*; Harvard University Press: Cambridge, Mass, 2002.

(44) Times, S. to T. N. Y. Vast Power of the Sun Is Tapped By Battery Using Sand Ingredient; NEW BATTERY TAPS SUN'S VAST POWER. *The New York Times*. April 26, 1954. https://www.nytimes.com/1954/04/26/archives/vast-power-of-the-sun-is-tapped-by-battery-using-sand-ingredient.html (accessed 2023-09-25).

(45) Philipps, D. S.; Ise, F.; Warmuth, W.; GmbH, P. P. Photovoltaics Report.

(46) Nemet, G. F. *How Solar Energy Became Cheap: A Model for Low-Carbon Innovation*, 1st edition.; Routledge: London ; New York, NY, 2019.

(47) Green, M. A. Silicon Photovoltaic Modules: A Brief History of the First 50 Years. *Progress in Photovoltaics: Research and Applications* **2005**, *13* (5), 447–455. https://doi.org/10.1002/pip.612.

(48) Kavlak, G.; McNerney, J.; Trancik, J. E. Evaluating the Causes of Cost Reduction in Photovoltaic Modules. *Energy Policy* **2018**, *123*, 700–710. https://doi.org/10.1016/j.enpol.2018.08.015.

(49) Hart, D. M. The Impact of China's Production Surge on Innovation in the Global Solar Photovoltaics Industry. *INFORMATION TECHNOLOGY* **2020**.

(50) Gillis, J. Sun and Wind Alter Global Landscape, Leaving Utilities Behind. *The New York Times*. September 14, 2014. https://www.nytimes.com/2014/09/14/science/earth/sun-and-wind-alter-german-landscape-leaving-utilities-behind.html (accessed 2024-02-15).

(51) *How Germany helped bring down the cost of PV*. Energy Transition. https://energytransition.org/2016/01/how-germany-helped-bring-down-the-cost-of-pv/ (accessed 2023-09-25).

(52) O'Regan, B.; Grätzel, M. A Low-Cost, High-Efficiency Solar Cell Based on Dye-Sensitized Colloidal TiO2 Films. *Nature* **1991**, *353* (6346), 737–740. https://doi.org/10.1038/353737a0.

(53) Halls, J. J. M.; Walsh, C. A.; Greenham, N. C.; Marseglia, E. A.; Friend, R. H.; Moratti, S. C.; Holmes, A. B. Efficient Photodiodes from Interpenetrating Polymer Networks. *Nature* **1995**, *376* (6540), 498–500. https://doi.org/10.1038/376498a0.

(54) Yu, G.; Gao, J.; Hummelen, J. C.; Wudl, F.; Heeger, A. J. Polymer Photovoltaic Cells : Enhanced Efficiencies via a Network of Internal Donor-Acceptor Heterojunctions. *Science* **1995**, *270* (5243), 1789–1791.

(55) Kojima, A.; Teshima, K.; Shirai, Y.; Miyasaka, T. Organometal Halide Perovskites as Visible-Light Sensitizers for Photovoltaic Cells. *J. Am. Chem. Soc.* **2009**, *131* (17), 6050–6051. https://doi.org/10.1021/ja809598r.

(56) Green, M. A.; Dunlop, E. D.; Yoshita, M.; Kopidakis, N.; Bothe, K.; Siefer, G.; Hao, X. Solar Cell Efficiency Tables (Version 63). *Progress in Photovoltaics: Research and Applications* **2024**, *32* (1), 3–13. https://doi.org/10.1002/pip.3750.

(57) Green, M. A.; Dunlop, E. D.; Yoshita, M.; Kopidakis, N.; Bothe, K.; Siefer, G.; Hinken, D.; Rauer, M.; Hohl-Ebinger, J.; Hao, X. Solar Cell Efficiency Tables (Version 64). *Progress in Photovoltaics: Research and Applications* **2024**, *32* (7), 425–441. https://doi.org/10.1002/pip.3831.

(58) Cornaro, C.; Di Carlo, A. Organic Photovoltaics for Energy Efficiency in Buildings. In *Nano and Biotech Based Materials for Energy Building Efficiency*; Pacheco Torgal, F., Buratti, C., Kalaiselvam, S., Granqvist, C.-G., Ivanov, V., Eds.; Springer International Publishing: Cham, 2016; pp 321–355.

(59) Chemisana, D.; Moreno, A.; Polo, M.; Aranda, C.; Riverola, A.; Ortega, E.; Lamnatou, Chr.; Domènech, A.; Blanco, G.; Cot, A. Performance and Stability of Semitransparent OPVs for Building Integration: A Benchmarking Analysis. *Renewable Energy* **2019**, *137*, 177–188. https://doi.org/10.1016/j.renene.2018.03.073.

(60) Emmott, C. J. M.; Röhr, J. A.; Campoy-Quiles, M.; Kirchartz, T.; Urbina, A.; Ekins-Daukes, N. J.; Nelson, J. Organic Photovoltaic Greenhouses: A Unique Application for Semi-Transparent PV? *Energy Environ. Sci.* **2015**, *8* (4), 1317–1328. https://doi.org/10.1039/C4EE03132F.

(61) Meitzner, R.; Schubert, U. S.; Hoppe, H. Agrivoltaics—The Perfect Fit for the Future of Organic Photovoltaics. *Advanced Energy Materials* **2021**, *11* (1), 2002551. https://doi.org/10.1002/aenm.202002551.

(62) La Notte, L.; Giordano, L.; Calabrò, E.; Bedini, R.; Colla, G.; Puglisi, G.; Reale, A. Hybrid and Organic Photovoltaics for Greenhouse Applications. *Applied Energy* **2020**, *278*, 115582. https://doi.org/10.1016/j.apenergy.2020.115582.

(63) Shi, H.; Xia, R.; Zhang, G.; Yip, H.-L.; Cao, Y. Spectral Engineering of Semitransparent Polymer Solar Cells for Greenhouse Applications. *Advanced Energy Materials* **2019**, *9* (5), 1803438. https://doi.org/10.1002/aenm.201803438.

(64) Magadley, E.; Teitel, M.; Peretz, M. F.; Kacira, M.; Yehia, I. Outdoor Behaviour of Organic Photovoltaics on a Greenhouse Roof. *Sustainable Energy Technologies and Assessments* **2020**, *37*, 100641. https://doi.org/10.1016/j.seta.2020.100641.

(65) Li, M.; Igbari, F.; Wang, Z.-K.; Liao, L.-S. Indoor Thin-Film Photovoltaics: Progress and Challenges. *Advanced Energy Materials* **2020**, *10* (28), 2000641. https://doi.org/10.1002/aenm.202000641.

(66) Bai, F.; Zhang, J.; Zeng, A.; Zhao, H.; Duan, K.; Yu, H.; Cheng, K.; Chai, G.; Chen, Y.; Liang, J.; Ma, W.; Yan, H. A Highly Crystalline Non-Fullerene Acceptor Enabling Efficient Indoor Organic Photovoltaics with High EQE and Fill Factor. *Joule* **2021**, *5* (5), 1231–1245. https://doi.org/10.1016/j.joule.2021.03.020.

(67) Park, S. Y.; Labanti, C.; Luke, J.; Chin, Y.-C.; Kim, J.-S. Organic Bilayer Photovoltaics for Efficient Indoor Light Harvesting. *Advanced Energy Materials* **2022**, *12* (3), 2103237. https://doi.org/10.1002/aenm.202103237.

(68) Riede, M.; Spoltore, D.; Leo, K. Organic Solar Cells—The Path to Commercial Success. *Advanced Energy Materials* **2021**, *11* (1), 2002653. https://doi.org/10.1002/aenm.202002653.

(69) Aydin, E.; Allen, T. G.; De Bastiani, M.; Razzaq, A.; Xu, L.; Ugur, E.; Liu, J.; De Wolf, S. Pathways toward Commercial Perovskite/Silicon Tandem Photovoltaics. *Science* **2024**, *383* (6679), eadh3849. https://doi.org/10.1126/science.adh3849.

2

FUNDAMENTALS OF ORGANIC PHOTOVOLTAICS

2. Fundamentals of Organic Photovoltaics

This chapter addresses the basics of solar cell operation in general and organic solar cells in particular. It summarises the origins of semi-conductivity in organic materials and the implications of their "soft nature". Examples of organic semiconductors for solar cell applications will be provided. Another focus will be on the differences in device architectures and manufacturing techniques – especially the difference between evaporation and solution-processing of organic semiconductors. Throughout, the scientific and commercial challenges facing organic solar cell researchers and engineers will be pointed out.

The interested reader is further encouraged to consult the following publications giving a more detailed overview of the physics of solar cells.[1–3] Many of the concepts and derivations are also explained in great detail in the PhD theses by Scot Wheeler and Jiaying Wu.[4,5]

2.1. Solar Cell Operation

Energy conversion in a solar or photovoltaic cell require three crucial steps: (1) light absorption leading to the formation of an excited state i.e., a bound pair of negatively charged electron and positively charged hole quasi particle, (2) separation of the excited electron and hole to create free charges and generate a potential difference, and (3) the extraction of the free charges by means of the potential difference into the external circuit.

In order to optimise the solar cell efficiency of converting sunlight into electrical energy all of the above three steps need to be optimised. The difference between the ground state energy and the excited state energy (the bandgap, E_g) sets the intrinsic limit to how many photons of the solar spectrum can be absorbed. Only those with an energy higher than the bandgap will lead to the formation of an electronically excited state. Any loss of absorption due to a low absorptivity of the photoactive material or reflective losses further extrinsically limits the maximum achievable current. An energetic difference is needed to prevent the excited state from falling back into the ground state or "recombine" and instead separate the excited state into free charges. In inorganic semiconductors free charges form spontaneously and are subsequently separated by the electric field provided by a so-called p-n-junction. While a p-n-junction consists of differently doped layers of the same inorganic semiconductor, organic solar cells use two materials with different energetic levels to provide a driving force for excited state separation as well as for spatial separation of free charges. The choice of the bandgap and

the energy level difference of the materials also set the upper limit to the achievable potential difference that drives charges through the external circuit to do electrical work. Finally, any resistance to charge extraction or recombination of free charges with opposite signs to form a ground state reduces the potential of the extracted charges and the maximum extractable current.

The trade-off between maximising current generation by choosing a small bandgap material and maximising the potential of the extracted charges (i.e. the voltage) by choosing a large bandgap material defines a fundamental intrinsic limit to a solar cell.[6] Of all the solar power incident on a solar cell only 33.7% can be converted into electrical energy. This limit may be broken when stacking multiple solar cells with different bandgap materials.[7]

2.2. Organic Semiconductors

2.2.1. The Origin of Semiconductivity in Organic Materials

Semiconductors fulfil the above criteria of a suitable bandgap. Inorganic semiconductors like silicon, gallium arsenide or cadmium telluride have suitable properties for solar cell applications due to their suitable bandgaps and good charge transport through their highly ordered crystal structure. Record silicon solar cells with a bandgap of 1.1 eV come close to their maximum theoretical conversion efficiency of 32% with 26.8% confirmed, recently.[8]

Here, the focus will be on organic semiconductors. Rather than consisting of individual atoms in a highly ordered crystal structure, these are molecular materials based mainly on carbon and hydrogen with additional atoms such as most commonly oxygen, nitrogen, sulphur or halides all covalently bonded. Organic semiconductors can therefore be synthesised from organic starting materials derived from petrochemicals or organic matter. As the exact electronic properties depend on the molecular structure rather than the fundamental properties of the atoms it is made up of, this means an infinite number of organic semiconductor materials with differing characteristics could possibly be synthesized.

Carbon in its atomic configuration has four valence electrons ($2s^2 2p_x^1 2p_y^1 2p_z^0$) and therefore reaches a quantum-mechanically stable closed-shell configuration upon formation of four covalent bonds. Semi-conductivity in carbon based organic materials arises from the formation of double bonds between two carbon atoms in addition to each carbon atom being covalently bonded to two other atoms. This puts the carbon atoms in a so called sp^2 hybridised state meaning that the 2s orbital and the $2p_x$ and $2p_y$ orbital form three covalent σ-bonds in

the x-y-plane. This leaves a single electron in the $2p_z$ orbital perpendicular to the x-y-plane. This electron is less tightly bound to the nucleus and can form a so called π-bond with the $2p_z$ electron on an adjacent carbon atom in the same sp^2 hybridisation. The two $2p_z$ atomic orbitals formed two π-molecular orbitals, one bonding (π) and one antibonding (π*). This is illustrated in **Figure 2.2.1 (a)**.

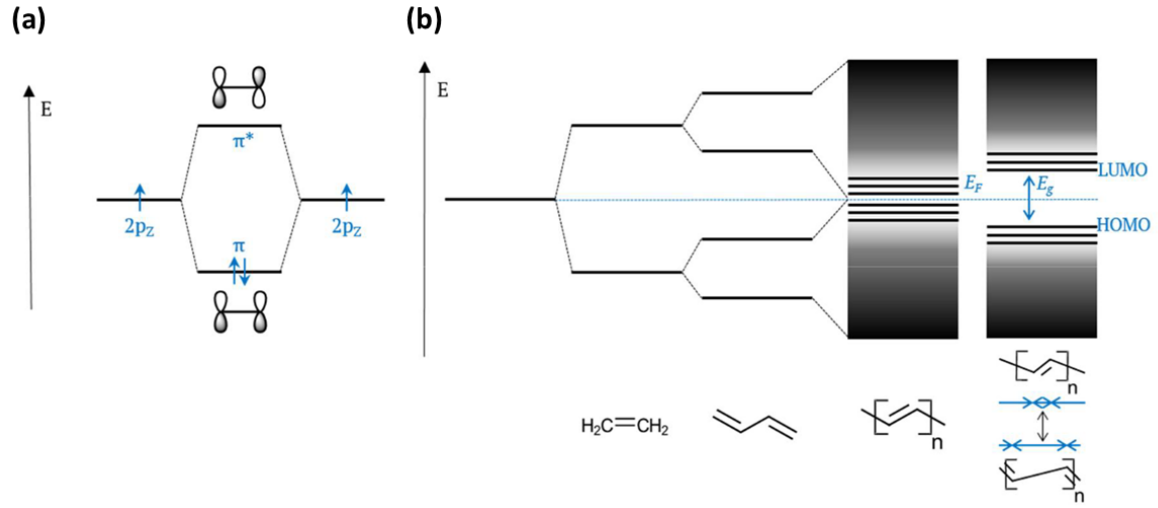


Figure 2.2.1. (a) The linear combination of atomic $2p_z$ orbitals leads to the formation of a bonding and antibonding π-molecular orbital. **(b)** Illustration of the formation of a band like structure upon extending the length of an alternating alkene chain. The asymmetric contraction and elongation of bonds resulting in Peierls distortion is also shown. Image obtained from the thesis by Scot Wheeler.[4]

In the ground state, the bonding and antibonding π-molecular orbitals are doubly filled and empty, respectively, making them the so called highest occupied and lowest occupied molecular orbital (HOMO and LUMO). The energy difference between the HOMO and the LUMO defines the bandgap of the material.

If a chain of carbon atoms is made up of alternating single and double bonds (i.e. polyacetylene), the π-molecular orbitals of neighbouring carbons overlap leading to the additional splitting of the π and π* orbitals for every additional atom in the chain. This leads to the narrowing of the gap between the HOMO and the LUMO and the emergence of a band like structure of a valence and conduction band, respectively. Such a chain of double bonds is called a π-conjugated system. For the more physics than chemistry inclined reader, imagine a particle in a 1-D box. As the box becomes wider, the energy difference between the quantum mechanical states becomes smaller. The box is the π-conjugated system.

However, as the π-conjugated system becomes infinitely long, the bandgap does not converge to zero due to what is called Peierls distortion.[9] This phenomenon describes an asymmetric

vibrational distortion of the carbon bonds due to the presence of electron density that stabilises the π and destabilises the π* orbital increasing the bandgap (see **Figure 2.2.1 (b)**).

2.2.2. Bandgap Engineering

Photovoltaic or other applications require organic semiconductors with specific application dependent energy levels for optimal performance. A variety of design strategies for conjugated small molecules and polymers have been studied previously and can be found summarised elsewhere.[10–15] For commercialisation, the trade-off between the synthetic complexity of materials and their performance has also been a key focus.[13,16–18]

As described above, the bandgap of the organic semiconductor depends critically on the size of the π-conjugated system. The inclusion of conjugated ring structures may additionally increase the size of the conjugated system and decrease the bandgap of the material while making the materials more rigid and crystalline as discussed below. Besides aromatic pure hydrocarbon ring structures (like benzene, naphthalene etc.), structures including heteroatoms (thiophene, furane, selenophene, pyrrole etc.) can be used. The use of electron withdrawing or donating substituents attached to the conjugated backbone enables further tuning of the electronic bandgap (i.e. substitution of hydrogen for fluorine, chlorine or a methyl group).[15] A key strategy to narrow the bandgap and harvest a greater proportion of the solar spectrum, is the introduction of organic semiconductors comprising electron-rich and electron-deficient units adjacent to each other that lead to the hybridization of the of the molecular orbitals.[14] Examples are so called push-pull polymers (i.e. PM6) or small molecules with a so called acceptor-donor-acceptor structure (i.e. IT-4F, Y6 or DCV-V-Fu-Ind-Fu-V) that will be introduced later.

2.2.3. Processing of Organic Semiconductors

In order to deposit a solid film of organic semiconductor material on a substrate, generally two methods have been used: the material can either be coated/printed from solution or thermally evaporated. Other less common processing methods include solid-state melting deposition[19–21] or in-situ synthesis[22] methods. In both, solution- or vacuum-processing cases, a low substrate temperature can generally be maintained allowing for flexible plastic substrates like polyethylene terephthalate (PET) to be used. This in turn enables large scale continuous deposition on PET substrates in roll-to-roll processes demonstrated for solution and evaporation based deposition alike.[23,24] While there are potential cost advantages for solution-

based techniques (especially due to the lower upfront investment), roll-to-roll evaporation based deposition of semiconductors was already shown to be commercially scalable in the field of organic light emitting diodes and more recently organic solar cells.[25–29]

While in principle, infinite combinations of large conjugated systems can be synthesised, limits to this are set by the viability of the synthetic route and the need for processability of the organic semiconductor. Processability from organic solvents requires the addition of aliphatic chains to the conjugated core of the organic semiconductor. The size of the conjugated core is less critical here if the added solubilising chains enable sufficient solvent interaction. Therefore large, conjugated structures including polymers and extensive aromatic ring structures may be deposited from organic solvents.

Evaporation on the other hand requires the molecules to be small enough to be sublimed in a vacuum. The sublimation temperature, that is determined mainly by the size of the molecule and intermolecular interactions of the solid, needs to remain below the temperature at which the material thermally decomposes. Overheating the substrate is not a relevant concern as the heat transfer of a thin layer of organic semiconductors deposited (< 100 nm) is minimal.

Figure 2.2.2 shows the chemical structure of selected materials that are central to this thesis. The top row shows two small molecule materials for vacuum-thermal processing while the materials at the bottom are a polymer and a “small” molecule that can be processed from organic solvents. The solubilising aliphatic chains of the latter are highlighted as well as the moieties with electron donating and accepting character. Other than these alkane chains the molecules are fully conjugated. Note here that “small” is relative here as the molecular weight of the solution processable small molecule is more than twice that of the evaporable small molecules.

The shape of the molecules as well as the presence of the solubilising chains will affect how the materials stack in solid films with implications for the electronic properties of the materials as addressed in more detail below. Differences in the operation of solution-processed and vacuum-processed organic solar cells are the topic of **Subchapter** Error! Reference source n ot found.**.1**.

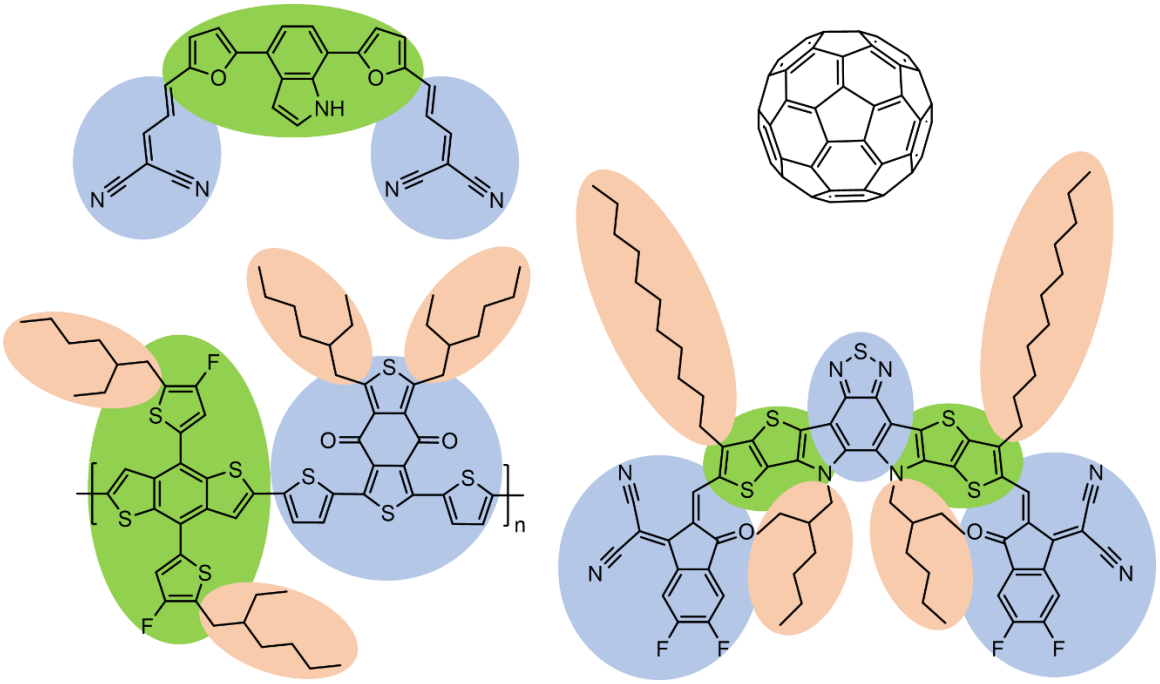


Figure 2.2.2. Chemical structure of semiconducting materials for organic solar cells manufactured by evaporation **(top)** and solution processing **(bottom).** The highlighted aliphatic chains are added to aid the solubility of the materials in organic solvents. Blue and green highlighted groups signify the electron accepting and donating groups, respectively. The names of the trivial names of the compounds are DCV-V-Fu-Ind-Fu-V **(top left)** and C_{60}-fullerene **(top right)**, PM6 **(bottom left)** and Y6 **(bottom right).** A comparison of the photovoltaic properties of these compounds will be provided in **Chapter 4**.

2.2.4. Disorder in Organic Semiconductors

The nature of the covalently bonded organic materials makes them “soft materials” prone to bending and twisting caused by their surroundings in solid films. Effectively, this can result in the breaking of the conjugation due to insufficient overlap of neighbouring π-orbitals. This is called static disorder and leads to local variations of the bandgap, so called tailstates within the valence and conduction band (see **Figure 2.2.3**). Furthermore, also chemical impurities can cause the presence of additional deeper “trap states” inside the bandgap (i.e., charge carriers in these states cannot be promoted to the band edge through their thermal energy). The functional shape of the bandtail density of states (DoS) depicted in **Figure 2.2.3** has been experimentally shown to have a Gaussian or exponential dependence on the energetic position.[30–34]

Additional distortions, as already mentioned when discussing Peierls distortion, occur dynamically due to the temperature dependent molecular vibrations and the interaction of the fluctuating electron density with surrounding nuclei. This electron-phonon interaction leads

to a stabilisation and localisation of the charge i.e. the formation of so called polarons. Due to the transient nature of the vibrations this is termed dynamic disorder. It overlays with the static disorder and causes an additional temperature dependent Gaussian broadening to the experimentally observed disorder. These concepts of disorder are central to the characteristics of organic semiconducting materials and the performance of organic solar cells.

Besides the density and orientation of the packing in solid films, the degree of static and dynamic disorder is clearly related to the rigidity of the organic semiconductor material in question. Poly-alkene chains depicted above in **Figure 2.2.1 (b)** are prone to twisting and the loss of conjugation. Incorporating aromatic ring structures such as benzene, furan, pyrrole or thiophene enables the synthesis of larger, more rigid conjugated systems. Additionally, organic chemists may design structures that make use of van der Waals forces between heteroatoms to aid the planarization of a conjugated system.[35] A range of publications focus on the different materials commonly used in vapour-[36] and solution processed organic solar cells[37].

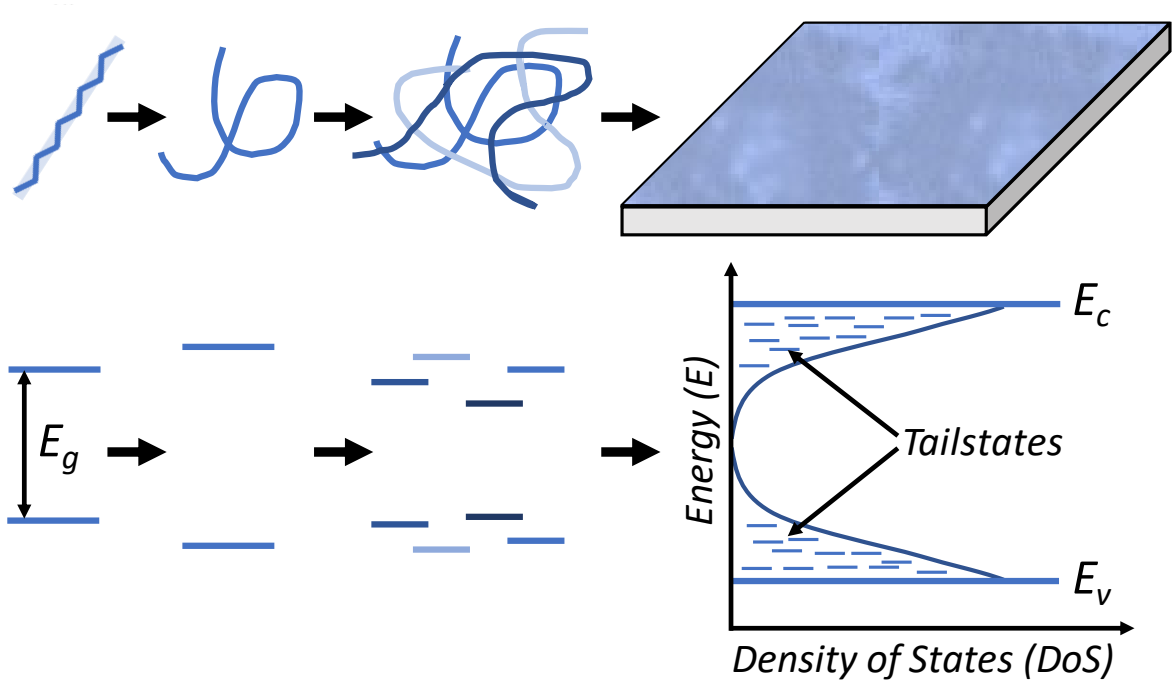


Figure 2.2.3. Visualisation of the effect of static disorder in organic semiconductors. The bandgap (E_g) changes when moving from an isolated, straight, conjugated alkene, to a bent chain, to mixing several chains and eventually a solid film consisting of many polymer chains with the emergence of a band of tailstates inside the gap of valence and conduction band (E_V and E_C, respectively).

2.2.5. Aggregation Dependent Effects on Energetic Levels

While torsion of conjugated molecules, especially polymers, in solid films can cause the loss of planarity and energetic disorder, close packing with surrounding molecules can also lead to the overlap of neighbouring π-orbital systems. Especially in small and/or regularly stacking organic semiconductors this has been shown to lead to changes of the energetic levels of the material caused. Experimentally such behaviour may be evident from a shift in the absorption or emission spectrum when moving from an isolated molecule (in solution) to tightly packed molecules (in a solid film).[38–43]

Besides the interaction of neighbouring π-conjugated systems, electrostatic interactions between neighbouring polar molecules have also been observed that can cause shifts of the E_C and E_V energy levels. In evaporated films for OLED applications, the highly anisotropic packing of molecules with an intrinsic dipole moment led to the observation of a "giant surface potential".[44–47] However, many molecules with a strong dipole moment stack alternatingly leading to the cancellation of any significant effect on the band energetics.[48,49] Additionally, many small molecules relevant to OSCs possess a point symmetric structure with a negligible dipole moment. In these point symmetric molecules, interactions of charges with the quadrupole of neighbouring molecules have been shown to be the dominant electrostatic interaction.[50–52] Due to the strong distance dependence of the electrostatic field (r^{-3}), particularly tightly stacking planar molecules with a face-on orientation are affected by this interaction.[52] Face-on refers to the stacking in the direction of the p_z atomic orbitals that form the π-molecular orbitals. This is often termed π-π-stacking and also leads to strong inductive effects. Differentiation between the two effects may be possible as the electrostatic effects shift both the HOMO and LUMO energy level by the same amount while inductive effects typically cause a narrowing of the bandgap.[52]

2.2.6. Charge Transport in Organic Semiconductors

In inorganic semiconductors, the high degree of structural order and the (relatively) low interaction of charge carriers with lattice phonons enables band like charge transport. In organic semiconductors, both, the static disorder and the dynamic polaron disorder can cause the localisation of charge carriers and inhibit the band like transport of charge carriers in the π-conjugated system, i.e., along an alternating alkene chain shown in **Figure 2.2.1 (b)**. Instead, localised charge carriers "hop" between different energetic sites which is enabled by

their thermal energy. For a low polaron binding energy (relative to the thermal energy) the transport will become band-like.

In addition to this intramolecular transport, charge carriers can also be transferred between different molecules. The rate at which such intermolecular charge transfer occurs is often described by Marcus theory and crucially depends on three parameters: (1) the overlap of the neighbouring molecules' molecular orbitals that depends on the structural order of the molecules in the bulk of the material (i.e., π-π-stacking), (2) the rigidity of the molecules that determines the reorganisation energy related to the charge transfer process, and (3) the thermal energy of the system. Intermolecular charge transfer is furthermore critical to generating free charges as will be discussed in more detail below.

2.3. Device Structure of Organic Solar Cells

2.3.1. Single Material Devices

The first evidence of the photovoltaic effect in solid organic semiconductor devices (1960s to 1970s) was observed when placing a single organic semiconductors between two metal electrodes with different work function.[53] Power conversion efficiencies of such device structures remained low due to the low yield of free charges from the excitons generated upon light absorption. Only under an applied electric field, a photocurrent could be measured.[54] In contrast to inorganic semiconductors, the dielectric constant of organic semiconductors is very low (< 5 versus > 12, respectively). While light absorption in inorganic semiconductors leads to direct efficient free charge generation, it leads to the formation of coulombically bound excitons in organic semiconductors due to the poor dielectric screening of the charges by the surrounding material. Typical binding energies are of the order of 0.1 to 0.3 eV in organics, while inorganics such as silicon or also perovskites they are typically around 0.01 eV.[55,56] Overcoming this binding energy requires the presence of an energetic offset.

2.3.2. Organic Planar Heterojunction

The first appreciable power conversion efficiency of almost 1% in an organic solar cell was reported by Tang in 1986.[57] By layering two different materials (CuPc and a perylene derivative), that possess different HOMO/LUMO levels, on top of each other, a driving force at the interface was created to separate the bound excitons into free charges without the need of an externally applied field. For this to occur, the excitons have to diffuse to the interface where they could be separated by charge transfer. By naming convention, the material with

the higher lying LUMO that donates an electron is termed the donor and the other material the (electron) acceptor. In principle, however, excitons can also be generated in the acceptor material and free charge generation occurs via hole transfer from the acceptor to the donor. Thereby the use of two materials in a heterojunction also enables complimentary absorption for additional photocurrent generation.

Exciton diffusion is an energy transfer process that occurs via Förster or Dexter energy transfer mechanism.[58] The typical lifetime of excitons is of the order of 0.1 to 1 ns which means that they can typically diffuse about 4 – 20 nm before decaying to the ground state.[55,58–61] Therefore, only absorption events that lead to the formation of an excitons within this exciton diffusion distance (L_D) away from the charge generating interface lead to charge generation. This limits the thickness of the planar heterojunction to the exciton diffusion length which in turn limits the absorption of the organic films and therefore the maximum achievable current in such planar heterojunction (PHJ) organic solar cells.

2.3.3. Organic Bulk Heterojunction

A similar problem had also arisen for solar cells using dye molecules as photosensitizers on top of wide bandgap inorganic semiconductors (dye-sensitized solar cells, DSSC). The low exciton diffusion length and mobility of charge carriers in the dye molecules mandated the use of a monomolecular layer sandwiched between contact layers for efficient charge separation and extraction. In both cases, the solution came through dramatically increasing the surface area of the material interface.

In 1991, O'Regan and Grätzel introduced a nano-porous titania scaffold for the dye molecules that dramatically increase the thickness and yet maintain a monolayer coverage of the dye. Infiltration of the pores by a liquid electrolyte made it possible to increase absorption while allowing for good charge separation and extraction yields.[62]

Yu *et al.* and Halls *et al.* in 1995 fully replaced the planar heterojunction with the so-called bulk heterojunction (BHJ).[63,64] Rather than depositing the donor (D) and acceptor (A) material on top of each other creating a planar junction, both components are blended and (ideally) phase separate on a length scale of the exciton diffusion length to allow for efficient exciton harvesting at the interface while also maintaining connecting pathways for charge extraction in the respective phases. By enabling efficient exciton separation at film thicknesses exceeding the exciton diffusion length, this can dramatically increase the maximum achievable

photocurrent while increasing the absorption in thick active layers. Efficient BHJs with active layer thicknesses in excess of 400 nm have been demonstrated.[65–67] **Figure 2.3.1** shows a schematic representation of the two different types of organic heterojunction. It should be noted that Hiramoto *et al.* already introduced a precursor to the BHJ architecture with a three-layer system consisting of a blended layer of two organic semiconductors sandwiched by a neat layer of each material to either side.[68]

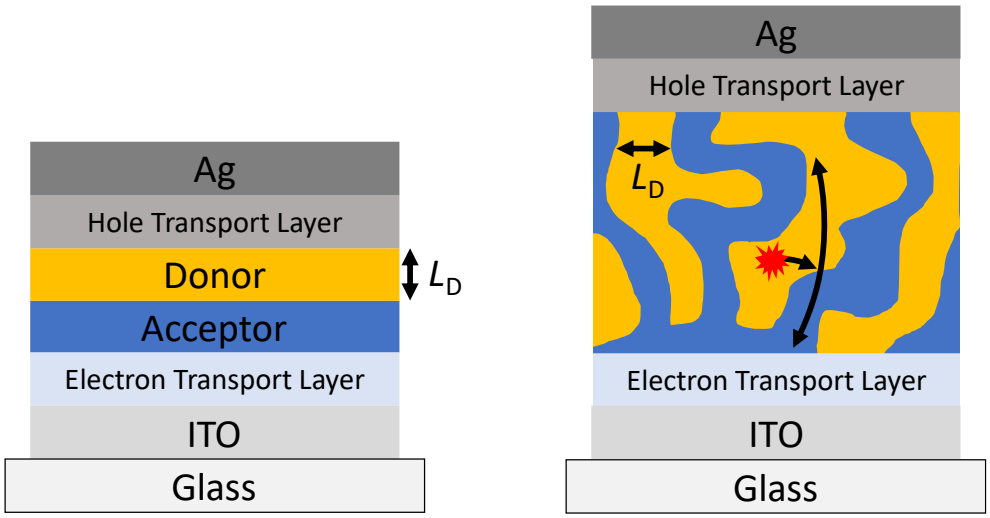


Figure 2.3.1. Schematic representation of the planar and bulk heterojunction device structure (left and right, respectively). The dimensions of the donor and acceptor phases are referenced to the exciton diffusion length (L_D). In the bulk heterojunction the pathway of the exciton diffusion to the donor/acceptor interface leading to charge transfer is depicted. Following that, the charge transfer state must be separated which is followed by extraction of the free charges to the respective transport layers as indicated by arrows. Additionally, the interlayers and electrodes in the inverted structure are shown, as discussed later in the text.

The introduction of the BHJ marked a breakthrough for the field of organic photovoltaics. Until today, all high performance OSCs, including the current efficiency record of more than 19%, were achieved using this concept.[8] And yet, the introduction of the BHJ also posed significant challenges to the field of OPV. Increasing the domain size too much leads to incomplete exciton separation. Highly intermixed blends on the other hand may introduce a large degree of disorder and inhibit the extraction of charges out of the BHJ. Achieving such an optimum morphology requires donor and acceptor materials with appropriate miscibility and intermolecular interaction (in addition for the appropriate energetics relevant for charge separation).[69,70] Additionally, the optimum BHJ morphology may not be thermodynamically stable.[71]

While BHJs can be deposited from thermal co-evaporation of the D and A component as well as solution-processing from a single solution,[27] achieving the optimum morphology often requires lengthy trial-and-error optimisation of the processing conditions (that more recently led to AI guided, automated procedures to optimise the parameter space).[72–74] A brief discussion of the active layer characteristics and their influence on the performance parameters of organic solar cells will follow below.

2.3.4. Interlayers and Electrodes

This section discusses the interlayer and electrode materials already shown in **Figure 2.3.1**. In order to extract the photocurrent generated in the active layer to the external circuit, electrodes must be applied to the active layer out of which at least one has to be transparent to allow for light to enter the photoactive layer. Typically, the transparent electrode is the one deposited on the transparent substrate (glass or PET) and typically is a transparent conductive oxide such as indium tin oxide (ITO) that can be deposited by sputtering. The other electrode can be a metal with high conductivity (e.g., silver). It can also act as a reflective surface for unabsorbed light to enter back into the active layer to maximise charge generation. For semi-transparent applications both electrodes need to be transparent.[75,76] **Figure 2.3.1** depicts the so called “inverted architecture” where the transparent electrode at the bottom forms the cathode, while the opaque top electrode is the anode.

Additionally, interlayers are included that serve two main purposes: (1) the better energy level matching of the active layer with the respective electrode work function and (2) the blocking of charge carriers from reaching the wrong electrode.[77] The latter would result in a loss of chemical potential due to surface recombination and may particularly occur in the BHJ architecture where the acceptor material is also in contact with the anode and the donor with the cathode. **Figure 2.3.2** illustrates the energetic cascade of the organic solar cell that provides a driving force for charge generation and extraction. It further depicts the electron and hole blocking character of the hole and electron transport layer, respectively.

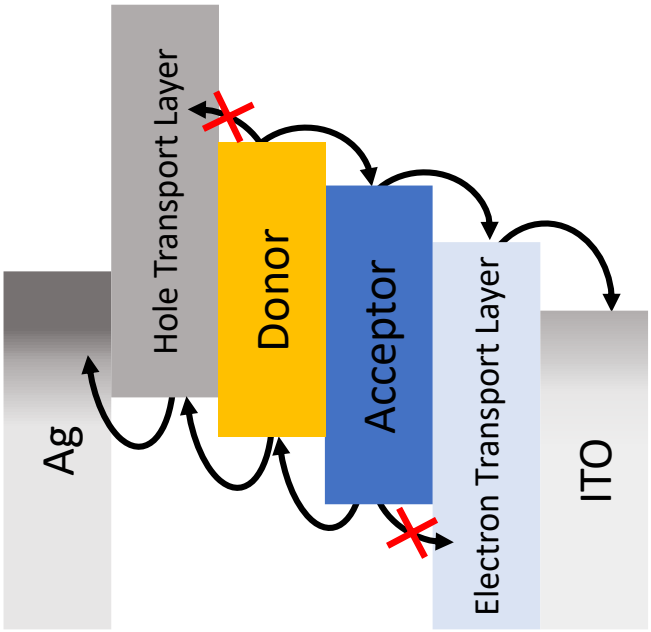


Figure 2.3.2. Exemplary energy band diagram depicting the energy level offsets of photoactive layer, interlayers and electrodes. Note that, in a BHJ, the donor and acceptor are also in contact with the opposite transport layer.

2.4. Device Operation of Organic Solar Cells

2.4.1. Current-Voltage Characteristics of Solar Cells

Due to the asymmetry arising from the different work function electrodes and use of electron/hole transport layers that also act as hole/electron blocking layers, the electrical characteristics of an OSCs, like other solar cells, resemble that of a diode with an additional current source in parallel.

The primary characterisation tool of any type of solar cell is a current density-voltage curve (*JV*-curve). This means that the current response of the solar cell under illumination is measured for varying applied voltages simulating variable load resistances connected to the solar cells external circuit. **Figure 2.4.1** shows an exemplary *JV*-curve measured on an organic solar cell. Under dark conditions, the rectifying characteristics resemble that of a diode. Upon illumination, the *JV*-curve is shifted downward by the negative photocurrent.

The functional shape of the *JV*-curve is well approximated by the non-ideal diode equation:

$$J(V) = -J_{gen} + J_0 \left[\exp\left(\frac{q(V + JAR_s)}{n_{id} kT} \right) - 1 \right] + \frac{V + JAR_s}{AR_{sh}}$$

where J_{gen} is the photogenerated current density, J_0 is the saturated dark current densit measured at reverse bias, A is the device area, n_{id} is the ideality factor, k the Boltzmann constant, T the temperature, q the electron charge, and R_s and R_{sh} the series and shunt resistance, respectively. The parasitic resistances of the diode equation account for the solar cells non-ideality and can be related to different loss mechanisms in organic solar cells.[78]

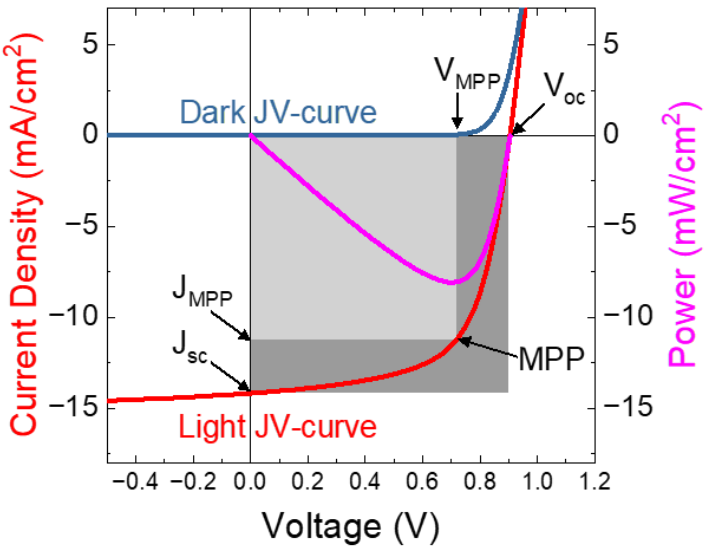


Figure 2.4.1. Current Density – Voltage Curve of an organic solar cell under light and in the dark. Various points of interest are marked and the fill factor is visualised as the ratio of the light and dark squares' area. The right axis shows the power output of the solar cell as a function of voltage.

On the right axis **Figure 2.4.1** shows the power output of the solar cell as a function of voltage. It also visualises various points of interest that are commonly used to characterise a solar cell: the short circuit density (J_{SC}) when there is no external voltage applied (no load connected), the V_{OC} where the extracted current density is zero (an infinitely large load is connected) and the maximum power point (*MPP*) with the associated values of J_{MPP} and V_{MPP}. It additionally visualises the fill factor (*FF*) that is defined as:

$$FF = \frac{J_{sc}V_{oc}}{J_{MPP}V_{MPP}}$$

and is a metric that accounts for deviations from ideal diode behaviour. Therefore, the maximum power output (P_{max}) of the solar cell may be expressed as the product:

$$P_{max} = FF \cdot J_{sc}V_{oc}$$

which yields the power conversion efficiency (PCE) when divided by the power of the incident solar irradiation. Since solar cells generally have a wavelength-dependent photon to current conversion efficiency, a global reference spectrum and power density has been defined to ensure comparability across research laboratories. The so called AM1.5 solar spectrum is based on the solar irradiance at the average latitude of the USA (1000 W/m^2 or 100 mW/cm^2).[79]

2.4.2. Simple Electrical Model of Organic Solar Cells

A simple model can be used to represent the basic functionality of a BHJ OSC. Due to the nature of the BHJ forming a finely intermixed blend, the assumption of an effective medium is made, with the HOMO or ionisation potential (I_P) defined by that of the donor and the LUMO or electron affinity (E_A) by that of the acceptor material. The effective bandgap of the material is therefore given by $E_g = E_{LUMO,\,A} - E_{HOMO,D}$. The respective energy levels are shown in **Figure 2.4.2 (a)**. Additionally, the work function of the contact layers as well as the energy offset with the relevant active layer energy levels are shown. In the dark without applied bias (**Figure 2.4.2 (b)**), the Fermi level (E_F) of the electrodes equilibrate by a small number of electrons passing through the junction from the cathode (right contact) to the anode (left contact). As a result, the cathode now carries a net positive charge. However, due to the metallic broad density of conducting states, the work function of the electrodes did not change and therefore an electric field equal to the difference of the electrode work functions divided by the thickness of the active layer applies ($E = (\varphi_A - \varphi_C)/d$).

If the device is now illuminated, the photogenerated charges are disturbing this equilibrium. Since the charges are no longer at equilibrium, there no longer is a flat Fermi level across the junction, instead the electron and hole population in the conduction and valence band, respectively, are now described by separate quasi-Fermi levels. At open circuit conditions (i.e., no current flowing in the external circuit), holes and electrons build up in the device resulting in the splitting of the quasi-Fermi levels (**Figure 2.4.2 (c)**). This so-called quasi-Fermi-level-splitting (QFLS) causes a potential difference to be generated between the electrodes as they charge up by transfer of electrons to the cathode and holes to the anode. This increase of the potential compared to dark equilibrium conditions can be measured externally as the V_{OC}.

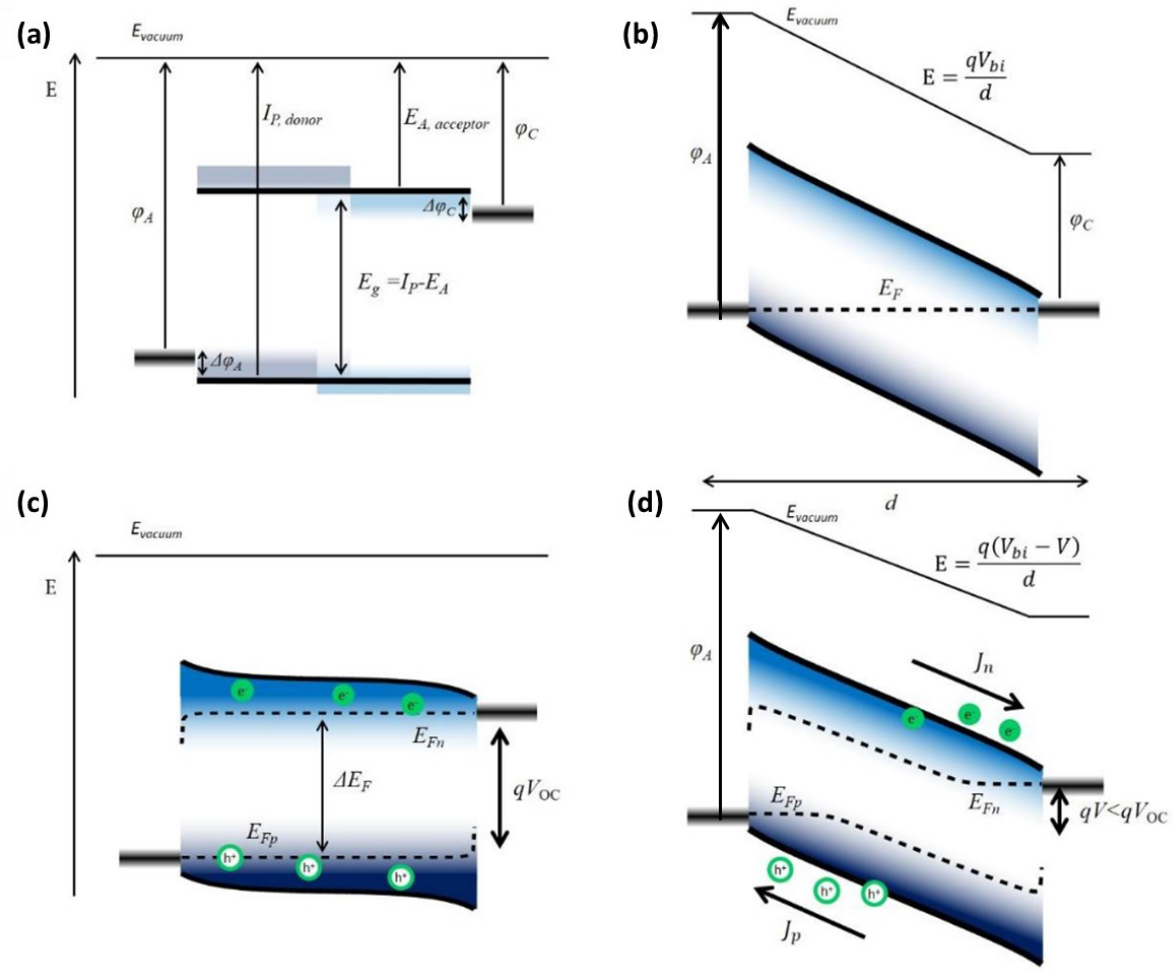


Figure 2.4.2. Simple energy level diagram to describe OSC operation. **(a)** Visualisation of the effective medium approach: the BHJ is treated as a single medium with the band gap defined by the acceptor LUMO and the donor HOMO (labelled here as the acceptor electron affinity $E_{A,acceptor}$ and the donor ionisation potential $I_{P,donor}$, respectively). **(b)** Band diagram in dark equilibrium conditions. **(c)** Visualisation of V_{OC} conditions and the quasi-Fermi level splitting. **(d)** Band diagram at an applied voltage close to *MPP*. Image obtained from the thesis by Scot Wheeler.[4]

From these observations it also follows that in BHJ OSCs, the V_{OC} cannot normally exceed the built-in potential.[80,81] However, high performance organic solar cells with contact layers matched to the respective band of the effective medium (small injection barriers $\Delta\varphi_A$ and $\Delta\varphi_C$) this typically is not limiting the V_{OC}. Instead, the maximum achievable V_{OC} is determined by the quasi-equilibrium between charge generation and the recombination of free charges. This makes open circuit conditions particularly useful to study free carrier (or non-geminate) recombination.

Considering the case of a finite external load (i.e., a small positive externally applied voltage in the *JV*-curve), the electric field across the active layer is normally equal to the difference of the V_{bi} and the applied voltage V_{app} divided by d and a drift current is flowing as a result of the

electric field (see **Figure 2.4.2 (d)**). The total drift current is the sum of the electron and hole drift current. These are governed determined by the product of their respective mobility (μ), carrier (n) density and the strength of the electric field (E).

Now that an overview of the materials, device structure and performance characterisation has been given, a more detailed account of the different recombination loss mechanisms in an organic solar cell is provided before the methods that were used to study these loss mechanisms are discussed.

2.5. Performance Limiting Factors in Organic Solar Cells

This section explores the factors limiting the short circuit current density (J_{SC}), open circuit voltage (V_{OC}) and fill factor (FF) and therefore the achievable power conversion efficiency in organic solar cells. Following this, the methods section will explore the different experimental techniques employed throughout this thesis to study its limitations.

2.5.1. The Choice of Bandgap

Only photons with an energy above the bandgap of the lower bandgap material in the photoactive layer are absorbed efficiently. Decreasing the bandgap of the blend components therefore results in an increase of the maximum achievable current while limiting the maximum achievable V_{OC}. This is a fundamental trade-off in single junction solar cells. By adjusting the detailed balance limit, that had previously been derived for inorganic solar cells, for the increased voltage losses in OSCs an optimum bandgap of 1.5 to 1.6 eV was predicted.[82,83] Novel materials that result in reduced voltage losses, e.g. the polymer/non-fullerene acceptor blend PM6:Y6 and their derivatives, challenge this theoretical prediction.[84]

2.5.2. Limitations of the Short Circuit Current Density

The efficiency of free charge generation is limited by three processes: (1) absorption, (2) exciton diffusion and charge transfer, and (3) the separation of interfacial charge transfer states.

Firstly, the absorption is determined by the absorption coefficients of the materials in the blend and the thickness of the photoactive layer. Additionally, interference effects of incident light with its reflection at the back electrode can influence the total absorption.[85] Values of absorption coefficients vary widely for organic semiconductor materials. Especially molecules with a high degree of symmetry like C_{60}-fullerene and its soluble derivatives suffer from low absorption coefficients requiring thick junctions (> 200 nm) for complete absorption.[65]

Due to the small dimensions of tightly bound excitons typically localised to one molecule, the exciton transport to the D/A interface is an electric field-independent process governed by diffusion. The exciton diffusion length and the mean distance excitons must travel to the D/A interface determine the efficiency of exciton separation. Additionally, the probability of electron (hole) transfer and subsequent separation of the bound charge transfer (CT) state depends on the energy level offset of the donor and acceptor LUMO (HOMO) levels.[55,86–88] The minimum required energy level offset for efficient charge generation and how to accurately determine this offset are topics still under debate.[86,89–91] Charge separation may further be aided by an externally applied electric field. Instead of separating, into free charges a transfer state may also decay back to the ground state. This is termed geminate recombination. If charge recombination occurs upon the encounter of previously separated free charges, this is termed non-geminate recombination (sometimes bimolecular recombination is used synonymously but strictly speaking non-geminate recombination does not have to be governed by second order kinetics). The details will be discussed further below.

Since the active layer is subject to a strong electric field at short circuit conditions (~10^7 V/m for an active layer thickness of 100 nm), the photogenerated charges are expected to be swept out efficiently. This leads to a low charge carrier density in the active layer which reduces the likelihood of non-geminate recombination. However, especially in devices with low charge carrier mobility or in thick junctions, significant non-geminate recombination occurs at short circuit resulting in additional losses to the short circuit current density (beyond limitations by absorption and free charge generation).[65]

2.5.3. Open Circuit Voltage and the Charge Carrier Density

The upper limit of the open circuit voltage is set by the material energetics, specifically the bandgap of the effective medium as previously discussed. It was also previously discussed how the quasi-equilibrium between free charge (i.e., non-geminate) recombination and generation determines the V_{OC} that may be used as an approximation for the QFLS for well-matched interlayers. Therefore, for a known generation rate, the V_{OC} is determined by the charge carrier density dependent recombination rate in the material active layer.

The following relationship between the QFLS and the charge carrier density (n) may be derived starting from the convolution of the density of states (DoS) and a probability occupation function (from Fermi-Dirac statistics):[1,92]

$$n = p = n_0 \exp\left(\frac{\Delta E_F}{2E_{ch}}\right)$$

where n and p are the electron and hole concentration, respectively; n_0 is the equilibrium charge carrier density; ΔE_F is the Fermi level splitting and E_{ch} is the characteristic energy. The characteristic energy describes the deviation of the bandtail of the DoS from that of a perfect semiconductor that is given by the thermal energy kT and provides a measure of the disorder in the organic semiconductor blend.[34,65,92,93]

Furthermore, the complex dependence of recombination mechanisms on the charge carrier density can be expressed as a power law, hence:

$$G = R = k_0 n^{\delta}$$

where k_0 is a density dependent rate constant and δ is the recombination order with respect to n which can be determined experimentally from the dependence of the lifetime on the charge carrier density. δ is classically assumed to take values between 1 and 2 (ignoring third order Auger type recombination). A recombination order of 1 is typically interpreted as a mechanism involving one trapped carrier and a free carrier (monomolecular), while δ = 2 indicates second order (bimolecular) recombination involving a free hole and a free electron.[92] Apparent recombination orders higher than 2 have previously been experimentally determined and related to the presence of broad tailstates[92] or experimental limitations caused by non-uniform charge carrier density distributions[94]. Ultimately, the following relation between open circuit voltage and generation rate can be derived by approximating the QFLS as the V_{OC}:

$$V_{oc} \approx \frac{\Delta E_F}{q} \propto \frac{2E_{ch}}{\delta q} \ln\left(\frac{G}{R_0}\right)$$

where R_0 is the equilibrium recombination rate and all other symbols have been previously defined. The light ideality factor n_{id} is theoretically defined by the equation:

$$R = R_0 \exp\left(\frac{\Delta E_F}{n_{id} kT}\right)$$

describing the exponential dependence of the recombination rate on the Fermi level splitting.[95,96] Therefore, the ideality factor determined from the logarithmic dependence of the

V_{OC} on the generation rate (which is proportional to the light intensity (Φ)) can be used as an indicator for the recombination order:

$$n_{id} = \frac{q}{kT}\frac{dV_{oc}}{d\ln(\Phi)}$$

Instead of referencing the V_{OC} to dark equilibrium constants, it may instead be studied relative to the energy of the charge transfer state that generation and charge recombination are presumed to occur through. This requires the determination of said CTs as discussed in the method section.[97,98] The solid state physics derivations shown above may be put into relation with this CT state model through rescaling the energy axis as previously discussed elsewhere.[99] This would allow the differentiation between the influence of the effective gap and the kinetics of non-geminate recombination on the device V_{OC}. As pointed out in previous studies, the magnitude of the effective gap and the changing CT state energy also affects the non-geminate recombination related voltage losses.[82,83,100,101]

2.5.4. Non-Geminate Recombination

After discussing the connection between the V_{OC} and non-geminate recombination, the different mechanisms of non-geminate recombination are discussed briefly here.

In organic solar cells, non-geminate recombination is expected to occur through interfacial charge transfer states upon the encounter of an electron in the acceptor phase with an electron in the donor phase. As is the case for excitons, the subsequent decay to the ground state may be mediated by the emission of a photon or through interactions with molecular vibrations (radiative and non-radiative recombination). As a result of the soft nature of organic semiconductors, charge phonon interactions are very strong leading to fast non-radiative recombination and high non-radiative voltage losses compared to highly emissive inorganic semiconductors.[82] Compared to the decay of excitons typically localised on one molecule, the decay of CT states stretched over an acceptor and donor molecule only has a much lower radiation yield. This is also predicted from the low absorption of these interfacial states through the reciprocity relation.[98]

Two different mechanisms have been argued to determine the non-geminate recombination rate constant. The first assumes that the recombination of free charges is encounter limited. Once oppositely charged carrier come into close proximity, they form a charge transfer state through Coulombic attraction and subsequently recombine to the ground state. Langevin

theory predicts the recombination rate in this case to depend on the sum of the respective electron and whole mobility, the dielectric screening and the product of electron and hole density:

$$R_L = k_L np$$

$$k_L = \frac{q}{\epsilon\epsilon_0}(\mu_e + \mu_h)$$

where k_L is called the Langevin recombination rate.

In reality it was found that the observed recombination rates were much lower which led to the introduction of the so called Langevin reduction factor that is defined as the ratio of the experimentally observed recombination rate constant and that expected from the determination of the mobilities.[66,102] Additionally, the experimental recombination rates and charge carrier mobility were shown to exhibit a charge carrier density dependence higher than the expected bimolecular (second order) behaviour. [103–105] This was interpreted through the influence of tailstates in slowing down mobility and thereby recombination: localised charge carriers in the bandtail of the organic semiconductors need to be thermally promoted to the mobility edge to become mobile which lowers the encounter rate.[106]

Also, strong phase separation protecting charge carriers from encountering each other (essentially a breakdown of the effective medium model) was invoked as a factor causing deviations from the Langevin limit.[107] Vandewal *et al.* demonstrated that a reduction in the size of the interfacial area where non-geminate recombination occurs leads to reduced voltage losses.[108] This may still be interpreted as an encounter limited process.

Finally, Burke *et al.* proposed a second model which assumes that a CT state formed upon encounter of free charges may re-dissociate creating a thermodynamic CT-charge equilibrium.[109] In the case of efficient re-dissociation, the recombination rate is limited by the decay to ground and such materials may experience large deviations from the encounter limited model.[110] The decay rate of CT states has previously been shown to increase with increasing CT energy.[82] While in systems with a low offset between local exciton and CT energy, the exciton decay rate may limit the overall lifetime due to hybridisation effects.[100] In other studies, it was also found that non-geminate recombination slowed down with increasing energy level offset at the interface.[101,111]A consequence of these considerations is

also, that material combinations that show efficient charge generation from thermally relaxed CT states should be re-dissociation rather than encounter limited.

2.5.5. Limitations of the Fill Factor

The behaviour under forward bias, the position of the MPP and therefore *FF* depend on a combination of the above-described phenomena. Firstly, the occurrence of field-dependent generation would result in the reduction of the generation current with increasing voltage as the field across the active layer is reduced.

The reduction of the field strength also leads to a lower drift velocity of the extracted charges. This leads to the increase of the non-geminate recombination losses during charge extraction further reducing the photocurrent. The *FF* therefore depends on the efficiency of charge separation as well as the mobility and non-geminate recombination kinetics.[112] Many publications assess the relationship of mobility and non-geminate recombination with the efficiency of charge collection and the *FF*.[113–116]

To conclude, the extracted photocurrent density as a function of bias may therefore be described as the product of the light flux and the quantum efficiency of absorption, the formation of the charge transfer state, the voltage dependent CT separation efficiency and the voltage dependent charge collection efficiency:

$$J(V) = \Phi \cdot \eta_{abs} \cdot \eta_{CT} \cdot \eta_{free}(V) \cdot \eta_{coll}(V)$$

In order to fully characterise a solar cell, knowledge of all of the above processes in necessary. This illustrates the need for techniques to accurately determine the non-geminate recombination rate as well as the mobility of charge carriers under device operating conditions.

2.6. Research Question and Thesis Outline

A combination of empirically and theoretically guided optimisation of the photoactive materials have led to impressive performance improvements of organic solar cells by addressing the limitations discussed above. Transient optoelectronic techniques have played a pivotal role in furthering our understanding of the performance limitations – especially voltage losses and fill factor limitations and their relation to the energetic disorder. Compared to inorganic solar cells, these still present the largest loss mechanisms. **Chapter 3** will give an overview of the transient optoelectronic techniques that are central to this thesis.

I will focus on the transient optoelectronic characterisation of a wide range of less studied organic solar cells – differing from the highest performance solution-processable BHJ OSCs – including vapour-processed OSCs as well as planar and bulk heterojunctions. While vapour-processed OSCs are of particular commercial interest, planar heterojunction devices are attractive for fundamental studies of charge recombination mechanisms and may result in higher stability than their BHJ counterparts. Below I will briefly set out the motivation for the choice of OSCs used in this study.

2.6.1. Vapour-Processed versus Solution-Processed Organic Solar Cells

Until 2016, high efficiency solution-processed and vapour-processed organic solar cells (SP-OSCs and VP-OSCs, respectively) relied on wide-gap fullerene acceptors paired with low-gap polymeric or small-molecule donors, respectively. Despite the different donor materials used over this period, the record efficiencies of both processing techniques developed in lockstep (see **Figure 2.6.1**).

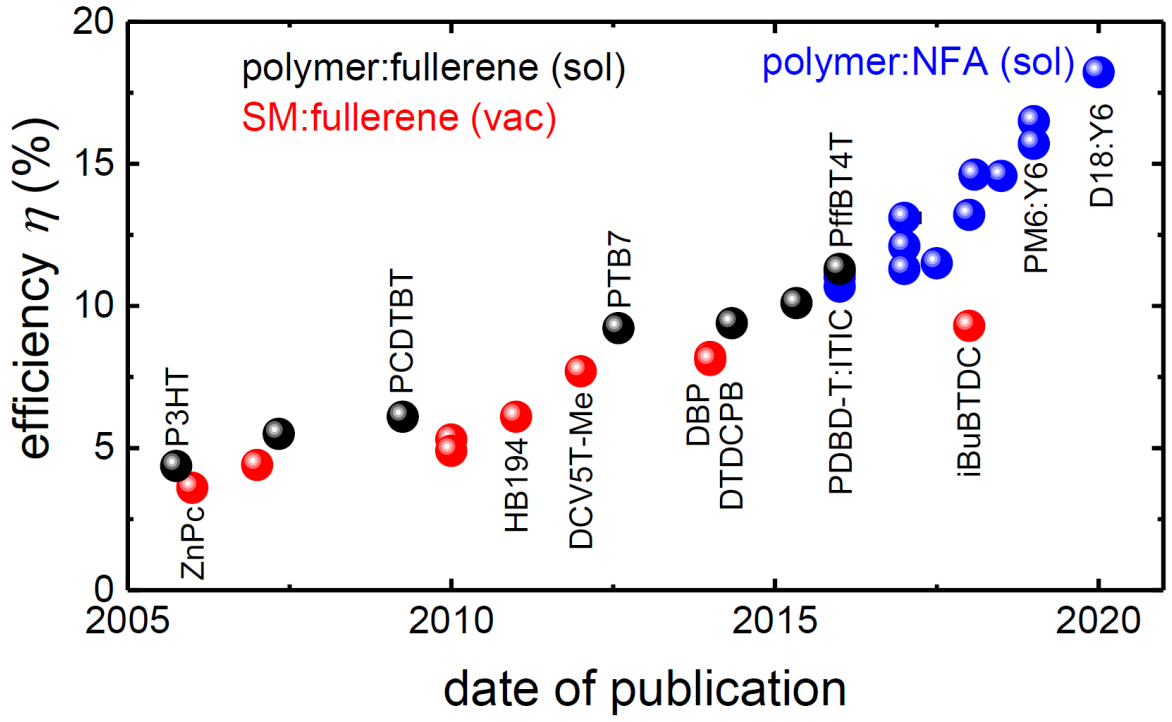


Figure 2.6.1 Development of the record power conversion efficiency of organic solar cells over time.

With the introduction of solution-processable non-fullerene acceptors based on so called acceptor-donor-acceptor structure (A-D-A), SP-OSCs achieved significant performance improvements due to the electronic tunability enabling the optimisation of the energy level offsets and higher absorption coefficients enabling complimentary IR-absorption with the

employed donor polymers.[13,15,37,117,118] A further performance jump came with the introduction of so called A-D-A'-D-A acceptor materials of the Y-family.[119–121]

Record SP-OSCs based on Y-type acceptors now achieve PCEs in excess of 19%.[122–125] Despite these achievements on a lab scale, large area module efficiencies are lacking behind with the highest certified submodule (~ 200 cm^2) and module (1475 cm^2) efficiency at 14.5% and 13.1%, respectively.[126,127] This is in part due to difficulties in transitioning from small scale manufacturing techniques (i.e. spin-coating) to large area printing methods (i.e. slot-die coating) while maintaining the bulk heterojunction morphology and reproducibility.[128] Other limiting factors in the commercialisation of SP-OSCs are their intrinsic morphological instability[71,129] and the high synthetic complexity of the highest performing materials[16,130].

2.6.2. Limitations of Vapour-Processed Organic Solar Cells

In contrast to solution-processing, thermal evaporation of small molecule organic semiconductor layers has already been shown to be viable on an industrial scale for OLED applications – including bulk heterojunction active layers (down to 10nm thickness), complex interlayer and tandem structures.[27] VP-OSCs currently possess the more viable route for large scale OPV commercialisation due to the high reproducibility, intrinsic thermal stability,[131] synthetic simplicity of small molecule materials,[132] the scalable deposition,[29] and the precise deposition control enabling tandem device architectures[133]. Most notably, tandem OSCs by Heliatek GmbH achieved a PCE of 13.2% in 2016, an OSC efficiency record at the time.[27,28] At the same time, the academic community largely focusses on SP-OSCs due to their record lab-scale efficiencies and the lower upfront costs.[27]

Unfortunately, the achievements made with NFAs in the field of SP-OSCs could not be mirrored for evaporable acceptors. Evaporation requires a sublimation temperature well below the decomposition temperature of the material ruling out large conjugated ring structures found in the highest performance NFAs.[36] While some high performing OSCs (e.g. DCV5T-Me:C_{60}) show comparable or even lower voltage losses than the best fullerene based SP-OSCs, they typically suffer from a poor charge carrier collection efficiency related to either fast non-geminate recombination or poor mobility.[134] Other highly crystalline VP-OSC materials (e.g. ZnPc:C_{60}) exhibit improved transport properties (albeit worse than the best SP-OSCs) but are electronically poorly matched limiting the V_{OC}.[134,135] The poor charge collection

efficiency in turn results in a trade-off between optimal light absorption in thick devices and charge collection and therefore fill factor of the device.

In **Chapter 4** of this thesis, performance limitations of a representative state-of-the-art VP-OSC system are investigated. The chosen small molecule donor DCV-V-Fu-Ind-Fu-V is structurally related to industrially relevant small molecules studied by Heliatek GmbH and the academically studied DCV5T-Me small molecule donor.[136] **Subchapter 4.2** addresses the relationship between morphology and device performance in DCV-V-Fu-Ind-Fu-V:C_{60} blends. Morphological optimisation was achieved by substrate heating during the co-evaporation of the BHJ.[137] My focus in this subchapter is on the efficiency of charge collection and disorder including a comparison with SP-OSC references.

In practice, the use of multi-junction systems with thinner sub-junctions may mitigate the losses due to the poor collection efficiency by stacking multiple thinner junctions. Two terminal multi-junctions are industrially viable as previously demonstrated by Heliatek GmbH due to the precise deposition control during evaporation.[28] As the voltage of the sub-cells is added up, reducing voltage losses of VP-OSC blends that may be used in multi-junctions is critical to increasing their performance. Therefore, **Subchapter 4.3** further explores the same active layer materials but focusses on strategies to reduce the large voltage losses in fullerene-based VP-OSCs (including variations of the donor/acceptor ratio and planar heterojunctions).

As previously discussed, changing the morphology through changes in D/A ratio or by employing planar heterojunctions may alter the material energetics through different electrostatic and inductive effects of the chemical environment of the organic semiconductor molecules.[42,48,52] Additionally, replacing the bulk with a planar heterojunction may influence the non-geminate recombination kinetics due to a reduction in the interfacial area and electrostatic effects on the charge carrier distribution.[108,138] Both effects may influence the resultant V_{OC}. In the literature, examples of increasing and decreasing V_{OC} in planar heterojunctions can be found illustrating the complex interplay between material energetics, interfacial area and disorder.[41,136,138–141] Understanding the role of these effects in the VP-OSC devices may help to reduce voltage losses – especially for multi-junction applications. A better understanding of these processes may also aid to further reduce voltage losses of high performing solution-processed blends!

2.6.3. Solution-Processed Bilayer and Single Component OSCs

In **Chapter 5**, I will discuss solution-processable high performing materials (including NFAs like IT-4F and Y6) in different device architectures (planar heterojunctions or single component) with the aim of furthering our understanding of the relationship between non-geminate recombination kinetics, energetic levels, and the open circuit voltage. Additionally, planar heterojunctions or single component devices may possess practical advantages in terms of reproducibility and stability due to their reduced complexity compared with BHJs.

As previously mentioned, BHJs of high performing NFAs of the Y-family paired with polymers such as Y6 suffer from morphological instabilities and poor reproducibility during large scale deposition.[71,128,129] Planar heterojunctions are expected to show much greater stability[142] but suffered from poor performance due to the low exciton diffusion length of organic semiconductors. The recently demonstrated long exciton diffusion length of non-fullerene acceptors such as IT-4F or Y6[143] raises the possibility for efficient bilayer devices. **Subchapter 5.2** focuses on PHJs made up of the polymer PM6 and NFA IT-4F with an acceptor thickness tailored to the exciton diffusion length and their corresponding BHJ reference. Similar to the results from vapour-processed planar *vs.* bulk heterojunctions, I observe an increase in the open circuit voltage for the planar junction. I use transient optoelectronic techniques and electroluminescence data by collaborators to investigate the differences in fill factor and open circuit voltage in these devices.

In **Subchapter 5.3**, I present a study on PM6/Y6 PHJs where the acceptor layers were spin-coated by collaborators using different solvents. This results in different Y6 packing motives. As a result of the different packing, collaborators demonstrated a large electrostatically induced shift of the Y6 energy levels. While these planar heterojunctions display overall poor performance and are of little practical relevance, with their well-defined interface they are also particularly useful model systems to study the effect of electrostatically shifted energy levels in Y6 compared to more complex blends.

A high molecular quadrupole moment that has recently been established to be a common feature of many high performing NFA materials.[144] As previously mentioned, the charge-quadrupole electrostatic interaction is highly distance sensitive and therefore affected by the packing of the NFA molecules in solid state. Using optoelectronic techniques, I investigate how the changing energy levels affect the V_{OC} of bilayer devices. Finally, I extend the same

methodology to BHJ solar cells deposited from the same solvent systems to investigate whether these effects translate to high performance devices. Interestingly, the planar heterojunctions consisting of PM6 and Y6 do not yield an increase in V_{OC} compared to their BHJ counterparts. Therefore, I conclude this subchapter by bringing together findings for the different PHJ and BHJ systems – including the VP-OSC and SP-OSC systems – to highlight differences in the voltage losses of different material systems.

Another aspect of modern NFAs' success that has been widely discussed is the mechanism of charge generation in blends. Some studies proposed that charge separation occurs within Y6 domains prior to hole transfer to the donor polymer.[145] Other studies investigated free charge generation in neat Y6 layers and claimed efficient free charge generation without the need for a donor molecule for hole transfer.[146]Previous studies have shown that boundaries between domains with different predominant molecular orientation can possess a significant energy level offset due to electrostatic quadrupole-charge interactions[147] which may also be behind the observed charge generation in neat Y6 layers. In **Subchapter 5.3**, I present results obtained from single-component devices made up of different neat NFA layers including Y6. Using optoelectronic techniques, I investigate the charge generation efficiency under different bias conditions as well as the non-geminate recombination kinetics to establish what limits Y6 single component device performance – free charge generation or non-geminate recombination.

Finally, I provide a summary and outlook of the work I present in this thesis with regard to the scientific learnings and commercial impact.

References

(1) Nelson, J. A. *The Physics Of Solar Cells*; World Scientific Publishing Company, 2003.

(2) Würfel, P.; Würfel, U. *Physics of Solar Cells: From Basic Principles to Advanced Concepts*, 3rd edition.; Wiley VCH: Weinheim, 2016.

(3) Tress, W. *Organic Solar Cells*; Springer Series in Materials Science; Springer International Publishing: Cham, 2014; Vol. 208. https://doi.org/10.1007/978-3-319-10097-5.

(4) Wheeler, S. G. M. Bulk and Surface Recombination Limitations to High Voltage Solution Processed Solar Cells. PhD Thesis, Imperial College London, London, 2017.

(5) Wu, J. The Impact of Tail States on the Performance of Organic Bulk Heterojunction Solar Cells. PhD Thesis, Imperial College London, London, 2019.

(6) Shockley, W.; Queisser, H. J. Detailed Balance Limit of Efficiency of P-n Junction Solar Cells. *Journal of Applied Physics* **1961**, *32* (3), 510–519. https://doi.org/10.1063/1.1736034.

(7) Dimroth, F.; Tibbits, T. N. D.; Niemeyer, M.; Predan, F.; Beutel, P.; Karcher, C.; Oliva, E.; Siefer, G.; Lackner, D.; Fuß-Kailuweit, P.; Bett, A. W.; Krause, R.; Drazek, C.; Guiot, E.; Wasselin, J.; Tauzin, A.; Signamarcheix, T. Four-Junction Wafer-Bonded Concentrator Solar Cells. *IEEE Journal of Photovoltaics* **2016**, *6* (1), 343–349. https://doi.org/10.1109/JPHOTOV.2015.2501729.

(8) Green, M. A.; Dunlop, E. D.; Yoshita, M.; Kopidakis, N.; Bothe, K.; Siefer, G.; Hao, X. Solar Cell Efficiency Tables (Version 63). *Progress in Photovoltaics: Research and Applications* **2024**, *32* (1), 3–13. https://doi.org/10.1002/pip.3750.

(9) Peierls, R. E. *Quantum Theory of Solids*; Clarendon Press, 1955.

(10) Zhou, H.; Yang, L.; You, W. Rational Design of High Performance Conjugated Polymers for Organic Solar Cells. *Macromolecules* **2012**, *45* (2), 607–632. https://doi.org/10.1021/ma201648t.

(11) Guo, X.; Baumgarten, M.; Müllen, K. Designing π-Conjugated Polymers for Organic Electronics. *Progress in Polymer Science* **2013**, *38* (12), 1832–1908. https://doi.org/10.1016/j.progpolymsci.2013.09.005.

(12) Roncali, J.; Leriche, P.; Blanchard, P. Molecular Materials for Organic Photovoltaics: Small Is Beautiful. *Advanced Materials* **2014**, *26* (23), 3821–3838. https://doi.org/10.1002/adma.201305999.

(13) Wadsworth, A.; Moser, M.; Marks, A.; S. Little, M.; Gasparini, N.; J. Brabec, C.; Baran, D.; McCulloch, I. Critical Review of the Molecular Design Progress in Non-Fullerene Electron Acceptors towards Commercially Viable Organic Solar Cells. *Chemical Society Reviews* **2019**, *48* (6), 1596–1625. https://doi.org/10.1039/C7CS00892A.

(14) Bronstein, H.; Nielsen, C. B.; Schroeder, B. C.; McCulloch, I. The Role of Chemical Design in the Performance of Organic Semiconductors. *Nat Rev Chem* **2020**, *4* (2), 66–77. https://doi.org/10.1038/s41570-019-0152-9.

(15) Wang, Y.; Lee, J.; Hou, X.; Labanti, C.; Yan, J.; Mazzolini, E.; Parhar, A.; Nelson, J.; Kim, J.-S.; Li, Z. Recent Progress and Challenges toward Highly Stable Nonfullerene Acceptor-Based Organic Solar Cells. *Advanced Energy Materials* **2021**, *11* (5), 2003002. https://doi.org/10.1002/aenm.202003002.

(16) Moser, M.; Wadsworth, A.; Gasparini, N.; McCulloch, I. Challenges to the Success of Commercial Organic Photovoltaic Products. *Advanced Energy Materials* **2021**, *11* (18), 2100056. https://doi.org/10.1002/aenm.202100056.

(17) Valkeneers, K.; Vandewal, K.; Maes, W. Benzothiadiazole-Based Push-Pull Copolymers – Balancing Synthetic Complexity against Organic Solar Cell Efficiency. *Organic Electronics* **2022**, *111*, 106667. https://doi.org/10.1016/j.orgel.2022.106667.

(18) Rimmele, M.; Qiao, Z.; Panidi, J.; Furlan, F.; Lee, C.; Liang Tan, W.; R. McNeill, C.; Kim, Y.; Gasparini, N.; Heeney, M. A Polymer Library Enables the Rapid Identification of a Highly Scalable and Efficient Donor Material for Organic Solar Cells. *Materials Horizons* **2023**, *10* (10), 4202–4212. https://doi.org/10.1039/D3MH00787A.

(19) Baklar, M. A.; Koch, F.; Kumar, A.; Domingo, E. B.; Campoy-Quiles, M.; Feldman, K.; Yu, L.; Wobkenberg, P.; Ball, J.; Wilson, R. M.; McCulloch, I.; Kreouzis, T.; Heeney, M.; Anthopoulos, T.; Smith, P.; Stingelin, N. Solid-State Processing of Organic Semiconductors. *Advanced Materials* **2010**, *22* (35), 3942–3947. https://doi.org/10.1002/adma.200904448.

(20) Rahmanudin, A.; Yao, L.; Jeanbourquin, X. A.; Liu, Y.; Sekar, A.; Ripaud, E.; Sivula, K. Melt-Processing of Small Molecule Organic Photovoltaics via Bulk Heterojunction Compatibilization. *Green Chem.* **2018**, *20* (10), 2218–2224. https://doi.org/10.1039/C8GC00335A.

(21) Ribierre, J.-C.; Li, Z.; Liu, X.; Lacaze, E.; Heinrich, B.; Méry, S.; Sleczkowski, P.; Xiao, Y.; Lafolet, F.; Hashizume, D.; Aoyama, T.; Uchiyama, M.; Wu, J. W.; Zaborova, E.; Fages, F.; D'Aléo, A.; Mathevet, F.; Adachi, C. A Solvent-Free and Vacuum-Free Melt-Processing Method to Fabricate Organic Semiconducting Layers with Large Crystal Size for Organic Electronic Applications. *J. Mater. Chem. C* **2019**, *7* (11), 3190–3198. https://doi.org/10.1039/C8TC04834G.

(22) Rahmanudin, A.; Marcial-Hernandez, R.; Zamhuri, A.; Walton, A. S.; Tate, D. J.; Khan, R. U.; Aphichatpanichakul, S.; Foster, A. B.; Broll, S.; Turner, M. L. Organic Semiconductors Processed from Synthesis-to-Device in Water. *Advanced Science* **2020**, *7* (21), 2002010. https://doi.org/10.1002/advs.202002010.

(23) Krebs, F. C. Fabrication and Processing of Polymer Solar Cells: A Review of Printing and Coating Techniques. *Solar Energy Materials and Solar Cells* **2009**, *93* (4), 394–412. https://doi.org/10.1016/j.solmat.2008.10.004.

(24) Taylor, D. M. Vacuum-Thermal-Evaporation: The Route for Roll-to-Roll Production of Large-Area Organic Electronic Circuits. *Semicond. Sci. Technol.* **2015**, *30* (5), 054002. https://doi.org/10.1088/0268-1242/30/5/054002.

(25) Machui, F.; Hösel, M.; Li, N.; Spyropoulos, G. D.; Ameri, T.; Søndergaard, R. R.; Jørgensen, M.; Scheel, A.; Gaiser, D.; Kreul, K.; Lenssen, D.; Legros, M.; Lemaitre, N.; Vilkman, M.; Välimäki, M.; Nordman, S.; Brabec, C. J.; Krebs, F. C. Cost Analysis of Roll-to-Roll Fabricated ITO Free Single and Tandem Organic Solar Modules Based on Data from Manufacture. *Energy Environ. Sci.* **2014**, *7* (9), 2792–2802. https://doi.org/10.1039/C4EE01222D.

(26) Angmo, D.; Hösel, M.; Krebs, F. C. Roll-to-Roll Processing of Polymer Solar Cells. In *Organic Photovoltaics*; Brabec, C., Scherf, U., Dyakonov, V., Eds.; Wiley-VCH Verlag GmbH & Co. KGaA, 2014; pp 561–586.

(27) Riede, M.; Spoltore, D.; Leo, K. Organic Solar Cells—The Path to Commercial Success. *Advanced Energy Materials* **2021**, *11* (1), 2002653. https://doi.org/10.1002/aenm.202002653.

(28) Uhrich, C.; Weiß, A.; Pfeiffer, M. Roll-to-Roll Production of Organic Solar Cells. In *Organic, Hybrid, and Perovskite Photovoltaics XVIII*; SPIE, 2017; Vol. 10363, pp 29–33. https://doi.org/10.1117/12.2273833.

(29) Qu, B.; Forrest, S. R. Continuous Roll-to-Roll Fabrication of Organic Photovoltaic Cells via Interconnected High-Vacuum and Low-Pressure Organic Vapor Phase Deposition Systems. *Applied Physics Letters* **2018**, *113* (5), 053302. https://doi.org/10.1063/1.5039701.

(30) Street, R. A. Localized State Distribution and Its Effect on Recombination in Organic Solar Cells. *Phys. Rev. B* **2011**, *84* (7), 075208. https://doi.org/10.1103/PhysRevB.84.075208.

(31) MacKenzie, R. C. I.; Shuttle, C. G.; Chabinyc, M. L.; Nelson, J. Extracting Microscopic Device Parameters from Transient Photocurrent Measurements of P3HT:PCBM Solar Cells. *Advanced Energy Materials* **2012**, *2* (6), 662–669. https://doi.org/10.1002/aenm.201100709.

(32) Linderl, T.; Zechel, T.; Hofmann, A.; Sato, T.; Shimizu, K.; Ishii, H.; Brütting, W. Crystalline versus Amorphous Donor-Acceptor Blends: Influence of Layer Morphology on the Charge-Transfer Density of States. *Phys. Rev. Applied* **2020**, *13* (2), 024061. https://doi.org/10.1103/PhysRevApplied.13.024061.

(33) Yan, J.; Rezasoltani, E.; Azzouzi, M.; Eisner, F.; Nelson, J. Influence of Static Disorder of Charge Transfer State on Voltage Loss in Organic Photovoltaics. *Nat Commun* **2021**, *12* (1), 3642. https://doi.org/10.1038/s41467-021-23975-3.

(34) Perdigón-Toro, L.; Phuong, L. Q.; Eller, F.; Freychet, G.; Saglamkaya, E.; Khan, J. I.; Wei, Q.; Zeiske, S.; Kroh, D.; Wedler, S.; Köhler, A.; Armin, A.; Laquai, F.; Herzig, E. M.; Zou, Y.; Shoaee, S.; Neher, D. Understanding the Role of Order in Y-Series Non-Fullerene Solar Cells to Realize High Open-Circuit Voltages. *Advanced Energy Materials* **2022**, *12* (12), 2103422. https://doi.org/10.1002/aenm.202103422.

(35) Conboy, G.; J. Spencer, H.; Angioni, E.; L. Kanibolotsky, A.; J. Findlay, N.; J. Coles, S.; Wilson, C.; B. Pitak, M.; Risko, C.; Coropceanu, V.; Brédas, J.-L.; J. Skabara, P. To Bend or Not to Bend – Are Heteroatom Interactions within Conjugated Molecules Effective in Dictating Conformation and Planarity? *Materials Horizons* **2016**, *3* (4), 333–339. https://doi.org/10.1039/C6MH00051G.

(36) Kaienburg, P.; Jungbluth, A.; Habib, I.; Kesava, S. V.; Nyman, M.; Riede, M. K. Assessing the Photovoltaic Quality of Vacuum-Thermal Evaporated Organic Semiconductor Blends. *Advanced Materials* **2022**, *34* (22), 2107584. https://doi.org/10.1002/adma.202107584.

(37) Luo, D.; Jang, W.; Babu, D. D.; Kim, M. S.; Wang, D. H.; Kyaw, A. K. K. Recent Progress in Organic Solar Cells Based on Non-Fullerene Acceptors: Materials to Devices. *J. Mater. Chem. A* **2022**, *10* (7), 3255–3295. https://doi.org/10.1039/D1TA10707K.

(38) Tsoi, W. C.; Spencer, S. J.; Yang, L.; Ballantyne, A. M.; Nicholson, P. G.; Turnbull, A.; Shard, A. G.; Murphy, C. E.; Bradley, D. D. C.; Nelson, J.; Kim, J.-S. Effect of Crystallization on the Electronic Energy Levels and Thin Film Morphology of P3HT:PCBM Blends. *Macromolecules* **2011**, *44* (8), 2944–2952. https://doi.org/10.1021/ma102841e.

(39) Seo, J. H.; Gutacker, A.; Sun, Y.; Wu, H.; Huang, F.; Cao, Y.; Scherf, U.; Heeger, A. J.; Bazan, G. C. Improved High-Efficiency Organic Solar Cells via Incorporation of a Conjugated Polyelectrolyte Interlayer. *J. Am. Chem. Soc.* **2011**, *133* (22), 8416–8419. https://doi.org/10.1021/ja2037673.

(40) C. Jamieson, F.; Buchaca Domingo, E.; McCarthy-Ward, T.; Heeney, M.; Stingelin, N.; R. Durrant, J. Fullerene Crystallisation as a Key Driver of Charge Separation in Polymer / Fullerene Bulk Heterojunction Solar Cells. *Chemical Science* **2012**, *3* (2), 485–492. https://doi.org/10.1039/C1SC00674F.

(41) Li, T.; Benduhn, J.; Qiao, Z.; Liu, Y.; Li, Y.; Shivhare, R.; Jaiser, F.; Wang, P.; Ma, J.; Zeika, O.; Neher, D.; Mannsfeld, S. C. B.; Ma, Z.; Vandewal, K.; Leo, K. Effect of H- and J-Aggregation on the Photophysical and Voltage Loss of Boron Dipyrromethene Small Molecules in Vacuum-Deposited Organic Solar Cells. *J. Phys. Chem. Lett.* **2019**, *10* (11), 2684–2691. https://doi.org/10.1021/acs.jpclett.9b01222.

(42) Cha, H.; Fish, G.; Luke, J.; Alraddadi, A.; Lee, H. H.; Zhang, W.; Dong, Y.; Limbu, S.; Wadsworth, A.; Maria, I. P.; Francàs, L.; Sou, H. L.; Du, T.; Kim, J.-S.; McLachlan, M. A.; McCulloch, I.; Durrant, J. R. Suppression of Recombination Losses in Polymer:Nonfullerene Acceptor Organic Solar Cells Due to Aggregation Dependence of Acceptor Electron Affinity. *Advanced Energy Materials* **2019**, *9* (27), 1901254. https://doi.org/10.1002/aenm.201901254.

(43) Natsuda, S.; Saito, T.; Shirouchi, R.; Sakamoto, Y.; Takeyama, T.; Tamai, Y.; Ohkita, H. Cascaded Energy Landscape as a Key Driver for Slow yet Efficient Charge Separation with Small Energy Offset in Organic Solar Cells. *Energy & Environmental Science* **2022**, *15* (4), 1545–1555. https://doi.org/10.1039/D1EE03565G.

(44) Ito, E.; Washizu, Y.; Hayashi, N.; Ishii, H.; Matsuie, N.; Tsuboi, K.; Ouchi, Y.; Harima, Y.; Yamashita, K.; Seki, K. Spontaneous Buildup of Giant Surface Potential by Vacuum Deposition of Alq3 and Its Removal by Visible Light Irradiation. *Journal of Applied Physics* **2002**, *92* (12), 7306–7310. https://doi.org/10.1063/1.1518759.

(45) Noguchi, Y.; Sato, N.; Miyazaki, Y.; Ishii, H. Light- and Ion-Gauge-Induced Space Charges in Tris-(8-Hydroxyquinolate) Aluminum-Based Organic Light-Emitting Diodes. *Applied Physics Letters* **2010**, *96* (14), 143305. https://doi.org/10.1063/1.3374405.

(46) Noguchi, Y.; Miyazaki, Y.; Tanaka, Y.; Sato, N.; Nakayama, Y.; Schmidt, T. D.; Brütting, W.; Ishii, H. Charge Accumulation at Organic Semiconductor Interfaces Due to a Permanent Dipole Moment and Its Orientational Order in Bilayer Devices. *Journal of Applied Physics* **2012**, *111* (11), 114508. https://doi.org/10.1063/1.4724349.

(47) Friederich, P.; Rodin, V.; Von Wrochem, F.; Wenzel, W. Built-In Potentials Induced by Molecular Order in Amorphous Organic Thin Films. *ACS Appl. Mater. Interfaces* **2018**, *10* (2), 1881–1887. https://doi.org/10.1021/acsami.7b11762.

(48) Poelking, C.; Tietze, M.; Elschner, C.; Olthof, S.; Hertel, D.; Baumeier, B.; Würthner, F.; Meerholz, K.; Leo, K.; Andrienko, D. Impact of Mesoscale Order on Open-Circuit Voltage in Organic Solar Cells. *Nature Mater* **2015**, *14* (4), 434–439. https://doi.org/10.1038/nmat4167.

(49) D'Avino, G.; Muccioli, L.; Castet, F.; Poelking, C.; Andrienko, D.; Soos, Z. G.; Cornil, J.; Beljonne, D. Electrostatic Phenomena in Organic Semiconductors: Fundamentals and Implications for Photovoltaics. *J. Phys.: Condens. Matter* **2016**, *28* (43), 433002. https://doi.org/10.1088/0953-8984/28/43/433002.

(50) Verlaak, S.; Beljonne, D.; Cheyns, D.; Rolin, C.; Linares, M.; Castet, F.; Cornil, J.; Heremans, P. Electronic Structure and Geminate Pair Energetics at Organic–Organic Interfaces: The Case of Pentacene/C60 Heterojunctions. *Advanced Functional Materials* **2009**, *19* (23), 3809–3814. https://doi.org/10.1002/adfm.200901233.

(51) Yamada, K.; Yanagisawa, S.; Koganezawa, T.; Mase, K.; Sato, N.; Yoshida, H. Impact of the Molecular Quadrupole Moment on Ionization Energy and Electron Affinity of Organic Thin Films: Experimental Determination of Electrostatic Potential and Electronic Polarization Energies. *Phys. Rev. B* **2018**, *97* (24), 245206. https://doi.org/10.1103/PhysRevB.97.245206.

(52) Schwarze, M.; Schellhammer, K. S.; Ortstein, K.; Benduhn, J.; Gaul, C.; Hinderhofer, A.; Perdigón Toro, L.; Scholz, R.; Kublitski, J.; Roland, S.; Lau, M.; Poelking, C.; Andrienko, D.; Cuniberti, G.; Schreiber, F.; Neher, D.; Vandewal, K.; Ortmann, F.; Leo, K. Impact of Molecular Quadrupole Moments on the Energy Levels at Organic Heterojunctions. *Nat Commun* **2019**, *10* (1), 2466. https://doi.org/10.1038/s41467-019-10435-2.

(53) Chamberlain, G. A. Organic Solar Cells: A Review. *Solar Cells* **1983**, *8* (1), 47–83. https://doi.org/10.1016/0379-6787(83)90039-X.

(54) Braun, C. L. Electric Field Assisted Dissociation of Charge Transfer States as a Mechanism of Photocarrier Production. *The Journal of Chemical Physics* **1984**, *80* (9), 4157–4161. https://doi.org/10.1063/1.447243.

(55) Clarke, T. M.; Durrant, J. R. Charge Photogeneration in Organic Solar Cells. *Chem. Rev.* **2010**, *110* (11), 6736–6767. https://doi.org/10.1021/cr900271s.

(56) Miyata, A.; Mitioglu, A.; Plochocka, P.; Portugall, O.; Wang, J. T.-W.; Stranks, S. D.; Snaith, H. J.; Nicholas, R. J. Direct Measurement of the Exciton Binding Energy and Effective Masses for Charge Carriers in Organic–Inorganic Tri-Halide Perovskites. *Nature Phys* **2015**, *11* (7), 582–587. https://doi.org/10.1038/nphys3357.

(57) Tang, C. W. Two-layer Organic Photovoltaic Cell. *Applied Physics Letters* **1986**, *48* (2), 183–185. https://doi.org/10.1063/1.96937.

(58) Mikhnenko, O. V.; Blom, P. W. M.; Nguyen, T.-Q. Exciton Diffusion in Organic Semiconductors. *Energy Environ. Sci.* **2015**, *8* (7), 1867–1888. https://doi.org/10.1039/C5EE00925A.

(59) Halls, J. J. M.; Pichler, K.; Friend, R. H.; Moratti, S. C.; Holmes, A. B. Exciton Diffusion and Dissociation in a Poly(P-phenylenevinylene)/C60 Heterojunction Photovoltaic Cell. *Applied Physics Letters* **1996**, *68* (22), 3120–3122. https://doi.org/10.1063/1.115797.

(60) Gommans, H.; Schols, S.; Kadashchuk, A.; Heremans, P.; Meskers, S. C. J. Exciton Diffusion Length and Lifetime in Subphthalocyanine Films. *J. Phys. Chem. C* **2009**, *113* (7), 2974–2979. https://doi.org/10.1021/jp809802q.

(61) Coakley, K. M.; McGehee, M. D. Conjugated Polymer Photovoltaic Cells. *Chem. Mater.* **2004**, *16* (23), 4533–4542. https://doi.org/10.1021/cm049654n.

(62) O'Regan, B.; Grätzel, M. A Low-Cost, High-Efficiency Solar Cell Based on Dye-Sensitized Colloidal TiO2 Films. *Nature* **1991**, *353* (6346), 737–740. https://doi.org/10.1038/353737a0.

(63) Yu, G.; Gao, J.; Hummelen, J. C.; Wudl, F.; Heeger, A. J. Polymer Photovoltaic Cells : Enhanced Efficiencies via a Network of Internal Donor-Acceptor Heterojunctions. *Science* **1995**, *270* (5243), 1789–1791.

(64) Halls, J. J. M.; Walsh, C. A.; Greenham, N. C.; Marseglia, E. A.; Friend, R. H.; Moratti, S. C.; Holmes, A. B. Efficient Photodiodes from Interpenetrating Polymer Networks. *Nature* **1995**, *376* (6540), 498–500. https://doi.org/10.1038/376498a0.

(65) Wu, J.; Luke, J.; Lee, H. K. H.; Shakya Tuladhar, P.; Cha, H.; Jang, S.-Y.; Tsoi, W. C.; Heeney, M.; Kang, H.; Lee, K.; Kirchartz, T.; Kim, J.-S.; Durrant, J. R. Tail State Limited Photocurrent Collection of Thick Photoactive Layers in Organic Solar Cells. *Nature Communications* **2019**, *10* (1), 5159. https://doi.org/10.1038/s41467-019-12951-7.

(66) Hosseini, S. M.; Tokmoldin, N.; Lee, Y. W.; Zou, Y.; Woo, H. Y.; Neher, D.; Shoaee, S. Putting Order into PM6:Y6 Solar Cells to Reduce the Langevin Recombination in 400 Nm Thick Junction. *Solar RRL* **2020**, *4* (11), 2000498. https://doi.org/10.1002/solr.202000498.

(67) Ma, L.; Zhang, S.; Yao, H.; Xu, Y.; Wang, J.; Zu, Y.; Hou, J. High-Efficiency Nonfullerene Organic Solar Cells Enabled by 1000 Nm Thick Active Layers with a Low Trap-State Density. *ACS Appl. Mater. Interfaces* **2020**, *12* (16), 18777–18784. https://doi.org/10.1021/acsami.0c05172.

(68) Hiramoto, M.; Fujiwara, H.; Yokoyama, M. Three-layered Organic Solar Cell with a Photoactive Interlayer of Codeposited Pigments. *Applied Physics Letters* **1991**, *58* (10), 1062–1064. https://doi.org/10.1063/1.104423.

(69) Ye, L.; Hu, H.; Ghasemi, M.; Wang, T.; Collins, B. A.; Kim, J.-H.; Jiang, K.; Carpenter, J. H.; Li, H.; Li, Z.; McAfee, T.; Zhao, J.; Chen, X.; Lai, J. L. Y.; Ma, T.; Bredas, J.-L.; Yan, H.; Ade, H. Quantitative Relations between Interaction Parameter, Miscibility and Function in Organic Solar Cells. *Nature Mater* **2018**, *17* (3), 253–260. https://doi.org/10.1038/s41563-017-0005-1.

(70) Peng, Z.; Stingelin, N.; Ade, H.; Michels, J. J. A Materials Physics Perspective on Structure–Processing–Function Relations in Blends of Organic Semiconductors. *Nat Rev Mater* **2023**, *8* (7), 439–455. https://doi.org/10.1038/s41578-023-00541-5.

(71) Qin, Y.; Balar, N.; Peng, Z.; Gadisa, A.; Angunawela, I.; Bagui, A.; Kashani, S.; Hou, J.; Ade, H. The Performance-Stability Conundrum of BTP-Based Organic Solar Cells. *Joule* **2021**, *5* (8), 2129–2147. https://doi.org/10.1016/j.joule.2021.06.006.

(72) Sánchez-Díaz, A.; Rodríguez-Martínez, X.; Córcoles-Guija, L.; Mora-Martín, G.; Campoy-Quiles, M. High-Throughput Multiparametric Screening of Solution Processed Bulk Heterojunction Solar Cells. *Advanced Electronic Materials* **2018**, 1700477. https://doi.org/10.1002/aelm.201700477.

(73) Du, X.; Lüer, L.; Heumueller, T.; Wagner, J.; Berger, C.; Osterrieder, T.; Wortmann, J.; Langner, S.; Vongsaysy, U.; Bertrand, M.; Li, N.; Stubhan, T.; Hauch, J.; Brabec, C. J. Elucidating the Full Potential of OPV Materials Utilizing a High-Throughput Robot-Based Platform and Machine Learning. *Joule* **2021**, *5* (2), 495–506. https://doi.org/10.1016/j.joule.2020.12.013.

(74) Osterrieder, T.; Schmitt, F.; Lüer, L.; Wagner, J.; Heumüller, T.; Hauch, J.; J. Brabec, C. Autonomous Optimization of an Organic Solar Cell in a 4-Dimensional Parameter Space. *Energy & Environmental Science* **2023**, *16* (9), 3984–3993. https://doi.org/10.1039/D3EE02027D.

(75) Berny, S.; Blouin, N.; Distler, A.; Egelhaaf, H.-J.; Krompiec, M.; Lohr, A.; Lozman, O. R.; Morse, G. E.; Nanson, L.; Pron, A.; Sauermann, T.; Seidler, N.; Tierney, S.; Tiwana, P.; Wagner, M.; Wilson, H. Solar Trees: First Large-Scale Demonstration of Fully Solution Coated, Semitransparent, Flexible Organic Photovoltaic Modules. *Advanced Science* **2016**, *3* (5), 1500342. https://doi.org/10.1002/advs.201500342.

(76) Lee, J.; Cha, H.; Yao, H.; Hou, J.; Suh, Y.-H.; Jeong, S.; Lee, K.; Durrant, J. R. Toward Visibly Transparent Organic Photovoltaic Cells Based on a Near-Infrared Harvesting Bulk Heterojunction Blend. *ACS Appl. Mater. Interfaces* **2020**, *12* (29), 32764–32770. https://doi.org/10.1021/acsami.0c08037.

(77) Ratcliff, E. L.; Zacher, B.; Armstrong, N. R. Selective Interlayers and Contacts in Organic Photovoltaic Cells. *J. Phys. Chem. Lett.* **2011**, *2* (11), 1337–1350. https://doi.org/10.1021/jz2002259.

(78) Foertig, A.; Rauh, J.; Dyakonov, V.; Deibel, C. Shockley Equation Parameters of P3HT:PCBM Solar Cells Determined by Transient Techniques. *Phys. Rev. B* **2012**, *86* (11), 115302. https://doi.org/10.1103/PhysRevB.86.115302.

(79) Gueymard, C. A.; Myers, D.; Emery, K. Proposed Reference Irradiance Spectra for Solar Energy Systems Testing. *Solar Energy* **2002**, *73* (6), 443–467. https://doi.org/10.1016/S0038-092X(03)00005-7.

(80) Tress, W.; Leo, K.; Riede, M. Influence of Hole-Transport Layers and Donor Materials on Open-Circuit Voltage and Shape of I–V Curves of Organic Solar Cells. *Advanced Functional Materials* **2011**, *21* (11), 2140–2149. https://doi.org/10.1002/adfm.201002669.

(81) Wheeler, S.; Deledalle, F.; Tokmoldin, N.; Kirchartz, T.; Nelson, J.; Durrant, J. R. Influence of Surface Recombination on Charge-Carrier Kinetics in Organic Bulk Heterojunction Solar Cells with Nickel Oxide Interlayers. *Phys. Rev. Applied* **2015**, *4* (2), 024020. https://doi.org/10.1103/PhysRevApplied.4.024020.

(82) Benduhn, J.; Tvingstedt, K.; Piersimoni, F.; Ullbrich, S.; Fan, Y.; Tropiano, M.; McGarry, K. A.; Zeika, O.; Riede, M. K.; Douglas, C. J.; Barlow, S.; Marder, S. R.; Neher, D.; Spoltore, D.; Vandewal, K. Intrinsic Non-Radiative Voltage Losses in Fullerene-Based

Organic Solar Cells. *Nature Energy* **2017**, *2* (6), nenergy201753. https://doi.org/10.1038/nenergy.2017.53.

(83) Azzouzi, M.; Yan, J.; Kirchartz, T.; Liu, K.; Wang, J.; Wu, H.; Nelson, J. Nonradiative Energy Losses in Bulk-Heterojunction Organic Photovoltaics. *Phys. Rev. X* **2018**, *8* (3), 031055. https://doi.org/10.1103/PhysRevX.8.031055.

(84) Shi, Y.; Chang, Y.; Lu, K.; Chen, Z.; Zhang, J.; Yan, Y.; Qiu, D.; Liu, Y.; Adil, M. A.; Ma, W.; Hao, X.; Zhu, L.; Wei, Z. Small Reorganization Energy Acceptors Enable Low Energy Losses in Non-Fullerene Organic Solar Cells. *Nat Commun* **2022**, *13* (1), 3256. https://doi.org/10.1038/s41467-022-30927-y.

(85) Kerremans, R.; Kaiser, C.; Li, W.; Zarrabi, N.; Meredith, P.; Armin, A. The Optical Constants of Solution-Processed Semiconductors—New Challenges with Perovskites and Non-Fullerene Acceptors. *Advanced Optical Materials* **2020**, *8* (16), 2000319. https://doi.org/10.1002/adom.202000319.

(86) Karuthedath, S.; Gorenflot, J.; Firdaus, Y.; Chaturvedi, N.; De Castro, C. S. P.; Harrison, G. T.; Khan, J. I.; Markina, A.; Balawi, A. H.; Peña, T. A. D.; Liu, W.; Liang, R.-Z.; Sharma, A.; Paleti, S. H. K.; Zhang, W.; Lin, Y.; Alarousu, E.; Anjum, D. H.; Beaujuge, P. M.; De Wolf, S.; McCulloch, I.; Anthopoulos, T. D.; Baran, D.; Andrienko, D.; Laquai, F. Intrinsic Efficiency Limits in Low-Bandgap Non-Fullerene Acceptor Organic Solar Cells. *Nat. Mater.* **2021**, *20* (3), 378–384. https://doi.org/10.1038/s41563-020-00835-x.

(87) Huang, Y.; Chung, S.; Karuthedath, S.; De Castro, C. S. P.; Tang, H.; Jeong, M.; Lu, S.; Cho, K.; Laquai, F.; Kan, Z. Charge Carrier Dynamics in Planar Heterojunction Organic Solar Cells. *Solar RRL* **2023**, *7* (12), 2300267. https://doi.org/10.1002/solr.202300267.

(88) Pranav, M.; Shukla, A.; Moser, D.; Rumeney, J.; Liu, W.; Wang, R.; Sun, B.; Smeets, S.; Tokmoldin, N.; Cao, Y.; He, G.; Beitz, T.; Jaiser, F.; Hultzsch, T.; Shoaee, S.; Maes, W.; Lüer, L.; Brabec, C.; Vandewal, K.; Andrienko, D.; Ludwigs, S.; Neher, D. On the Critical Competition between Singlet Exciton Decay and Free Charge Generation in Non-Fullerene Based Organic Solar Cells with Low Energetic Offsets. *Energy Environ. Sci.* **2024**. https://doi.org/10.1039/D4EE01409J.

(89) Perdigón-Toro, L.; Zhang, H.; Markina, A.; Yuan, J.; Hosseini, S. M.; Wolff, C. M.; Zuo, G.; Stolterfoht, M.; Zou, Y.; Gao, F.; Andrienko, D.; Shoaee, S.; Neher, D. Barrierless Free Charge Generation in the High-Performance PM6:Y6 Bulk Heterojunction Non-Fullerene Solar Cell. *Advanced Materials* **2020**, *32* (9), 1906763. https://doi.org/10.1002/adma.201906763.

(90) Neusser, D.; Sun, B.; Liang Tan, W.; Thomsen, L.; Schultz, T.; Perdigón-Toro, L.; Koch, N.; Shoaee, S.; R. McNeill, C.; Neher, D.; Ludwigs, S. Spectroelectrochemically Determined Energy Levels of PM6 : Y6 Blends and Their Relevance to Solar Cell Performance. *Journal of Materials Chemistry C* **2022**, *10* (32), 11565–11578. https://doi.org/10.1039/D2TC01918C.

(91) Bertrandie, J.; Han, J.; De Castro, C. S. P.; Yengel, E.; Gorenflot, J.; Anthopoulos, T.; Laquai, F.; Sharma, A.; Baran, D. The Energy Level Conundrum of Organic Semiconductors in Solar Cells. *Advanced Materials* **2022**, *34* (35), 2202575. https://doi.org/10.1002/adma.202202575.

(92) Kirchartz, T.; Nelson, J. Meaning of Reaction Orders in Polymer:Fullerene Solar Cells. *Physical Review B* **2012**, *86* (16). https://doi.org/10.1103/PhysRevB.86.165201.

(93) Wu, J.; Lee, J.; Chin, Y.-C.; Yao, H.; Cha, H.; Luke, J.; Hou, J.; Kim, J.-S.; Durrant, J. R. Exceptionally Low Charge Trapping Enables Highly Efficient Organic Bulk Heterojunction Solar Cells. *Energy Environ. Sci.* **2020**, *13* (8), 2422–2430. https://doi.org/10.1039/D0EE01338B.

(94) Deledalle, F.; Shakya Tuladhar, P.; Nelson, J.; Durrant, J. R.; Kirchartz, T. Understanding the Apparent Charge Density Dependence of Mobility and Lifetime in Organic Bulk Heterojunction Solar Cells. *J. Phys. Chem. C* **2014**, *118* (17), 8837–8842. https://doi.org/10.1021/jp502948y.

(95) Foertig, A.; Rauh, J.; Dyakonov, V.; Deibel, C. Shockley Equation Parameters of P3HT:PCBM Solar Cells Determined by Transient Techniques. *Phys. Rev. B* **2012**, *86* (11), 115302. https://doi.org/10.1103/PhysRevB.86.115302.

(96) Kirchartz, T.; Deledalle, F.; Tuladhar, P. S.; Durrant, J. R.; Nelson, J. On the Differences between Dark and Light Ideality Factor in Polymer:Fullerene Solar Cells. *J. Phys. Chem. Lett.* **2013**, *4* (14), 2371–2376. https://doi.org/10.1021/jz4012146.

(97) Vandewal, K. Interfacial Charge Transfer States in Condensed Phase Systems. *Annual Review of Physical Chemistry* **2016**, *67* (1), null. https://doi.org/10.1146/annurev-physchem-040215-112144.

(98) Jungbluth, A.; Kaienburg, P.; Riede, M. Charge Transfer State Characterization and Voltage Losses of Organic Solar Cells. *J. Phys. Mater.* **2022**, *5* (2), 024002. https://doi.org/10.1088/2515-7639/ac44d9.

(99) Credgington, D.; Durrant, J. R. Insights from Transient Optoelectronic Analyses on the Open-Circuit Voltage of Organic Solar Cells. *J. Phys. Chem. Lett.* **2012**, *3* (11), 1465–1478. https://doi.org/10.1021/jz300293q.

(100) Dong, Y.; Cha, H.; Bristow, H. L.; Lee, J.; Kumar, A.; Tuladhar, P. S.; McCulloch, I.; Bakulin, A. A.; Durrant, J. R. Correlating Charge-Transfer State Lifetimes with Material Energetics in Polymer:Non-Fullerene Acceptor Organic Solar Cells. *J. Am. Chem. Soc.* **2021**, *143* (20), 7599–7603. https://doi.org/10.1021/jacs.1c00584.

(101) Azzouzi, M.; P. Gallop, N.; Eisner, F.; Yan, J.; Zheng, X.; Cha, H.; He, Q.; Fei, Z.; Heeney, M.; A. Bakulin, A.; Nelson, J. Reconciling Models of Interfacial State Kinetics and Device Performance in Organic Solar Cells: Impact of the Energy Offsets on the Power Conversion Efficiency. *Energy & Environmental Science* **2022**, *15* (3), 1256–1270. https://doi.org/10.1039/D1EE02788C.

(102) Juška, G.; Arlauskas, K.; Stuchlik, J.; Österbacka, R. Non-Langevin Bimolecular Recombination in Low-Mobility Materials. *Journal of Non-Crystalline Solids* **2006**, *352* (9), 1167–1171. https://doi.org/10.1016/j.jnoncrysol.2005.11.099.

(103) Shuttle, C. G.; O'Regan, B.; Ballantyne, A. M.; Nelson, J.; Bradley, D. D. C.; de Mello, J.; Durrant, J. R. Experimental Determination of the Rate Law for Charge Carrier Decay in a Polythiophene: Fullerene Solar Cell. *Appl. Phys. Lett.* **2008**, *92* (9), 093311. https://doi.org/10.1063/1.2891871.

(104) Shuttle, C. G.; Hamilton, R.; Nelson, J.; O'Regan, B. C.; Durrant, J. R. Measurement of Charge-Density Dependence of Carrier Mobility in an Organic Semiconductor Blend.

Advanced Functional Materials **2010**, *20* (5), 698–702. https://doi.org/10.1002/adfm.200901734.

(105) Rauh, D.; Deibel, C.; Dyakonov, V. Charge Density Dependent Nongeminate Recombination in Organic Bulk Heterojunction Solar Cells. *Advanced Functional Materials* **2012**, *22* (16), 3371–3377. https://doi.org/10.1002/adfm.201103118.

(106) Kirchartz, T.; Pieters, B. E.; Kirkpatrick, J.; Rau, U.; Nelson, J. Recombination via Tail States in Polythiophene:Fullerene Solar Cells. *PHYSICAL REVIEW B* **2011**, 18.

(107) Heiber, M. C.; Baumbach, C.; Dyakonov, V.; Deibel, C. Encounter-Limited Charge-Carrier Recombination in Phase-Separated Organic Semiconductor Blends. *Phys. Rev. Lett.* **2015**, *114* (13), 136602. https://doi.org/10.1103/PhysRevLett.114.136602.

(108) Vandewal, K.; Widmer, J.; Heumueller, T.; Brabec, C. J.; McGehee, M. D.; Leo, K.; Riede, M.; Salleo, A. Increased Open-Circuit Voltage of Organic Solar Cells by Reduced Donor-Acceptor Interface Area. *Adv. Mater.* **2014**, *26* (23), 3839–3843. https://doi.org/10.1002/adma.201400114.

(109) Burke, T. M.; Sweetnam, S.; Vandewal, K.; McGehee, M. D. Beyond Langevin Recombination: How Equilibrium Between Free Carriers and Charge Transfer States Determines the Open-Circuit Voltage of Organic Solar Cells. *Advanced Energy Materials* **2015**, *5* (11). https://doi.org/10.1002/aenm.201500123.

(110) Ullbrich, S.; Benduhn, J.; Jia, X.; Nikolis, V. C.; Tvingstedt, K.; Piersimoni, F.; Roland, S.; Liu, Y.; Wu, J.; Fischer, A.; Neher, D.; Reineke, S.; Spoltore, D.; Vandewal, K. Emissive and Charge-Generating Donor–Acceptor Interfaces for Organic Optoelectronics with Low Voltage Losses. *Nat. Mater.* **2019**, *18* (5), 459–464. https://doi.org/10.1038/s41563-019-0324-5.

(111) Sun, B.; Tokmoldin, N.; Alqahtani, O.; Patterson, A.; De Castro, C. S. P.; Riley, D. B.; Pranav, M.; Armin, A.; Laquai, F.; Collins, B. A.; Neher, D.; Shoaee, S. Toward More Efficient Organic Solar Cells: A Detailed Study of Loss Pathway and Its Impact on Overall Device Performance in Low-Offset Organic Solar Cells. *Advanced Energy Materials* **2023**, *13* (26), 2300980. https://doi.org/10.1002/aenm.202300980.

(112) Credgington, D.; Jamieson, F. C.; Walker, B.; Nguyen, T.-Q.; Durrant, J. R. Quantification of Geminate and Non-Geminate Recombination Losses within a Solution-Processed Small-Molecule Bulk Heterojunction Solar Cell. *Advanced Materials* **2012**, *24* (16), 2135–2141. https://doi.org/10.1002/adma.201104738.

(113) Bartesaghi, D.; Pérez, I. del C.; Kniepert, J.; Roland, S.; Turbiez, M.; Neher, D.; Koster, L. J. A. Competition between Recombination and Extraction of Free Charges Determines the Fill Factor of Organic Solar Cells. *Nat Commun* **2015**, *6* (1), 7083. https://doi.org/10.1038/ncomms8083.

(114) Kaienburg, P.; Rau, U.; Kirchartz, T. Extracting Information about the Electronic Quality of Organic Solar-Cell Absorbers from Fill Factor and Thickness. *Phys. Rev. Appl.* **2016**, *6* (2), 024001. https://doi.org/10.1103/PhysRevApplied.6.024001.

(115) Hosseini, S. M.; Roland, S.; Kurpiers, J.; Chen, Z.; Zhang, K.; Huang, F.; Armin, A.; Neher, D.; Shoaee, S. Impact of Bimolecular Recombination on the Fill Factor of Fullerene and Nonfullerene-Based Solar Cells: A Comparative Study of Charge

Generation and Extraction. *J. Phys. Chem. C* **2019**, *123* (11), 6823–6830. https://doi.org/10.1021/acs.jpcc.8b11669.

(116) Xiao, B.; Calado, P.; MacKenzie, R. C. I.; Kirchartz, T.; Yan, J.; Nelson, J. Relationship between Fill Factor and Light Intensity in Solar Cells Based on Organic Disordered Semiconductors: The Role of Tail States. *Phys. Rev. Applied* **2020**, *14* (2), 024034. https://doi.org/10.1103/PhysRevApplied.14.024034.

(117) Yan, C.; Barlow, S.; Wang, Z.; Yan, H.; Jen, A. K.-Y.; Marder, S. R.; Zhan, X. Non-Fullerene Acceptors for Organic Solar Cells. *Nat Rev Mater* **2018**, *3* (3), 1–19. https://doi.org/10.1038/natrevmats.2018.3.

(118) Cheng, P.; Li, G.; Zhan, X.; Yang, Y. Next-Generation Organic Photovoltaics Based on Non-Fullerene Acceptors. *Nature Photon* **2018**, *12* (3), 131–142. https://doi.org/10.1038/s41566-018-0104-9.

(119) Yuan, J.; Zhang, Y.; Zhou, L.; Zhang, G.; Yip, H.-L.; Lau, T.-K.; Lu, X.; Zhu, C.; Peng, H.; Johnson, P. A.; Leclerc, M.; Cao, Y.; Ulanski, J.; Li, Y.; Zou, Y. Single-Junction Organic Solar Cell with over 15% Efficiency Using Fused-Ring Acceptor with Electron-Deficient Core. *Joule* **2019**. https://doi.org/10.1016/j.joule.2019.01.004.

(120) Yang, Y. The Original Design Principles of the Y-Series Nonfullerene Acceptors, from Y1 to Y6. *ACS Nano* **2021**, *15* (12), 18679–18682. https://doi.org/10.1021/acsnano.1c10365.

(121) Yuan, J.; Zou, Y. The History and Development of Y6. *Organic Electronics* **2022**, *102*, 106436. https://doi.org/10.1016/j.orgel.2022.106436.

(122) Cui, Y.; Xu, Y.; Yao, H.; Bi, P.; Hong, L.; Zhang, J.; Zu, Y.; Zhang, T.; Qin, J.; Ren, J.; Chen, Z.; He, C.; Hao, X.; Wei, Z.; Hou, J. Single-Junction Organic Photovoltaic Cell with 19% Efficiency. *Advanced Materials* **2021**, *33* (41), 2102420. https://doi.org/10.1002/adma.202102420.

(123) Wei, Y.; Chen, Z.; Lu, G.; Yu, N.; Li, C.; Gao, J.; Gu, X.; Hao, X.; Lu, G.; Tang, Z.; Zhang, J.; Wei, Z.; Zhang, X.; Huang, H. Binary Organic Solar Cells Breaking 19% via Manipulating the Vertical Component Distribution. *Advanced Materials* **2022**, *34* (33), 2204718. https://doi.org/10.1002/adma.202204718.

(124) Zhu, L.; Zhang, M.; Xu, J.; Li, C.; Yan, J.; Zhou, G.; Zhong, W.; Hao, T.; Song, J.; Xue, X.; Zhou, Z.; Zeng, R.; Zhu, H.; Chen, C.-C.; MacKenzie, R. C. I.; Zou, Y.; Nelson, J.; Zhang, Y.; Sun, Y.; Liu, F. Single-Junction Organic Solar Cells with over 19% Efficiency Enabled by a Refined Double-Fibril Network Morphology. *Nat. Mater.* **2022**, *21* (6), 656–663. https://doi.org/10.1038/s41563-022-01244-y.

(125) Sun, R.; Wu, Y.; Yang, X.; Gao, Y.; Chen, Z.; Li, K.; Qiao, J.; Wang, T.; Guo, J.; Liu, C.; Hao, X.; Zhu, H.; Min, J. Single-Junction Organic Solar Cells with 19.17% Efficiency Enabled by Introducing One Asymmetric Guest Acceptor. *Advanced Materials* **2022**, *34* (26), 2110147. https://doi.org/10.1002/adma.202110147.

(126) Green, M. A.; Dunlop, E. D.; Yoshita, M.; Kopidakis, N.; Bothe, K.; Siefer, G.; Hinken, D.; Rauer, M.; Hohl-Ebinger, J.; Hao, X. Solar Cell Efficiency Tables (Version 64). *Progress in Photovoltaics: Research and Applications* **2024**, *32* (7), 425–441. https://doi.org/10.1002/pip.3831.

(127) *Large area organic PV module achieves world record efficiency of 14.5%*. pv magazine International. https://www.pv-magazine.com/2024/03/08/large-area-organic-pv-module-achieves-world-record-efficiency-of-14-5/ (accessed 2024-09-23).

(128) Sun, R.; Wu, Q.; Guo, J.; Wang, T.; Wu, Y.; Qiu, B.; Luo, Z.; Yang, W.; Hu, Z.; Guo, J.; Shi, M.; Yang, C.; Huang, F.; Li, Y.; Min, J. A Layer-by-Layer Architecture for Printable Organic Solar Cells Overcoming the Scaling Lag of Module Efficiency. *Joule* **2020**, *4* (2), 407–419. https://doi.org/10.1016/j.joule.2019.12.004.

(129) Luke, J.; Yang, E. J.; Labanti, C.; Park, S. Y.; Kim, J.-S. Key Molecular Perspectives for High Stability in Organic Photovoltaics. *Nat Rev Mater* **2023**, *8* (12), 839–852. https://doi.org/10.1038/s41578-023-00606-5.

(130) Po, R.; Bianchi, G.; Carbonera, C.; Pellegrino, A. "All That Glisters Is Not Gold": An Analysis of the Synthetic Complexity of Efficient Polymer Donors for Polymer Solar Cells. *Macromolecules* **2015**, *48* (3), 453–461. https://doi.org/10.1021/ma501894w.

(131) Burlingame, Q.; Huang, X.; Liu, X.; Jeong, C.; Coburn, C.; Forrest, S. R. Intrinsically Stable Organic Solar Cells under High-Intensity Illumination. *Nature* **2019**, *573* (7774), 394–397. https://doi.org/10.1038/s41586-019-1544-1.

(132) Mishra, A.; Bäuerle, P. Vacuum-Processed Donor Materials for Organic Photovoltaics. In *Organic Photovoltaics*; Brabec, C., Scherf, U., Dyakonov, V., Eds.; Wiley-VCH Verlag GmbH & Co. KGaA, 2014; pp 139–170.

(133) Che, X.; Xiao, X.; Zimmerman, J. D.; Fan, D.; Forrest, S. R. High-Efficiency, Vacuum-Deposited, Small-Molecule Organic Tandem and Triple-Junction Photovoltaic Cells. *Advanced Energy Materials* **2014**, *4* (18), 1400568. https://doi.org/10.1002/aenm.201400568.

(134) Kaienburg, P.; Jungbluth, A.; Habib, I.; Kesava, S. V.; Nyman, M.; Riede, M. K. Assessing the Photovoltaic Quality of Vacuum-Thermal Evaporated Organic Semiconductor Blends. *Advanced Materials n/a* (n/a), 2107584. https://doi.org/10.1002/adma.202107584.

(135) Pfuetzner, S.; Meiss, J.; Petrich, A.; Riede, M.; Leo, K. Thick C60:ZnPc Bulk Heterojunction Solar Cells with Improved Performance by Film Deposition on Heated Substrates. *Applied Physics Letters* **2009**, *94* (25), 253303. https://doi.org/10.1063/1.3154554.

(136) Fitzner, R.; Reinold, E.; Mishra, A.; Mena-Osteritz, E.; Ziehlke, H.; Körner, C.; Leo, K.; Riede, M.; Weil, M.; Tsaryova, O.; Weiß, A.; Uhrich, C.; Pfeiffer, M.; Bäuerle, P. Dicyanovinyl–Substituted Oligothiophenes: Structure-Property Relationships and Application in Vacuum-Processed Small Molecule Organic Solar Cells. *Advanced Functional Materials* **2011**, *21* (5), 897–910. https://doi.org/10.1002/adfm.201001639.

(137) Zheng, Y.-Q.; Zhang, J.; Yang, F.; Komino, T.; Wei, B.; Zhang, J.; Wang, Z.; Pu, W.; Yang, C.; Adachi, C. Influence of Deposition Substrate Temperature on the Morphology and Molecular Orientation of Chloroaluminum Phthalocyanine Films as Well the Performance of Organic Photovoltaic Cells. *Nanotechnology* **2015**, *26* (40), 405202. https://doi.org/10.1088/0957-4484/26/40/405202.

(138) Foertig, A.; Wagenpfahl, A.; Gerbich, T.; Cheyns, D.; Dyakonov, V.; Deibel, C. Nongeminate Recombination in Planar and Bulk Heterojunction Organic Solar Cells. *Advanced Energy Materials* **2012**, *2* (12), 1483–1489. https://doi.org/10.1002/aenm.201200718.

(139) Khan, S.-U.-Z.; Bertrandie, J.; Gui, M.; Sharma, A.; Alsufyani, W.; Gorenflot, J. F.; Laquai, F.; Baran, D.; Rand, B. P. Quantifying the Effect of Energetic Disorder on Organic Solar Cell Energy Loss. *Joule* **2022**. https://doi.org/10.1016/j.joule.2022.10.012.

(140) Zhao, Z.; Zhao, J.; Chung, S.; Cho, K.; Xu, W.; Kan, Z. Suppressing Bimolecular Charge Recombination and Energetic Disorder with Planar Heterojunction Active Layer Enables 18.1% Efficiency Binary Organic Solar Cells. *ACS Materials Lett.* **2023**, *5* (6), 1718–1726. https://doi.org/10.1021/acsmaterialslett.3c00236.

(141) Nakano, K.; Kaji, Y.; Tajima, K. Origin of Electric Field-Dependent Charge Generation in Organic Photovoltaics with Planar and Bulk Heterojunctions. *J. Mater. Chem. A* **2023**, *11* (48), 26499–26507. https://doi.org/10.1039/D3TA06835H.

(142) Li, Y.; Lin, Y. Planar Heterojunctions for Reduced Non-Radiative Open-Circuit Voltage Loss and Enhanced Stability of Organic Solar Cells. *J. Mater. Chem. C* **2021**, *9* (35), 11715–11721. https://doi.org/10.1039/D1TC01536B.

(143) Firdaus, Y.; Le Corre, V. M.; Karuthedath, S.; Liu, W.; Markina, A.; Huang, W.; Chattopadhyay, S.; Nahid, M. M.; Nugraha, M. I.; Lin, Y.; Seitkhan, A.; Basu, A.; Zhang, W.; McCulloch, I.; Ade, H.; Labram, J.; Laquai, F.; Andrienko, D.; Koster, L. J. A.; Anthopoulos, T. D. Long-Range Exciton Diffusion in Molecular Non-Fullerene Acceptors. *Nat Commun* **2020**, *11* (1), 5220. https://doi.org/10.1038/s41467-020-19029-9.

(144) Markina, A.; Lin, K.-H.; Liu, W.; Poelking, C.; Firdaus, Y.; Villalva, D. R.; Khan, J. I.; Paleti, S. H. K.; Harrison, G. T.; Gorenflot, J.; Zhang, W.; De Wolf, S.; McCulloch, I.; Anthopoulos, T. D.; Baran, D.; Laquai, F.; Andrienko, D. Chemical Design Rules for Non-Fullerene Acceptors in Organic Solar Cells. *Advanced Energy Materials* **2021**, *11* (44), 2102363. https://doi.org/10.1002/aenm.202102363.

(145) Wang, R.; Zhang, C.; Li, Q.; Zhang, Z.; Wang, X.; Xiao, M. Charge Separation from an Intra-Moiety Intermediate State in the High-Performance PM6:Y6 Organic Photovoltaic Blend. *J. Am. Chem. Soc.* **2020**, *142* (29), 12751–12759. https://doi.org/10.1021/jacs.0c04890.

(146) Price, M. B.; Hume, P. A.; Ilina, A.; Wagner, I.; Tamming, R. R.; Thorn, K. E.; Jiao, W.; Goldingay, A.; Conaghan, P. J.; Lakhwani, G.; Davis, N. J. L. K.; Wang, Y.; Xue, P.; Lu, H.; Chen, K.; Zhan, X.; Hodgkiss, J. M. Free Charge Photogeneration in a Single Component High Photovoltaic Efficiency Organic Semiconductor. *Nat Commun* **2022**, *13* (1), 2827. https://doi.org/10.1038/s41467-022-30127-8.

(147) Dong, Y.; Nikolis, V. C.; Talnack, F.; Chin, Y.-C.; Benduhn, J.; Londi, G.; Kublitski, J.; Zheng, X.; Mannsfeld, S. C. B.; Spoltore, D.; Muccioli, L.; Li, J.; Blase, X.; Beljonne, D.; Kim, J.-S.; Bakulin, A. A.; D'Avino, G.; Durrant, J. R.; Vandewal, K. Orientation Dependent Molecular Electrostatics Drives Efficient Charge Generation in Homojunction Organic Solar Cells. *Nature Communications* **2020**, *11* (1), 4617. https://doi.org/10.1038/s41467-020-18439-z.

3

EXPERIMENTAL METHODS

3. Experimental Methods

Throughout this chapter, the core experimental techniques underlying the results presented in the results chapters are presented. Additional information for the experimental conditions of other techniques not central to this thesis may be found in the respective publications. The reader is furthermore directed to the theses of Scot Wheeler and Jiaying Wu for further background of the experimental techniques.[1,2] A useful overview of different transient optoelectronic techniques is provided by Deibel and Kirchartz.[3]

3.1. Device Fabrication

3.1.1. Organic Semiconductor Materials

The active layer materials as well as the organic hole transport material BPAPF used in **Chapter 4** are shown in **Figure 3.1.1** with the full chemical name provided in the caption. Additional non-fullerene acceptor materials are shown in **Figure 5.4.1** in the results section.

3.1.2. Vapour-Processed Organic Solar Cells

The vapour-processed organic solar cells studied in **Chapter 4** were kindly provided by Heliatek GmbH, Dresden, Germany. All the layers were deposited using thermal evaporation within an ultra-high vacuum chamber onto a cleaned glass substrate with structured indium tin oxide (ITO) as the transparent contact. The electron transport layer, comprising 5 nm of n-doped (20%) C_{60} and 15 nm of undoped C_{60}, was applied. The active layer, composed of DCV-V-Fu-Ind-Fu-V:C60 (2:1 or 1:2 w/w), was co-evaporated onto a substrate that can be heated (room temperature, 40°C and 50°C as specified in the results chapters), followed by a subsequent cooling period of 60 minutes. The same procedure was followed for the for the planar heterojunctions replacing the BHJ with 5 and 15 nm thick donor layers (40°C). Subsequently, the substrate was coated with a hole transport layer consisting of 10 nm of BPAPF (Lumtec, Taiwan) and 20 nm of p-doped (10%) BPAPF. Finalizing the solar cell involved adding a 100 nm thick Al electrode, resulting in an active area of 7.2 mm^2. The devices deposited for the D/A ratio and PHJ study contained a proprietary hole transport material instead of the undoped BPAPF. Following fabrication, the device was encapsulated under a nitrogen atmosphere with a glass lid and a moisture absorbing material. Films for optical characterisation were deposited analogously but without the opaque moisture absorbing material. The same active layer material has previously been reported.[4]

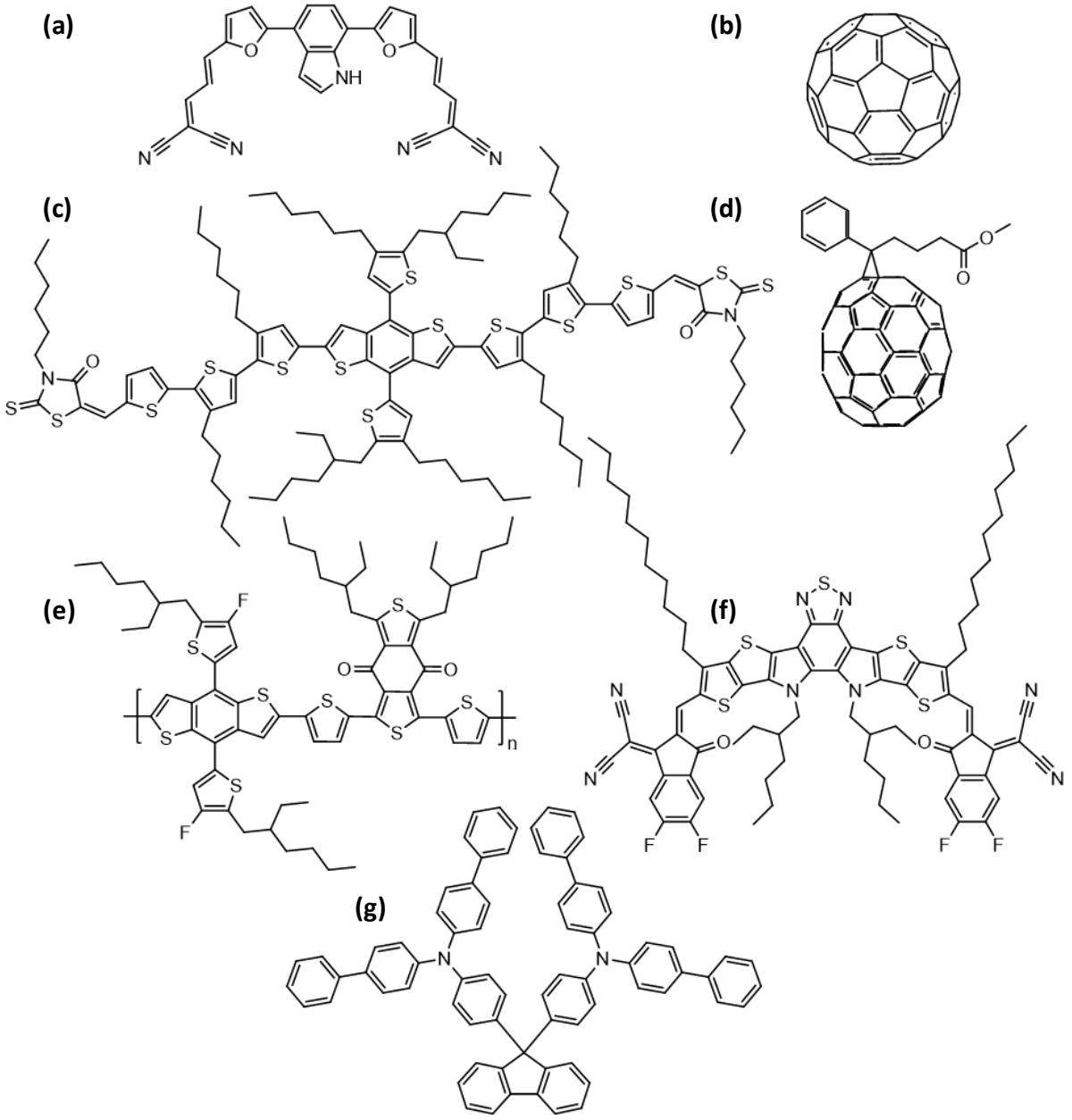


Figure 3.1.1. Chemical structure of active layer components and the organic hole transporting material BPAPF used in **Chapter 4**: **(a)** DCV-V-Fu-Ind-Fu-V (2,2'-((2E,2'E)-((1H-indole-4,7-diyl)bis(furan-5,2-diyl))bis(prop-2-en-3-yl-1-ylidene))dimalononitrile) **(b)** C_{60} – fullerene **(c)** BTR (5,5'-[[4,8-bis[5-(2-ethylhexyl)-4-hexyl-2-thienyl]benzo[1,2-b:4,5-b']dithiophene-2,6-diyl]bis [(3',3''-dihexyl[2,2':5',2''-terthiophene]-5'',5-diyl)methylidyne]] bis[3-hexyl-2-thioxo-4-thiazolidinone]) **(d)** $PC_{70}BM$ ([6,6]-Phenyl-C71-butyric acid methyl ester) **(e)** PM6 (Poly[(2,6-(4,8-bis(5-(2-ethylhexyl-3-fluoro)thiophen-2-yl)-benzo[1,2-b:4,5-b']dithiophene))-alt-(5,5-(1',3'-di-2-thienyl-5',7'-bis(2-ethyl-hexyl) benzo [1',2'-c:4',5'-c']dithiophene-4,8-dione)]) **(f)** Y6 (2,2'-((2Z,2'Z)-((12,13-bis(2-ethylhexyl)-3,9-diundecyl-12,13-dihydro-[1,2,5]thiadiazolo[3,4-e]thieno[2'',3'':4',5']thieno[2',3':4,5] pyrrolo[3,2-g]thieno [2',3':4,5] thieno[3,2-b]indole-2,10-diyl)bis(methanylylidene))bis(5,6-difluoro-3-oxo-2,3-dihydro-1H-indene-2,1-diylidene)) dimalononitrile) **(g)** BPAPF (9,9-Bis[4-(N,N-bis-biphenyl-4-yl-amino) phenyl]-9H-fluorene)

3.1.3. Solution-Processed Organic Solar Cells

The solution processed BHJ devices studied herein were fabricated by Tack Ho Lee, Song Yi Park, and Yuang Fu. Tack Ho Lee also provided the planar heterojunction devices. Single component devices were produced by Song Yi Park and Chiara Labanti.

All devices were fabricated with the inverted architecture using ZnO and MoO_3 as the interlayers as well as ITO and Ag as the bottom and top electrode, respectively. ITO substrates were sequentially cleaned by ultrasonication in deionized water, acetone, and isopropyl alcohol. Following an additional oxygen plasma treatment, ZnO layers were spin-coated onto the ITO substrates in ambient air using the sol–gel method. The ZnO precursor solution was created by dissolving zinc acetate dihydrate in 2-methoxyethanol at a concentration of 100 mg mL^{-1}, supplemented with 60 µL of ethanolamine. The resulting solution was sonicated for over 2 hours, spun on ITO, and subsequently annealed in air at 200 °C for 20 minutes. MoO_3 and Ag layers (10 and 100 nm, respectively) were deposited through thermal evaporation in a vacuum chamber with pressure reduced to below approximately 10^{-7} mbar.

The IT-4F/PM6 active layers studied in **Section 5.2** were fabricated as follows: For the fabrication of PHJ films, IT-4F films were spin-coated on the ZnO layer. The IT-4F films, with thicknesses of 40, 60, and 70 nm, were produced using IT-4F solution concentrations of 8, 12, and 16 mg/mL in chloroform, respectively. These IT-4F films were annealed at 100°C for 60s within an N_2-filled glove box. To deposit the PM6 film (35 nm) onto the IT4F film, 15 µL of PM6 solution (15 mg/mL in chlorobenzene and 1 vol.% 1,8-diiodooctane) was dropped onto deionised water in a petri dish. The resulting PM6 film was then transferred onto the IT4F film according to previous reports.[5]The overall IT-4F/PM6 PHJ thickness ranged from 75 to 105 nm, making their active layer thickness comparable to the 90 nm thick BHJ films. For the BHJ films, an IT-4F:PM6 blend solution (1:1 weight ratio, 20 mg/mL in chlorobenzene and 1 vol.% 1,8-diiodooctane) was spin-coated onto the ZnO layer and subsequently annealed at 120°C for 10 min.

The active layers studied in **Section 5.3** were produced according to this recipe: Y6 (Organtec) was dissolved in chloroform (CF, 8 mg/mL) and chlorobenzene (CB, 10 mg/mL). The Y6 solutions were spin-cast onto the substrates and annealed at 100 °C for 5 minutes in a N_2-filled glove box. PM6 (Organtec) was dissolved in CB:1,8-diiodooctane (99:1 volume ratio) with a concentration of 20 mg/mL. Droplets (15 µL) of PM6 solutions formed pristine films

on distilled water, and these films were subsequently transferred on top of the Y6 layer by gently stamping the Y6-ZnO substrate onto the floated PM6 film. The samples were annealed at 100 °C for 10 minutes in the N2-filled glove box.

For the fabrication of bulk heterojunction (BHJ) films, a PM6:Y6 blend solution (1:1.2 weight ratio, 14 mg/mL in CF and 0.5 vol% 1-chloronaphthalene, or 20 mg/mL in CB) was spin-coated on the ZnO layer, followed by annealing at 100°C for 10 minutes.

The single component devices studied in **Section 5.4** were prepared with the same interlayers and electrodes. IDIC, O-IDFBR, Y6 and IT-4F solutions were prepared in CF with 10 mg/mL concentration and stirred overnight at 40 °C prior to spin casting.

3.2. *J-V*-Characterisation & External Quantum Efficiency

J-V characteristics of solar cells were collected with a Keithley 2400 source (calibrated with a certified reference silicon cell) measurement under AM 1.5 G illumination at 100 mW/cm^2 using a xenon lamp (Oriel Instruments AAA Solar Simulator) in a nitrogen encapsulated chamber as for all device characterisations reported here. External quantum efficiency (EQE) measures the wavelength dependent photocurrent response of the solar cell. The measurements were performed using a Bentham PVE300 with monochromatic light from a dual xenon/quartz halogen light source with nitrogen encapsulated chamber.

The J_{SC} values obtained from the solar simulator measurements are later used to calibrate the current density of the LED lights in optoelectronic measurements. Single component devices in **Section 5.4** were instead calibrated with the integrated EQE spectrum.

3.3. Light Intensity Dependent *J-V*-Measurements

Light intensity dependent *JV*-curves were carried out using a ring consisting of six warm and cold white light LEDs each (Luxeon Star LEDs with 3300K and 5000K colour temperature, respectively).[6,7] The light intensity was calibrated to match the solar simulator as described above. Measurements of the V_{OC} and J_{SC} up to high light intensities were carried out without measuring a full *JV*-curve to avoid overheating. For the lowest light intensity measurements, additional neutral density filters were applied as the LED light intensity becomes unstable and the reference diode response becomes unreliable. Measurements of the V_{OC} versus the light intensity were used to calculate the light ideality factor n_{id}.[8] The light intensity dependence of

the J_{SC} can be used to identify the presence of bimolecular recombination losses under short circuit conditions.[9]

3.4. Transient Optoelectronic Techniques

A wide range of transient optoelectronic techniques are commonly applied to study organic photovoltaics and their recombination kinetics and charge transport properties. They all rely on the measurement of an electronic response to optical excitations and/or electronic bias and therefore are typically carried out on full working devices. Since the response is electronically detected, the measurements can be carried out at much lower excitation densities that are relevant to device operation (0.01 to 10 sun equivalent illumination) while optically detected transient absorption or related experiments are typically carried out at significantly higher light intensities.

In principle most of these techniques share a similar experimental setup, illustrated in **Figure 3.4.1**, consisting of transient and steady state light sources (typically pulsed lasers and LEDs, respectively), a variable power source, an oscilloscope to record current or voltage transients and a metal oxide semiconductor field effect transistor (MOSFET) controlled by a "data acquisition system" (DAQ) to switch between different bias conditions. Note, that not all components are used for every measurement.

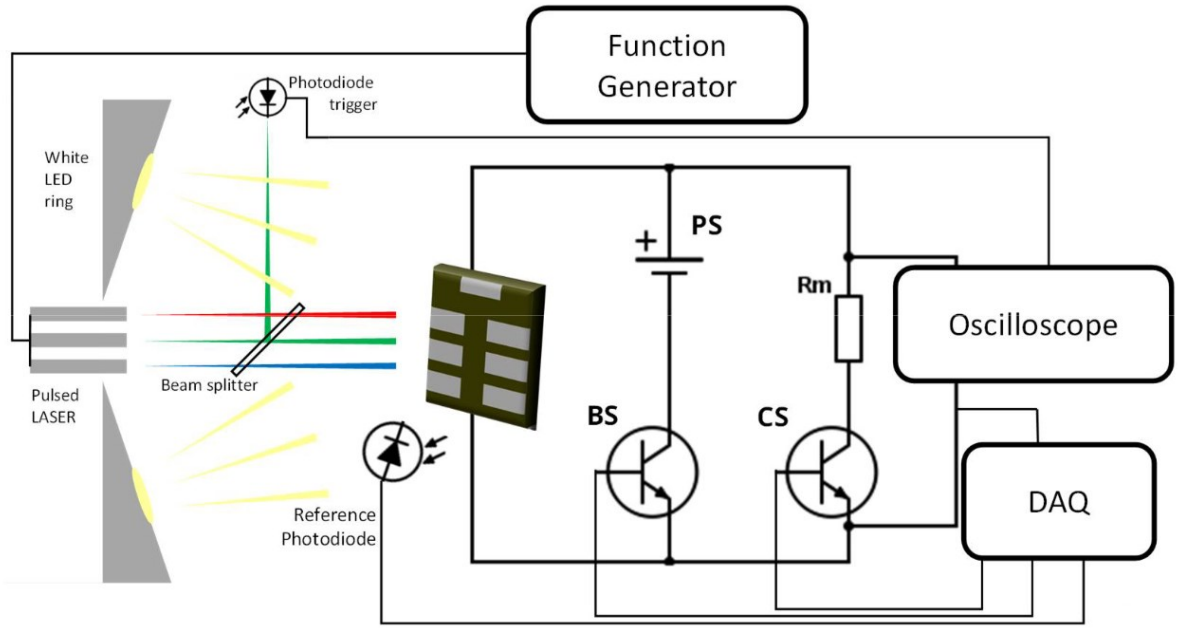


Figure 3.4.1. Schematic illustrating the basic setup of commonly used transient optoelectronic systems. The MOSFETS are labelled BS and CS denoting cell switch and bias switch, respectively. PS

stands for power supply. R_m is a measurement resistor. Figure obtained from the thesis of Scot Wheeler.[1]

The oscilloscope utilized is a Tektronix TDS 3032B. Depending on the type of measurement carried out it can be triggered either in parallel with the cell switch gate signal controlled by the DAQ or by a photodiode with nanosecond response time situated between the laser and the sample. The DAQ used in here is an NI-PCI-6251 connected through an NI-SCC-68 connector block. A Continuum Minilite Nd:YAG (532 nm, 5 ns pulse) is used as the transient laser source. The power supply is a Keithley 2400 sourcemeter. All components are managed by the computer using in-house software developed in Wavemetrics IGOR Pro software.

3.4.1. Charge Extraction

Charge extraction (CE) measurements are applied to solar cells to determine the charge carrier density present in the device at a certain operating condition prior to switching the device to short circuit.[10] The resultant current transient is recorded using an oscilloscope and integrated to yield the charge present in the device under the pre-switch condition. Recombination losses that may occur during extraction can be accounted for if the charge carrier lifetime is known by performing an iterative calculation[10] or through an analytical model[11]. Experimentally, recombination losses during charge extraction can be avoided by applying a reverse bias during extraction. This method is termed bias assisted charge extraction (BACE).[12,13]

An example is the determination of the charge carrier density present in the device at open circuit. By varying the light intensity, the charge carrier density can be measured as a function of V_{OC}. Due to the bias switch from open circuit to short circuit, the total integrated charge carrier density needs to be corrected for the current flowing due to the equilibration of the electrodes. The capacitance of the electrodes may be approximated by a plate capacitor with the active layer as the dielectric and subtracted from the total integrated charge.

$$Q_{AL}(V_{oc}) = Q_{total}(V_{oc}) - V_{oc}C_{geo}$$

$$C_{geo} = \frac{A\epsilon_r\epsilon}{d}$$

where $Q_{AL}(V_{oc})$ is the charge in the active layer as a function of the V_{OC}, Q_{total} is the total extracted charge measured by integration of the current transient, C_{geo} is the constant geometric capacitance, A and d are the solar cell area and the active layer thickness, respectively and $\epsilon_r\epsilon$ is the product of the dielectric constant of the active layer(typically

between 3.2 and 4.5) and the permittivity of free space. Non-uniform charge carrier distributions in the active layer may induce an additional surface charge in the electrodes that requires correction.[14,15] The geometric capacitance can also be measured directly by applying a reverse bias to the device in the dark and measuring the charge extracted from that.[16]

The relationship between the charge carrier density (n) and the V_{OC} enables the determination of the characteristic energy of the device as previously discussed. The active layer charge carrier density is given by:

$$n_{AL} = \frac{Q_{AL}}{qAd}$$

and has been shown to have the following dependence on the V_{OC}:

$$n_{AL}(V_{oc}) = n_0 \exp\left(\frac{qV_{oc}}{mkT}\right)$$

where n_0 is the dark equilibrium charge carrier density, m is the ideality factor related to the shape of the exponential DoS and is related to the characteristic energy via:

$$m = \frac{2E_{ch}}{kT}$$

where a value > 2 is evidence for the presence of tailstates. Note that this is gives an effective value convoluting the shape of the acceptor LUMO and donor HOMO DoS and it further assumes a uniform distribution of the charge carrier density in the active layer (zero-dimensional model).[17] Experimental conditions can significantly deviate from this approximation.[17–19]

The charge carrier density determined from charge extraction can be combined with charge carrier lifetimes determined using measurements such as transient photovoltage (discussed below) to determine the rate law of recombination for the studied solar cell.

3.4.2. Transient Photovoltage

The technique was first developed for the application to dye-sensitized solar cells[20–22] and later applied to organic[23,24] (including planar heterojunctions)[25,26] and perovskite solar cells[27,28]. Transient photovoltage (TPV) allows for the charge carrier lifetime to be directly related to the charge density measured by charge extraction from open circuit conditions. The device is held at open circuit with the equivalent LED light bias as applied to the device in charge extraction

measurements prior to extraction. In addition to this, a short laser pulse generates a small perturbation of the steady state V_{OC} that is tracked via the high impedance channel of the oscilloscope. Immediately following the laser perturbation, the voltage decays back to the steady state V_{OC} generated by the LED light bias. Fitting the recorded voltage transients with a single exponential decay yields the small perturbation lifetime:

$$\Delta V_{oc}(t) = \Delta V_{oc}(0) \exp\left(-\frac{t}{\tau_{\Delta n}}\right)$$

where $\Delta V_{oc}(t)$ is the time dependent small perturbation voltage, t is the time and $\tau_{\Delta n}$ is the small perturbation TPV lifetime that is assumed to track the decay of the excess charge carrier density in the device. For the voltage decay to track the decay of the excess charge carrier density in the active layer, an equilibrium between the potential of the electrodes and the QFLS in the active layer has to be assumed. It is therefore necessary to experimentally validate that the measured lifetimes exceed the capacitive discharge time (RC-time) to fulfil this assumption.[15,16,29] Here-in, a correction for the RC-time of the devices is employed that treats the active layer and electrode capacitances as capacitors in series as discussed below in **Section 3.4.3**.[26]

For a charge carrier density increasing exponentially with the V_{OC} and the non-geminate recombination rate being described by a power law, the following relation between V_{OC} and the TPV lifetime is expected:

$$\tau_{\Delta n}(V_{oc}) = \tau_{\Delta n0} \exp\left(-\frac{qV_{oc}}{\theta kT}\right)$$

where $\tau_{\Delta n_0}$ is the lifetime under dark conditions and θ is the slope parameter connecting the recombination order and the exponential relationship of the V_{OC} and charge carrier density. The empirically determined recombination order is determined by:

$$\delta = \frac{m}{\theta} + 1$$

as shown by Shuttle *et al.*[23] The pseudo first order total charge carrier lifetime can then be calculated as $\tau_n = \delta\tau_{\Delta n}$.

3.4.3. Transient Photocurrent and Differential Charging

Differential charging offers an alternative method to determine the charge carrier density in the device without the need for complete extraction as in CE – and is therefore more suited for devices with poor charge extraction efficiency. The voltage perturbation caused by the laser can be used to calculate the differential capacitance of the device if the charge generated by the laser is known:

$$C(V_{oc}) = \frac{\Delta Q}{\Delta V_{oc}(V_{oc})}$$

where C is the differential capacitance of the device, ΔQ is the charge generated by the laser pulse and ΔV_{oc} is the peak of the voltage perturbation caused by the laser pulse. The charge generated by the laser can be determined by keeping the device under short circuit conditions and recording the current transient using the oscilloscope (transient photocurrent measurement or TPC). Integration yields the small perturbation charge ΔQ. Given that the laser perturbation only generates a small number of charges, ΔQ can be assumed to be unaffected by non-geminate recombination during extraction – for reasonably efficient solar cells. To study non-geminate recombination, the TPC experiments can be carried out with an additional steady state background illumination.

The differential capacitance method assumes field independent generation as the charge generated at short circuit may not match the charge generated in TPV experiments carried out at open circuit. Methods such as time-delayed collection field (TDCF)[30] measurements may be used to determine the charge generated under different bias conditions and thereby correct for the discrepancy in generation efficiencies between short circuit and open circuit conditions.

Also note that the determination of the maximum voltage perturbation ΔV_{oc} recorded using the oscilloscope may be limited by a slow risetime of the voltage signal. This leads to an underestimation of the maximum voltage perturbation and correspondingly an overestimation of the differential capacitance. To avoid this, rather than using the peak of the voltage perturbation, the extrapolation of an exponential (or biexponential) fit to the origin may be used instead. This method may also avoid issues with electrical noise of the recorded voltage transient that could affect the maximum voltage deflection.

At low light intensity, the differential capacitance is observed to saturate to the constant geometric capacitance value corresponding to the charge stored on the electrodes. For thin active layers, also the capacitance of the interlayers may need to be considered when determining the active layer capacitance from the total value. In this case, the active layers and interlayers are treated as series connected capacitors.[31] Using the differential capacitance value corrected for this geometric term allows for the calculation of the charge carrier density in the device by integrating the differential capacitance with respect to the voltage:

$$n_{AL}(V_{oc}) = \int_0^{V_{oc}} C_{AL}\,dV = n_0 \exp\left(\frac{qV_{oc}}{mkT}\right)$$

In practice, the capacitance is semi-numerically integrated by fitting an exponential function to C_{AL}:

$$C_{AL}(V_{oc}) = C_0 \exp(\eta V_{oc})$$

where η and C_0 are fitting parameters. Therefore:

$$n_{AL} = \frac{1}{\eta}(C_0 \exp(\eta V_{oc}) - C_0) = \frac{C_{AL} - C_0}{\eta}.$$

Comparing the charge carrier density determined from charge extraction and differential capacitance measurements can provide a useful sanity check of the results. Note that due to the differing start and end conditions of the measurements, the correction applied to the different techniques to account for capacitive and surface charges may differ significantly. While the charge extraction measurement relies on switching the device from light/open circuit to dark/short circuit conditions, the induced surface charge has to be taken into account. In differential capacitance measurements, the device is kept at open circuit throughout and the additional small perturbation charge induced by the laser does not cause a significant change to the profile of the total carrier density. The relationship between n and V_{OC} allows for the determination of the characteristic energy E_{ch} analogous to the description above (**Section 3.4.1**). Wood *et al.* provided useful guidelines for ensuring adherence to the assumptions of the small perturbation regime.[32]

For devices with a high geometric capacitance, TPV lifetimes may be dominated by capacitive decay (RC) times rather than the charge carrier lifetime in the active layer. Typically, such effects are small in efficient solar cells employing thick active layers. However, in devices with

thin active layers (~ 50 nm), they may be relevant. Therefore, the following correction that was derived by treating the device as a series of a geometric and active layer capacitance is routinely applied to the TPV lifetime:[33]

$$\tau_{AL} = \tau_{TPV} \frac{C_{Al}}{C_{Al} + C_{geo}}.$$

3.4.4. Loss Current & Open Circuit Voltage Reconstruction

The measured charge carrier density and lifetime can be used to calculate the loss current in the device at open circuit.[28] Given that no current is extracted under open circuit conditions, the calculated loss current should equal the generation current that may be approximated roughly by the J_{SC} serving as a sanity check for the measurements. The loss current is given by

$$J_{loss} = qd \frac{n(V)}{\tau_n(n)}$$

Additionally, the voltage can be reconstructed from the fitting parameters of the lifetime and charge carrier density:

$$V_{oc} = \frac{mkT}{\delta q} \ln\left(\frac{J_{gen}\delta\tau_{\Delta n0}}{qdn_0}\right).$$

Accurately reproducing the loss current and V_{OC} for different light intensities from the measured values of the lifetime and charge carrier density increases the confidence in the measured values.

3.4.5. Note on the Meaning of TPV Lifetime Analysis

As previously noted in a range of publications, there are concerns over the meaning of TPV lifetimes due to possible limitations by RC time constants as well as non-uniform charge carrier distributions on the determined charge carrier density especially in thin active layers.[15,16,18,29] These concerns also apply to frequency domain based techniques. Additionally, as shown by Azzouzi *et al.* at fast recombination and a low carrier mobility may result in the lifetimes to be determined by non-uniform charge carrier densities and transport times.[34] They proposed an experimentally more challenging modification to the TPV experiment by tracking the decay of the laser induced small perturbation charge by switching the device to short circuit at different times following the laser perturbation and integrating the resulting

current transient. The technique was termed transient photocharge (TPQ) and has a similar experimental setup to a TDCF measurement.

It should be stressed that any lifetime and charge carrier density determination should undergo the sanity check of comparing the calculated loss current and the J_{SC} as well as the reconstruction of the V_{OC}. In practice, the corrections for electrode capacitance and RC decay times have proven to be effective in determining the spatially averaged recombination kinetics that dominate device performance (but may not always give an accurate picture of the recombination of a local scale). Additional validation of experimental data may be provided through drift-diffusion modelling.

3.4.6. Experimental Determination of Energetic Disorder

The charge extraction at open circuit and differential capacitance measurements described in **Section 3.4.1** and **Section 3.4.3**, respectively, can be used to determine the energetic disorder of the active layer as previously discussed.[14,35] More recently, temperature dependent measurements of the charge carrier density have been used to analyse the shape of the DoS in more detail.[36] As discussed above, a key requirement is the uniform distribution of charges throughout the active layer for the range used in the fitting of the charge carrier density versus the open circuit voltage. Therefore, the measurements may be highly sensitive to the device geometry. Additionally, as noted above, the characteristic energy represents a convolution of the hole and electron DoS. Other measurements to characterise the combined characteristic energy that are indirectly based on the charge carrier density in a device are based on temperature dependent measurements of the light ideality factor (determined from the dependence of the open circuit voltage on the light intensity).[4]

Alternatively, transport-based techniques like temperature dependent space-charge limited current (SCLC(T)) measurements on hole and electron only devices may be used to study the disorder of hole and electron polarons in BHJs.[36–39]

Another transport based method to study energetic disorder is based on a time-of-flight type experiment in which high resolution current transients are recorded using an oscilloscope measuring the voltage drop across variable load resistors.[40] Following the extraction of a conduction current, at longer time scales progressively charges from progressively lower lying tailstates are extracted allowing for the quantification of the energetic disorder. The DoS can be calculated as follows:

$$g(t) = \frac{i(t)t}{qAdfkT}$$

Where $g(t)$ is the density of states that is proportional to the product of the time t and the extracted current $i(t)$. A is the active area, d is the active layer thickness, f is the fraction of filled states, q is the elementary charge and kT the thermal energy. The energetic position of the extracted charges can be calculated as follows:

$$E(t) = kTln(v_0 t)$$

where v_0 is the attempt to escape frequency of the charge carriers de-trapping from the tailstates.

The measurements can be carried out at variable voltages and temperatures specifically to determine the attempt to escape frequency.[40,41] Fitting of $g(t)$ versus $E(t)$ has been used to determine the characteristic energy experimentally. This has previously been applied in conjunction with drift-diffusion simulations.[41,42]

3.4.7. Charge Extraction at Short Circuit

Charge extraction at short circuit is a technique similar to that described above but rather than keeping the device at open circuit prior to switching the light off and recording the current transient, the device is kept in light at short circuit. It is intended to determine the charge carrier density present in the device under short circuit at varying light intensity which in turn can be used to qualitatively and quantitatively assess the charge carrier mobility of the device in question. At short circuit, the charge carrier density in the device is only a function of the generation and extraction rate (assuming negligible non-geminate recombination). Therefore, a relationship between the steady state charge carrier density in the device at short circuit and the generation current allows for the effective combined drift mobility to be calculated by:

$$J_{sc} = -qn_{sc}\mu_{eff}Ef(\delta)$$

where n_{sc} is the steady-state charge carrier density in the device at short circuit, μ_{eff} is the effective mobility that is expected to be dominated by the slower of the two carrier mobilities[43] and E is the electric field across the active layer which may be approximated by the built-in potential divided by the active layer thickness (in principle a bias may be applied as well).

Finally, an analytical function $f(\delta) = (2+\delta)(1+2\delta)/(1+\delta)^2$ accounting for the inhomogeneous charge carrier density in the device is used.

A full derivation of the equations provided herein is provided in the thesis by Scot Wheeler as well as the original publications.[1,10,23,26,33,43]

References

(1) Wheeler, S. G. M. Bulk and Surface Recombination Limitations to High Voltage Solution Processed Solar Cells. PhD Thesis, Imperial College London, London, 2017.

(2) Wu, J. The Impact of Tail States on the Performance of Organic Bulk Heterojunction Solar Cells. PhD Thesis, Imperial College London, London, 2019.

(3) Deibel, C.; Kirchartz, T. Transient Optoelectronic Characterization of Thin-FilmSolar Cells. In *Advanced Characterization Techniques for Thin Film Solar Cells*; Abou-Ras, D., Kirchartz, T., Rau, U., Eds.; Wiley-VCH Verlag GmbH & Co. KGaA, 2016; pp 147–162. https://doi.org/10.1002/9783527699025.ch6.

(4) Saladina, M.; Wöpke, C.; Göhler, C.; Ramirez, I.; Gerdes, O.; Liu, C.; Li, N.; Heumüller, T.; Brabec, C. J.; Walzer, K.; Pfeiffer, M.; Deibel, C. Power-Law Density of States in Organic Solar Cells Revealed by the Open-Circuit Voltage Dependence of the Ideality Factor. *Phys. Rev. Lett.* **2023**, *130* (23), 236403. https://doi.org/10.1103/PhysRevLett.130.236403.

(5) Lee, T. H.; Park, W.-W.; Park, S. Y.; Cho, S.; Kwon, O.-H.; Kim, J. Y. Planar Organic Bilayer Heterojunctions Fabricated on Water with Ultrafast Donor-to-Acceptor Charge Transfer. *Solar RRL* **2021**, *5* (8), 2100326. https://doi.org/10.1002/solr.202100326.

(6) *Luxeon Star/O LED - Warm White Batwing; 17 lm @ 350mA*. https://luxeonstar.com/. https://luxeonstar.com/product/lxhl-nwg8/ (accessed 2024-08-15).

(7) *Luxeon Star/O LED - White Batwing; 45 lm @ 350mA*. https://luxeonstar.com/. https://luxeonstar.com/product/lxhl-nwe8/ (accessed 2024-08-15).

(8) Kirchartz, T.; Deledalle, F.; Tuladhar, P. S.; Durrant, J. R.; Nelson, J. On the Differences between Dark and Light Ideality Factor in Polymer:Fullerene Solar Cells. *J. Phys. Chem. Lett.* **2013**, *4* (14), 2371–2376. https://doi.org/10.1021/jz4012146.

(9) Hartnagel, P.; Kirchartz, T. Understanding the Light-Intensity Dependence of the Short-Circuit Current of Organic Solar Cells. *Advanced Theory and Simulations* **2020**, *3* (10), 2000116. https://doi.org/10.1002/adts.202000116.

(10) Shuttle, C. G.; Maurano, A.; Hamilton, R.; O'Regan, B.; de Mello, J. C.; Durrant, J. R. Charge Extraction Analysis of Charge Carrier Densities in a Polythiophene/Fullerene Solar Cell: Analysis of the Origin of the Device Dark Current. *Appl. Phys. Lett.* **2008**, *93* (18), 183501. https://doi.org/10.1063/1.3006316.

(11) Kay, A. M.; Riley, D. B.; Meredith, P.; Armin, A.; Sandberg, O. J. A New Framework for Understanding Recombination-Limited Charge Extraction in Disordered Semiconductors. *J. Phys. Chem. Lett.* **2024**, *15* (16), 4416–4421. https://doi.org/10.1021/acs.jpclett.4c00218.

(12) Kniepert, J.; Lange, I.; van der Kaap, N. J.; Koster, L. J. A.; Neher, D. A Conclusive View on Charge Generation, Recombination, and Extraction in As-Prepared and Annealed P3HT:PCBM Blends: Combined Experimental and Simulation Work. *Advanced Energy Materials* **2014**, *4* (7), 1301401. https://doi.org/10.1002/aenm.201301401.

(13) Sun, B.; Gerber, B.; Shoaee, S.; Neher, D. An Analytical Model for Describing Transient Photocurrents in Bias-Assisted Charge Extraction for Low-Mobility Organic Solar Cells. *Solar RRL* **2024**, *8* (12), 2400211. https://doi.org/10.1002/solr.202400211.

(14) Kirchartz, T.; Nelson, J. Meaning of Reaction Orders in Polymer:Fullerene Solar Cells. *Phys. Rev. B* **2012**, *86* (16), 165201. https://doi.org/10.1103/PhysRevB.86.165201.
(15) Sandberg, O. J.; Tvingstedt, K.; Meredith, P.; Armin, A. Theoretical Perspective on Transient Photovoltage and Charge Extraction Techniques. *J. Phys. Chem. C* **2019**, *123* (23), 14261–14271. https://doi.org/10.1021/acs.jpcc.9b03133.
(16) Kiermasch, D.; Gil-Escrig, L.; Baumann, A.; J. Bolink, H.; Dyakonov, V.; Tvingstedt, K. Unravelling Steady-State Bulk Recombination Dynamics in Thick Efficient Vacuum-Deposited Perovskite Solar Cells by Transient Methods. *Journal of Materials Chemistry A* **2019**, *7* (24), 14712–14722. https://doi.org/10.1039/C9TA04367E.
(17) Kirchartz, T.; Nelson, J. Meaning of Reaction Orders in Polymer:Fullerene Solar Cells. *Physical Review B* **2012**, *86* (16). https://doi.org/10.1103/PhysRevB.86.165201.
(18) Deledalle, F.; Shakya Tuladhar, P.; Nelson, J.; Durrant, J. R.; Kirchartz, T. Understanding the Apparent Charge Density Dependence of Mobility and Lifetime in Organic Bulk Heterojunction Solar Cells. *J. Phys. Chem. C* **2014**, *118* (17), 8837–8842. https://doi.org/10.1021/jp502948y.
(19) Deledalle, F.; Kirchartz, T.; Vezie, M. S.; Campoy-Quiles, M.; Shakya Tuladhar, P.; Nelson, J.; Durrant, J. R. Understanding the Effect of Unintentional Doping on Transport Optimization and Analysis in Efficient Organic Bulk-Heterojunction Solar Cells. *Phys. Rev. X* **2015**, *5* (1), 011032. https://doi.org/10.1103/PhysRevX.5.011032.
(20) Duffy, N. W.; Peter, L. M.; Rajapakse, R. M. G.; Wijayantha, K. G. U. Investigation of the Kinetics of the Back Reaction of Electrons with Tri-Iodide in Dye-Sensitized Nanocrystalline Photovoltaic Cells. *The Journal of Physical Chemistry B* **2000**, *104* (38), 8916–8919. https://doi.org/10.1021/jp001185z.
(21) O'Regan, B. C.; Scully, S.; Mayer, A. C.; Palomares, E.; Durrant, J. The Effect of Al_2O_3 Barrier Layers in TiO_2/Dye/CuSCN Photovoltaic Cells Explored by Recombination and DOS Characterization Using Transient Photovoltage Measurements. *The Journal of Physical Chemistry B* **2005**, *109* (10), 4616–4623. https://doi.org/10.1021/jp0468049.
(22) O'Regan, B. C.; Durrant, J. R. Calculation of Activation Energies for Transport and Recombination in Mesoporous TiO_2/Dye/Electrolyte FilmsTaking into Account Surface Charge Shifts with Temperature. *The Journal of Physical Chemistry B* **2006**, *110* (17), 8544–8547. https://doi.org/10.1021/jp060979w.
(23) Shuttle, C. G.; O'Regan, B.; Ballantyne, A. M.; Nelson, J.; Bradley, D. D. C.; Durrant, J. R. Bimolecular Recombination Losses in Polythiophene: Fullerene Solar Cells. *Phys. Rev. B* **2008**, *78* (11), 113201. https://doi.org/10.1103/PhysRevB.78.113201.
(24) Rauh, D.; Deibel, C.; Dyakonov, V. Charge Density Dependent Nongeminate Recombination in Organic Bulk Heterojunction Solar Cells. *Advanced Functional Materials* **2012**, *22* (16), 3371–3377. https://doi.org/10.1002/adfm.201103118.
(25) Foertig, A.; Wagenpfahl, A.; Gerbich, T.; Cheyns, D.; Dyakonov, V.; Deibel, C. Nongeminate Recombination in Planar and Bulk Heterojunction Organic Solar Cells. *Advanced Energy Materials* **2012**, *2* (12), 1483–1489. https://doi.org/10.1002/aenm.201200718.

(26) Credgington, D.; Liu, S.-W.; Nelson, J.; Durrant, J. R. In Situ Measurement of Energy Level Shifts and Recombination Rates in Subphthalocyanine/C_{60} Bilayer Solar Cells. *The Journal of Physical Chemistry C* **2014**, *118* (40), 22858–22864. https://doi.org/10.1021/jp505297u.

(27) Roiati, V.; Colella, S.; Lerario, G.; Marco, L. D.; Rizzo, A.; Listorti, A.; Gigli, G. Investigating Charge Dynamics in Halide Perovskite-Sensitized Mesostructured Solar Cells. *Energy Environ. Sci.* **2014**, *7* (6), 1889–1894. https://doi.org/10.1039/C3EE43991G.

(28) Wheeler, S.; Bryant, D.; Troughton, J.; Kirchartz, T.; Watson, T.; Nelson, J.; Durrant, J. R. Transient Optoelectronic Analysis of the Impact of Material Energetics and Recombination Kinetics on the Open-Circuit Voltage of Hybrid Perovskite Solar Cells. *The Journal of Physical Chemistry C* **2017**, *121* (25), 13496–13506. https://doi.org/10.1021/acs.jpcc.7b02411.

(29) Kiermasch, D.; Baumann, A.; Fischer, M.; Dyakonov, V.; Tvingstedt, K. Revisiting Lifetimes from Transient Electrical Characterization of Thin Film Solar Cells; a Capacitive Concern Evaluated for Silicon, Organic and Perovskite Devices. *Energy & Environmental Science* **2018**, *11* (3), 629–640. https://doi.org/10.1039/C7EE03155F.

(30) Kniepert, J.; Schubert, M.; Blakesley, J. C.; Neher, D. Photogeneration and Recombination in P3HT/PCBM Solar Cells Probed by Time-Delayed Collection Field Experiments. *The Journal of Physical Chemistry Letters* **2011**, *2* (7), 700–705. https://doi.org/10.1021/jz200155b.

(31) Vollbrecht, J.; Tokmoldin, N.; Sun, B.; Brus, V. V.; Shoaee, S.; Neher, D. Determination of the Charge Carrier Density in Organic Solar Cells: A Tutorial. *Journal of Applied Physics* **2022**, *131* (22), 221101. https://doi.org/10.1063/5.0094955.

(32) Wood, S.; Blakesley, J. C.; Castro, F. A. Assessing the Validity of Transient Photovoltage Measurements and Analysis for Organic Solar Cells. *Physical Review Applied* **2018**, *10* (2). https://doi.org/10.1103/PhysRevApplied.10.024038.

(33) Credgington, D.; Kim, Y.; Labram, J.; Anthopoulos, T. D.; Durrant, J. R. Analysis of Recombination Losses in a Pentacene/C_{60} Organic Bilayer Solar Cell. *The Journal of Physical Chemistry Letters* **2011**, *2* (21), 2759–2763. https://doi.org/10.1021/jz201338d.

(34) Azzouzi, M.; Calado, P.; Telford, A. M.; Eisner, F.; Hou, X.; Kirchartz, T.; Barnes, P. R. F.; Nelson, J. Overcoming the Limitations of Transient Photovoltage Measurements for Studying Recombination in Organic Solar Cells. *Solar RRL n/a* (n/a), 1900581. https://doi.org/10.1002/solr.201900581.

(35) Wu, J.; Lee, J.; Chin, Y.-C.; Yao, H.; Cha, H.; Luke, J.; Hou, J.; Kim, J.-S.; Durrant, J. R. Exceptionally Low Charge Trapping Enables Highly Efficient Organic Bulk Heterojunction Solar Cells. *Energy Environ. Sci.* **2020**, *13* (8), 2422–2430. https://doi.org/10.1039/D0EE01338B.

(36) Perdigón-Toro, L.; Phuong, L. Q.; Eller, F.; Freychet, G.; Saglamkaya, E.; Khan, J. I.; Wei, Q.; Zeiske, S.; Kroh, D.; Wedler, S.; Köhler, A.; Armin, A.; Laquai, F.; Herzig, E. M.; Zou, Y.; Shoaee, S.; Neher, D. Understanding the Role of Order in Y-Series Non-Fullerene

Solar Cells to Realize High Open-Circuit Voltages. *Advanced Energy Materials* **2022**, *12* (12), 2103422. https://doi.org/10.1002/aenm.202103422.

(37) Pasveer, W. F.; Cottaar, J.; Tanase, C.; Coehoorn, R.; Bobbert, P. A.; Blom, P. W. M.; de Leeuw, D. M.; Michels, M. A. J. Unified Description of Charge-Carrier Mobilities in Disordered Semiconducting Polymers. *Phys. Rev. Lett.* **2005**, *94* (20), 206601. https://doi.org/10.1103/PhysRevLett.94.206601.

(38) Felekidis, N.; Melianas, A.; Kemerink, M. Automated Open-Source Software for Charge Transport Analysis in Single-Carrier Organic Semiconductor Diodes. *Organic Electronics* **2018**, *61*, 318–328. https://doi.org/10.1016/j.orgel.2018.06.010.

(39) Hosseini, S. M.; Wilken, S.; Sun, B.; Huang, F.; Jeong, S. Y.; Woo, H. Y.; Coropceanu, V.; Shoaee, S. Relationship between Energetic Disorder and Reduced Recombination of Free Carriers in Organic Solar Cells. *Advanced Energy Materials n/a* (n/a), 2203576. https://doi.org/10.1002/aenm.202203576.

(40) Street, R. A. Localized State Distribution and Its Effect on Recombination in Organic Solar Cells. *Phys. Rev. B* **2011**, *84* (7), 075208. https://doi.org/10.1103/PhysRevB.84.075208.

(41) MacKenzie, R. C. I.; Shuttle, C. G.; Dibb, G. F.; Treat, N.; von Hauff, E.; Robb, M. J.; Hawker, C. J.; Chabinyc, M. L.; Nelson, J. Interpreting the Density of States Extracted from Organic Solar Cells Using Transient Photocurrent Measurements. *J. Phys. Chem. C* **2013**, *117* (24), 12407–12414. https://doi.org/10.1021/jp4010828.

(42) MacKenzie, R. C. I.; Shuttle, C. G.; Chabinyc, M. L.; Nelson, J. Extracting Microscopic Device Parameters from Transient Photocurrent Measurements of P3HT:PCBM Solar Cells. *Advanced Energy Materials* **2012**, *2* (6), 662–669. https://doi.org/10.1002/aenm.201100709.

(43) Shuttle, C. G.; Hamilton, R.; Nelson, J.; O'Regan, B. C.; Durrant, J. R. Measurement of Charge-Density Dependence of Carrier Mobility in an Organic Semiconductor Blend. *Advanced Functional Materials* **2010**, *20* (5), 698–702. https://doi.org/10.1002/adfm.200901734.

4

LIMITATIONS OF STATE-OF-THE-ART VAPOUR-PROCESSED ORGANIC SOLAR CELLS

4. Limitations of State-of-the-Art Evaporated Organic Solar Cells

4.1. Introduction

As previously outlined, VP-OSCs currently possess the most viable route for commercialisation[1] with a commercial scale production line recently being opened by Heliatek GmbH[2] and their vapour-processed modules being the first OSC modules to achieve the industrial grade stability certification (IEC 61215)[3]. This results chapter focuses on the performance limitations of a state-of-the-art vapour-processed organic solar cells (VP-OSC) provided by Heliatek GmbH. Specifically, this chapter will investigate single-junction solar cells based on DCV-V-Fu-Ind-Fu-V & C_{60}. It will be split into two parts.

The first subchapter (**Subchapter 4.2**) focuses on the impact of the BHJ morphology on device performance. Detailed studies about the relation between morphology, charge generation, non-geminate recombination and charge extraction for VP-OSCs are rare in the literature. Here, I study the origin of the increased current density and fill factor enabled by substrate heating during co-evaporation of the BHJ. Collaborators characterised the morphology by grazing-incidence wide-angle scattering (GIWAXS) and resonant soft X-ray spectroscopy (RSoXS). The observed increase in the current generation is explained by improved absorption due to changes in orientation and crystallinity in the heated samples. Transient absorption measurements reveal only minor differences in the efficiency of exciton and charge separation. To better understand the collection efficiency and fill factor of the devices, I employed transient optoelectronic characterisations and device simulations to show that the charge carrier kinetics in the studied devices are governed by a large density of trap states. While the energetic disorder and non-geminate recombination kinetics under open circuit conditions remain largely unchanged, the increased effective mobility and the observed lower energetic transport disorder explain the overall increase in collection efficiency. The morphological characterisation is key to pinpoint the improved mobility to the increased phase purity and the reduction of isolated donor phases in the heated device. I propose that non-geminate recombination and charge transport are governed by different aspects of the energetic and spatial disorder. Quantitative comparison of the collection efficiency with high fill factor solution processed OSCs reveals that the low mobility is the main bottleneck towards increasing device fill factor. Finally, device simulations were used to give an outlook for future

performance increases if the transport disorder in this material blend is further improved through further optimisation of the morphology.

In **Subchapter 4.3**, I address the voltage losses in the same material system and different mitigation strategies based on active layer structure. Despite the differing morphology, the V_{OC} of the devices discussed in **Subchapter 4.2** remained unchanged due to the unchanged material energetics and non-geminate recombination losses. However, compared to NFA based SP-OSCs the voltage losses in VP-OSCs constitute the biggest intrinsic difference. While the collection efficiency was shown to be a key performance limiting factor in the single-junction BHJ devices, in **Subchapter 4.2**, I also illustrated the mitigation of its effect in thinner devices at the expense of limited absorption. Multi-junction devices have the potential to combine good collection efficiency with high absorption by stacking multiple thin junctions. However, they are particularly affected by voltage losses adding up across the monolithic sub-cells. This chapter will therefore focus on devices using the same active layer materials but yielding an increased V_{OC} to address strategies to reduce voltage losses that pose a fundamental limit to the maximum OSC performance. For this purpose, different D/A ratios (2:1 vs 1:2) and device architectures (BHJ vs PHJ) are studied. These affect the material energetics as well as the recombination kinetics which I studied by applying different measurements of the material energetics (absorption onset, electroluminescence) and optoelectronic techniques (TPV, DC, CE) to explain the observed differences in V_{OC}. While the main emphasis is on the V_{OC}, further observations relating disorder, charge generation and charge extraction and their effect will also be addressed later, along with a discussion of future experiments to link these observations. I will provide an estimate of potential performance gains in DCV-V-Fu-Ind-Fu-V:C_{60} devices by employing a multi-junction architecture and trade-offs between V_{OC} and collection efficiency that may result in different optimal sub-cell structures compared to the optimum single-junction cells.

4.2. Charge Carrier Dynamics of Vapour-Processed Organic Solar Cells – The Impact of Morphology

4.2.1. Background

The high PCEs of SP-OSC are motivating extensive studies of their underlying photo-physics, nanomorphology and charge carrier dynamics to guide further performance enhancement. In contrast, despite their commercial potential, there are relatively few studies of the underlying factors determining the PCEs of VP-OSCs.[1] Herein, I focus on the correlation between nanomorphology and charge carrier dynamics in high performance BHJ VP-OSCs fabricated from a small molecule donor and C_{60} acceptor, and how these compare to those observed in SP-OSCs.

To date, the efficiency advances achieved with non-fullerene acceptors in SP-OSCs – such as their low voltage losses and absorption range extending to the near-infrared – have not been mirrored in VP-OSCs, due at least in part to the smaller molecular size constraint imposed by thermal evaporation.[1,4] This difference in molecular size also plays a role in the aggregation behaviour of solution versus vacuum processed BHJ films. High performance polymer-fullerene SP-OSC systems typically exhibit very ordered domains.[5] Phase separation and purity can be further aided through the use of solvent additives or post-deposition thermal/solvent-vapour annealing.[6–9] In contrast, evaporable small molecule donors paired with fullerene acceptors often form highly intermixed blends, related to their similar size and stronger intermolecular interactions between donor and acceptor molecules.[10] Common ways to achieve some limited morphological optimisation for VP-OSC[11] include the use of templating substrates,[10,12] co-evaporants inducing crystallization,[13–16] thermal annealing[17–19] or by altering the substrate temperature during evaporation[17,20].

Vacuum processed intermixed blends, such as DCV5T-Me : C_{60}, one of the highest performing VP-OSC systems, exhibit poorer charge collection capabilities than efficient SP-OSC's, resulting primarily from less favourable competition between charge extraction and non-geminate recombination. Empirically, the poorer collection functionality of most VP-OSCs is evident from the drop in fill factor (*FF*) typically observed for active layers thicker than 50 nm, thus limiting film optical absorption and hence current density (J_{SC}). Donors of the ZnPc family are a notable exception that exhibits more ordered films when paired with C_{60} (especially when deposited at elevated substrate temperatures or together with co-evaporants

inducing crystallisation)[10,13,15,16,20] but exhibit high voltage losses and poor absorption coefficients.[4] In contrast, SP-OSCs typically achieve the highest performance at active layer thicknesses ≈ 100 nm[21,22], indeed for some devices > 300 nm.[23–27] A key challenge for VP-OSC is therefore gaining a better understanding of the interplay between active layer morphology and the efficiency of charge collection (transport versus non-geminate recombination) and how this can guide strategies to enable further advances in the *PCE*s of VP-OSCS.

Previous studies on the kinetic competition between the non-geminate recombination rate and charge mobility, primarily undertaken on SP-OSCs, have employed a range of optoelectronic techniques such as transient photovoltage and photocurrent, photo-CELIV, time-delayed collection field and charge extraction.[4,28–33] In order to quantify the impact of charge mobility and recombination on device *FF* and compare the collection efficiency across different materials, several figures of merit have been discussed. These include the Langevin reduction factor γ, the collection efficiency θ and the electronic quality *Q*.[28,34] Studies on fullerene and NFA based SP-OSCs have revealed a correlation between more ordered morphologies and lower energetic disorder with higher collection efficiencies and thickness scalability.[30–32] However, similar studies linking the collection efficiency with morphology and optoelectronic measurements for VP-OSCs are very limited to date[4,35,36,19] with direct comparison of these dynamics in between VP- and SP-OSCs largely absent from the literature.

Here, I present a study on the interplay between morphology, charge carrier dynamics and device performance for a state-of-the-art VP-OSC system: DCV-V-Fu-Ind-Fu-V : C_{60} provided by Heliatek GmbH.[37] This donor material is representative of a class of A-D-A type donors with di-cyano-vinyl endgroups that have been shown to hold great promise in VP-OSCs. The active layer morphology is altered by substrate heating during evaporation. Grazing-incidence Wide-Angle X-Ray Scattering (GIWAXS) and Resonant Soft X-Ray Scattering (RSoXS) were carried out by collaborators to study differences induced by substrate heating in molecular orientation and crystallinity, and the size and purity of phase-separated domains, respectively. Subsequently, I analyse the impact of the changed active layer morphology on multiple aspects of solar cell operation from charge generation (absorption, exciton quenching efficiency, charge separation) to charge collection (non-geminate recombination versus charge extraction). Active layer films were characterised using UV/Vis absorption,

photoluminescence and ultra-fast transient absorption spectroscopy. To address the collection efficiency limitations critical to VP-OSC performance, I employed transient photovoltage/photocurrent measurements and charge extraction analyses, focusing in particular on the impact of the energetic disorder in the blends.

These analyses of collection efficiency are compared to two SP-OSC references – employing small-molecule : fullerene (BTR : $PC_{70}BM$) and polymer : NFA (PM6 : Y6) photoactive layers. PM6 : Y6 is a well-established high efficiency SP-OSC, whilst BTR & $PC_{70}BM$ are more analogous in terms of molecular sizes to DCV-V-Fu-Ind-Fu-V & C_{60}. The reference materials were chosen to highlight the difference (especially in collection efficiency) between the classes of materials utilised for solution- and vapour-processing, respectively, not with the intention of comparing film growth in the different deposition techniques. Due to the size restrictions imposed by evaporation, neither Y6 nor BTR can be utilised in VP-OSCs. However, Kaienburg *et al.* reported a hybrid PHJ device consisting of a solution-processed Y6-layer with an evaporated donor layer on top that yielded exceptionally low voltage losses.[38] Both of these solution processed references are known for their high collection efficiencies and thickness tolerance.[25,30,31,39] I quantify the Langevin reduction factor and the electronic quality of both DCV-V-Fu-Ind-Fu-V : C_{60} devices and highlight improvements through morphological optimisation as well the comparison with solution processed references. Finally, with the help of Roderick Mackenzie, I employ device simulations using the software package OghmaNano to link the physical measurements and device parameters. I conclude by providing an outlook for possible performance increases that could be achievable by further optimisation of the deposition control and/or adjustments of the molecular structure that could yield improved aggregation.

4.2.2. Contributions

This chapter was prepared for publication[40] and further experimental details can be found there-in. Many collaborators contributed to this work through experimental work. Transient absorption spectroscopy measurements were carried out by Yifan Dong. Julian Heger and Eva Bittrich provided GIWAXS measurements. Pascal Kaienburg measured the RSoXs data with support by Subhrangsu Mukherjee. Global fitting of the experimental data with the drift-diffusion simulation OghmaNano was performed by Roderick Mackenzie. All devices were supplied by Heliatek GmbH. Special thanks to Ivan Ramirez, Seyed Mehrdad Hosseini, Marieta Levichkova and Martin Pfeiffer for supplying the devices and valuable discussions.

4.2.3. Materials, Device Architecture & Performance

The structures of the evaporated donor and acceptor molecules, DCV-V-Fu-Ind-Fu-V and C_{60}, are shown in **Figure 4.2.1 (a)** (see **Figure 3.1.1** for the structures of the SP-OSC reference materials BTR : PCBM and PM6 : Y6, as well as device fabrication details).

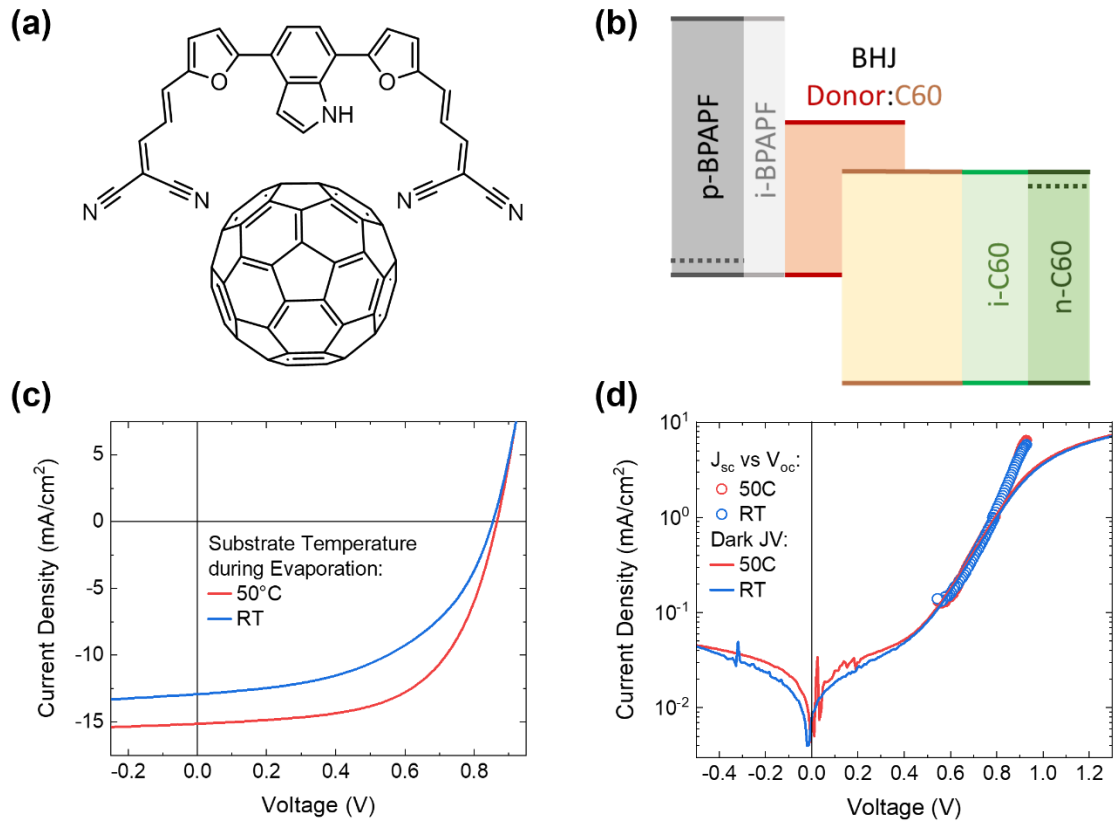


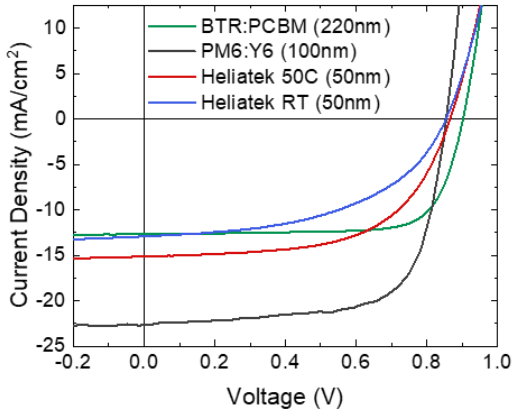
Figure 4.2.1. (a) Chemical structure of the donor molecule DCV-V-Fu-Ind-Fu-V and the acceptor C_{60}. **(b)** Schematic of the energy level alignment of the active layer and interlayers. Note that the relative energetic alignment is deduced from a combination of literature and experimental values as described in the main text. **(c)** *JV*-curve of the devices with 50 nm active layer thickness used for the analysis herein. **(d)** Corresponding dark *JV*-curves and J_{SC} vs V_{OC} graphs.

The DCV-V-Fu-Ind-Fu-V donor molecule is related to the more widely studied DCV5T-Me donor with A-D-A structure and was synthesized by Heliatek GmbH. The BHJ was produced by co-evaporation in a 2:1 D-A-ratio. During evaporation, the substrate was either kept at room temperature or heated to 50 °C (referred to as *RT* and *50C*, respectively). The active layer thickness of 50 nm was chosen as a compromise between absorption and charge carrier collection efficiency. While the optimum performance is achieved for thinner active layers, 50 nm also helps to reduce the impact of the device capacitance on optoelectronic measurements, as discussed in the methods section. The active layer is evaporated on a thin layer of undoped C_{60} and capped with undoped BPAPF (see **Figure 3.1.1** for the structure), the electron and

hole selective contacts, respectively. This interlayer structure minimises the effect of surface recombination of minority carriers at the contacts. An additional layer of n-doped C_{60} and p-doped BPAPF complete the respective interlayers. These aid the reduction of the series resistance by making the bulk of the transport layers more conductive.

Figure 4.2.1 (b) shows a visual representation of the energy alignment of the device. Note that the offsets at the interfaces are not to scale. Further details about the device preparation can be found in the **Section 3.1**. **Figure 4.2.1 (c)** shows the *JV*-curve of the *RT* and *50C* device. Heating the substrate during evaporation yields an improved *FF* (61 vs 53 %) and J_{SC} (15.1 vs 12.9 mA/cm²) resulting in an improvement of the *PCE* from 5.8% to 7.9%. The V_{OC} of the *50C* device only shows a small increase of about 10 mV compared to the *RT* device. This together with the very similar dark *JV*-curves shown in **Figure 4.2.1 (d)** indicate similar voltage losses in the system.

Hero devices using a proprietary hole transport layer (HTL) are (deposited at 50 °C, active layer thickness 50 nm) achieve a PCE of 8.4%. To the best of my knowledge, this is among the highest PCEs currently published for an evaporated single junction OSC using C_{60} as the acceptor (up to 10 % can be achieved using the more expensive C_{70}).[41] **Figure 4.2.2** shows the *JV*-curves of the chosen SP-OSC references.



	J_{SC} [mA/cm²]	FF [%]	V_{OC} [V]	PCE [%]
DCV-V-Fu-Ind-Fu-V:C_{60} (RT)	12.9	50	0.85	5.5
DCV-V-Fu-Ind-Fu-V:C_{60} (50C)	15.1	59	0.86	7.8
BTR:PCBM	12.7	75	0.90	8.6
PM6:Y6	22.7	69	0.85	13.4

Figure 4.2.2 (left) *JV*-curves of evaporated OSCs and solution processed reference OSCs. The legend shows the active layer thickness. Note that these *JV*-curves were obtained using an LED light source calibrated to the same J_{SC} value. **(right)** *JV*-parameters of the OSCs.

4.2.4. Light Intensity Dependent JV-Curves

To decouple the influence of different loss mechanisms on the differences in device *FF* and J_{SC} described above, I first turn to the light intensity dependence of the device *JV*-parameters.

Figure 4.2.3 **(a)**, **(b)** and **(c)** show the normalised *JV*-curves of the *50C* and *RT* device, the BTR : PCBM reference and the PM6 : Y6 reference, respectively. Around the maximum power point, a strong intensity dependence of the *JV*-curves indicates that the VP-OSCs are limited by the collection efficiency as the non-geminate recombination rate (recombination order > 1) increases at higher generation rates. The evaporated devices exhibit a loss in *FF* of more than 10 % between 0.05 and 1 sun equivalent LED illumination, dominating the light intensity dependence of the *PCE* (see also **Figure 4.2.3** **(d)** and **(e)**). The evaporate devices both exhibit lower *FF*s and a loss of J_{SC} at lower light intensities (**Figure 4.2.3** **(f)**) than the SP-OSC references. In contrast, the SP-OSC references only show very little dependence of the *FF* and *PCE* on the light intensity. These data all indicate that the VP-OSCs, and particularly the RT device, exhibit less efficient charge collection than the SP- references, despite their thinner, 50 nm photoactive layer thickness, compared to 100 nm for PM6 : Y6 and 230 nm for BTR : PCBM.

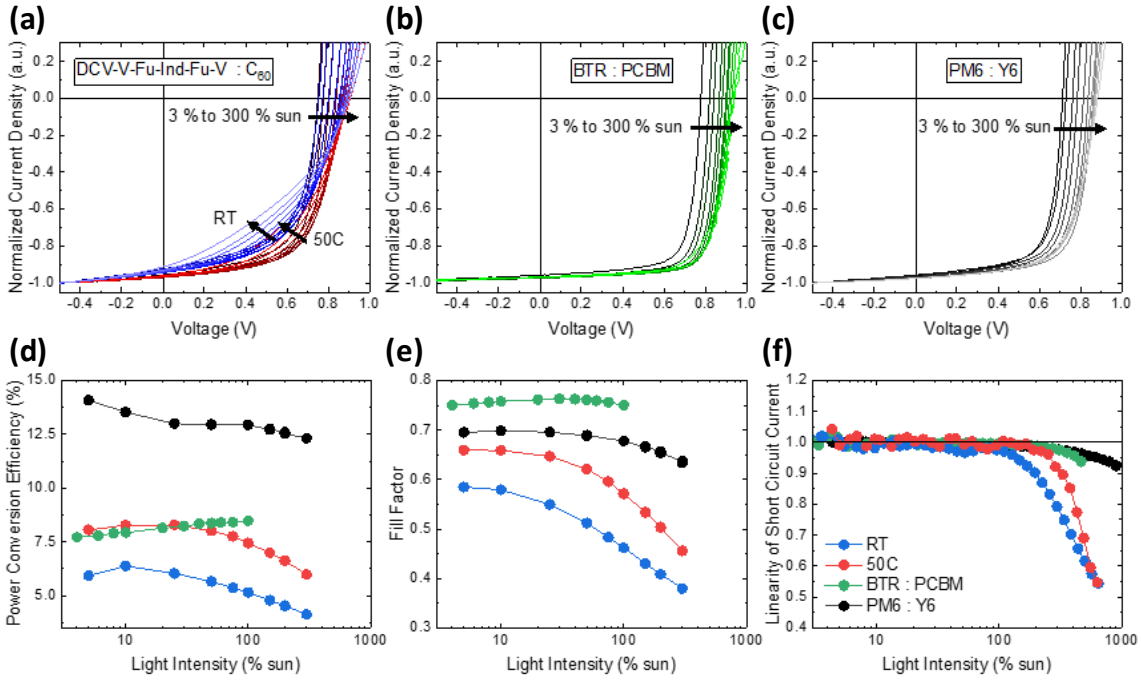


Figure 4.2.3. (a), (b), (c) Normalised *JV*-curves of DCV-V-Fu-Ind-Fu-V : C_{60} (RT and 50C, blue and red, respectively), BTR : PCBM and PM6 : Y6, respectively, for the range of 3 % to 300 % of 1 sun equivalent light intensity. **(d), (e), (f)** Light intensity dependence of power conversion efficiency, fill factor and linearity of the short circuit current density, respectively. See **(f)** for the legend.

At reverse and low forward bias, both VP-OSCs show very little variation in the normalised *JV*-curve shape with increasing light intensity indicative of the slope of the *JV*-curves being dominated by a first order process rather than intensity dependent charge collection. Efficient charge collection at J_{SC} up to 1 sun equivalent light irradiation is also demonstrated by the

excellent J_{SC} linearity in **Figure 4.2.3 (f)**. The reduced J_{SC} in the *RT* device compared to that deposited at *50C* is therefore more likely related to differences in absorption and field dependent geminate losses, as indicated by the slightly larger intensity independent slope in the reverse bias region. The current saturation of the *50C* device around J_{SC} is improved and comparable with that of the non-fullerene reference, while the large offset fullerene reference shows the highest current saturation at J_{SC}.

These results indicate that the morphological modifications achieved by varying the substrate temperature during the evaporation process improves both the charge generation and collection elements of device function. Poor charge collection constitutes the main loss mechanism of the VP-OSCs compared to the SP-OSC references at 1 sun illumination. In the following, charge generation, recombination and extraction will be assessed in more detail. A particular focus will be put on studying the competition between non-geminate recombination and charge transport and their relation to the morphology and energetic disorder.

4.2.5. Morphology Analysis

Figure 4.2.4 (a) and **(b)** show the 2D GIWAXS data of the *50C* and *RT* film, respectively. The *50C* film has a strongly increased scattering intensity, indicating a significant higher overall crystallinity with preferential orientation. In **Figure 4.2.4 (c)**, the out-of-plane intensities obtained from azimuthally integrated cake cuts are shown against q. The reflexes located at (0.73 ± 0.01) $Å^{-1}$ and (1.81 ± 0.01) $Å^{-1}$ for the *RT* film are assigned to the (100) and (010) lattice planes of the orthorhombic unit cell, corresponding to lamellar and π-π stacking of the donor molecule, respectively, and shift to (0.77 ± 0.01) $Å^{-1}$ and (1.86 ± 0.01) $Å^{-1}$ for the *50C* film. Hence, the corresponding lattice spacings d_{100} and d_{010} shift from (8.63 ± 0.05) Å to (8.18 ± 0.04) Å and from (3.47 ± 0.01) Å to (3.38 ± 0.01) Å, respectively, indicating a slightly denser molecular arrangement of the crystalline phase in the *50C* film. Considering the lattice being formed by a stack of donor molecules, the (010) reflex is related to the π-π-stacking.[42] By comparison to similar GIWAXS patterns of vapour-deposited small organic molecular donors,[12,43] the (100) reflex can either resemble a tilted π-π-stacking of the molecule or stacking along the shortest axis.

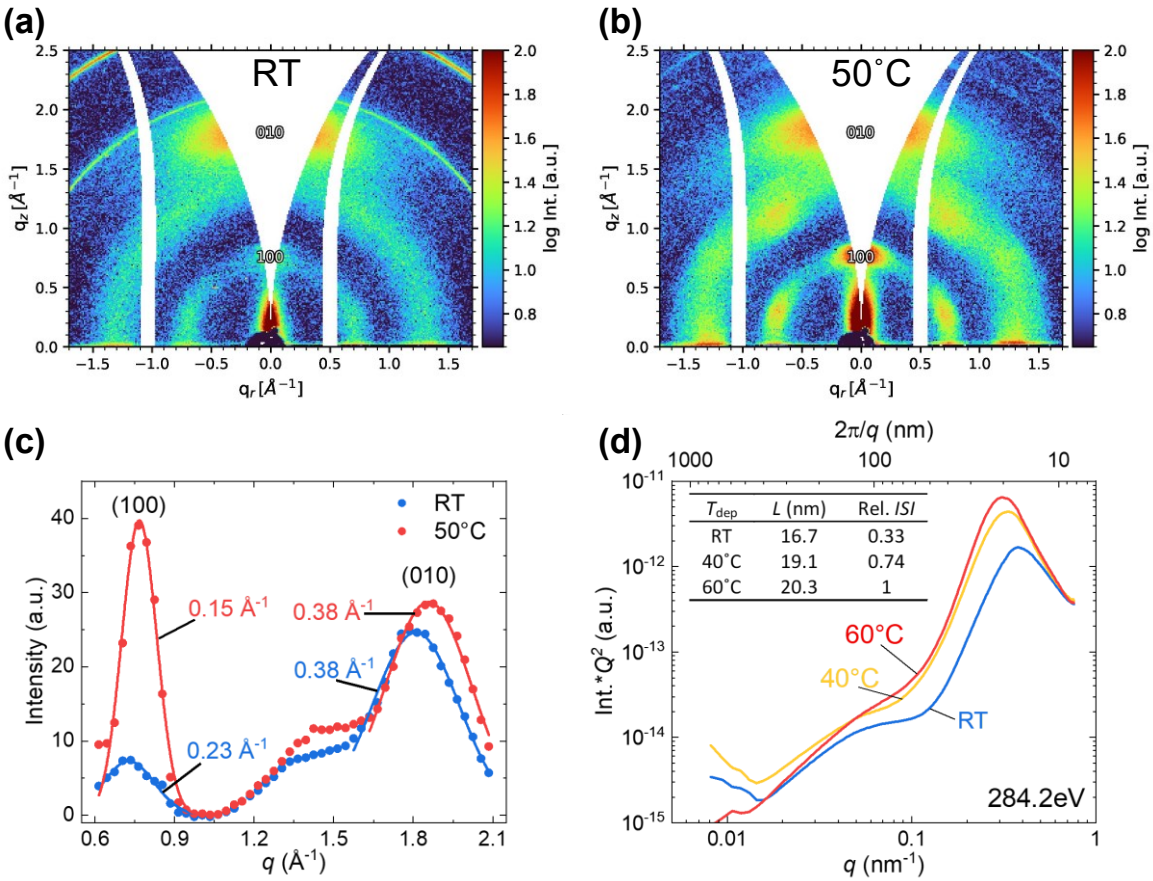


Figure 4.2.4. (a), **(b)** 2D-GIWAXS diffraction patterns for *RT* and *50C* films, respectively. The sharp reflection in **(a)** is due to specular reflection from the edged Si substrate (see **Figure 4.2.5 (a)**). **(c)** 1D diffraction patterns obtained from out-of-plane cake cuts of the RT and 50C film, respectively. The Gaussian fits are shown in solid lines together with the corresponding FWHM values used to calculate the coherence length in the main text. **(d)** RSoXS data at resonance on a log-log scale for samples deposited at different substrate temperatures. The stack is SiN/C_{60} (10 nm)/BHJ (50 nm, D:A 3:2 wt%)/BPAPF(10 nm). The *40C* sample was 30 nm and its intensity scaled accordingly. The table indicates the long period *L* and integrated scattering intensity *ISI* normalized to the *60C* sample. GIWAXS measurements and analysis were carried out by Julian E. Heger and Eva Bittrich. Pascal Kaienburg provided the RSoXS results with support from Subhrangsu Mukherjee.

The full width at half maximum (FWHM) of the reflexes is a measure of the coherence length of the respective lattice planes (hkl), which is related to the crystallite size according to the Scherrer equation, where the size $L_{hkl} \sim 2\pi/FWHM$.[44] Additional broadening effects due to the semicrystalline nature of soft matter make a defined calculation of crystallite sizes non-trivial,[45] however, a qualitative estimation of their lower limit is possible. In **Figure 4.2.4 (c)**, the FWHM of the (010) reflex remains constant at (0.38 ± 0.01) Å^{-1}, while the FWHM of the (100) reflex narrows from (0.23 ± 0.01) Å^{-1} to (0.15 ± 0.01) Å^{-1} upon increasing the substrate temperature. This evolution suggests that the minimum crystallite size along the

[010] direction remains constant, while it is of about 1.5 times larger along the [100] direction in the *50C* film.

Pole figures of radially integrated tube cuts along the (100) reflex (**Figure 4.2.4 (e)**) and the (010) reflex (**Figure 4.2.4 (f)**) reveal the material quantity of crystallites in preferred orientation with respect to the substrate.[46] Also see **Figure 4.2.5 (b)** and **(c)** for azimuthal tube cuts of the reflexes.

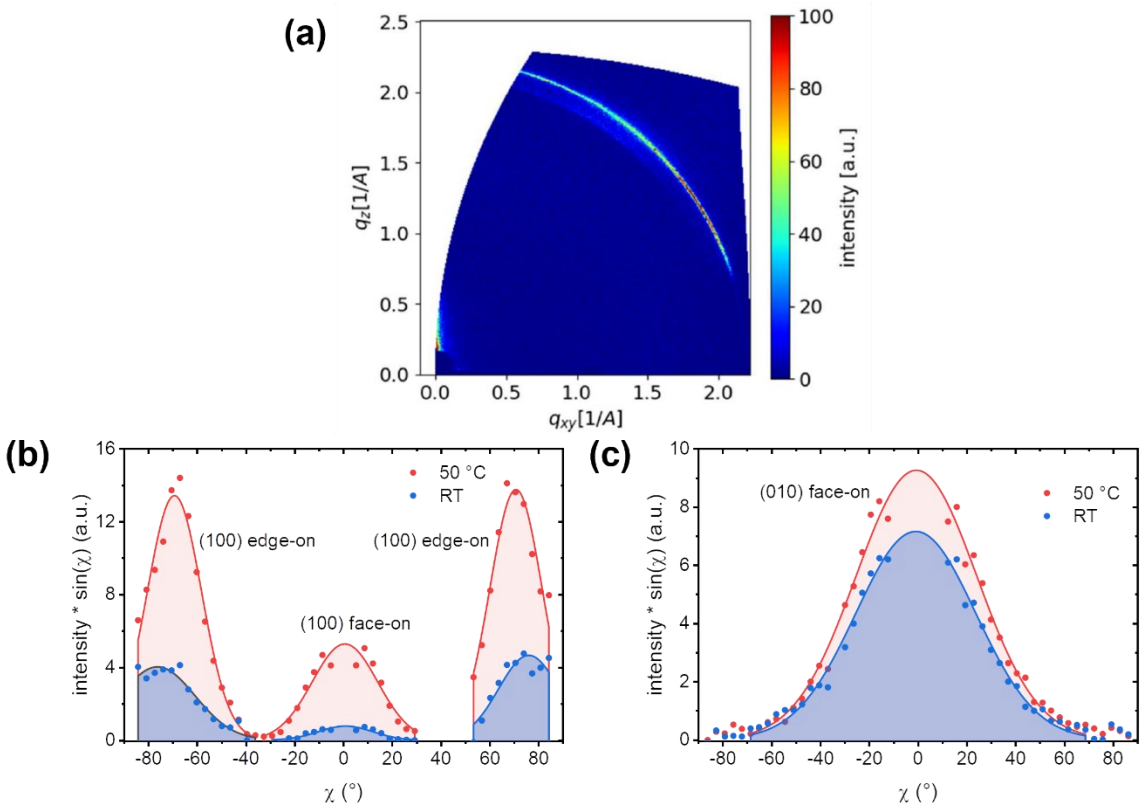


Figure 4.2.5. (a) 2D-GIWAXS diffraction pattern of the edged Si substrate showing a similar specular reflection as observed for the *RT* diffraction pattern shown in the main text. This demonstrates that this feature arises from the Si substrate rather than the organic layers as would be expected for such a sharp feature. **(b)**, **(e)** Pole figures obtained from azimuthal tube cuts of the (100) and (010) reflexes, respectively. The Gaussian fits are shown in solid lines. GIWAXS measurements and analysis were carried out by Julian E. Heger and Eva Bittrich.

For both substrate temperatures, face-on and edge-on populations are observed. The results show a strongly increased preferential orientation for the (100) reflex in the *50C* film judged by relative changes in scattering intensity, with about 3 times more crystallites in edge-on orientation and about 6 times more in face-on orientation, as compared to the *RT* film. When comparing the different preferential orientations for the (100) reflex, the amount edge-on orientation is about 5 times higher than face-on orientation in the *RT* film, and about 2.5 times

higher in the *50C* film. The (010) reflex shows an about 1.3 times higher face-on orientation in the *50C* film compared to the *RT* film. The increase in the (100) out-of-plane reflection and in overall crystallinity is likely to increase the fraction of the integral transition dipole moment within the substrate plane for the *50C* film, thus enhancing the absorption of incident visible light within the photoactive blend, as I discuss further below.

Besides the average crystallinity, the size of phase-separated domains and their purity are critical for BHJ device operation. Resonant soft X-ray Scattering (RSoXS) is a technique capable of measuring the relative composition of domains as well as quantify the size of the domains.[47] **Figure 4.2.4** **(d)** shows blends deposited at different substrate temperatures. The presence of a strong peak at $q \sim 0.3$ nm^{-1} shows that phase separation occurs already at room temperature. With increasing substrate temperature, the long period L – indicative of the domain size - continuously increases from 16.7 nm at room temperature to 20.3 nm at *60C*. The increase in domain size coincides with increased domain purity. This can be seen qualitatively by the higher RSoXS scattering intensity for higher temperature samples. When quantifying the relative domain composition with the relative integrated scattering intensity *ISI*,[48] the *RT ISI* is a third of *60C* sample. Note, that to be as close as possible to the device stack, the blends are sandwiched between layers of C_{60} and BPAPF which makes a quantitative interpretation of the *ISI* challenging. However, trends and the qualitative behaviour of the blends upon annealing can be deduced from the data. See the supplementary information of the published manuscript for further information about the measurement.[40]

In summary, the *RT* sample already shows some degree of crystalline order and phase separation. Two populations of crystallites with edge-on and face-on orientation are observed. For the *50C* sample, the measurements reveal an overall higher degree of crystallinity, tighter packing of molecules, larger crystallites in the lamellar direction and phase-separated domains becoming larger and purer. The crystallite size in π-π direction seems unchanged. Both orientation populations are also observed at *50C* but the relative share of donor molecules with face-on orientation increases.

4.2.6. Absorption & Free Charge Generation

To address the origin of the increased J_{SC} achieved through substrate heating, the optical properties of films with the two different active layer morphologies were studied. The neat

donor DCV-V-Fu-Ind-Fu-V shows a high absorption coefficient similar to other small molecule donor[4,49] and NFA materials with analogous A-D-A structures and di-cyano endgroups. In blends, the *50C* deposited films exhibit a stronger absorbance in the donor region (500 to 800 nm) compared to the *RT* films (**Figure 4.2.6 (a)**), suggesting a better in-plane alignment of the donor transition dipole. These observations agree with the GIWAXS data discussed above. The higher degree of order observed in the *50C* film indicates that fewer molecules are tilted upwards towards an end-on orientation, which consistent with the increased optical absorption.

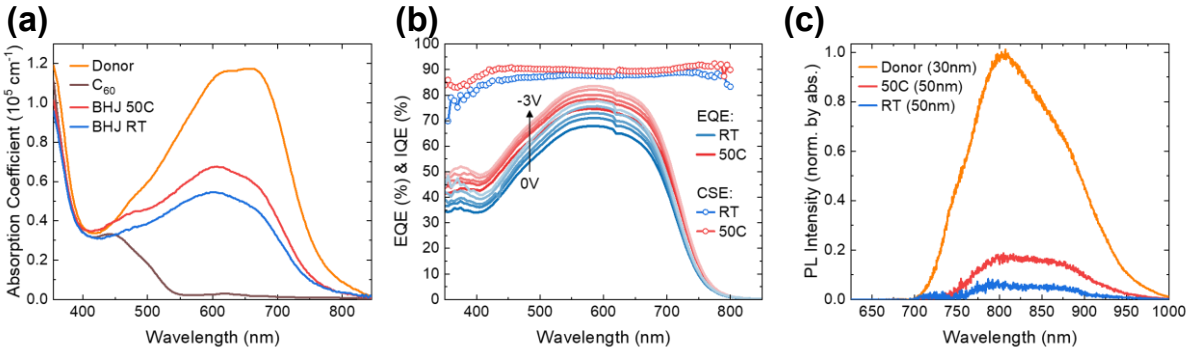


Figure 4.2.6. (a) Absorption spectra of the neat donor DCV-V-Fu-Ind-Fu-V, acceptor C_{60} and blend films deposited at 50˚C and room temperature. **(b)** Field-dependent external quantum efficiency (EQE) spectra of the *50C* and *RT* devices. Also shown is the relative charge separation efficiency (CSE) that was calculated as the ratio of the EQE at 0V and -3V. **(c)** Donor photoluminescence spectra of the neat donor, *RT* and *50C* blends normalized by their absorption.

Interestingly, the change in donor aggregation determined from the GIWAXS data does not lead to a shift in absorption, as observed in related DCV based small molecule donors upon increased aggregation.[35,50] This is also evident from the small shift of the effective photovoltaic gap as calculated from the derivatives of the EQE spectra (≈1.72 eV).

The external quantum efficiency (EQE) data (**Figure 4.2.6 (b)**) indicate that the increase in film absorption observed for the *50C* films is also reflected in an increase in photocurrent generation in complete devices. Measurements of the field dependent EQE were used to determine the quantum efficiency of charge separation by calculating the ratio of the EQE determined at 0V and -3V (**Figure 4.2.6 (b)**). It indicates a small improvement in the efficiency of charge separation for the *50C* device, especially in the C_{60} absorption region. This is in line with the slightly improved saturation at reverse bias as discussed above for the light intensity dependent *JV*-curves. This most likely stems from a small reduction in field dependent geminate recombination.

To assess the efficiency of exciton separation, I measured the photoluminescence quenching efficiency (PLQE) of the BHJs, as is commonly done for fullerene-based devices. **Figure 4.2.6 (c)** shows that the absorption corrected donor PL intensity is reduced by 86 % and 96 % in the *50C* and *RT* blends respectively, relative to neat donor films. To further investigate the efficiency of exciton separation, the exciton decay lifetime upon optically pumping the donor was measured via ultrafast transient absorption spectroscopy (see **Figure 4.2.7**).

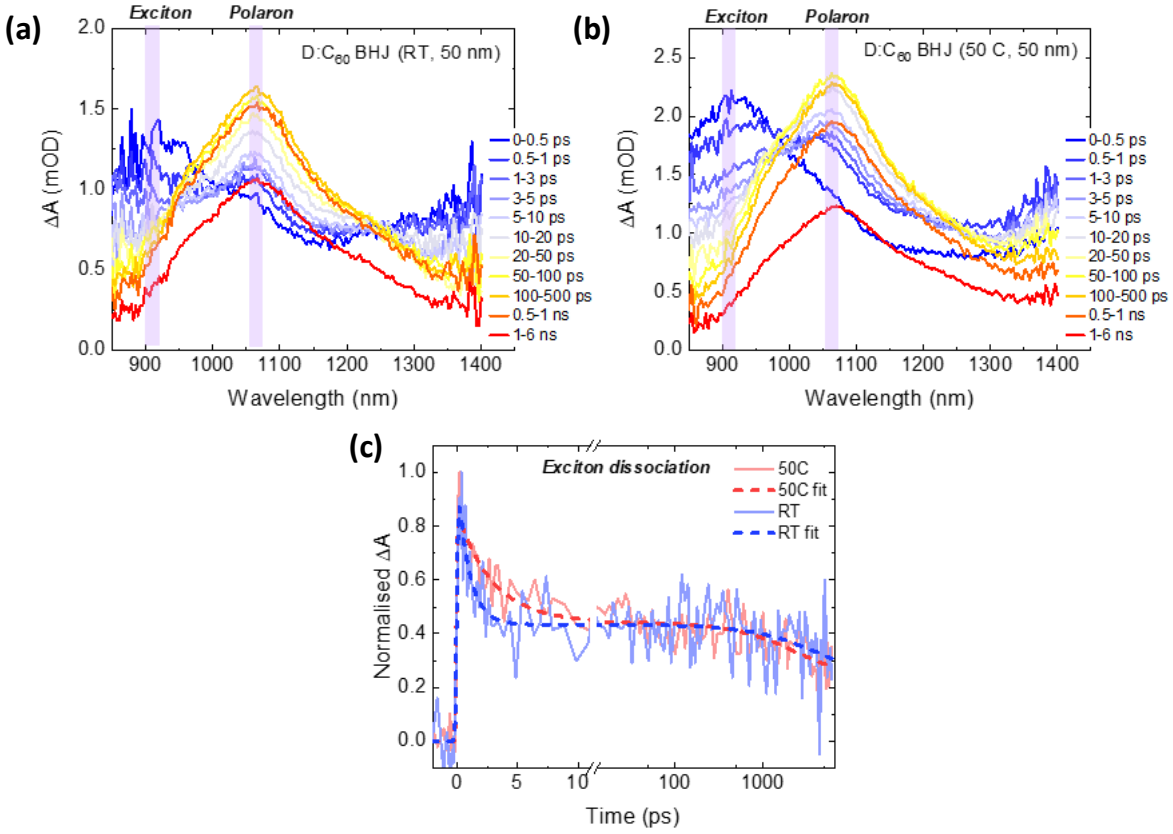


Figure 4.2.7. (a), (b) Transient absorption spectra of *RT* and *50C* films, respectively, after selectively pumping the donor at 600 nm with a fluence of 48 μJ cm^{-2}. **(c)** Time evolution of the exciton signal between 900 and 920 nm together with fits of the exciton decay with lifetimes of 0.9 and 2.9 ps for *RT* and *50C*, respectively. TAS spectra were measured by Yifan Dong.

The time resolved measurements show a reduction of the exciton lifetime (photo-induced absorption signal around 900 to 920 nm, see **Figure 4.2.7 (a)** and **(b)**) from 53 ps in the neat donor film to 2.9 ps and 0.9 ps for the *50C* and *RT* films, respectively (see kinetic data **Figure 4.2.7 (c)**). The neat donor lifetime and spectra as well as fluence dependent kinetics are available in **Figure 4.2.8**.

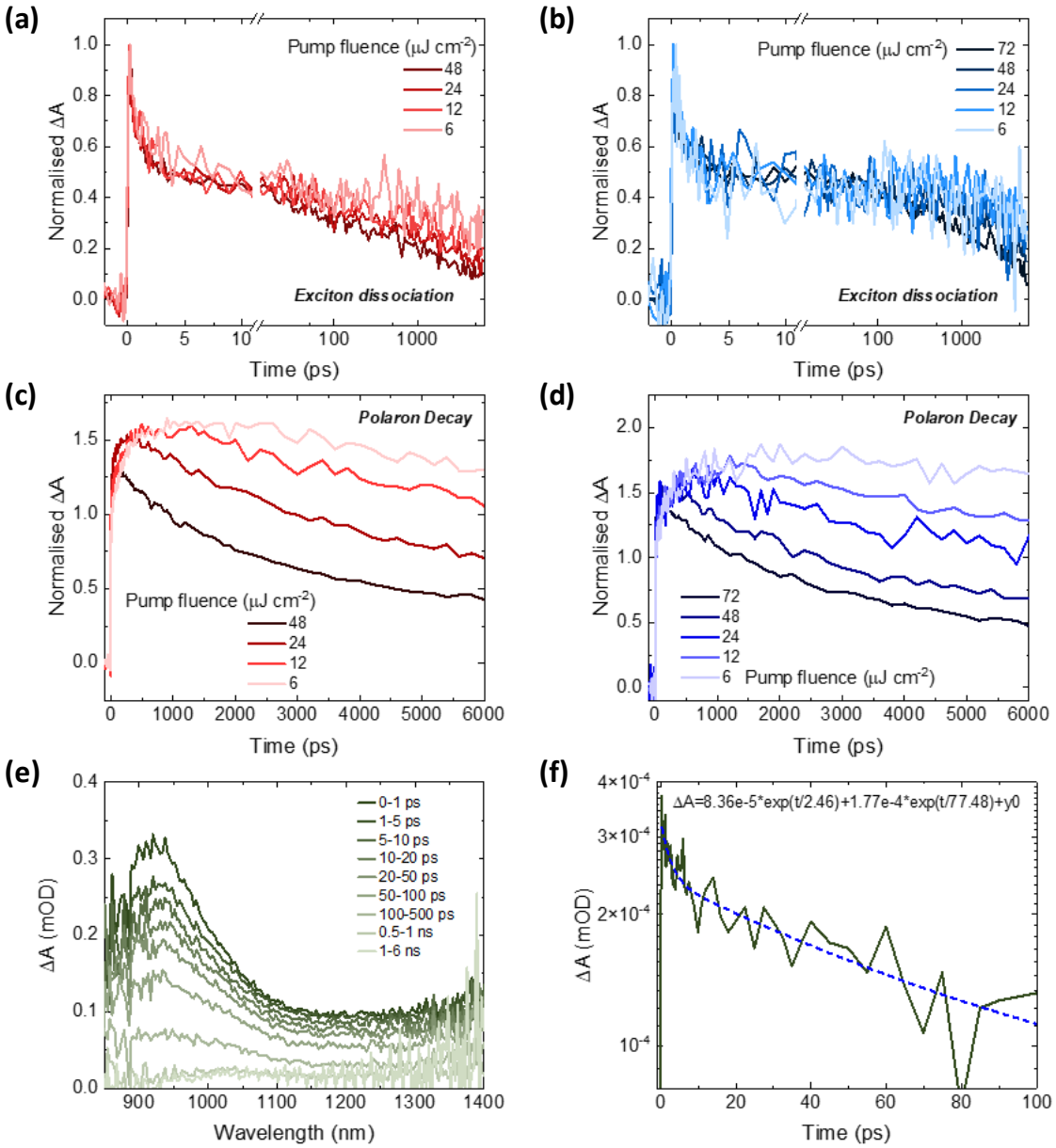


Figure 4.2.8. (a), (b) Fluence dependent decay of the exciton signal between 900 and 920 nm for the 50C and RT film, respectively. **(c), (d)** Fluence dependent decay of the signal assigned to the hole polaron between 1050 and 1070 nm for the 50C and RT film, respectively. Bimolecular fits to these spectra were used to calculate k_{bi} together with the charge carrier density estimated from the pump power and the film absorbance. **(e)** Ultrafast TAS spectra of the neat donor film recorded under identical conditions as the BHJ films. A pump fluence of 2 μJ cm^{-2} was chosen to minimize exciton-exciton annihilation effects. The amplitude weighted biexponential lifetimes were used to calculate an exciton lifetime of approximately 53 ps. TAS measurements were carried out by Yifan Dong.

These exciton decay times are in good agreement with the observed PLQE data. The higher PLQE and faster exciton decay observed for the *RT* films are indicative of a more intermixed morphology, reducing the distance excitons must diffuse to reach a donor : acceptor interface,[51] in agreement with the GIWAXS (smaller crystallites for *RT*) and RSoXS (smaller

and less pure domains for *RT*) data discussed above. However, these differences are relatively minor compared to the enhanced light absorption of the *50C* device, consistent with its overall higher J_{SC}.

4.2.7. Disorder, Non-Geminate Recombination & Transport

As demonstrated above in **Figure 4.2.3**, the intensity dependence of the device *FF* upon light intensity indicates the *FF* of VP-OSCs studied herein is limited by carrier density dependent competition between non-geminate recombination and charge extraction. Both processes are known to be strongly impacted by the density of tail (shallow trap) states below the electronic gap of the bulk heterojunction.[30,52] I characterise the resultant energetic disorder for the VP-OSCs as well as the SP-OSC references by measuring the total charge carrier density from differential capacitance (DC) versus device V_{OC} as a function of light intensity, following previously reported methodologies (see **Figure 4.2.9**).[53–57]

Despite the thin active layer thickness, the differential capacitance results in **Figure 4.2.9** **(a)** demonstrate that the chemical capacitance can clearly be distinguished from the constant geometric capacitance for the VP-OSCs. Over the measured range, the dependence of the chemical capacitance on the QFLS is well approximated by an exponential density of states with characteristic energy E_{ch}, as previously observed for a wide range of SP-OSC materials.

Figure 4.2.9 **(b)** shows the spatially averaged charge carrier density of the VP-OSCs and reference SP-OSCs plotted versus the V_{OC} used as a proxy of the quasi-Fermi level splitting (QFLS). For better comparison of the slope of the tail state density against the solution processed references, the x-axis was referenced to the V_{OC} at 2 sun equivalent illumination. Additionally, the ideal semiconductor charge density, with E_{ch} equal to the thermal energy, is shown (this is also the value expected for the characteristic energy for the case of a Gaussian density of tail states).[58] The charge carrier densities and fitted E_{ch} values only show minor differences between the *RT* and *50C* device. These characteristic energies, 53 and 50 meV for the *RT* and *50C* devices respectively, are typical of many SP-OSC's[31,51] but significantly larger than the values obtained for BTR : PCBM (37 meV) and PM6 : Y6 (31 meV). It should be noted that low E_{ch} values, and therefore low energetic disorder, for BTR : PCBM and PM6 : Y6 have been linked with their abilities to support efficient charge collection for thicker photoactive layers.

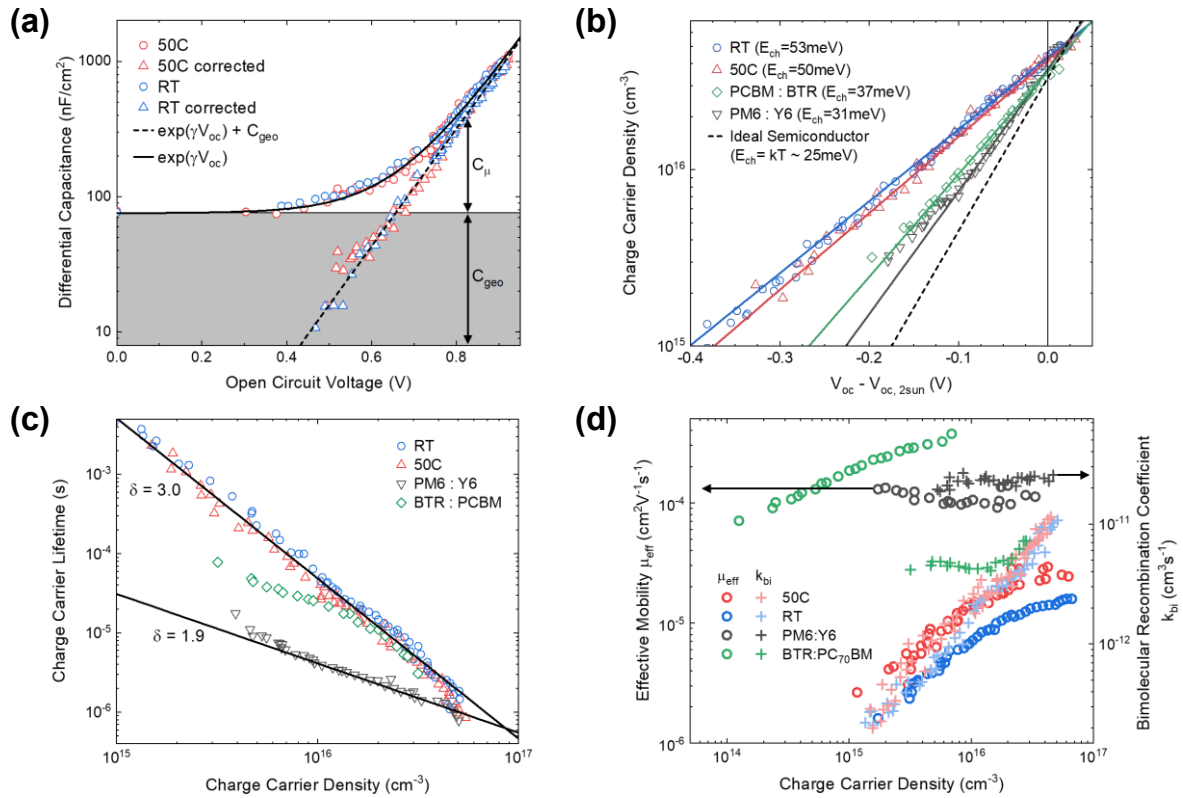


Figure 4.2.9. (a) Differential capacitance vs open circuit voltage (as measured and corrected for geometric capacitance) together with the respective fits for the *RT* and *50C* device. **(b)** Charge carrier density vs the open circuit voltage rescaled by the open circuit voltage at 2 sun equivalent illumination to enable a better comparison of the slopes. Exponential fits of the form $n_0 \exp(qV_{oc}/2E_{ch})$ and the bandtail of an ideal semiconductor are shown. **(c)** Charge carrier lifetime determined by TPV versus the spatially averaged charge carrier density determined from CE measurements. **(d)** Effective mobility and effective bimolecular recombination coefficient vs charge carrier density. Both axes scaled proportionally to each other to reveal the proportionality of the charge carrier dependence of mobility and recombination coefficient.

Transient photovoltage (TPV) measurements were employed to determine the charge carrier recombination kinetics at the same open circuit and light bias conditions (up to 6 sun) as the CE results presented above. Based on the lifetimes τ and charge carrier densities *n* (see **Figure 4.2.9 (c)** for τ versus n), an effective bimolecular recombination coefficient can be calculated as $k_{BI} = (n\tau)^{-1}$.[59] The right axis of **Figure 4.2.9 (d)** shows these effective bimolecular recombination coefficient versus the charge carrier density for the four devices studied. The *50C* and *RT* device show similar k_{BI}, with a slightly increased recombination rate observed for the *50C* device. For the charge carrier density range characterised herein, both the VP-OSCs and the BTR : PCBM reference exhibit significantly slower recombination compared to PM6 : Y6. For the SP-OSC references, the values are in excellent agreement with those determined by other methods such as bias-assisted charge extraction (BACE).[32]

The solution processed reference solar cells exhibit near ideal second order recombination kinetics as illustrated by in **Figure 4.2.9 (c)** the near constant k_{bi} in **Figure 4.2.9 (d)**. The VP-OSC devices exhibit non-ideal (apparent third order) recombination and consequently a charge carrier density dependent k_{BI}, attributed to their higher E_{ch} values.[57] To verify the validity these experimental analyses, the V_{OC} was reconstructed using the lifetime and carrier density data as well as J_{SC} as a proxy for the generation current. An excellent agreement is obtained between the measured and reconstructed V_{OC}, as shown in **Figure 4.2.10**, highlighting the reliability of the between these reconstructed and the directly measured V_{OC} for all light intensities. This shows that the recombination current calculated from the charge carrier density and lifetime data yields a good approximation of the generation current. In particular the agreement of the calculated versus directly measured V_{OC} vs light intensity ideality supports the experimentally determined apparent recombination orders.

To further investigate the collection efficiency and observed differences in *FF*, I turn to measurements of the effective charge carrier mobility (μ_{eff}). The effective mobility was assessed by measuring the charge carrier density accumulated in the device under short circuit conditions with varying background light intensities (up to 6 sun equivalent illumination).[60] See **Figure 4.2.11 (a)** for normalised charge extraction of the VP-OSC and SP-OSC devices transients recorded at 1 sun equivalent illumination.

This method yields a charge carrier density dependent effective mobility dominated by the slower carrier type that has been shown to dominate the electronic quality and *FF*.[34] This method was chosen as it can be performed on devices under operating conditions (without the need for different interlayers as in single carrier devices) and under realistic charge carrier densities.[61,62] The resulting values of the charge carrier density dependent mobility are plotted on the left axis of **Figure 4.2.9 (d)**. The mobility of the *50C* device shows an improvement by a factor of two relative to the *RT* device across the whole range of the measured charge carrier. Given their similar recombination coefficients, this increase in mobility is likely to be the primary origin of the increased *FF* of the *50C* device, as I discuss further below. As both y-axes are plotted proportionally to each other, it is possible to compare directly the charge carrier dependence of both μ_{eff} and the k_{BI}. Both VP-OSCs show a strong charge carrier dependence in μ_{eff} similar to the k_{BI} at low charge carrier densities. BTR : PCBM shows only a

weak carrier density dependence while PM6 : Y6 shows virtually no carrier density dependence of the mobility, consistent with the lower energetic disorder of these SP-OSCs.

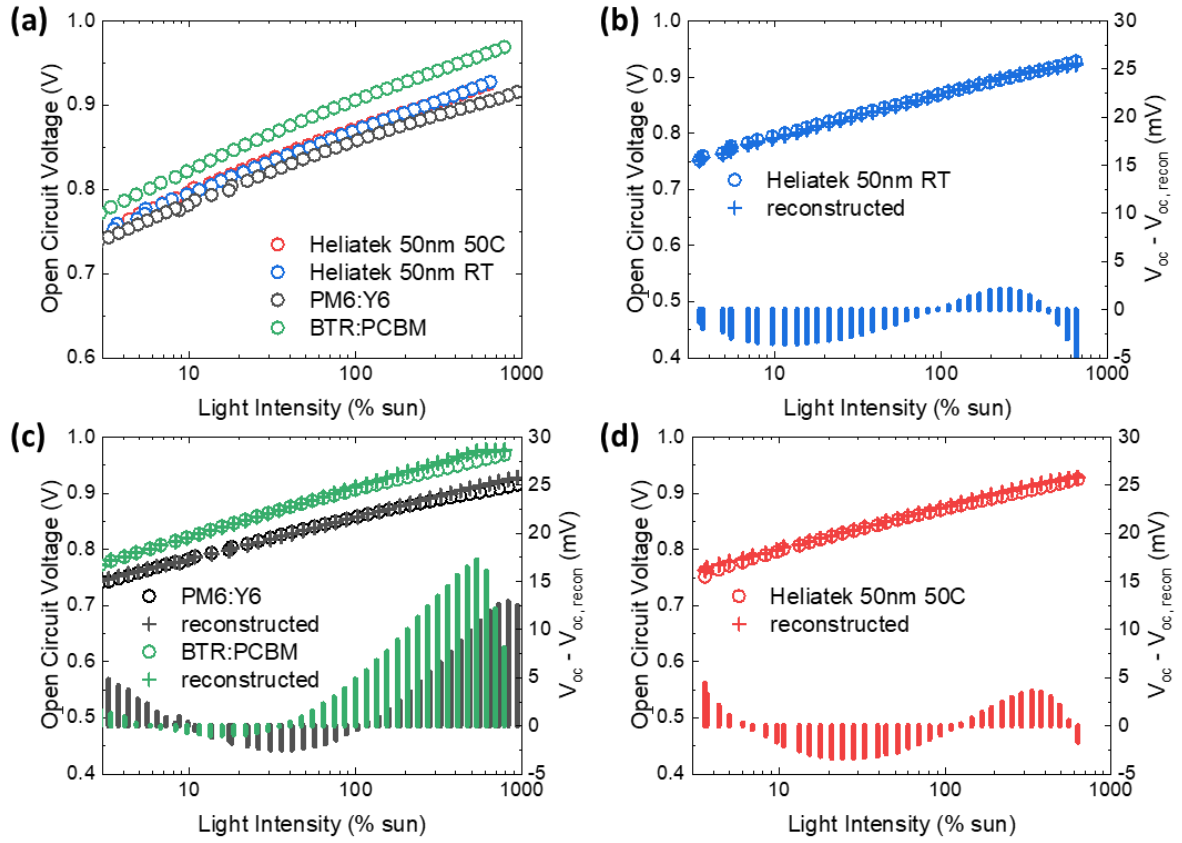


Figure 4.2.10. (a) Open circuit voltage as a function of light intensity. **(b), (c), (d)** Measured and reconstructed open circuit voltage of the respective devices. The right axis shows the residual of the reconstructed value subtracted from the measured value.

Figure 4.2.9 (d) shows normalised photocurrent transients; these were used to determine the charge density in the devices at short circuit. The faster current transients of the SP-OSC devices qualitatively indicate a higher mobility in these blends, consistent with **Figure 4.2.9 (c)**. The strong biphasic character observed for the VP-OSC devices has previously been related to slow extraction from deeper trap states in evaporated bulk heterojunctions.[18] **Figure 4.2.12** shows the normalised charge extraction transients at varying light intensities for the *RT* and *50C* device. The strongly pronounced second slow extraction phase at low light intensities indicates a trap filling effect and a larger energetic disorder in the *RT* device.

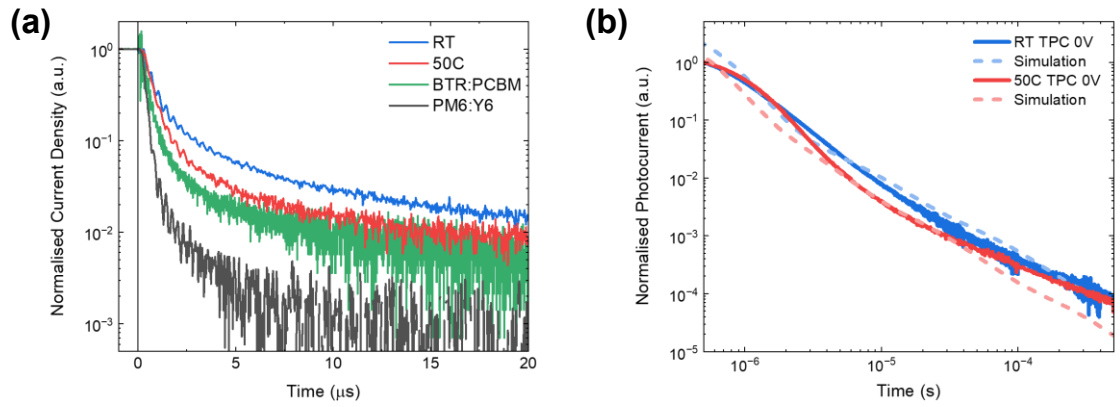


Figure 4.2.11. (a) Charge extraction transients of VP-OSCs and SP-OSC references recorded upon switching from steady-state 1 sun equivalent illumination to dark while the device is kept under short circuit conditions. **(b)** Normalised high-resolution photocurrent transients following laser excitation. Additionally shown are the current transients simulated using OghmaNano following a global fit of a large set of optoelectronic data as discussed below. The global fir was carried out by Roderick MacKenzie. The simulated transients correspond to values of E_{ch} of 121 and 89 meV for the *RT* and *50C* device, respectively.

High resolution transient photocurrent measurements have previously also been used to quantitively assess the characteristic energy.[63–65] **Figure 4.2.11 (b)** shows the high resolution current transients measured with variable load resistances for the *RT* and *50C* devices. In contrast with the energetic disorder derived from the carrier density versus V_{OC}, these transport-based measurements combined with a global fit of the optoelectronic data using drift-diffusion simulations (OghmaNano) indicate higher values of E_{ch} with a best global fit of all data resulting in values of 121 meV and 89 meV for the *RT* and *50C* devices, respectively. I therefore assign the improved collection efficiency in the *50C* device to the overall increased effective mobility and a reduction in the transport related disorder as observed in these current transients. To further investigate the impact of hole and electron transport separately, SCLC measurements on hole and electron only devices may be useful. As previously discussed, changing the substrate for hole and electron only devices may have profound impact on the active layer morphology potentially limiting the comparability. The different magnitudes of energetic disorder from our open circuit charge extraction measurements (**Figure 4.2.9 (b)**) and short circuit photocurrent transient (**Figure 4.2.11 (b)**) analyses are discussed below.

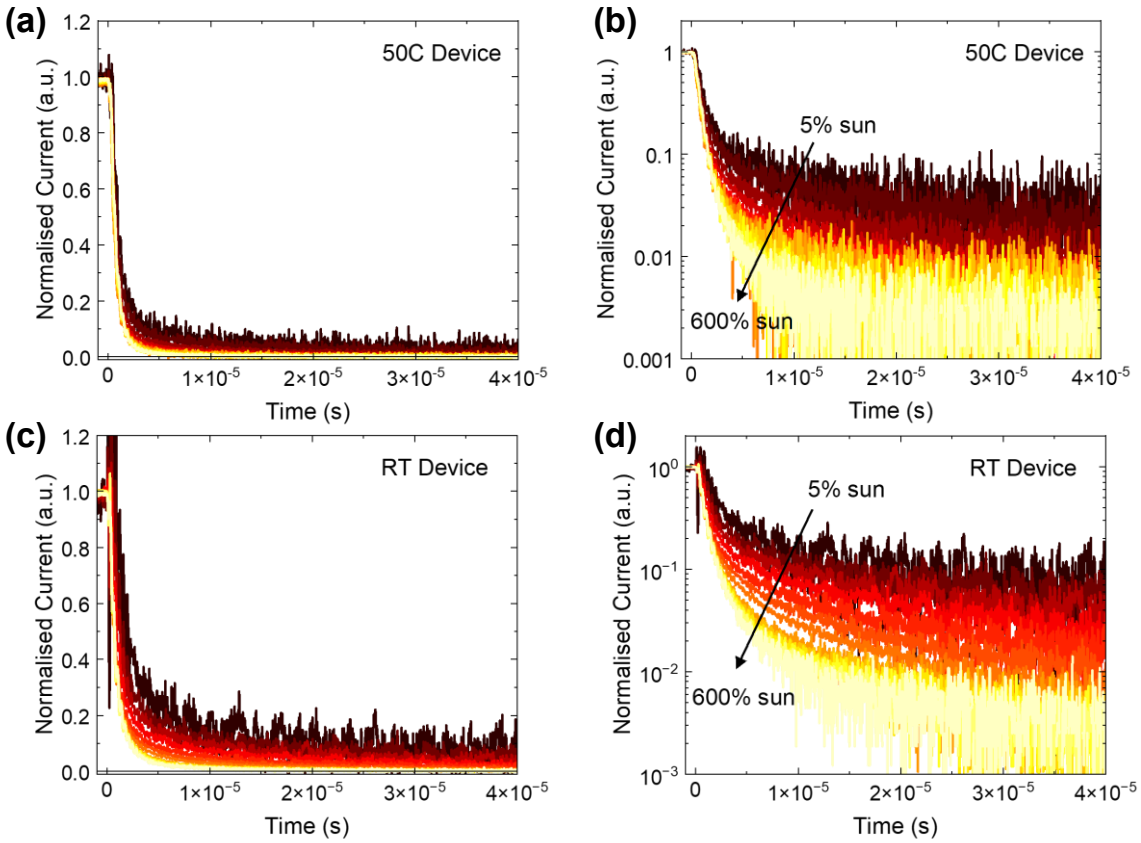


Figure 4.2.12. Charge extraction transients upon switching off the LED illumination at short circuit conditions that were used to characterise the effective mobility. Normalised transients recorded following different levels of LED illumination from 5% to 600% 1 sun equivalent illumination on a linear and logarithmic scale for the 50C (**(a)** and **(b)**, respectively) and RT device (**(c)** and **(d)**, respectively).

4.2.8. Discussion

To summarize our results on the difference in charge generation between the *RT* and *50C* devices, I can conclude that heating the substrate during evaporation results in a preferential molecular alignment which increases light absorption (**Figure 4.2.6 (a)**), resulting in the observed enhanced J_{SC}. The small improvement in the field dependence of charge separation inferred from the field-dependent EQE (**Figure 4.2.6 (b)**) is in line with the improved saturation observed in the *JV*-curves. Improved field dependence of generation has previously been linked to an increase in phase purity and crystallinity aiding charge delocalisation or providing an energetic gradient through changes in the fullerene electron affinity.[66–69] This is in line with the morphological data presented here-in showing greater phase purity while the crystallinity of the C_{60} phase cannot easily been studied because any GIWAXS results will be dominated by the neat C_{60} ETL the active layer has been deposited on. The increase in absorption and suppressed geminate recombination outweigh the small reduction in exciton

separation efficiency observed for the larger phase-separated domains in the *50C* device through PLQE and ultrafast exciton dynamics data (**Figure 4.2.6 (c)** and **Figure 4.2.7**).

Both VP-OSCs studied herein exhibit an absorption onset around 800 nm (E_g = 1.72eV) together with a V_{OC} of around 0.85 V. This voltage loss (E_g/q - V_{OC}) compares unfavourably with PM6 : Y6 which exhibits a similar V_{OC} at a much smaller optical bandgap of 930 nm (E_g = 1.33eV). It is however more comparable to typical voltage losses observed for SP-OSC's employing fullerene based acceptors including BTR : PCBM (E_g = 1.92, V_{OC} = 0.90 V), attributed at least in part to a larger energetic offset requirement for efficient exciton separation with fullerene acceptors.[38,70,71]

As indicated by the light intensity dependent *JV*-curves in **Figure 4.2.3**, the main limitation of the VP-OSC performance, aside from the voltage losses common for fullerene-based blends, arises from the poor charge collection efficiency limiting the device *FF* even in 50 nm thin devices. While the charge carrier build-up and non-geminate recombination kinetics in the *RT* and *50C* devices at V_{OC} show no significant differences, the increased mobility in the *50C* device leads to the overall improvements in collection efficiency. The comparison with higher collection efficiency SP-OSCs indicates that recombination and mobility in the VP-OSCs show a much stronger carrier density dependence and overall lower mobility, in line with a pronounced role of trap states in these films.

4.2.8.1. Quantifying the Collection Efficiency

Several methods to quantify an OSCs ability to extract charges have previously been used in the literature. The deviation of the non-geminate recombination constant from the encounter limited Langevin rate constant ($k_{Langevin} \propto \mu$) is measured by a Langevin reduction factor (γ) that accounts for the experimentally observed reduction of the theoretical Langevin recombination rate due to re-dissociation of non-geminately formed CT states,[72] and the effects of domain size[73] and trap states in slowing down the encounter rate. γ is proportional to the mobility-lifetime product ($\gamma \propto \mu/k_{BI} \propto \mu\tau$). It can therefore be used to crudely quantify the collection efficiency using experimentally determined mobility and lifetime values. To better relate mobility and recombination coefficients directly to the *FF* and compare these across different material systems, Bartesaghi *et al.* derived a collection efficiency term $\theta \propto \mu^2/k_{BI}$ with different weighting of mobility and recombination rate constants.[28] This has been

further improved by Kaienburg *et al.* to account for other effects such as the influence of imbalanced mobilities, yielding an electronic quality factor $Q = \mu^2/k_{BI}^{0.8}$.[34] In addition to determining the electronic quality factor from measured values of μ and k_{BI}, it is also possible to estimate Q based solely on data extracted from the *JV*-curve and the active layer thickness for devices with negligible voltage dependence of the generation current, making it an effective screening tool.[34] The equation derived by Kaienburg *et al.* assuming direct band-to-band recombination relates Q_{JV} to the *JV*-parameters in the following way:

$$Q_{JV} = \gamma_{0,dir} \frac{d^{3.5} J_{SC}^{0.5}}{V_{OC}^2} \exp\left(\frac{\operatorname{arctanh} FF_n}{\alpha_{dir}}\right)$$

where α_{dir} and $\gamma_{0,dir}$ are fit parameters based on their simulation, d is the active layer thickness and FF_n is a normalised *FF* value determined by:

$$FF_n = 2\,\frac{FF - FF_{min}}{FF_{max} - FF_{min}} - 1$$

where FF_{min} is 25% and FF_{max} is calculated as $(aV_{OC})/(V_{OC}+b)$ with a = 0.92 and b = 0.09.

Table 4.2.1 lists the values of the effective mobility, calculated Langevin recombination coefficient, experimental bimolecular recombination coefficient as well as the Langevin reduction factor and electronic quality Q determined at a charge carrier density corresponding to *MPP* under 1 sun equivalent illumination.

The charge carrier density was determined by calculating the loss current from the difference between J_{SC} and J_{MPP}, and assuming charge carrier kinetics roughly equivalent to open circuit conditions. Additionally, Q_{JV} was calculated using the equation provided by Kaienburg *et al.* and the *JV*-data reproducing the trends of the experimental values. The value of Q obtained for the *RT* device is comparable to those reported for similar donor molecules such as the DCV5T-Me : C_{60} blend.[4] While it is improved 3-4 fold in the *50C* device to values of 0.53 and 0.39 for Q_{Exp} and Q_{JV}, respectively, more crystalline blends like ZnPc : C_{60} achieve values in excess of 1.[74] The values determined herein for the SP-OSCs are within the range reported previously. BTR : PCBM stands out, highlighting the superior electronic quality of some fullerene-based devices even compared to high performing NFAs.[4,34]

Table 4.2.1. Effective mobility (μ_{eff}), Langevin recombination coefficient (k_L), measured effective bimolecular recombination coefficient (k_{BI}), Langevin reduction factor (γ) and electronic quality (Q_{Exp})

assessed at a charge carrier density corresponding to MPP conditions at 1 sun illumination. Additionally, the electronic quality determined from the 1 sun *JV*-curve (Q_{JV}) is listed.

Material	μ_{eff} [$cm^2V^{-1}s^{-1}$]	k_L [cm^3s^{-1}]	k_{BI} [cm^3s^{-1}]	γ	Q_{Exp} [$cm^{1.6}V^{-2}s^{1.2}$]	Q_{JV} [$cm^{1.6}V^{-2}s^{1.2}$]
DCV-V-Fu-Ind-Fu-V:C_{60} (RT)	1.2×10^{-5}	6.1×10^{-12}	4.3×10^{-12}	1.4	0.18	0.10
DCV-V-Fu-Ind-Fu-V:C_{60} (50C)	2.0×10^{-5}	1.1×10^{-11}	4.1×10^{-12}	2.6	0.53	0.39
BTR:PCBM	3.5×10^{-4}	1.8×10^{-10}	4.5×10^{-12}	40	142	819
PM6:Y6	1.2×10^{-4}	6.4×10^{-11}	2.3×10^{-11}	2.8	5.0	23.3

Since the mobility and bimolecular recombination coefficient are strongly charge density dependent in the evaporated cells, Q, k_L and γ also vary with light intensity (see **Figure 4.2.13** for the light intensity dependence of Q_{Exp}, Q_{JV} and γ).

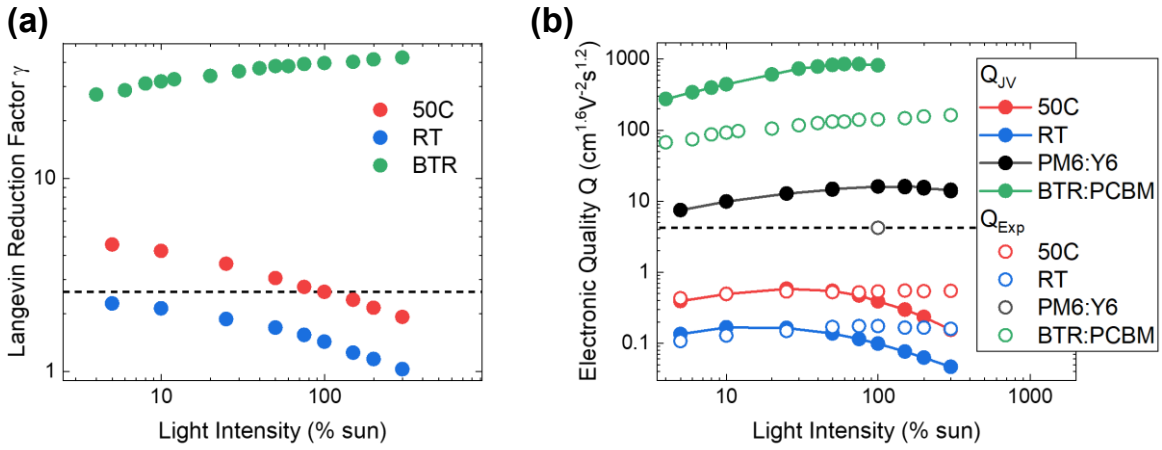


Figure 4.2.13. (a), (b) Light intensity dependence of the Langevin reduction factor and electronic quality, respectively. The electronic quality Q was determined from JV-curves (Q_{JV}) and optoelectronic measurements (Q_{Exp}). The results demonstrate that quoting a single value for the Langevin reduction factor without reference of the charge carrier density may be less comparable across different devices. The discrepancies between the values of Q determined by the different methods may have a variety of reasons such as the oversimplification of equating the generation current and J_{SC}, especially at high light intensity. To calculate $Q_{Exp.}$ the charge carrier density at MPP was estimated by assuming the difference of J_{SC} and J_{MPP} to be a reasonable measure for the bimolecular loss current. By applying the recombination kinetics determined from TPV and DC measurements, an estimate of the charge carrier density corresponding to the loss current is possible when assuming a simple zero-dimensional model. μ_{eff} and k_{bi} are taken at this value of n_{MPP} to calculate γ and $Q_{Exp.}$.

Comparison with a single value of γ, as often quoted in the literature, may therefore be misleading, especially if it is based on a value of k_L calculated from SCLC mobilities determined at higher charge carrier densities unrepresentative of 1 sun operating conditions. It is evident from **Table 4.2.1** that the Langevin reduction factors of the PM6 : Y6 and the *50C* devices are

similar at 1 sun, and therefore that this Langevin based analysis is insufficient to explain the greater charge collection and *FF* limitations of the 50C devices.

By giving a higher weighting to the mobility, the electronic quality Q_{Exp} proves to be a more suitable measure to explain the *FF* variations. The similarity between the values obtained from transient optoelectronic experiments and those directly calculated from the *JV*s highlight the potential of Q_{JV} as a screening tool. Overall both measurements of *Q* correlate well with the collection limitations apparent from **Figure 4.2.3**, with the *RT* device having the greatest collection limitations and the BTR : PCBM the least as expected.[31]

4.2.8.2. Recombination Mechanism & Drift-Diffusion Simulation

Previous studies have correlated strong charge carrier density dependencies of charge mobilities and effective recombination rate constants, as observed herein for our VP-OSC's, with the presence of energetic disorder.[56,57,60] Energetic disorder will lead to large populations of shallowly trapped electrons and holes, the density and energetic distribution of which will be strongly dependent on applied voltage and light intensity. The effective hole and electron mobilities will depend on the mobility of free carriers as well as the fraction of trapped carriers. Similarly, recombination in the presence of a large density of sub-gap traps can be described as free electrons (holes) recombining with trapped holes (electrons) as well as free-to-free recombination. As the charge carrier density increases, the relative contribution of these channels to the overall recombination flux changes can explain deviations from ideal second order kinetics.[75]

The presence of energetic disorder can often lead to discrepancies in experimentally determined lifetime data, depending on the charge carrier density regime these were measured at.[76] To illustrate this, I used the fluence dependent decay of the polaron signal in the transient absorption measurements (see **Figure 4.2.8**) to calculate the $k_{BI.}$ A rough estimate of the charge carrier density excited by the laser pulse was calculated from the device EQE at the excitation wavelength. **Figure 4.2.14** shows the results of the calculation side by side with the values obtained by the combination of TPV and DC measurements. It is apparent that the optoelectronic measurements are conducted at light intensities relevant to solar irradiation conditions, while the pump pulses used for transient absorption measurements generate orders of magnitude higher charge carrier densities. In the case of a charge carrier density dependent bimolecular recombination coefficients – as observed previously for

fullerene based SP-OSCs[54,77,78] as well as the VP-OSCs studied herein – this will lead to discrepancies between high-fluence TAS and comparatively low light intensity optoelectronic measurements. Here, it allows us to show that the k_{BI} saturates above a carrier density of 10^{18} cm^{-3} for the VP-OSCs. Such a behaviour was previously reported in the literature for fullerene based SP-OSCs known to exhibit a charge carrier density dependent k_{BI}.[77] While the recombination kinetics at irradiation levels relevant to device operation were similar, the *50C* device shows a two-fold increased saturated k_{BI} of about 6×10^{11} cm^3s^{-1}. Both saturated values exceed the value obtained for the PM6 : Y6 reference. It is also striking that for PM6 : Y6, I obtaining good agreement between the k_{BI} determined from TAS and TPV/CE studies, consistent with greatly suppressed energetic disorder in this device and near ideal bimolecular kinetics, even when measured over this very broad range of carrier densities and timescales.

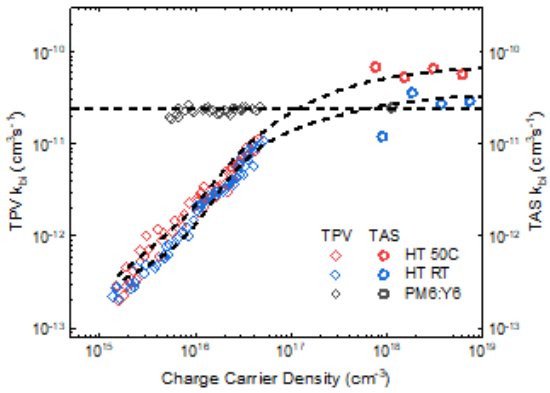


Figure 4.2.14. Bimolecular recombination coefficients of PM6:Y6, the *RT* and *50C* device measured by transient photovoltage/differential capacitance and transient absorption spectroscopy. For PM6:Y6 the dashed line is a guide to the eye demonstrating the good agreement of the values obtained with both methods. For the *RT* and *50C* device, the dashed lines are based on OghmaNano simulations with an additional recombination coefficient for free electron to free hole recombination set to match the k_{BI} value obtained from the transient absorption measurements.

To investigate the contribution of the different recombination channels in more detail as well as shed light on the origin of the slow phase observed in current transients, Roderick MacKenzie employed the simulation software OghmaNano. The software treats intra-gap trap states as an ensemble of trap states with discrete energy levels making up an exponential tail and solving the trapping and recombination rate equations for every trap level independently.[64] The simulation parameters shown in **Table 4.2.2** were extracted by performing a global fit to light and dark *JV*-curves, the 1 sun TPV transient, high resolution photocurrent transients at variable bias (-1V, 0V, 0.5V) as well as V_{OC}, J_{SC} and n versus light

intensity (see **Figure 4.2.15** and **Figure 4.2.16**). The charge carrier lifetimes and effective mobility were extracted from the simulations and compared to the values determined experimentally (see **Figure 4.2.17**).

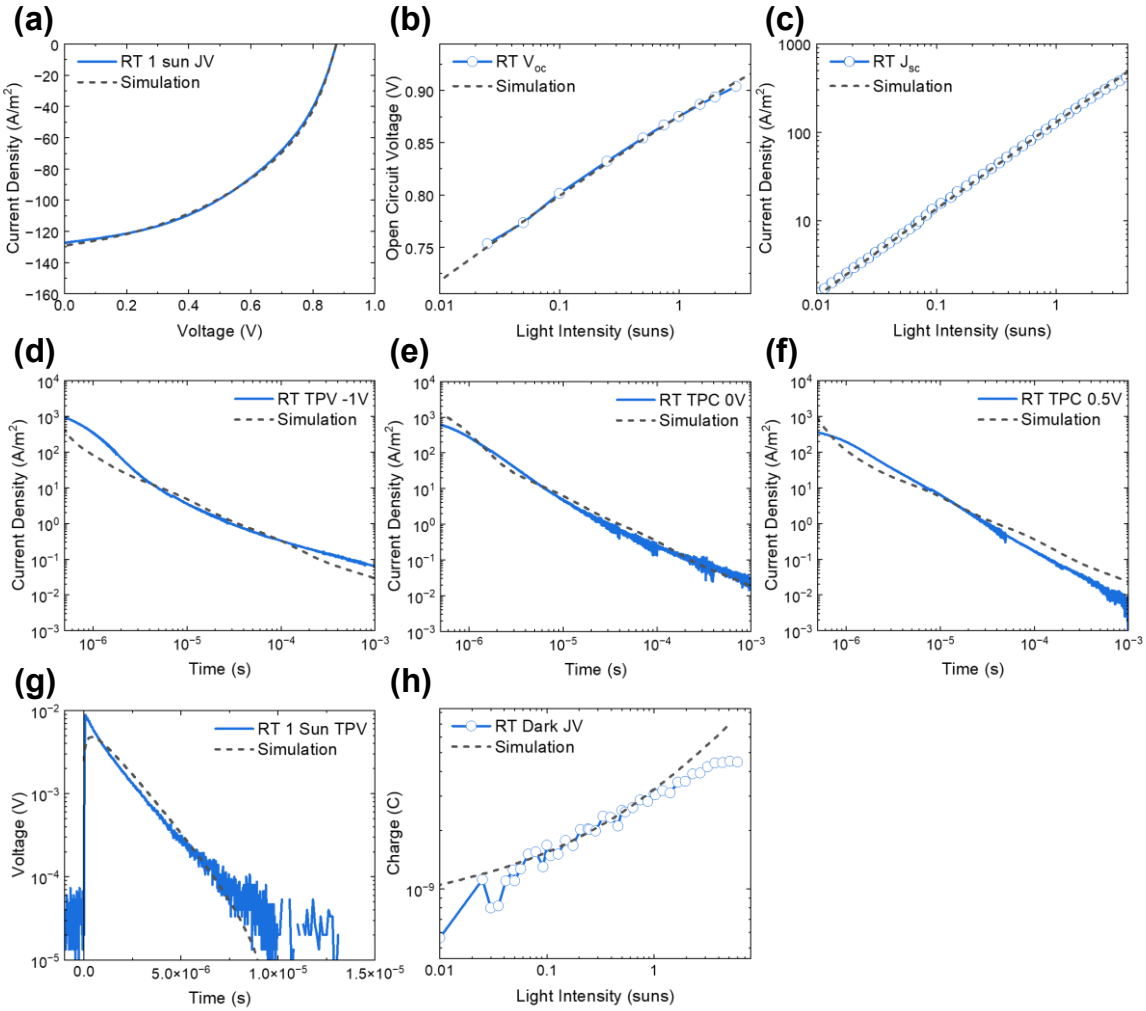


Figure 4.2.15. Global fit of experimental data using simulation software OghmaNano for the RT device. **(a)** 1 sun JV-curve. **(b)** V_{OC} vs. light intensity. **(c)** J_{SC} vs. light intensity. **(d), (e), (f)** Photocurrent transients recorded at -1V, 0V and 0.5V, respectively. Photocurrent transients were recorded as outlined by Street.[63] **(g)** 1 sun TPV transient. **(h)** Charge vs. light intensity. The global fitting was carried out by Roderick MacKenzie.

The good agreement in the general trends and the small deviation in absolute values within a factor of two indicate the overall applicability of the model to the devices studied herein. Note that, no free-electron-to-free-hole recombination channel was necessary to reproduce the optoelectronic experimental results. However, at the much higher fluences experienced by the device in a TAS experiment, an additional direct free-to-free recombination channel ($k_{\text{free-to-free}}$ of 6.6×10^{-11} and 3.3×10^{-11} cm^3s^{-1} for *50C* and *RT*, respectively) was added in order to reproduce the higher light intensity trends (see dashed lines in **Figure 4.2.14**). This may be

expected in TAS experiments generating a large number of hot charge carriers which are initially not thermalized and hence are likely to recombine with each other rather than just the trapped carriers.

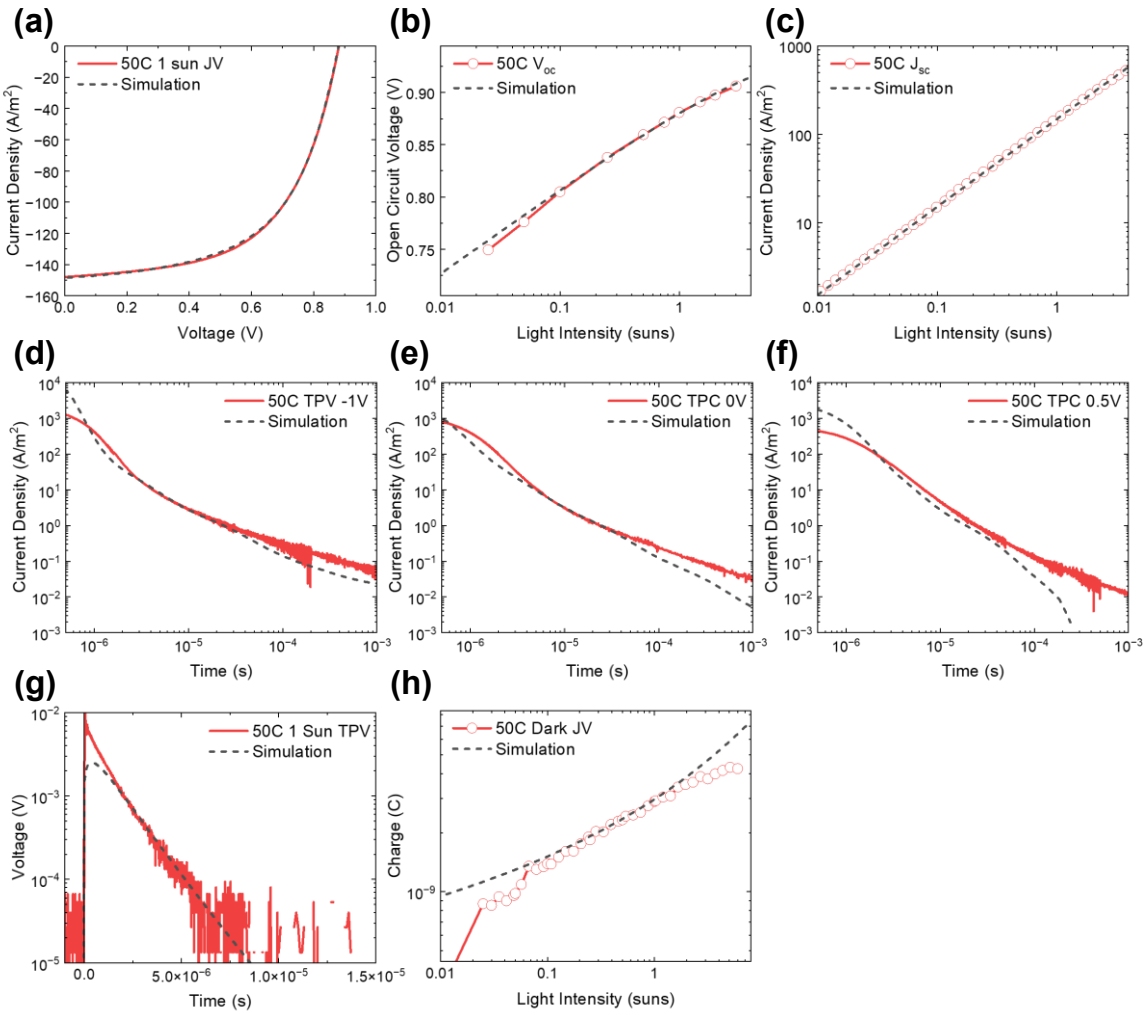


Figure 4.2.16. Global fit of experimental data using simulation software OghmaNano for the RT device. **(a)** 1 sun JV-curve. **(b)** V_{OC} vs. light intensity. **(c)** J_{SC} vs. light intensity. **(d), (e), (f)** Photocurrent transients recorded at -1V, 0V and 0.5V, respectively. Photocurrent transients were recorded as outlined by Street.[63] **(g)** 1 sun TPV transient. **(h)** Charge vs. light intensity. The global fitting was carried out by Roderick MacKenzie.

A takeaway from the modelling is the reduction of E_{ch} for the *50C* device is dominated by the fitting of the current transients. Additionally, the *50C* device shows a more symmetric trap density resulting in more balanced effective hole and electron mobility. The trapping and recombination cross-sections as well as the free hole and electron mobility values increased for the *50C* device.

The characteristic energy values determined from the global fit to the circuit photocurrent transients (121 meV and 89 meV for *RT* and *50C*, respectively) differ significantly from the

value obtained for the combined tailslopes as determined from charge density measurements versus V_{OC} (53 meV and 50 meV for *RT* and *50C*, respectively). The latter together with lifetime data from TPV was used to accurately reconstruct the experimentally determined V_{OC} including their ideality, as shown in **Figure 4.2.10**.

Table 4.2.2. Simulation parameters used for the OghmaNano simulations. The parameters for the RT and 50C device were obtained by a global fit to the experimental data as shown in **Figure 4.2.15** and **Figure 4.2.16**. The last column shows hypothetical parameters to achieve 9.4 % PCE and 10 % PCE for an active layer thickness of 50 nm and 70 nm, respectively. The changed parameters are highlighted in bold.

Parameter	Units	*RT*	*50C*	*50C* + E_{ch} + n_{trap} + μ_{free}
Electron Trap Density	$m^{-3}\ eV^{-1}$	1.11×10^{23}	4.14×10^{24}	$\mathbf{2 \times 10^{24}}$
Hole Trap Density	$m^{-3}\ eV^{-1}$	7.87×10^{24}	4.00×10^{24}	$\mathbf{2 \times 10^{24}}$
Electron Tail Slope	eV	0.120	0.089	**0.05**
Hole Tail Slope	eV	0.120	0.089	**0.05**
Free Electron Mobility	$m^2\ V^{-1}\ s^{-1}$	8.43×10^{-9}	1.17×10^{-8}	$\mathbf{2.17 \times 10^{8}}$
Free Hole Mobility	$m^2\ V^{-1}\ s^{-1}$	8.43×10^{-9}	1.17×10^{-8}	$\mathbf{2.17 \times 10^{8}}$
Free Electron to Trapped Electron	m^{-2}	2.54×10^{-22}	8.21×10^{-22}	8.21×10^{-22}
Trapped Electron to Free Hole	m^{-2}	5.32×10^{-23}	1.04×10^{-22}	1.04×10^{-22}
Trapped Hole to Free Electron	m^{-2}	5.32×10^{-23}	1.04×10^{-22}	1.04×10^{-22}
Free Hole to Trapped Hole	m^{-2}	2.54×10^{-22}	8.21×10^{-22}	8.21×10^{-22}
Effective Gap	eV	1.3	1.3	1.3
Photon Efficiency	%	88.1	96.4	96.4

This indicates that the disorder obtained from charge extraction measurements determines non-geminate recombination at open circuit conditions in the charge density regime assessed in our experiments (10^{15} to 10^{17} cm^{-3}). At the same time, current transients are described by a much larger degree of disorder differing significantly for the *RT* and *50C* device. This may point to different aspects of the morphology and disorder governing recombination and charge transport, respectively, and raise concerns over the applicability of transport-based disorder parameters to explain (non-encounter limited) recombination and vice versa.

Recently, Saladina *et al.* reported a power law DoS in DCV-V-Fu-Ind-Fu-V : C_{60} determined by light and temperature dependent ideality factors.[37] They inferred this power law DoS from

the observed increase in E_{ch} below 1 sun V_{OC} (measured at room temperature). A consequence of their observations would be a narrower DoS compared to an exponential bandtail but with an increasing breadth of states (increasing E_{ch}) deeper into the bandgap. This would be in line with our observations of a larger E_{ch} fitted to the slow phase of current transients corresponding to states deeper in the gap.

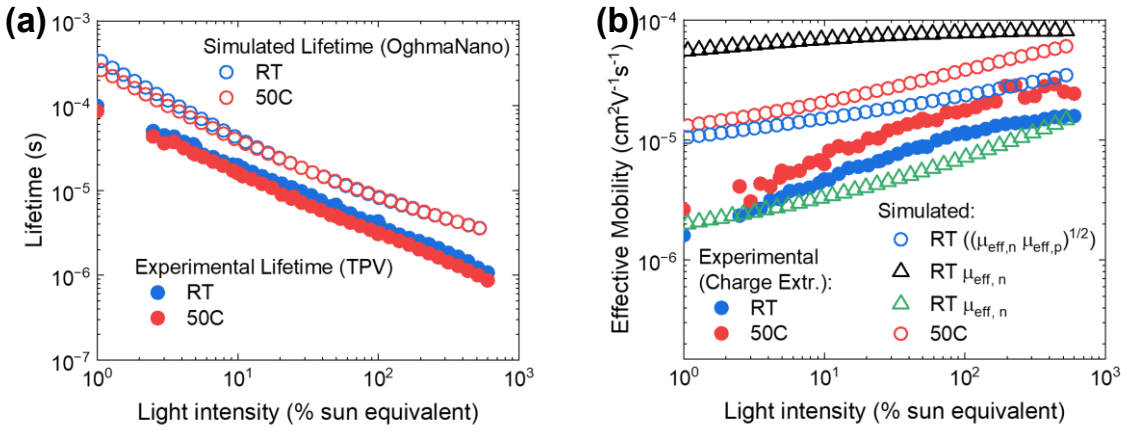


Figure 4.2.17. Comparison of experimental data with simulated data obtained from global fit parameters shown in SI Table 1 for the RT and 50C device. **(a)** Experimental obtained from TPV and simulated spatially averaged charge carrier lifetime. **(b)** Experimental effective mobility obtained from charge extraction measurements and simulated effective mobility. Note that in the case of 50C, the tailslopes and free mobility values for holes and electrons were assumed to be near identical leading to identical effective mobilities at different levels of trap filling. For RT the tailslopes were not identical and therefore the effective electron and hole mobility are shown as well as their geometric mean. The geometric mean was chosen following work by Heiber et al.[73]

A possible explanation for the observed behaviour may also be the increased presence of spatially isolated domains in the *RT* film as supported by the lower phase purity and smaller domain size shown in RSoXS and GIWAXS data, respectively. While contributing to non-geminate recombination, these domains may slow down charge extraction as charge carriers have to travel through amorphous and intermixed regions leading to the observed disorder in current transients (see **Figure 4.2.18**). Comparisons with current transients obtained for active layers with a lower donor content (donor/acceptor ratio 1:2) also show a pronounced slow phase. As discussed further in the next sub-chapter (**Subchapter 4.3**) the donor is expected to be less aggregated in the case of the 1:2 D/A further supporting the assignment of slow current transients to amorphous or spatially isolated donor domains. Temperature dependent space-charge limited current (SCLC) measurements may provide a suitable strategy to investigate this further but require different substrates potentially compromising the active layer morphology.[10,12] Charge transport between isolated donor domains via

tunnelling or hole transport through C_{60} has previously been discussed.[79] This may also point to fundamental discrepancies in the determination of disorder through transport based techniques (current transients, temperature SCLC), techniques relating charge accumulation and QFLS (impedance spectroscopy, charge extraction vs V_{OC}, V_{OC} ideality), and techniques based on the fitting of CT state emission/absorption. These have previously yielded a wide range of disorder parameters and even differ in the DoS shape (Gaussian vs exponential vs power law).[30–32,37,58,80] A full discussion of the different techniques and results is however beyond the scope of this study.

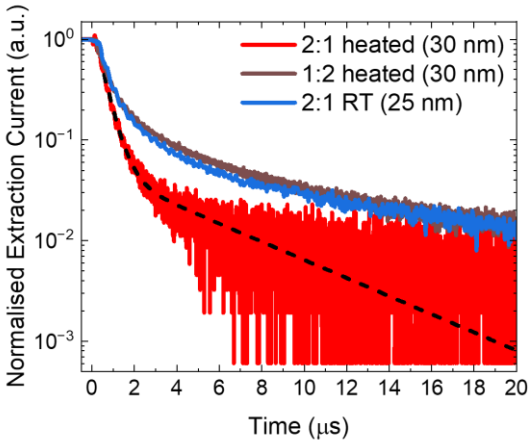


Figure 4.2.18. Normalised charge extraction current transients recorded upon switching from 1 sun equivalent LED illumination to dark at short circuit conditions. The device thickness of the 1:2 and 2:1 D/A ratio samples differs slightly from that of the *RT* sample.

In summary, charge carrier built-up and recombination under open circuit conditions are unaffected by the change in substrate temperature during deposition. Both are characterised by a broad distribution of tailstates compared to PM6 : Y6 and BTR : PCBM but comparable to other SP-OSC materials as measured by the same methodology. Simulation results consistently explain the observed charge carrier density dependence of the effective recombination coefficient and mobility through a recombination formalism involving trapped and free carriers. Our results show that while the non-geminate recombination rate at operational charge carrier densities is sufficiently slow compared to the SP-OSC references, the observed low collection efficiency and *FF* can be rationalized by the overall low mobility, likely resulting from large energetic disorder during charge transport. Depositing at higher substrate temperatures induces favourable changes in microstructure, improving structural order and phase separation, which goes along with improved energetic disorder for charge transport and a twofold increase in effective mobility. In the following, I explore the gains in

device performance that would result from further improving morphology, disorder and charge carrier dynamics.

4.2.8.3. Quantifying the Performance Bottleneck using Simulations

To deconvolute the influence of the different simulation parameters on the *JV*-curves and performance of the devices, I adjusted the parameters of the *RT* device iteratively until reproducing the *50C* parameters (see **Figure 4.2.19 (a)** and **(c)**). The plot indicates that the trap density and the characteristic energy dominate the observed changes in *FF* and *PCE* while the increased free mobility values and trapping/recombination capture cross-sections only result in a small reduction of V_{OC} due to the slightly increased recombination rate, while J_{SC} and *FF* increase due to better charge collection. Using the OghmaNano drift-diffusion model, I further explored what improvements in device parameters would be necessary to achieve 10 % *PCE* in a single junction device using DCV-V-Fu-Ind-Fu-V : C_{60} as the photoactive layer. Further reducing transport E_{ch} to 50 meV yields a large improvement in *FF*.

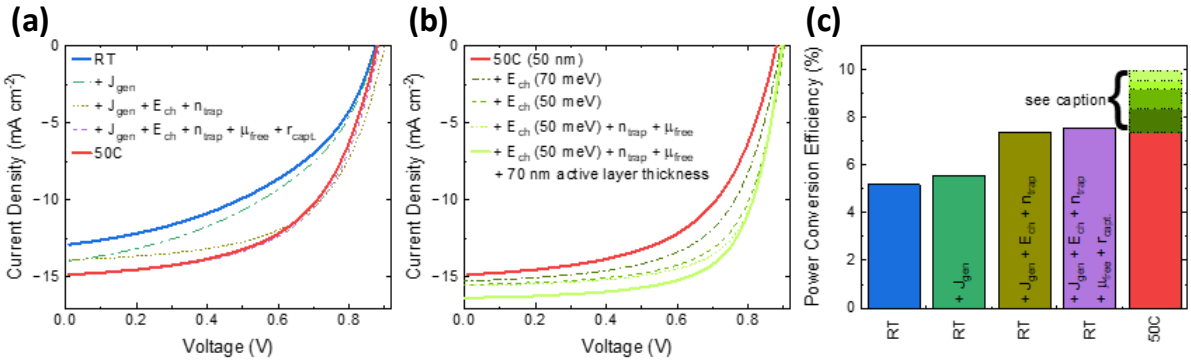


Figure 4.2.19. (a) Simulated fitted JV-curves of the *RT* and *50C* device. Additionally shown are the *JV*-curves for the *RT* device with iteratively changing the generation current (*J*gen), the trap symmetry and density (n_{trap}), and the mobility of carriers at the band edge (μ_{free}) and the capture cross-section of the charge carriers ($r_{capture}$) to the values obtained from the global fit of the *50C* device. **(b)** Simulated *JV*-curves visualising the effect of adjusting E_{ch}, free mobility, trap density and active layer thickness to achieve 10 % PCE. **(c)** *PCE* corresponding to the simulated *JV*-curves in **(a)** and **(b)**. The full list of modelling parameters can be found in **Table 4.2.2**.

Comparatively, the influence of halving the trap density and an increased free mobility yields only small further improvements (see **Table 4.2.2** for the full list of simulation parameters). This reduction in the energetic disorder improves the collection efficiency and allows for the active layer thickness to be increased to 70 nm. At 70 nm the absorption of the active layer reaches its first interference maximum leading to an improved J_{SC} outweighing the reduction in *FF* (see **Figure 4.2.20** for transfer matrix simulations).

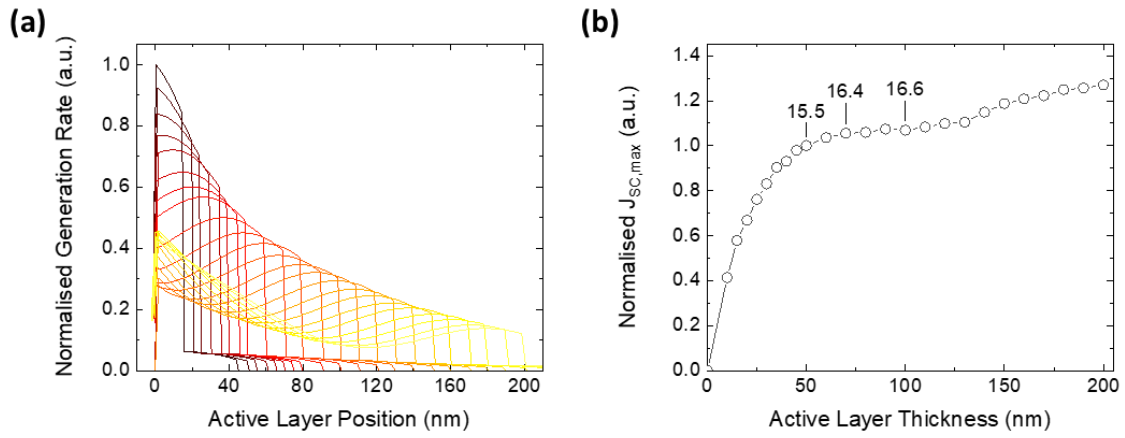


Figure 4.2.20. (a) Absorption profile calculated using transfer-matrix simulations built-in to OghmaNano with n, k data obtained by Heliatek GmbH. Note that the interlayer configuration was not changed and the thickness of doped transport layers that can act as optical spacers was not optimised. **(b)** Maximum achievable generation current as calculated from the integrated absorption profiles.

Note that in VP-OSCs the inclusion of doped transport layers as optical spacers can shift the absorption maximum.[4] The optical simulations here-in were carried out for the interlayer configuration of the studied devices without additional optical spacers. This demonstrates the potential that lies in improving the collection efficiency through morphological and structural modifications of existing high-performance systems.

4.2.9. Conclusions and Outlook

Morphological optimisation through substrate heating during the vapour deposition of organic solar cells made from the state-of-the-art material combination DCV-V-Fu-Ind-Fu-V : C_{60} was shown to greatly improve the device performance. Absorption spectroscopy and GIWAXS measurements revealed that the origin of the improved J_{SC} lies in the improved crystallinity and preferential orientation of the donor's transition dipole parallel to the substrate for the films deposited at 50˚C rather than room temperature.

Substrate heating also led to a substantial increase in *FF*. To investigate this, I determined the non-geminate recombination rate constants and effective mobility. Both are highly charge density dependent characteristic of charge carrier dynamics in the presence of a high trap density. The origin of the *FF* improvement lies in the two-fold increase of the effective mobility related to the reduction in energetic disorder and deep lying tailstates inhibiting charge transport while the recombination kinetics remained largely unaffected under operational conditions. The reduced mobility and the slow phase in current transients are tentatively assigned to amorphous/spatially isolated donor phases that trap holes.

Our morphological data together with the optical and optoelectronic characterisations suggest that the phase purity and the decrease in amorphous phase size are key to reducing the disorder related to charge transport that limits the device *FF*. Further increasing the substrate temperature during evaporation may increase the size of crystalline domains leading to further reduction of the exciton quenching efficiency or cause changes in the molecular orientation resulting in a loss in absorption. Due to the large anisotropy of the small molecule blends, our results demonstrate that morphological optimisation of evaporated organic solar cells is non-trivial but may enable large performance increases.

Simulations revealed that the reduction in intra-gap states without negatively affecting other aspects of device performance could lead to further significant performance increases in this state-of-the-art evaporated model system beyond 10 % *PCE* for single junction devices. This requires careful morphological optimisation and may further be aided by modifications of the molecular structure that could aid aggregation e.g. steric groups that have been shown to affect morphology in blends.[81] Further boosting the single junction efficiency of evaporated solar cells will further raise the prospects of their large scale commercialisation.

4.3. Analysing Energetics & Kinetics in Evaporated Bulk & Planar Heterojunctions

4.3.1. Background

4.3.1.1. Multi-Junction Evaporated Organic Solar Cells

Compared to solution processed systems, the collection efficiency (i.e.: poor 'electronic quality') constitutes a major performance limitation for evaporated cells in single junction devices. In order to maximise light absorption and J_{SC}, thick active layers are needed. This in turn limits the *FF* of VP-OSCs due to the poor collection efficiency in thick active layers. However, the precise deposition control of VP-OSCs enables the deposition of two-terminal multi-junctions consisting of multiple thinner organic heterojunctions connected in series by recombination layers. Such multijunction devices, which are more challenging to fabricate by solution processing, offer a strategy to increase the collection efficiency of each individual, relatively thin, sub-cell whilst still achieving efficient light absorption, thereby enhancing overall device efficiency.

In a two-terminal, monolithic multi-junction device, the current of each sub-cells needs to be matched while their voltage is added up. Current matching of the individual junctions can be achieved by using complimentary absorbers and adjusting the thickness of the junctions. Meerheim *et al.* demonstrated that even in a triple junction with each junction consisting of the same donor-acceptor blend (DCV5T-Me:C_{60}), current matching of the sub-cells can be achieved by adjusting the thickness of optical spacer layers, recombination layers and the photoactive layers, making use of strong micro-cavity effects aided by optical modelling.[49] As shown by Kaienburg *et al.*, DCV5T-Me is one of the evaporated donor molecules with comparatively low voltage losses (for a fullerene system) but poor electronic quality, as also discussed in **Subchapter 4.2**.[4] In a multi-junction device, the reduced junction thickness of the sub-cells therefore can results in a significant increase of the collection efficiency in the individual junctions, yielding an improvement of the *FF* from 65.8 % to 72.4% for the triple junction compared to a thick single junction.[49] Due to the reduced charge generation in the thin current matched sub-cells, the overall series J_{SC} is reduced to 4.8 mA/cm^2 for the multijunction, compared to 13.2 mA/cm^2 for the single junction. This still presents an increase in photon-utilisation as the total generated current added across the three junctions is 14.4 mA/cm^2. Together with the tripled V_{OC} (0.96 V vs. 2.79 V) this results in an overall *PCE* improvement from 8.3 % for the single junction to 9.7 % for the triple junction devices. When

the cell area is increased to more than 100 mm^2, the differences in the performance between single and triple junction (7.6 % and 9.5 %) become even larger. This is due to the roughly three-fold reduction in current leading to lower resistive losses of the device electrode in the case of the triple junction that has been shown to be a major bottleneck for large area OPV modules.[82]

While the complexity of manufacturing increases with each junction, raising the factor of cost for the commercial application of multi-junctions, the above-mentioned results demonstrate that the limit posed by the collection efficiency can be effectively mitigated in multi-junctions. Additional performance increases are possible in multi-junctions that employ complementary absorbers.[83] The published record efficiency for an evaporated multi-junction system is 13.2 % reported in 2016.[ref] However, this remains far off the 19 % threshold that has recently been breached by solution-processed polymer-NFA single junctions.[84–86]

4.3.1.2. Challenges for Multi-Junctions

There are two main reasons for the efficiency gap between multi-junction VP-OSCs and single junction NFA SP-OSCs, both of which are connected to the persistent use of fullerenes as the acceptor in VP-OSCs due to a lack of high-performing evaporable NFA alternatives.[4] Firstly, high performing NFA SP-OSCs benefit from the broad complementary absorption of the wide gap polymer donor and the narrow bandgap NFA extending the absorption into the infrared part of the solar spectrum. Members of the Y6 acceptor family, that enabled the current efficiency records, absorb beyond 900 nm. In contrast to this, high-performing VP-OSCs rely on wide-gap fullerenes (with an indirect bandgap and low-absorption coefficients) as the acceptor and the small molecule donor constitutes the low bandgap component. As previously discussed, synthesising materials with a high level of conjugation while also ensuring processability by evaporation is non-trivial. Therefore, evaporable small molecule donors typically do not absorb beyond 800 nm.[4,87] Notable exceptions are organo-metallic compounds such as phtalocyanines[88,89] or BODIPY[87,90–92] based donors as well as a family of asymmetric D-A-A donors[93,94]. Understanding the loss mechanisms of these systems together with further materials innovation will help to address the issue of the absorption onset in multi-junction systems.

The second fundamental limitation of fullerene-based multi-junction evaporated systems is related to their open circuit voltage. While J_{SC} and *FF* losses may be mitigated by

monolithically stacking multiple junctions, voltage losses will add up for each sub-cell. Fullerene acceptors are known to exhibit high voltage losses with both evaporated and solution-processed donors.[38] Solution-processed NFAs on the other hand have been shown to exhibit reduced voltage losses due to the tunability of their energetics which allows for energy level matching with the employed donors. Due to the increased exciton lifetime, low offset. Furthermore, high performing NFA systems allow for efficient charge generation even at low energy level offset.[38,95] Kaienburg *et al.* recently demonstrated low voltage losses in unconventional planar heterojunctions made up of spin-coated Y6 and evaporated donor molecules.[38] The work demonstrates that in principle low voltage losses comparable to the highest performing NFA SP-OSCs can be achieved using evaporated donor molecules. However, the low current density and difficult route to upscaling such a junction may limit the potential of this approach. For fully evaporated systems, the highest reported efficiencies and lowest voltage losses are still achieved using fullerene acceptors.[38] However, also for a given fullerene-based evaporated material system, it is possible to improve the open circuit voltage of a sub-cell in a multijunction device relative to the optimal single junction cells where approaches to minimise voltage losses need to be weighed up against charge generation and collection more carefully.

4.3.1.3. Morphology Dependence of the Open Circuit Voltage

Previous reports have shown that V_{OC} and voltage losses in OSCs can be strongly affected by the morphology and donor/acceptor ratio of the BHJ. Also, the extreme case of phase separation in the form of planar heterojunctions (PHJs) has been studied for evaporated (and a lesser extend solution-processed) systems, with examples in the literature showing both positive and negative effects for the device V_{OC} relative to their BHJ counterpart.[55,80,92,96,97]

Different effects have been invoked to understand morphology dependent changes in device voltage. The 1 sun V_{OC} can be understood as the sum of an energetic component and a kinetic component determined by the thermodynamic equilibrium established between charge generation and non-geminate recombination – both are affected by changes of the morphology and aggregation. Molecular aggregation and orientation can affect the energy levels of the organic semiconductors through inductive or electrostatic effects.[98–103] In evaporated PHJs, changes in molecular orientation at the well-defined interface have also been shown to affect the molecular coupling between donor and acceptor molecules altering the energy of the lowest observed CT state as well as the CT lifetime.[104–106]

While the material energetics of the donor and acceptor material (and crucially the energy of interfacial CT states) determine the upper limit of the V_{OC}, the equilibrium between charge generation and non-geminate recombination determines the losses relative to the upper limit and hence experimentally observed value of the V_{OC}.[72,107] The degree of phase segregation and particularly the interfacial area between donor and acceptor domains has previously been related to the non-geminate recombination kinetics. Vandewal *et al.* demonstrated that a reduced interfacial area results in an increase of the V_{OC}.[108] Other studies linked the morphology dependent structural disorder to non-geminate recombination losses.[32,80,109] Perdigon-Toro *et al.* also demonstrated that careful consideration of the energetic disorder and charge carrier built-up is crucial to understand the light intensity and temperature dependence of the V_{OC} as a single value for the CT and transport energy level is insufficient.[58]

Voltage losses relative to the energetic maximum are often characterized using a detailed balance method with a top-down approach – calculating the losses due to reduced generation, radiative recombination and non-radiative recombination in turn and subtracting them from the upper limit of V_{OC}.[110] This requires accurate measurements of CT emission (at low injection current, obeying quasi-thermal equilibrium conditions) and/or absorption spectra (sensitive EQE spectra resolving any sub-gap CT features). Here, a bottom-up approach with reference to the dark equilibrium condition (analogous to the diode equation) is used by combining the generation current (approximated by the J_{SC}) with the charge carrier kinetics determined at open circuit from TPV (lifetime) and DC (charge carrier density).[107] Light intensity dependent measurements allow for the determination of the apparent recombination order and to take the effect of energetic disorder and charge carrier accumulation into account.

Combining measurements of the materials energetics with transient optoelectronic measurements, the voltage losses in thin single-junction VP-OSCs with different active layer configurations (changing D/A ratio, PHJ vs BHJ) are investigated here-in. While the devices constitute non-optimal configurations for single-junctions, the observed V_{OC} increases may offer a pathway to increasing the overall performance of monolithic multi-junction devices.

4.3.2. Contributions

Electroluminescence and Photoluminescence spectra were recorded by Flurin Eisner. Samples were provided by Heliatek GmbH.

4.3.3. Device Structure and Performance

The devices studied herein were provided by Heliatek and possess a similar device structure to those studied in **Subchapter 4.2** with the exception of the intrinsic HTL that was chosen to be a proprietary material with a deeper HOMO than BPAPF to maximise the built-in potential. The device structure is as follows: ITO/n-C_{60}/i-C_{60}/BHJ (2:1 or 1:2, 30 nm) or donor (5 or 15 nm)/i-HTL/p-HTL/MoO_x/Ag (see **Figure 4.3.1 (a)** and **(b)**). The 30 nm thick BHJ layer was deposited at an elevated substrate temperature of 40 ˚C for both D/A ratios (slightly lower than the 50 ˚C in **Subchapter 4.2**).

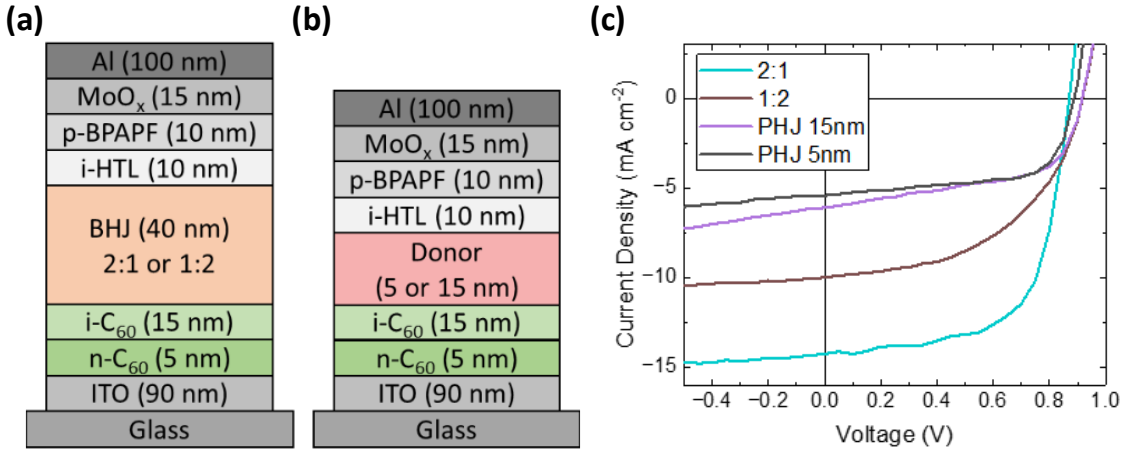


Figure 4.3.1. (a), (b) Device architecture of the BHJ and PHJ devices, respectively. The molecular structures have been shown in **Chapter 3**. The intrinsic HTL and the molecular dopants are proprietary materials of Heliatek GmbH. **(c)** *JV*-curve of the BHJ and PHJ devices at 1 sun light intensity.

Figure 4.3.1 (c) shows the *JV*-curves of the devices. See **Table 4.3.1** for the summary of the *JV*-parameters. The 2:1 device shows the highest performance with a V_{OC} of 0.87 V, similar to the values reported for the same D/A ratio and 25 nm active layer thickness in chapter 5. At a D/A ratio of 1:2, both the *FF* and J_{SC} decreased significantly, while V_{OC} increased substantially to 0.92 V. This chapter mainly focuses on the observed differences in the device V_{OC}, critical to maximising performance in multi-junction devices. Observations about the collection efficiency in analogy with **Subchapter 4.2** will be addressed briefly in the **Appendix** of this chapter (**Appendix IV**).

For the PHJs, the overall performance is lower than that of the BHJs likely due to the limited absorption of the thin donor layer resulting in poor J_{SC} values. Interestingly when comparing the PHJs, increasing the donor thickness from 5 nm to 15 nm does not yield a significant increase of the J_{SC}. This may indicate that the additional absorption in the thicker donor layer

does not result in charge generation due to the short exciton diffusion length. At reverse bias, the photocurrent of the 15 nm PHJ further increases significantly. The dark current density in **Appendix I** rules out that this is due to a low shunt resistance. Instead, this may indicate an additional generation pathway in the thick PHJ possibly related to field dependent charge generation in the neat donor layer. The TAS results reported in **Subchapter 4.2** indicate a low density of free charges generated in the neat donor film. Finally, regarding the V_{OC}, both PHJs show an increase compared to the 2:1 device with values of 0.89 V and 0.92 V for the thin and thick PHJ, respectively.

Table 4.3.1. *JV*-characteristics of the BHJ (D/A ratio 2:1 and 1:2) and PHJ (donor thickness 5 and 15 nm) devices.

Device	*PCE* (%)	J_{SC} (mA/cm²)	*FF*	V_{OC} (V)
BHJ 2:1	7.9	14.3	64	0.87
BHJ 1:2	4.6	10.0	51	0.92
PHJ 5 nm	3.1	5.4	66	0.89
PHJ 15 nm	3.1	6.0	56	0.92

Despite the reduced single-junction performance due to the reduced J_{SC} and *FF*, incorporating sub-cells with increased V_{OC} such as the 1:2 or PHJ devices into a multi-junction may yield an improved PCE if the added EQE of the sub-cells can match the optimum single-junction J_{SC} of the 2:1 device. In the following, the voltage losses in the devices relative to the photovoltaic gap will be addressed in more detail.

4.3.4. External Quantum Efficiency & the Photovoltaic Gap

To explain the observed trends in photocurrent, EQE spectra were measured for the four devices (**Figure 4.3.2**). For the 2:1 vs 1:2 comparison, it indicates that the lower J_{SC} is explained by the reduced absorption in the donor region of the spectrum (75 % vs 57 % for the 2:1 and 1:2, respectively) rather than bimolecular losses. The EQE of the PHJ devices in the donor region is reduced significantly to 25 % and 21 % for the thick and thin PHJ, respectively. The increase in donor EQE is partially counteracted by the decrease in generation in the acceptor portion of the spectra for the 15 nm PHJ.

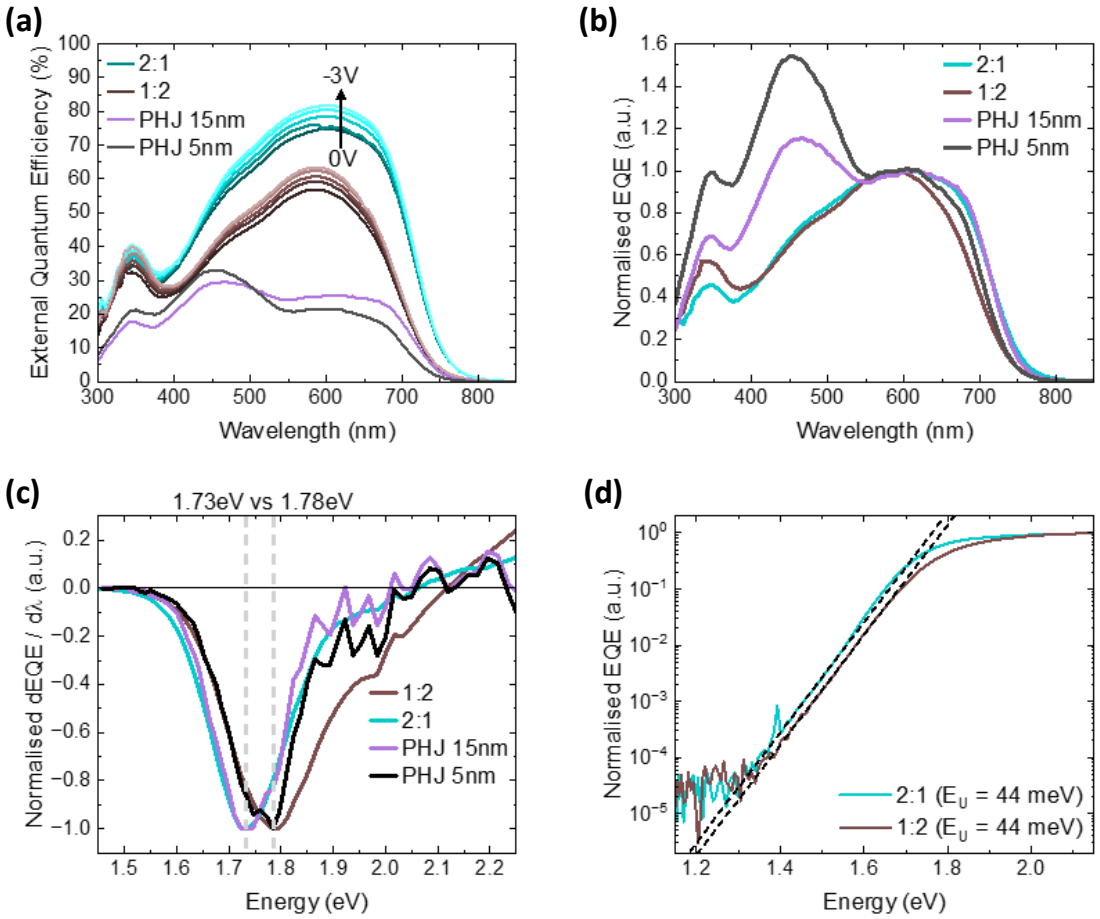


Figure 4.3.2. (a) External quantum efficiency spectra for the BHJ and PHJ devices. The BHJs exhibit a moderate field dependence of the EQE. **(b)** Normalised EQE spectra. **, (c)** Derivative of the EQE with respect to energy illustrating the blueshift of the absorption onset for the 5 nm PHJ and 1:2 BHJ devices. **(d)** Normalised EQE on a log-scale with fitted Urbach tails.

Figure 4.3.2 (b) shows the normalised EQE spectra used to assess the absorption onset of the different devices. To better quantify the absorption onset and the photovoltaic gap, **Figure 4.3.2 (b)** shows the derivative of the EQE with respect to the wavelength. The photovoltaic gap is given by the inflection point of the EQE spectra. This has been proposed as a suitable measure to analyse energy losses relative to the detailed balance limit.[111] While the absorption onset of the 2:1 device is similar to the previously reported photovoltaic gap for the 2:1 *RT* and *50C* device in **Subchapter 4.2**, the 1:2 device shows a clear blueshift of the absorption onset by about 60 meV – similar to the measured V_{OC} improvement. This indicates that the morphological changes in the different blend ratios are more severe than those caused by the alteration in substrate temperature during evaporation that have been discussed in **Subchapter 4.2**.

For the planar heterojunctions, the absorption onset varies for the two different donor layer thicknesses. While the EQE onset of the 15 nm thick donor layer resembles that of the 2:1 device, the 5 nm thick layer shows a blueshift similar to that of the 1:2 device. A possible explanation may be that a threshold thickness is needed to yield a level of donor aggregation found in 2:1 devices and the 15 nm donor layer. A more amorphous morphology within the first few nanometres of the donor layer may explain the blueshift of the 5 nm device. Note that potentially spectral shifts in the absorption may also be caused by interference phenomena in thin films by varying the film thickness. Ellipsometry measurements of thin donor films may be used to rule this out in the future. In any case, the recorded shifts in the photovoltaic gap contradict the trends in V_{OC} of the PHJs.

Sensitive EQE measurements often enable the direct determination of a CT energy by fitting any Gaussian sub-gap features. **Figure 4.3.2 (d)** depicts the sensitive EQE measurements on a log-scale. Within the sensitivity of the measurement, no Gaussian sub-gap states are discernible, and the spectra are best fitted by an exponential tail with an Urbach energy of 44 and 44 meV for the 1:2 and 2:1 (below 1.55 eV) BHJs. It should be noted that the existence of a CT feature below 1.4 eV cannot be ruled out from these measurements alone. However, unpublished data from collaborators Clemens Göhler, Maria Saladina and Carsten Deibel suggest that even with a higher sensitivity (up to 10^{-6}) no CT shoulder becomes discernible in 2:1 BHJs and the spectra are dominated by an exponential tail similar to the donor absorption. Unfortunately, the encapsulation of the PHJ device failed prior to recording this measurement resulting in film degradation. Given the reduced interfacial area in PHJs, I expect any CT feature to be even less pronounced than in the BHJ case.

4.3.5. Analysing Emission Spectra

The photovoltaic gap as determined from the derivative of the EQE is dominated by the optical gap of the smaller bandgap component (i.e. the donor). It therefore does not necessarily reflect changes in the energetic offsets of the molecular orbitals ($HOMO_{Acceptor}$ - $LUMO_{Donor}$) or the energy of the CT state formed at the interface. To probe differences in the interfacial energetics, electroluminescence measurements were carried out by Flurin Eisner. Due to the low emissivity of the studied samples, injection current densities in excess of 28 mA/cm² for the BHJs (> 2 J_{SC} BHJ) and 70 mA/cm² for the PHJs (> 10 J_{SC} PHJ) were required to yield a sufficient signal to noise ratio. The low emissivity as well as the absence of clear CT features in the BHJ EQE may point towards a low oscillator strength of the involved CT states.

Normalised spectra recorded at low injection currents can be seen in **Figure 4.3.3 (a)**. The EL emission of the 1:2 device shows a blueshift relative to the 2:1 device (1.24 eV vs 1.18 eV at 28 mA/cm²), while their PL emission **Figure 4.3.3 (b)**) shows the opposite trend (1.38 eV vs 1.45 eV). The latter implies a larger Stokes shift of the donor exciton in the 1:2 device.

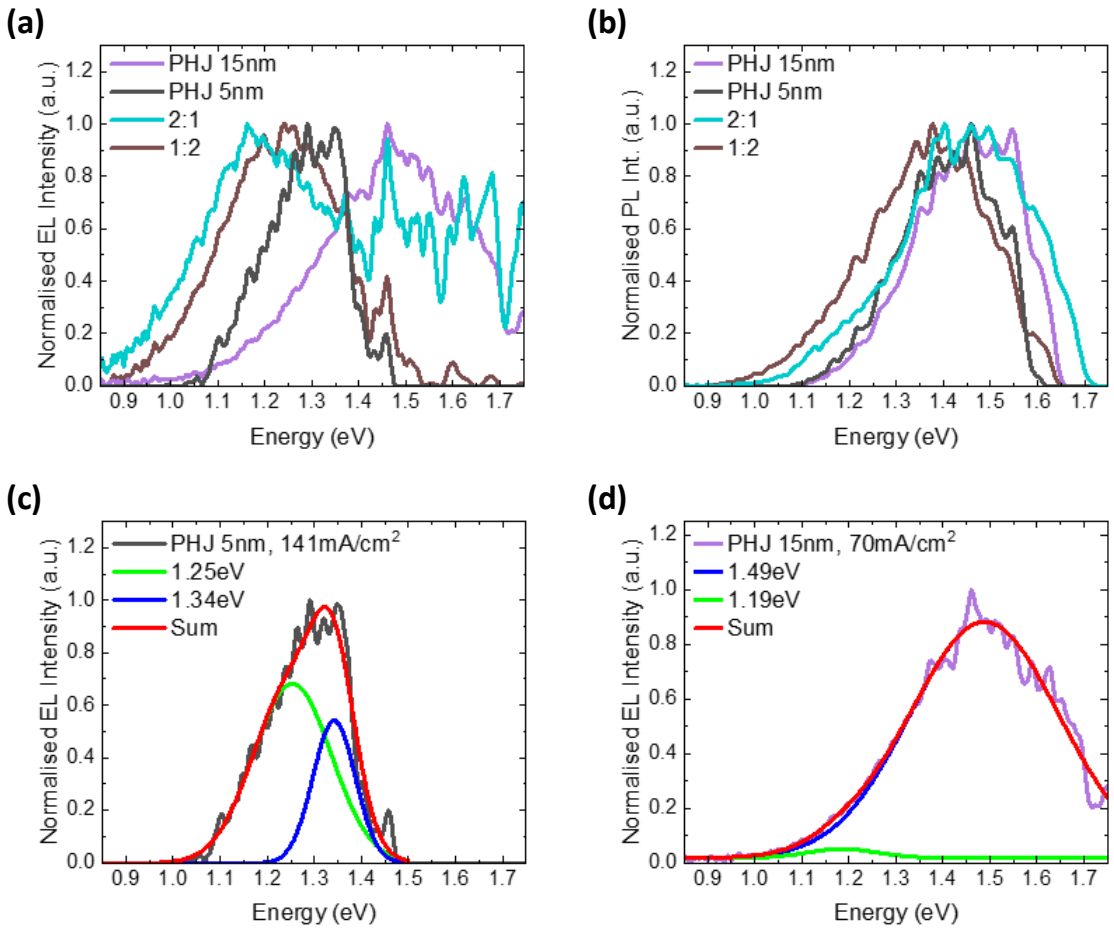


Figure 4.3.3. (a) Electroluminescence spectra of the PHJ and BHJ devices recorded at 28 mA/cm² (BHJs), 70 mA/cm² (15 nm PHJ) and 141 mA/cm² (5 nm PHJ). These values correspond to the lowest injection currents that a spectrum could be resolved at. **(b)** Photoluminescence spectra. **(c), (d)** Fitting of the PHJ spectra to resolve the low energy emission peak.

For the PHJs, the dominance of excitonic emission makes the identification of the CT emission peak more challenging (compare to the PL in **Figure 4.3.3 (b)).** The 5 nm PHJ EL obtained at 70 mA/cm² showed an EL emission peak centred around 1.29 eV (see **Appendix II**). Applying a Gaussian fit to the poorly resolved emission spectrum yields a peak position of 1.25 eV, similar to that of the 1:2 device. At 141 mA/cm², the 5 nm PHJ exhibits a significant blueshift of the emission (see **Figure 4.3.3 (a)**). Fitting two Gaussian peaks with a width of at least 90 meV yields a best fit with peaks centred at 1.25 and 1.34 eV assigned to the CT and excitonic donor emission, respectively. The fitting restraint was set to avoid fitting to noise

peaks. It corresponds to a reorganisation energy in classical Marcus theory of about 160 meV (which is well below the values obtained for the BHJs). The fitting further supports the peak position determined at the lowest measured injection current that is assigned to CT emission. The emission peak at 1.34 eV bears resemblance to the PL emission peak of the 1:2 device in line with the interpretation of the thin donor layer not being sufficiently aggregated to yield a similar absorption redshift as the thick donor layer.

For the 15 nm PHJ, even at an injection current of 70 mA/cm^2, the emission of the thick PHJ is clearly dominated by the PL emission of the donor (see **Figure 4.3.3 (b)**). An unconstrained fit of two Gaussians (**Figure 4.3.3 (d)**) shows that the signal can be accurately fit by a large peak at 1.48 eV (resembling the donor PL) and a 27 times weaker peak at 1.19 eV (resembling that of the 2:1 CT emission). Again, the fitting of two Gaussians was used to account for the apparent overlap of the excitonic donor emission (determined from the PL) and that of the CT state (with a similar position to the low injection current EL measurements in the BHJs).

The low resolution of the EL spectra as well as the absence of clear Gaussian features in the EQE_{PV} make the determination of reorganisation and CT energy difficult – and therefore a molecular or morphological interpretation of the spectra difficult. While an accurate determination of the absolute radiative V_{OC} limit ($V_{OC,rad}$) directly from EQE_{PV} or through reciprocal conversion of the EL spectra is unreliable here, EL measurements of the BHJ devices yield similar line widths of the EL spectra. The peak shift may therefore be used as a proxy for the change in the radiative limit ($\Delta V_{OC,rad}$). This therefore confirms the trend of the relative changes of the energetic contribution to the $V_{OC,}$ i.e. the change in the photovoltaic gap determined from the EQE onset, ($\Delta V_{OC,rad} = \Delta E_{EL} = 70$ meV, $\Delta E_g = 60$ meV). Peak fitting tentatively suggests CT emission peaks at low injection currents for the 15 nm and 5 nm PHJs similar to those of the 2:1 and 1:2, respectively, in line with what might be expected from the absorption onset. A more in-depth discussion of the emission data fitting and the EL dependence on the injection current (an potential links to the device morphology) will be given in **Appendix II** and **Appendix III**, respectively.

4.3.6. Summary of Photovoltaic Gap and Emission Spectra

The peak positions of the low-injection EL and PL emission, photovoltaic gap and V_{OC} are summarized in **Figure 4.3.4** and **Table 4.3.2**. The increase of V_{OC} for the 1:2 BHJ relative

to the 2:1 BHJ is consistently explained by the energetic contributions from an increased photovoltaic gap while the total voltage loss is comparable for both devices (0.86 eV). Energetic V_{OC} gains – as observed for the 1:2 device – come at the expense of current generation in the IR region of absorption and therefore would also limit current generation of the sub-cell in a tandem configuration made up exclusively of 1:2 BHJs of this material combination.

In the case of the 15 nm PHJ, the increase of V_{OC} cannot be explained with a shift in the photovoltaic gap. The thick PHJ shows the lowest voltage losses with respect to the EL peak emission (0.27 vs 0.32 eV for the 2:1 BHJ) and the photovoltaic gap (0.81 vs 0.86 eV for the 2:1 BHJ) while the photovoltaic gap and EL peak have a similar energy. The 5 nm PHJ device shows the highest voltage losses both with respect to the photovoltaic gap as well as to the EL emission peak. The small increase in V_{OC} may therefore be explained by the increase in the photovoltaic gap while contributions from recombination – or possibly shunting due to the low layer thickness – increase.

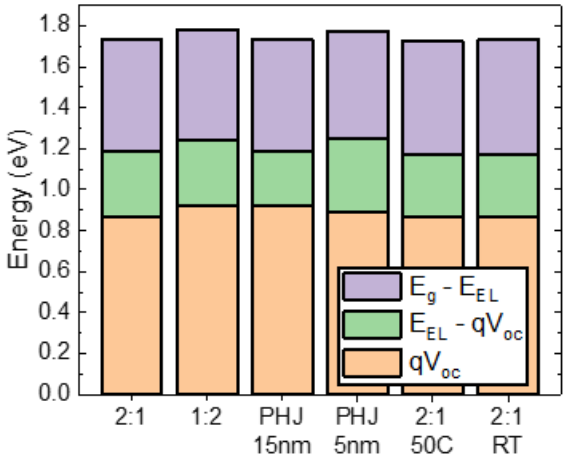


Figure 4.3.4. Comparison of the photovoltaic gap determined from the derivative of the EQE, EL peak energy and V_{OC} for the 2:1 BHJ, 1:2 BHJ, 5 nm PHJ and 15 nm PHJ. The quantities were chosen for the comparison due to the uncertainty in fitting the EL and EQE_{PV} spectra to determine the radiative limit. Additionally, the values obtained from the *RT* and *50C* devices studied in **Subchapter 4.2** are shown. Note that due to the difficulties in fitting the low intensity EL peaks, the values listed below correspond to EL peak energies rather than Marcus fits of the CT energy.

The total voltage losses are comparable to typical high-performing fullerene SP-OSCs[112,113] and the structurally related DCV-5T:C_{60} VP-OSC[49], while NFA SP-OSCs show values of E_g - qV_{OC} as low as 0.53 V determined using the same technique.[38,84,114,115] While the energetic

offset required in fullerene-based devices for efficient charge generation needs addressing, the above findings illustrate that reducing voltage losses due to non-geminate recombination is another key challenge for VP-OSCs that may be addressed by PHJ architectures. In the following, the focus will turn from observations of the energetic component of the V_{OC} to an assessment of the kinetic contribution from the equilibrium between generation and non-geminate recombination to explain the reduced voltage losses in the thick PHJ device.

Table 4.3.2 Open circuit voltage, photovoltaic gap, electroluminescence and photoluminescence emission peak energy, and energy differences for the BHJ and PHJ devices.

Device	V_{OC} (V)	E_g (eV)	E_{EL} (eV)	E_{PL} (eV)	$E_g - qV_{OC}$ (eV)	$E_{EL} - qV_{OC}$ (eV)
BHJ 2:1	0.87	1.73	1.19	1.45	0.86	0.32
BHJ 1:2	0.92	1.78	1.24	1.39	0.86	0.32
PHJ 5 nm	0.89	1.77	1.25	1.43	0.88	0.36
PHJ 15 nm	0.92	1.73	1.19	1.46	0.81	0.27

4.3.7. Non-Geminate Recombination

While there are several studies comparing (mostly evaporated) planar and bulk heterojunction OSCs, studies linking these differences to transient optoelectronic measurements and non-geminate recombination kinetics are rare in the literature.[55,116] Due to the higher V_{OC} of the 15 nm PHJ and the thicker active layer that is expected to reduce the effect of the geometric capacitance on the optoelectronic measurements, the measurements herein are focused on the BHJs (2:1, 1:2) and this thick PHJ device. Following a qualitative assessment of the non-geminate recombination kinetics, this section will focus on a quantitative assessment based on experimentally determined charge carrier density and lifetime data.

4.3.7.1. Light Intensity dependence of V_{OC} and J_{SC}

The light intensity dependence of the J_{SC} (**Figure 4.3.5 (a)**) can be used to qualitatively assess the non-geminate bimolecular recombination. Up to 1 sun equivalent illumination, the good linearity of the photo-current demonstrates that the differences in 1 sun J_{SC} are a result of differences in absorption or generation efficiency rather than bimolecular losses. At high light intensity, all three devices show a sub-linear J_{SC} as would be expected for a bimolecular recombination mechanism – with the PHJ maintaining a higher linearity at high light intensity relative to the BHJs. Between the BHJs, the 2:1 device shows greater linearity, indicative of reduced bimolecular losses, as may be expected from the higher *FF*. It should be

noted that when plotting the linearity of the J_{SC} in relation with the current generation rather than the light intensity, the PHJ shows a pronounced bimolecular reduction of photocurrent at high light levels relative to the 2:1 device (**Figure 4.3.5 (b)**). This considers the reduced generation current due to the limited absorption and smaller charge generating interface in the PHJ device and suggests that at high current densities, the increased charge carrier density at the interface leads to significant bimolecular recombination in the PHJ despite the spatial separation of the charge carriers across the well-defined heterojunction.

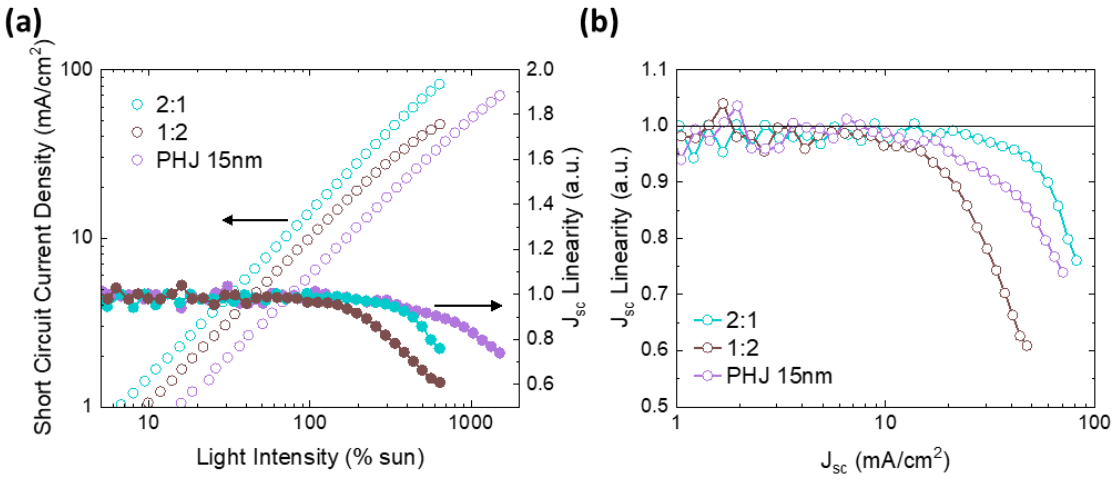


Figure 4.3.5. (a) J_{SC} (left scale) and J_{SC} linearity (right scale) versus light intensity. **(b)** J_{SC} linearity versus J_{SC} illustrating the effect of the reduced generation current of the PHJ on the onset of the linearity drop.

Turning to an assessment of the non-geminate recombination and its influence on V_{OC}, the light intensity dependence and ideality of the V_{OC} (**Figure 4.3.6**) shows remarkably similar ideality factors – close to 1, also indicative of a bimolecular recombination mechanism – for the PHJ and BHJ devices. This is in contrast to previous reports showing significantly higher light ideality values for PHJ devices[55,92] that had been assigned to the effect of injected electrode charges dominating recombination at low light intensity.[55] Instead the V_{OC} of the PHJ studied herein seems to be dominated by bimolecular recombination of photogenerated charges at the donor/acceptor interface, resulting in the comparable ideality to the BHJ devices. Importantly, the increased V_{OC} of the 1:2 and PHJ devices compared to the optimal 2:1 single junction BHJ also at light intensities below 1 sun demonstrate their potential to enhance the total V_{OC} of multi-junctions when paired with lower photovoltaic gap sub-cells.

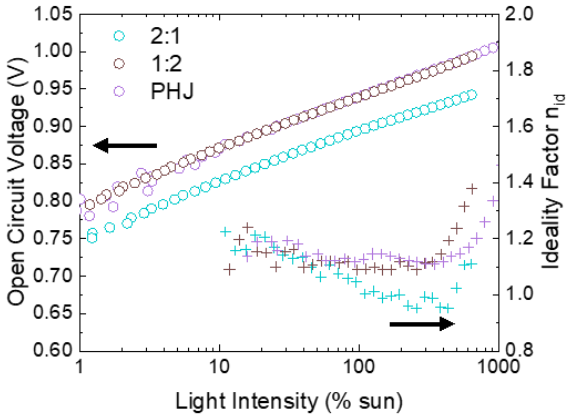


Figure 4.3.6. V_{OC} (left scale) and light ideality factor n_{id} (right scale) versus light intensity.

The V_{OC} of PHJs has previously been shown to be independent of the injection barrier of the contact layers while the built-in potential sets the upper voltage limit in BHJs.[96,97] Neither of the BHJs show any saturation behaviour of the V_{OC} ($n_{id} < 1$) at high light intensities implying that the V_{OC} is not limited by the V_{bi}.

Both BHJs and the PHJ seemingly show similar recombination mechanisms dominated by photogenerated charge carriers. The reduction of donor-acceptor interfacial area and the limited absorption within the exciton diffusion length from this area cause a reduction in the photocurrent for the PHJ device. Relative to the photocurrent, the reduction due to bimolecular recombination (sublinear behaviour at high light intensity) is interestingly not reduced, which may point towards a high charge carrier density built-up at the D/A interface. Also, the effect that the inhomogeneous charge carrier distribution has on the electric field and hence drift of carriers away from the charge generating interface of the PHJ could be further addressed by drift-diffusion simulations. Qualitatively, increasing generation at the interface could lead to an increased screening of the field due to the built-in potential at short circuit conditions and consequently a slower drift transport away from the interface. To quantify the non-geminate recombination rates TPV, DC and CE measurements were carried out.

4.3.7.2. Correcting for Capacitive Effects in BHJs and PHJs

In **Subchapter 4.2**, the comparison of the charge carrier kinetics of BHJs with different active layer morphology and thickness showed that the kinetic approach to quantifying V_{OC} can reliably reproduce the measured V_{OC}. The method has also been applied to the study of PHJ devices in the past.[55,117,118] However, the application of the experimental method as well as the interpretation of the results to understand non-geminate recombination kinetics in PHJ

systems is not straight forward. Crucially, the assumption of a homogeneous charge distribution in an effective medium (the BHJ) can no longer be upheld.[55] Furthermore, the small device thickness and the resulting capacitive effects need to be taken into account. This section will focus on addressing these technical issues prior to discussing the results and the interpretation of the non-geminate recombination kinetics.

In **Subchapter 4.2**, it was demonstrated that for the evaporated BHJs the charge carrier densities determined by CE and DC are in excellent agreement. Before analysing the recombination current and its impact on V_{OC}, the applicability of the experimental techniques to PHJs is investigated here.

Figure 4.3.7 **(a)** and **(b)** show the total differential capacitance of the PHJ and BHJ devices, respectively, as well as the corrected active layer capacitance. All three devices can be well fitted using a combination of a constant geometric capacitance and an exponential chemical capacitance. For the BHJs, the values of the geometric capacitance are in good agreement with the values obtained for the same interlayers in Chapter 4 and consistent with a model that considers the undoped interlayer capacitance to determine the overall geometric capacitance. The value obtained for the much thinner PHJ exceeds the expectation of the proposed model, potentially due to a higher error on the layer thickness or other factors influencing the dark equilibrium charge density in the device.

Nevertheless, the exponential portion of the differential capacitance can be used to calculate the active layer charge (plus intrinsic interlayer charge) by integration as discussed above. This can then be compared to the value determined by charge extraction upon correcting for the capacitive charge. **Figure 4.3.8** **(a)** shows the PHJ's total charge together with the capacitance corrected charge at V_{OC} as well as the charge determined from charge extraction at an applied bias in the dark. The latter was used to calculate the capacitive correction term as previously discussed. It illustrates that the excess photo-generated charge at open circuit as determined by charge extraction does not significantly exceed the injected charges in the dark at an applied bias. This has previously been observed for other PHJ devices.[117] Fitting the data using a linear geometric and an exponential term yields a significantly different result from the value obtained by differential capacitance measurements also shown in **Figure 4.3.8** **(a)**. **Figure 4.3.8** **(b)** shows the charge extraction results of all three devices including the fitting of the linear geometric charge term.

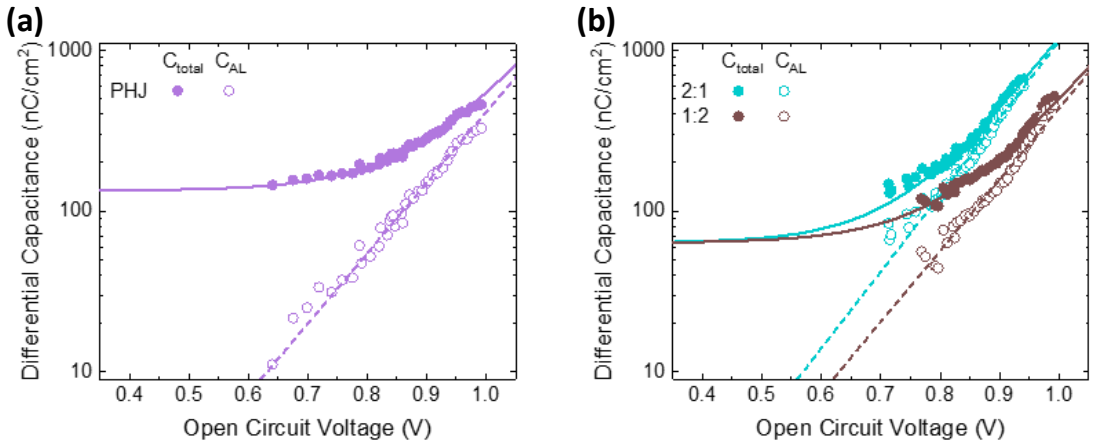


Figure 4.3.7. (a), (b) Total differential capacitance (C_{total}) and active layer capacitance (C_{AL}) determined by subtracting the geometric capacitance (C_{geo}) for the PHJ and BHJ devices, respectively. The fitted ideality factors of the devices were determined to be 10.1 V^{-1}, 11.0 V^{-1} and 10.2 V^{-1} for the PHJ, 2:1 and 1:2 device respectively.

Both datasets – CE and DC – are self consistently fit with differing values for the geometric capacitance (6.1 vs 9.5 nF for the PHJ and 4.0 vs 4.5 nF for the BHJs determined by CE and DC, respectively). As previously discussed, charge extraction may be subject to a significant third capacitive term caused by surface charges induced by a highly inhomogeneous charge distribution.[119] While CE is accompanied by a bias switch from open circuit to short circuit and consequently includes this contribution, the device is kept under open circuit conditions with just a small voltage perturbation during the TPV experiments used to calculate the DC. Such surface charge effects would be particularly severe in the case of a PHJ where the majority of the hole and electron population are separated across the junction.[55] Therefore, the DC results were used for further analysis of the PHJ results consistent with previous studies.[118]

For the BHJs, DC and CE yield very similar gradients but show an offset between the two measurements as shown in **Figure 4.3.9 (a)**. Discrepancies between the measurements may arise from overestimation of the DC for devices with field dependent generation (discrepancy between the integrated charge measured by TPC at short circuit and the charge generated by the laser at open circuit) or underestimation of the CE due to incomplete integration of the charges or recombination losses during extraction.

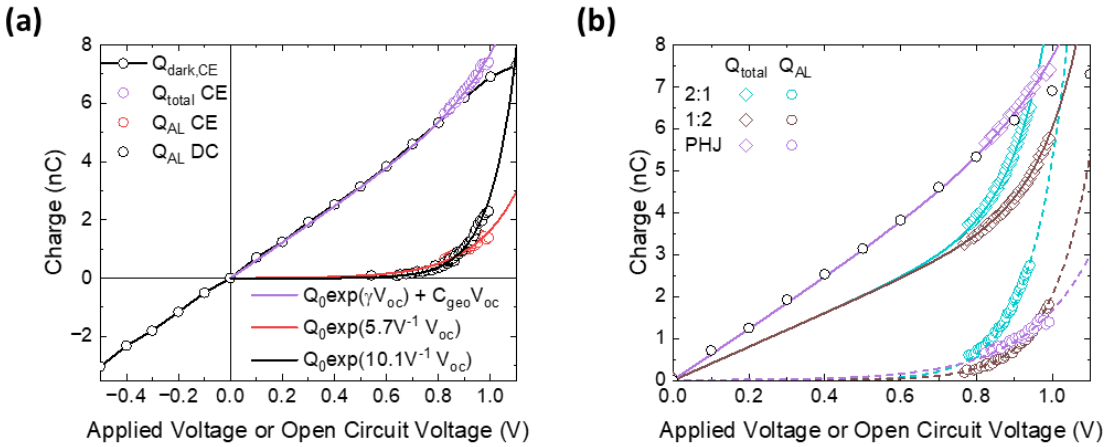


Figure 4.3.8. (a) Charge extraction results of the 15nm PHJ device illustrating the correction for the linear geometric charge term. Also shown is the result from differential capacitance measurements with a significantly different slope parameter and overall charge. **(b)** Charge extraction results for the PHJ and BHJ devices including the corrected charge. The ideality factors of the charge vs V_{OC} were determined to be 5.7 V^{-1}, 10.7 V^{-1} and 9.8 V^{-1} for the PHJ, 2:1 and 1:2 device, respectively.

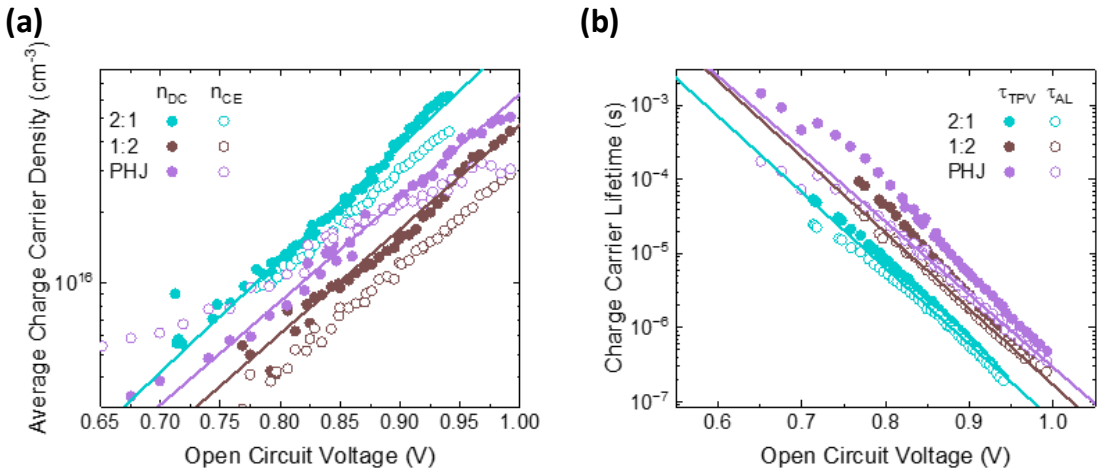


Figure 4.3.9 (a) Side-by-side comparison of the spatially averaged charge carrier density determined from charge extraction and differential capacitance measurements. The fitted ideality factors of the devices were determined to be 10.1 V^{-1}, 11.0 V^{-1} and 10.2 V^{-1} for the PHJ, 2:1 and 1:2 device respectively. **(b)** TPV lifetime and active layer lifetime value calculated as previously shown[118]. The fitted exponentials were used for the V_{OC} reconstruction. The fitted ideality factors of the devices were determined to be 22.6 V^{-1} and 23.6 V^{-1} for the PHJ and BHJs, respectively.

In the following, the charge density determined from DC will be used for the analysis because the influence of induced surface charges is expected to be minimal here.

Figure 4.3.9 **(b)** shows the measured TPV lifetime of the PHJ and BHJ devices. The TPV lifetime was corrected by applying the capacitive correction as set out by Credgington *et al.* ($\tau_{AL} = \tau_{TPV} \cdot (C_{AL}/C_{geo}$)). The capacitance corrected lifetime multiplied by the experimentally

determined recombination order together with the charge carrier density determined from differential capacitance were used to calculate the loss current. **Figure 4.3.10 (a)** shows the comparison of the calculated loss current with the experimentally determined J_{SC} at various light intensities. The fitting parameters of the DC average charge carrier density and the corrected lifetime (see **Table 4.3.3**) were used to reconstruct V_{OC} as shown below in **Figure 4.3.10 (b)**.

Table 4.3.3. Fitting parameters and ideality factors derived from the relationship of the charge carrier density and lifetime with V_{OC}. Additionally, the calculated recombination order δ and the ideality factors determined from the optoelectronic measurements as well as from the light intensity dependence of the V_{OC} around 1 sun equivalent illumination are shown.

	n_0 (10^{12} cm^{-3})	γ (V^{-1})	τ_0 (s)	β (V^{-1})	δ	$n_{id,kin}$	n_{id}
2:1	1.90	11.0	1000	23.6	3.15	1.07	1.0
1:2	1.75	10.2	3000	23.6	3.31	1.10	1.1
PHJ 15nm	2.60	10.1	1900	22.6	3.23	1.13	1.1

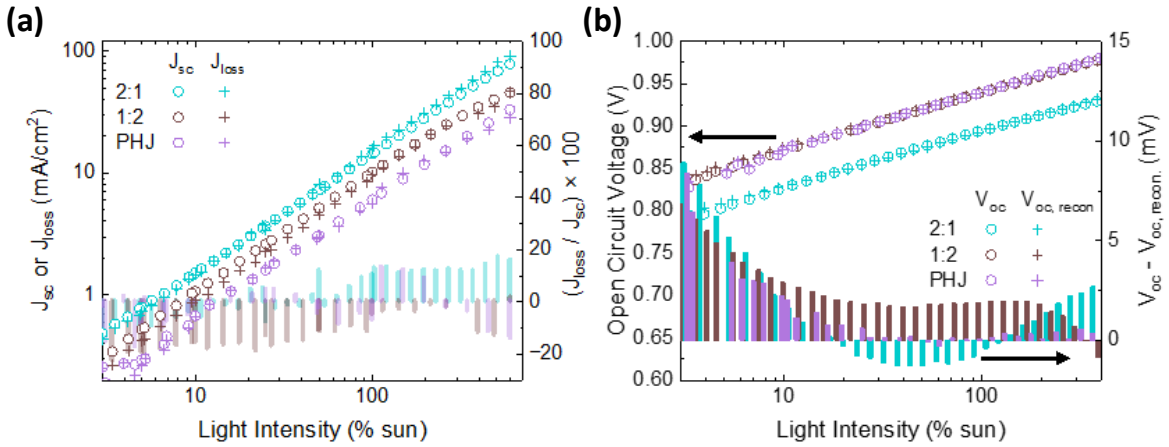


Figure 4.3.10. (a) Comparison of the calculated loss current and J_{SC} at varying light intensity. The bars on the right axis show the percentage deviation between the two values.

The loss current deviates by less than 20% from the J_{SC}. Reconstructed and experimental V_{OC} differ by less than 5 mV – with the ideality of the reconstruction in excellent agreement with experiments above 10% sun. Below this value, the effect of the shunt resistance starts to dominate. Overall, this demonstrates the validity of the experimental procedure in determining spatially averaged recombination kinetics. Note, that a field dependent reduction of the generation current between short circuit and open circuit conditions will affect the J_{SC} and the small perturbation charge determined from TPC the same (used for the determination of the charge carrier density by DC). Its influence on the reconstructed V_{OC} therefore cancels

out and the DC determined charge carrier density may therefore be overestimated by the percentage of geminate reduction of the generation current.

4.3.7.3. Kinetic Contribution to V_{OC}

After demonstrating the validity of the experimental method in determining a spatially averaged charge carrier density and the corresponding active layer charge carrier lifetime, this section will turn to an interpretation of the measurements for BHJ and PHJ devices to explain differences in non-geminate recombination kinetics and relate these to changes in the V_{OC}.

Firstly, the comparison of the dependence of the charge carrier density on V_{OC} (see **Figure 4.3.11**) between the BHJs reveals an apparent shift along the voltage axis by about 80 meV for the 1:2 BHJ with similar values of the characteristic energy (45 meV and 49 meV for 2:1 and 1:2, respectively) calculated from the exponential scaling factor γ. This interpretation assumes an effective medium approach and a spatially homogeneous charge carrier density across the active layer. The values are similar to those determined from fitting the exponential tail of the EQE (42 meV and 44 meV for 2:1 and 1:2, respectively). Compared to the increase in the photovoltaic gap and EL emission peak energy described above, a larger shift in the charge built-up is observed (60 vs 80 meV). To visualise this, **Figure 4.3.11 (b)** shows the data from **Figure 4.3.11 (a)** with a rescaled x-axis by the energy of the EL peak emission (again, this is done because the lowest injection current EL spectra could not be fitted reliably using Marcus theory to determine E_{CT} and λ_{CT} as set out by Vandewal *et al*[120,121]). It should be noted that the charge carrier density measures an effective gap that is also influenced by the combined width of the DoS rather than the single energetic value.

Simultaneously, there also appears to be a change in the recombination kinetics signified by a smaller shift of the lifetime versus the V_{OC} (~50 meV) as shown in **Figure 4.3.12 (b)**. Plotting the lifetime versus the spatially averaged charge carrier density consequently shows a reduction in the carrier lifetime at equal charge carrier densities (**Figure 4.3.12 (b)**). Using the simple kinetic model outlined previously,[107] the lifetime reduction by a factor of 2.2 together with the decrease in generation current (approximated by the J_{SC}) results in a kinetic V_{OC} loss of about 30 meV. Combined, these observations consistently explain the observed increase in V_{OC}.

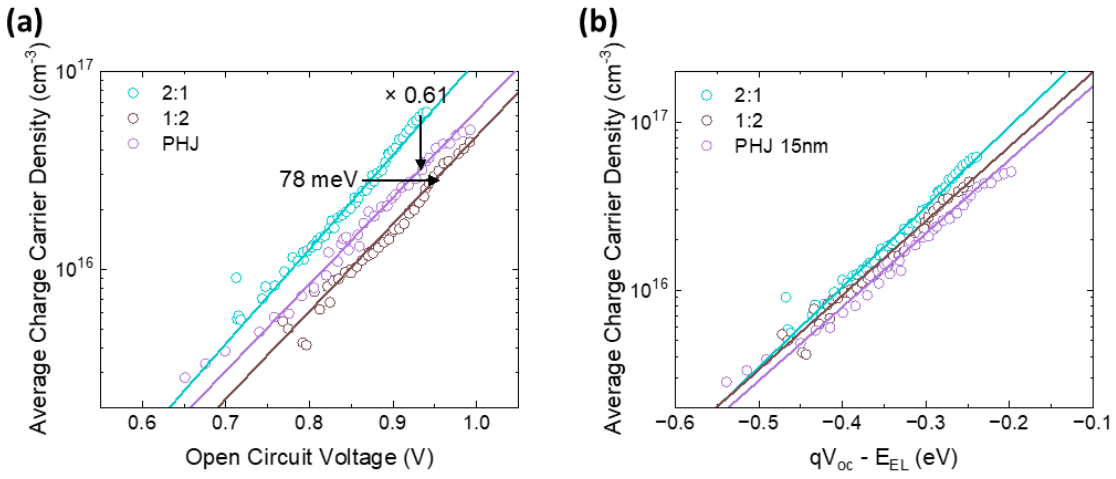


Figure 4.3.11. (a) Spatially averaged charge carrier density versus V_{OC} determined from DC measurements. The arrows signify changes relative to the 2:1 device. **(b)** Equivalent data plot with the x-axis rescaled by the position of the EL emission peak to illustrate the changes of the effective electronic bandgap relative to the change in the photovoltaic bandgap and the EL emission (both shifted by ~50-60 meV from 2:1 to 1:2).

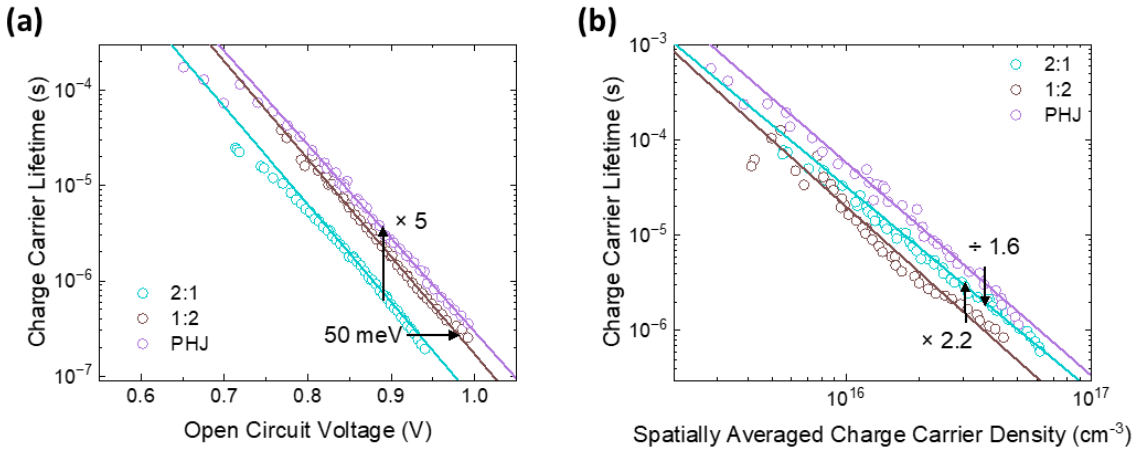


Figure 4.3.12. (a) Small perturbation lifetime determined from TPV versus the open circuit voltage. **(b)** Charge carrier lifetime versus the spatially averaged charge carrier density. The arrows in both plots signify changes relative to the 2:1 device discussed in the main text.

For the PHJ, the charge carrier density and lifetime are shifted towards a higher potential by about 50 and 65 mV, respectively, relative to the 2:1 BHJ. This results in an overall increase of the charge carrier lifetime by a factor of 1.6. Together with the reduced generation current (6.0 vs 14.3 mA/cm^2) this means a kinetic V_{OC} decrease of less than 10 mV despite the longer lifetime and a net increase of 40 mV similar to the experimental observation.

4.3.8. Interpretation of Energetic and Kinetic Results

The assumption of a (spatially homogeneous) charge distribution in an effective medium as employed for BHJ devices is clearly not valid when considering the case of a PHJ and its

spatially separated hole and electron populations (as would be expected for a significant EA and IP offset where injection of minority carriers across the junction is expected to be low).[55] An apparent shift in the measured effective bandgap of PHJ devices can therefore not be understood directly as a shift in interfacial energetics as in the case of the BHJs where shifts in EL emission and photovoltaic gap show similar trends and magnitudes to the shift in the effective electronic gap. Furthermore, also the slope parameter of the charge carrier density does not reflect a measure of the energetic disorder alone but is also influenced by the charge carrier distribution.

Assuming instead – based on measurements of the photovoltaic gap as well as the fitted EL emission peak – that the energetics at the donor/acceptor interface resemble those of the 2:1 device, a shift along the voltage axis is instead explained by a change in the interfacial area itself. As derived by Cheyns *et al.* the V_{OC} in a PHJ device primarily depends on the charge carrier density at the interface besides the interfacial energetics.[122] The reduction in charge carrier density at equivalent V_{OC} can therefore be explained by the PHJ's reduction in interfacial area and spatial separation of holes and electrons compared to the 2:1 BHJ[55] – essentially an increased charge carrier density per unit interfacial area while the involved interfacial energy values remain unchanged. At the same time the lifetime shows an approximately five-fold increase at the equivalent V_{OC} which suggests that there is a reservoir of charges away from the interface not directly contributing to recombination.

Qualitatively, the lifetime versus V_{OC} data resembles the observations by Vandewal *et al.* for BHJs with controlled interfacial area.[108] By using blends with a low donor loading (1 to 10 %) they ensured that the CT energy remained unchanged but observed an increase in the V_{OC} and an apparent lifetime shift along the voltage axis. This lifetime change therefore does not imply a change in the nature of the CT states that the recombination proceeds through but rather a change in the encounter rate of carriers that is dependent on the interfacial area and the density of such CT states.

The data shown here-in demonstrates that an understanding of the transient optoelectronic data requires a reference of the involved energetic levels in order to distinguish between an increase of the effective electronic gap caused by changes to the interfacial area (PHJ vs 2:1) and those caused by changes in the involved energy levels (1:2 vs 2:1). The former has been shown here to lead to a reduction in voltage losses, while the latter leads to an increase in the

open circuit voltage due to material energetics while the voltage losses relative to that remain similar. Nevertheless, the lifetime analysis is suitable to analyse voltage losses in the devices

4.3.9. Potential for Multi-Junction Performance Increases

In this section, rough estimations of possible performance increases in multi-junction cells based on DCV-V-Fu-Ind-Fu-V:C_{60} PHJs, 2:1 and 1:2 BHJs will be discussed to show the potential of multi-junctions to alleviate limits set by the collection efficiency while also allowing for high photon conversion efficiencies. Multi-junction systems are highly complex and while commercial products including such device architectures are available, the academic literature is limited to a few examples.[49,83] Consequently, it is difficult to predict based on literature how single-junction performance may translate to multi-junctions.

The benchmark for any comparison is the 2:1 BHJ device with its higher single-junction performance. **Table 4.3.4** lists the corresponding figures of merit of the 2:1 BHJ as well as the values for the 1:2 and PHJ devices. EQE values quoted here correspond to the maximum EQE in the donor region. Below that, **Table 4.3.4** lists values for hypothetical triple junction configurations – firstly considering triple-junctions made up of three 2:1, 1:2 or PHJ sub-cells. The hypothetical figures of merit were estimated as follows:

Table 4.3.4. Single-junction and estimated multi-junction device performance for different device architectures. The assumptions made for the calculation are discussed in the text. EQE values marked with an (*) are values of the average EQE above the photovoltaic gap.

Stack	V_{OC} (V)	Total *EQE* (%)	J_{SC} (mA/cm²)	*FF*	*PCE* (%)
2:1	0.87	74*	14.1	65	7.9
1:2	0.92	57*	10.0	51	4.6
PHJ	0.92	26*	6.0	56	3.1
2:1 / 2:1 / 2:1	2.61	65	4.7 (14.1)	70	8.6
1:2 / 1:2 / 1:2	2.76	65	4.4 (13.1)	60	7.3
1:2 / 1:2 / 2:1	2.71	65	4.7 (14.1)	60	7.6
PHJ / PHJ / PHJ	2.79	65	4.7 (14.1)	66	8.7
IR D / 2:1 / 2:1	2.26	65 (30 in IR)	5.9 (17.7)	70	9.3

Based on the experience by Meerheim *et al.*, voltage losses caused by the recombination layers are low, especially when including a reduced sub-cell voltage due to decreased generation density in each sub-cell. For this study, such limitations will be ignored. The current

generation in multi-junctions is highly dependent on interference effects. The optimisation of active layer and interlayer thickness goes beyond the scope of this study. Instead, an average total EQE summed over all sub-cells of 65 % is assumed (see **Figure 4.3.13 (a)**). In the case of the 2:1 device this corresponds to the single-junction J_{SC}. This is a conservative estimation as demonstrated by Meerheim *et al.*[49] Especially in C_{60} region of absorption, the overall EQE may in fact exceed the single-junction current generation and micro-cavity effects may lead to an improved absorption in the low-energy tail. Exact predictions of the *FF* of the triple-junction are difficult as they depend on both the generation density as well as the thickness of the sub-cells. An estimate is made here-in by determining the *FF* of the single-junction BHJs as a function of light intensity (**Figure 4.3.13 (b) - (d)**). By measuring the *FF* at the light intensity corresponding to the generation rate of a sub-cell (one third of the overall generation rate), reduced non-geminate losses during collection are accounted for. An increase from 65 % to 70 % for 2:1 device and 51 % to 60 % for the 1:2 device is assumed based on this analysis. For a further discussion of the origin of the reduced *FF* in the 1:2 device and its increased light intensity dependence, please see the **Appendix IV** of this chapter. The effect of changing sub-cell thickness remains unaccounted for here. The fact that current matching must be achieved not only for short circuit conditions but also at MPP introduces additional uncertainty in some of these estimations.

The 2:1 triple-junction shows an increased performance relative to the single-junction. It also outperforms the 1:2 triple-junction since voltage gains are offset by current losses and the additional limit due to the lower *FF*. The reasonable estimates of the triple-junction performance relative to the single-junctions illustrates how the collection efficiency limitations can effectively be mitigated.

Another realistic scenario to find a balance between current and voltage losses would be a combination of sub-cells with different D:A ratio (or ideally of sub-cells with different photovoltaic bandgaps). Here, due to the lower *FF*, this does not give an advantage over the 2:1 triple-junction.

The case of the PHJ triple-junction differs from the above. Here, the current that would need to be achieved by the individual sub-cells is close to that of the single-junction PHJ at 1 sun. Optimistically, it was assumed that through the application of optical spacers, a total EQE of 65 % is achievable and an optimistic *FF* of 66 % was assumed (equivalent to the 5 nm PHJ).

In such a scenario, a small performance increase over the 2:1 triple-junction could be achieved thanks to the increased sub-cell voltage.

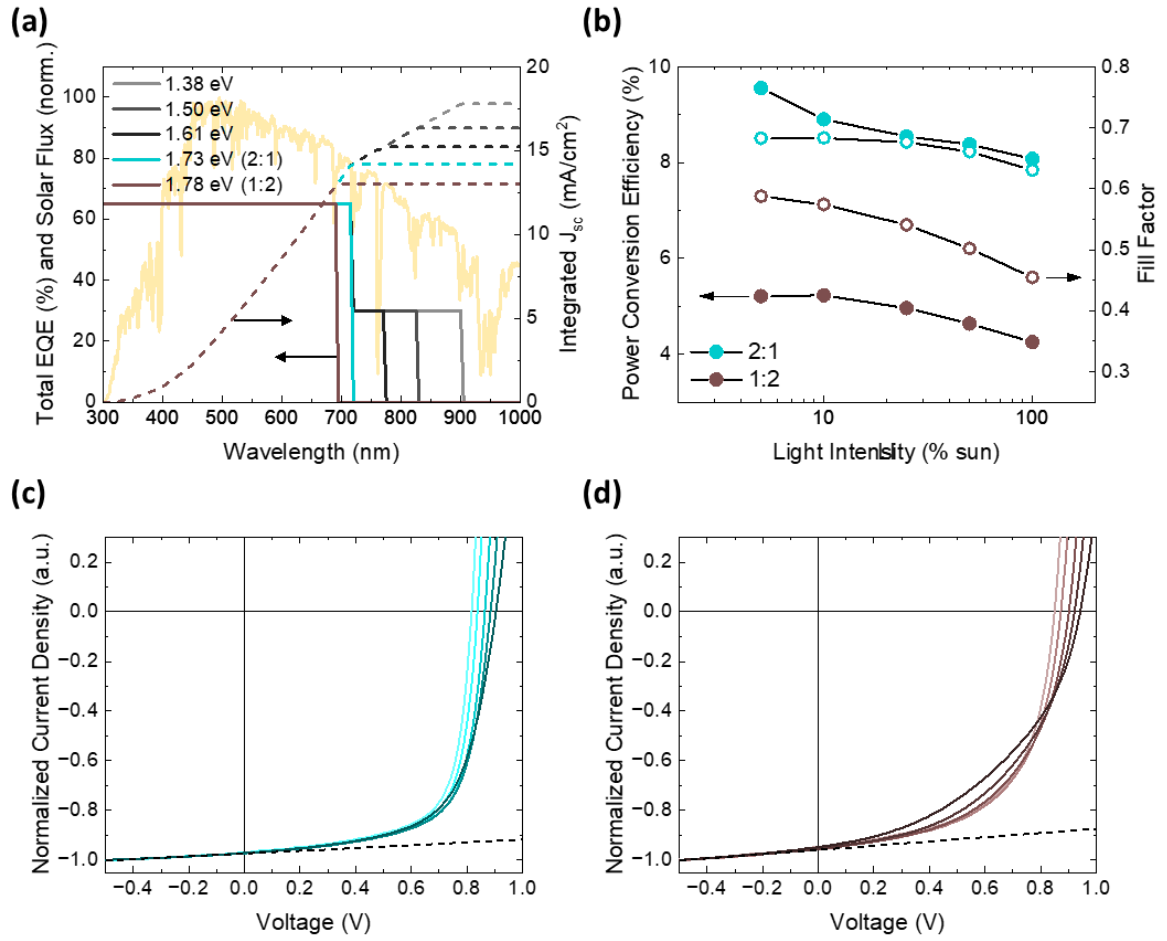


Figure 4.3.13. **(a)** Total EQE and corresponding integrated current density of different hypothetical multi-junction combinations. **(b)** Fill factor as a function of light intensity for the BHJ devices. **(c), (d)** Light Intensity dependent JV-curves of the 1:2 and 2:1 device, respectively.

By far the most significant increase in efficiency, however, would be achieved by using complimentary absorbers, ideally into the infra-red part of the solar spectrum. **Figure 4.3.13 (a)** shows hypothetical extensions to the absorption spectrum and the corresponding J_{SC} increases. To the best of my knowledge, an evaporable high-performing donor material with a bandgap as low as 1.38 eV has not currently been published. It roughly corresponds to the gap of Y6. A complimentarily absorbing sub-cell even with a modest EQE of just 30 % in the IR could significantly boost efficiency of the triple-junction as shown in **Table 4.3.4**. In the absence of IR absorbing evaporated donors, depositing a hybrid solution-processed/evaporated bilayer as demonstrated by Kaienburg *et al.* could potentially be applied

here (leaving the question of scalability aside for the time being).[38] In the absence of evaporable materials absorbing far into the IR, such approaches should be further explored.

4.3.10. Conclusion

While limits of the collection efficiency can be mitigated by the application of multi-junction devices, voltage losses pose a more fundamental limit to the efficiency of VP-OSCs. This poses the question whether non-optimal single-junction device structures may result in increased photovoltage in multi-junctions. The material system studied here-in shows voltage losses representative of fullerene-based material combinations. Changing the donor-acceptor ratio from 2:1 to 1:2 as well as using a PHJ architecture was shown to increase the V_{OC} (by 50 mV and 60 mV, respectively). In the case of the 1:2 donor-acceptor ratio, the voltage increase correlated with a change in material energetics and the effective bandgap while voltage losses due to non-geminate recombination remained unchanged. For the PHJ, the measured photovoltaic gap and the EL emission peak matched that of the 2:1 device suggesting that the voltage increase is related to a reduction in non-geminate losses. Indeed, a lower recombination rate was measured experimentally and related to the limited donor-acceptor interface. An overall lower volume-averaged charge carrier density is required to support the QFLS at the limited interface and additional charges accumulate inside the PHJ outside of the effective recombination radius, overall slowing down the measured recombination kinetics. The results suggest that the application of PHJs could effectively increase the open circuit voltage when appropriate contacts are used, and the main recombination channel is bimolecular recombination of photogenerated charges at the donor-acceptor interface. Nevertheless, the performance of PHJ devices, also when used in a multi-junction, suffers from the low exciton diffusion length and the reduced *FF* in thicker junctions that is tentatively assigned to a field dependent generation mechanism in the neat donor away from the donor-acceptor interface (or potentially at the donor-HTL interface). While the proposed generation in the neat film partially mitigates the limitations of the low exciton diffusion length at *Jsc,* the resulting low FF limits the device performance. Novel donor molecules optimised for their exciton diffusion length and ideally IR-absorption could further boost multi-junction performances. The application of PHJs would alleviate the need for optimising the donor aggregation in BHJs and has the potential of enabling high V_{OC}. Ultimately, replacing fullerene acceptors in VP-OSCs could help further reduce voltage losses. Synthesising small molecule acceptors and infrared absorbing donors “that fly” remains a veritable challenge! Additionally,

higher sensitivity electroluminescence and external quantum efficiency spectra may help further elucidate the origin of the voltage losses, spectral linewidth and their relationship with interfacial area and disorder – a topic hotly debated in recent literature.[72,80,109,123–125] Correlating this with morphological evidence as shown in **Subchapter 4.2** may also allow to elucidate the molecular origin of the behaviour. Further data and possible corresponding fits are shown in **Appendix III** together with a tentative explanation for the observed measurements.

Appendix

Appendix I: Dark JV-Curve

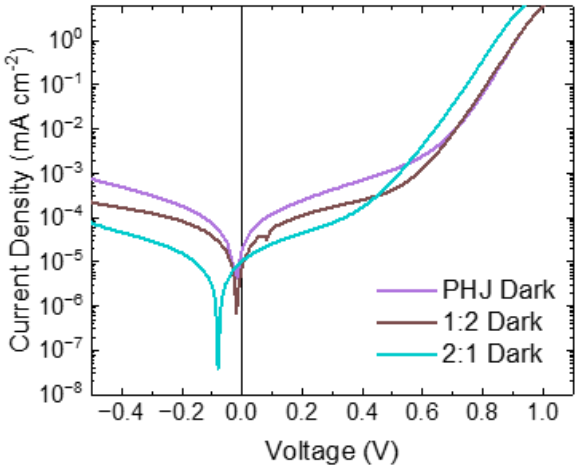


Figure 4.3.14: Dark JV-curves of the PHJ and BHJ devices illustrating that the large gradient in the PHJ light JV-curves cannot be explained by an excessive leakage current.

Appendix II: Fitting of 5 nm PHJ Electroluminescence

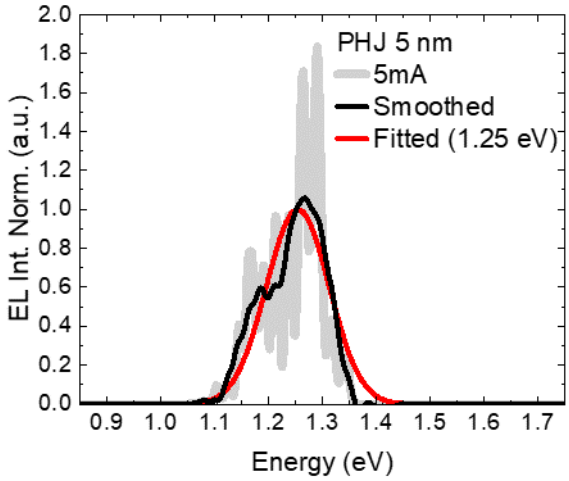


Figure 4.3.15: Fitting of the 5 nm PHJ electroluminescence emission spectrum recorded at 70 mA/cm². The raw data was fitted yielding an emission peak of 1.254 eV and a width of the emission peak of 0.116 eV (corresponding to a values of E_{CT} = 1.50 eV and λ_{CT} = 0.25 eV)

Appendix III: Electroluminescence Fitting Details

As previously described, the low emissivity and high noise of the recorded electroluminescence spectra makes the accurate fitting of Markus theory parameters (CT energy E_{CT}, reorganisation energy λ, oscillator strength *f*) unfeasible. In the main text, the energy at the emission peak is quoted (equivalent to E_{CT} - λ in basic Marcus theory)[120].Additionally, EQE_{PV} spectra did not show a clear Gaussian feature in the sub-gap region. To try and elucidate the CT energy and reorganisation energy and offer a potential interpretation of the energetic data shown here-in, the electroluminescence, photoluminescence and EQE_{PV} were fitted simultaneously for the two BHJ devices. This has been proposed to offer a more robust way of determining the involved parameters.[110] By using standard Marcus theory as proposed by Vandewal *et al.*[120,121] effects of disorder,[72,123] CT states manifold,[124] or high frequency vibrations[126] are ignored and therefore the values determined for the CT and reorganisation energy should not be over-interpreted. **Figure 4.3.16 (a)** and **(b)** show the fitting of the reduced EL and EQE_{PV} spectra and **Figure 4.3.16 (c)** and **(d)** of the PL and EQE_{PV} for the 2:1 and 1:2 BHJ, respectively. Note, that fitting the spectra presented a challenge due to the challenging background correction of the emission data in the region of the high energy tail. Improved noise of the spectra as well as temperature dependent measurements are necessary to elucidate the contribution of static disorder to the line broadening. This is particularly important as the

values for the linewidth and correspondingly the reorganisation energy fitted here are high compared to other previous reports.

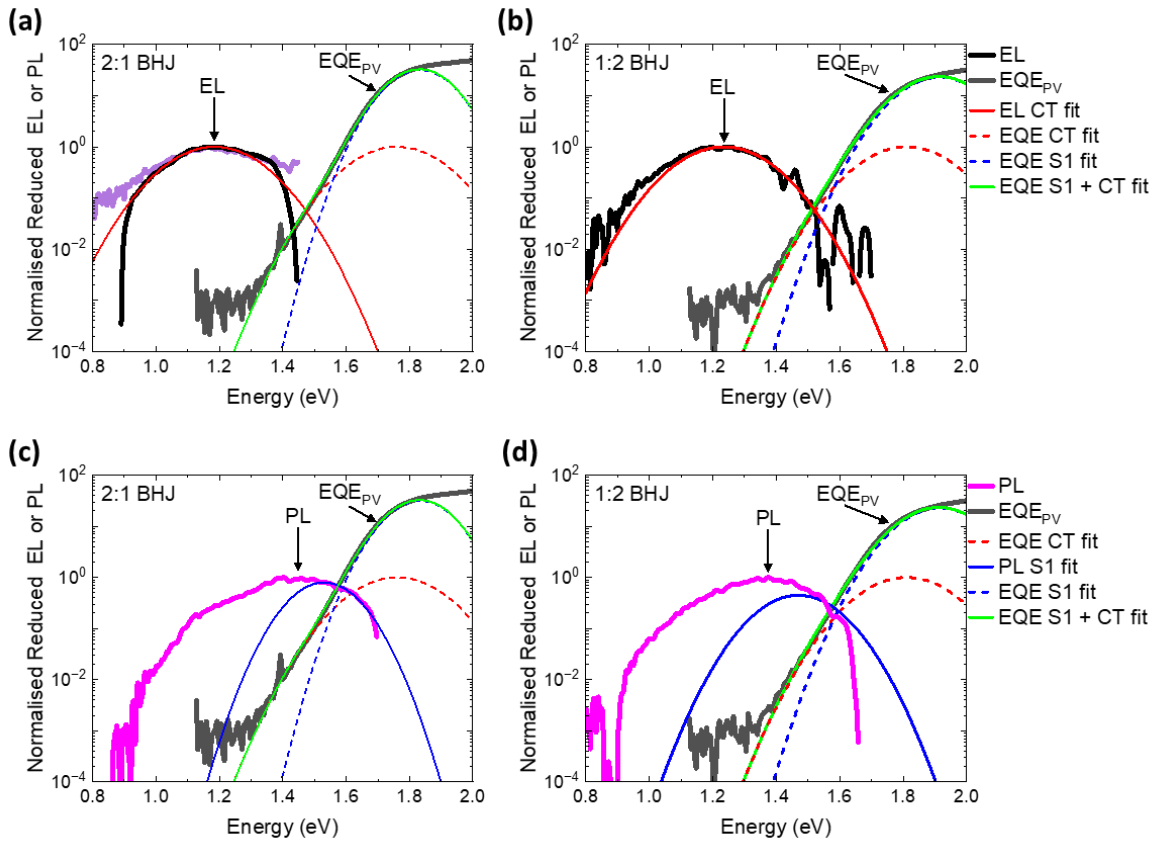


Figure 4.3.16: Normalised reduced EL and EQE_{PV} spectra (**(a)** and **(b)**) and PL and EQE_{PV} spectra (**(c)** and **(d)**) of the 2:1 and 1:2 BHJ, respectively. **(a)** shows the 2:1 EL obtained at injection currents of 14 and 35 mA/cm². Due to the reduced noise, the EL is fitted to the higher injection current. Note the fitting of the PL emission being focused on the high energy tail. The PL spectra are well described by a weighted sum of this high energy tail and the EL emission for both BHJs.

Table 4.3.5 lists the fitting parameters. Reasonably good overall fitting results can be achieved by fitting the CT emission and EQE_{PV} spectra with the same reorganization energy and a shifted E_{CT}. Especially the excitonic feature of the EQE_{PV} (also visible from the shape of the EQE onset) and the larger Stokes shift suggests a broader linewidth of the excitonic state parameterised here as an increase in reorganisation energy (but could be argued to stem from a disorder term instead). Meanwhile the energy of the S1 state is rather similar for the two devices studied here. Drawing a parallel to the similar Urbach energies determined for the absorption tail and the linewidth of either of the two states may be misleading since the Urbach energy is convoluting the absorption of both states.

Table 4.3.5: Fitting parameters used for the fitting of the CT and donor excitonic (S1) emission and absorption in **Figure 4.3.16** and **Figure 4.3.17** (marked with *). The two different fittings of the 1:2 BHJ device illustrate the challenges in giving the correct interpretation of the origin of the

Device	E_{CT} (eV)	λ_{CT} (eV)	E_{S1} (eV)	λ_{S1} (eV)
2:1 BHJ	1.473	0.288	1.68	0.151
1:2 BHJ	1.523	0.288	1.69	0.223
1:2 BHJ*	1.477	0.242	1.69	0.223

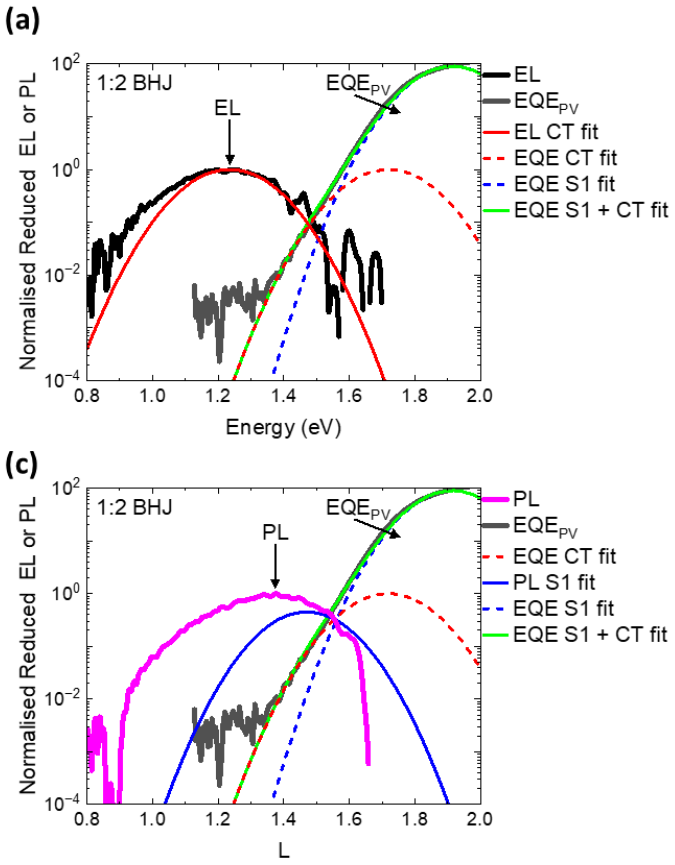


Figure 4.3.17: Alternative fitting assuming similar E_{CT} in the 1:2 BHJ as determined for 2:1 above with a changing reorganisation energy to illustrate the difficulty in determining the fitting parameters reliably. Here a larger weighting is given to the high energy tail of the CT emission justified by the poor background correction.

To illustrate the difficulty in fitting especially the high energetic tail, another scenario with similar CT energy but varied reorganisation energy was fitted for the 1:2 BHJ. Again, reasonably good agreement an be found through rescaling the EQE_{PV} to reproduce the Stokes shift as a result of the changed reorganisation energy. In conclusion, the quality of the data and the fact that the CT absorption cannot be clearly distiguished makes such analyses prone to errors and overinterpretation. The position and the estimated linewidth of the emission

peak and the fitted Urbach energy do however allow to give a rough estimate for the shift in the radiative V_{OC} limit ($\Delta V_{OC, rad}$). A shift of a similar order as the shift of the absorption onset and thereby allows for the interpretation of the kinetic and energetic contribution to voltage losses as described in the main text.

Appendix IV: Varying the Injection Current

As previously noted, reliably fitting the EL spectra recorded at low injection currents presented a challenge. Differentiating between contributions from dynamic and static line broadening additionally would require the collection of temperature dependent data.[110] Different studies have recently found static disorder of the CT states to be linked with increased non-radiative recombination.[32,80] Previously, effects of energetic disorder have also been studied by observing the injection current dependence of the EL spectra.[123,127,128]

Figure 4.3.18 shows the normalised injection-current dependent emission spectra of the 2:1 and 1:2 BHJ devices (deposited at 40˚C), the 5 nm and 15 nm PHJ devices as well as the two 2:1 BHJ devices studied in **Subchapter 4.2** (deposited at RT and 50˚C). The BHJs studied in **Subchapter 4.2** exhibit a comparable EL peak intensity and optical gap compared to the 2:1 BHJ studied in this chapter, despite the changing morphology. As previously discussed, the EL of the bilayers was dominated by the emission of the donor excitonic state even at low injection currents. Interestingly, at increasing injection currents also BHJs show a shift in the emission peak that is most pronounced in the 2:1 devices deposited at elevated substrate temperatures (40 ˚C and 50˚C). **Figure 4.3.19 (a)** summarises the peak shift of the EL emission also in relation to PL spectra dominated by the donor excitonic emission. The magnitude of the observed emission peak shift, especially for the PHJs and the 2:1 BHJ deposited at 50˚C, seem to suggest the origin of the emission shift to lie in the increase of donor PL spectra as the devices no longer are in quasi-thermal equilibrium. A state-filling picture of an exponential DoS leading to an EL peak shift would predict much lower peak shifts than those observed in the 2:1 devices.[123]

Since no absolute EL or PL data could be recorded due to equipment limitations, a comparison of the EL quantum efficiency across the devices is not possible here. However, the change in integrated emission peaks divided by the injection current density can be used to compare the relative change in emissivity for different injection currents throughout the devices. **Figure 4.3.19 (b)** shows the EL quantum efficiency versus the injection current normalised to the

value at the highest injection current. For the PHJs and 2:1 devices this further supports the interpretation of an increasing excitonic emission character since the emission yield of excitonic states is expected to exceed the weakly emitting CT states (quantification of the oscillator strength of both transitions from fitting of the excitonic and CT EQE_{PV} feature is unreliable here). Only the 1:2 BHJ exhibits a near constant EL quantum efficiency as well as the smallest EL peak shift. It is also the only BHJ device exhibiting a significant blue shift in absorption and emission spectra.

In **Subchapter 4.2**, the increase in crystallinity and domain size when depositing devices at an elevated substrate temperature were confirmed by means of GIWAXS and RSoXS data. Such an increased domain size and decrease of amorphous donor domains would be expected to result in a reduction of the donor/acceptor interfacial area. Building on this structural information, a trend of EL peak shift and increase in emissivity with decreasing interfacial area becomes apparent. The changes are most pronounced for the fully segregated 15 nm PHJ, followed by the 2:1 *50C*, 2:1 *40C* and 2:1 *RT* device. Despite the changing behaviour at increased injection current density, the three BHJ devices present a similar photovoltaic gap, lowest injection current EL peak and V_{OC} – demonstrating that the behaviour at high injection current densities does not affect the V_{OC} under 1 sun conditions. Only the PHJ device benefits from the changing interfacial area and shows an increased V_{OC}. This further demonstrates that while the transport properties vary between the different 2:1 BHJs (as evidenced by the differing *FF*), the donor aggregation even in the 2:1 *RT* BHJ is sufficient to dominate the (radiative) recombination under device operating conditions (as evidenced from the similar emission peaks).

The 1:2 device presents a different case. It could be postulated that the decrease in donor content leads to the donor forming poorly phase separated amorphous phases without the redshift in absorption and EL peak intensity observed in the 2:1 devices or PHJ. This would further explain the observations of the increase in a slow current transient as described in **Appendix V** to explain the reduced *FF* in the 1:2 devices.

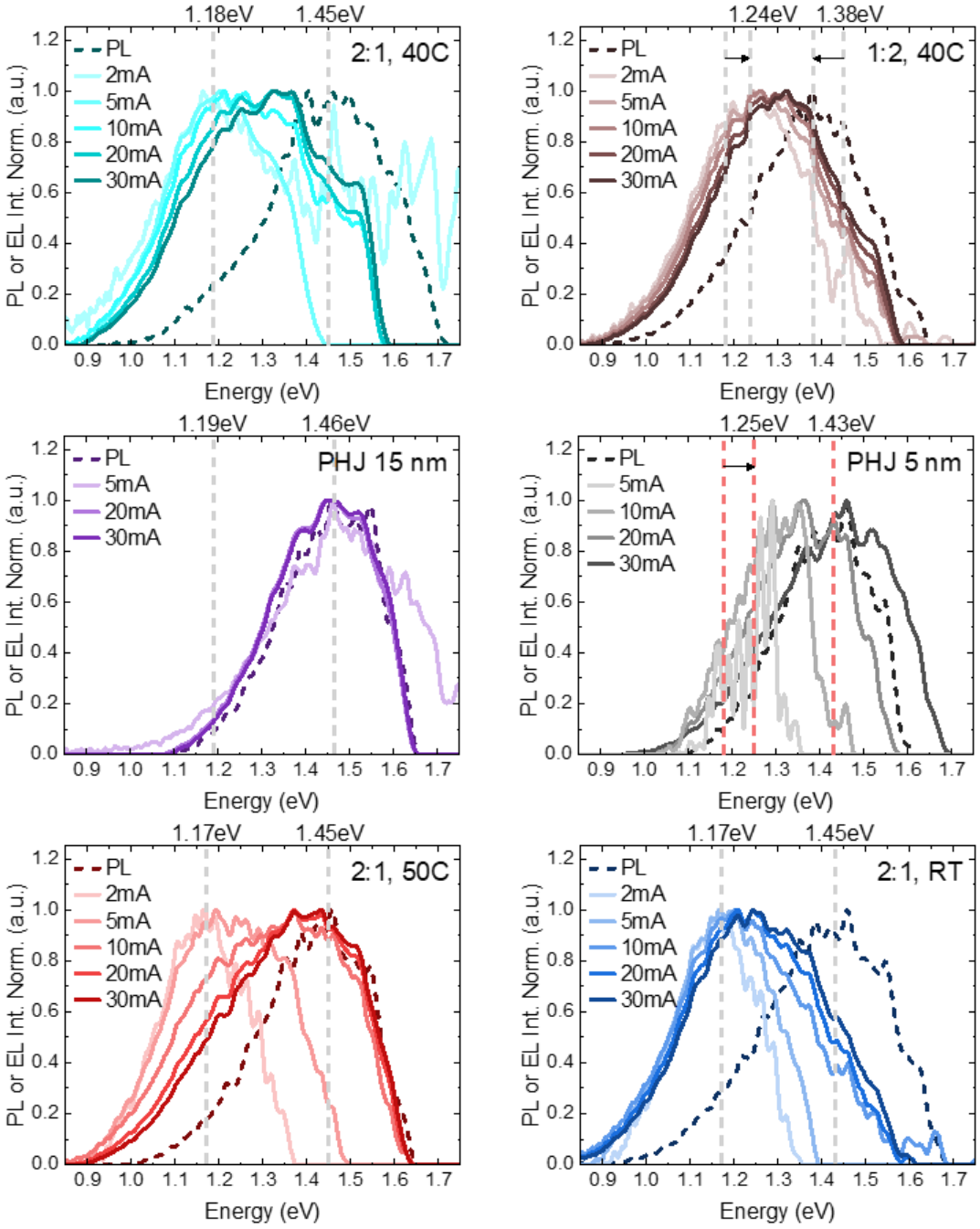


Figure 4.3.18. Normalised electroluminescence and photoluminescence emission spectra for the BHJ and PHJ devices studied in this chapter as well as the BHJ devices studied in **Chapter 3** (RT and 50C). The dashed lines are a guide to the eye marking the position of the low injection current EL and PL emission peaks as well as their shift relative to the 2:1 40C BHJ device (for the 1:2 BHJ and 5 nm PHJ).

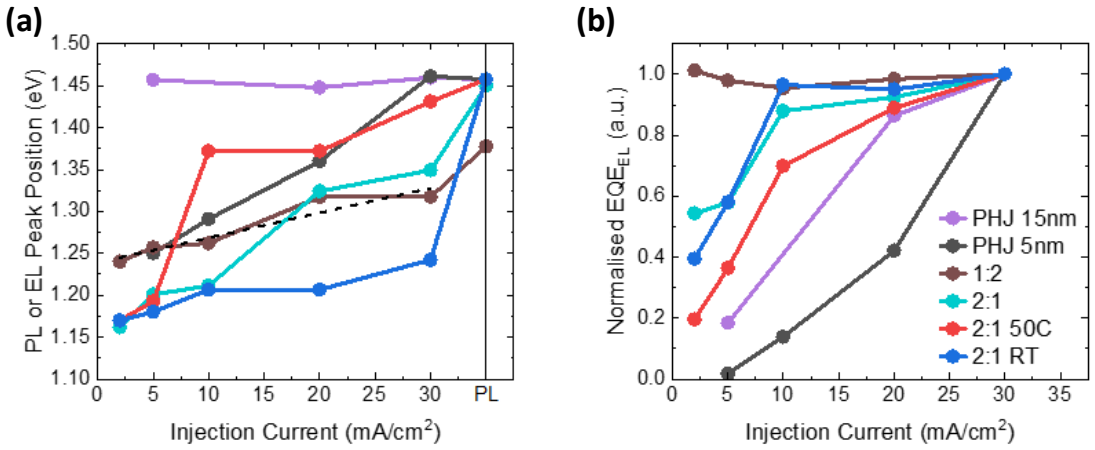


Figure 4.3.19. (a) Shift of the electroluminescence peak position as a function of injection current (equivalent to current densities of 28 to 422 mA/cm²) together with the position of the photoluminescence emission peak. **(b)** Normalised EL quantum yield versus the injection current. The values were calculated by integrating the EL emission peaks and normalising by the value obtained at the highest measured injection current.

Appendix V: Origin of Fill Factor Limitations

Besides the increased recombination rate in the 1:2 BHJ relative to the 2:1 BHJ shown above, the lower *FF* and its stronger light intensity dependence can be related to a reduced mobility. Similar to the discussions in **Subchapter 4.2**, a more pronounced slow phase in short circuit current transients was observed for the 1:2 devices as shown in **Figure 4.3.20**. The fitted biexponential decays were used to calculate the charge extracted in each of the two phases. The results are plotted in **Figure 4.3.21**. While the charge collected in the fast phase is similar for both devices and shows an approximately proportional increase with short circuit current density, the charge collected in the slower phase is significantly increased in the 1:2 BHJ and both devices exhibit a lower slope. The behaviour of the fast phase is indicative of a charge carrier density independent mobility. The latter would indicate an increasing mobility as tail states fill up. In **Subchapter 4.2**, such behaviour was assigned to electron and hole extraction, respectively. An increase in the abundance of amorphous, poorly percolated donor phases could lead to slower current extraction. Similarly, the 1:2 BHJ is expected to exhibit an increase in isolated and/or amorphous donor phases. The reduced *FF* and collection efficiency is therefore assigned to this observation in analogy with **Subchapter 4.2**. This is also in line with the observed blue shift in absorption and emission that may be expected from amorphous donor domains.

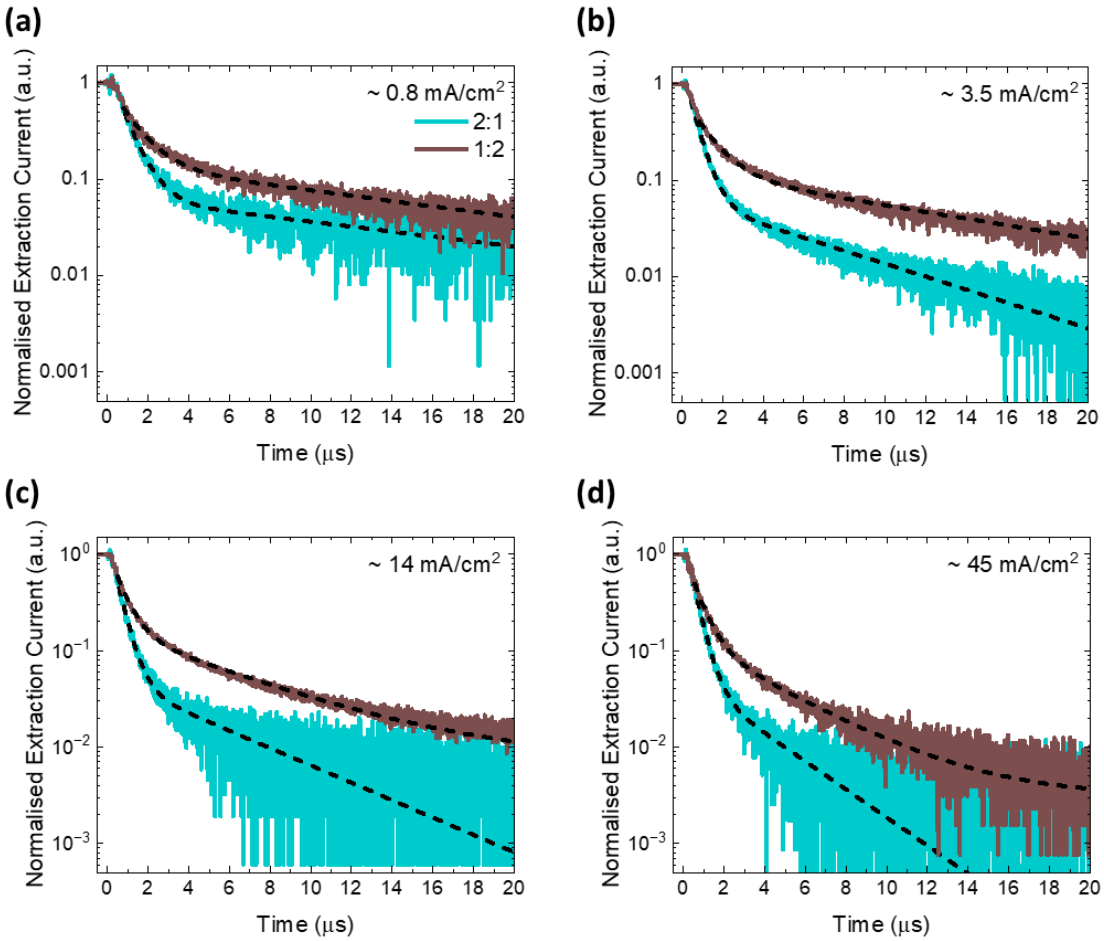


Figure 4.3.20. Charge extraction transients recorded upon switching off the LED light source while the device is kept at short circuit. The transients were recorded at different short circuit current density values of roughly 0.8, 3.5, 14 and 45 mA/cm² (**(a)**, **(b)**, **(c)** and **(d)**, respectively). Fits representing biexponential decays are shown in dashed lines.

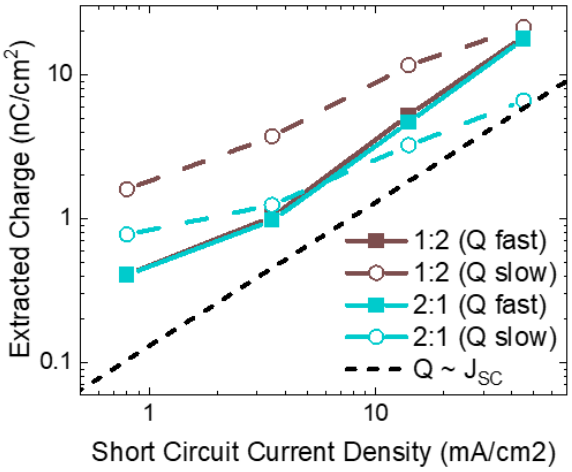


Figure 4.3.21. Extracted charge in the slow and fast phase of the current transients shown above for the 2:1 and 1:2 BHJ. The dashed line signifies a proportionality between the extracted charge and the short circuit current density (equivalent to a power law exponent of 1). The charge extracted from the slow phase exhibits a reduced power law exponent indicative of a charge carrier density dependent mobility related to the filling of tailstates.

4.4. Summary of Results for DCV-V-Fu-Ind-Fu-V:C_{60}

To conclude the study of evaporated solar cells based on DCV-V-Fu-Ind-Fu-V:C60, **Figure 4.4.1** depicts the main conclusions on the relationship between morphology and device functionality. Aggregated donor domains are present in all devices (even deposited at room temperature) except the 1:2 donor acceptor ratio. They cause the observed redshift of the EL emission and absorption and govern the V_{OC}. Meanwhile the presence of amorphous and isolated domains controls the charge collection efficiency due to the slow transport in these energetically disordered domains. The morphology dependent blueshift of the EL emission with increasing injection current appears to correlate with the degree of phase separation. Rather than a state filling effect as previously demonstrated for disordered systems,[128] a shift from CT emission to excitonic emission was observed that may point to emission occurring from non-equilibrated states in the case of highly phase separated (in the extreme case a PHJ) devices. This observation is similar to the previously reported EL shifts in disordered systems of DPI and DBP blended with C_{60}.[123]

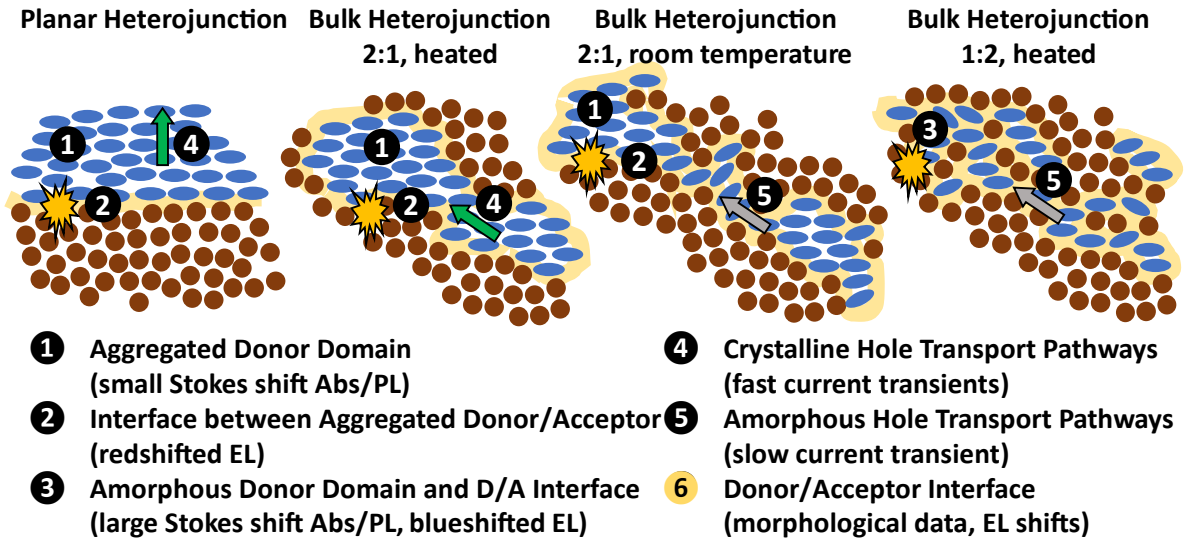


Figure 4.4.1 Schematic depiction of the morphological characteristics and their relation to device functionality.

References

(1) Riede, M.; Spoltore, D.; Leo, K. Organic Solar Cells—The Path to Commercial Success. *Advanced Energy Materials* **2021**, *11* (1), 2002653. https://doi.org/10.1002/aenm.202002653.

(2) *Inauguration ceremony of Heliatek's organic solar film series production*. Heliatek GmbH. https://www.heliatek.com/en/media/news/detail/inauguration-ceremony-of-heliateks-organic-solar-film-series-production/ (accessed 2024-09-25).

(3) *Heliatek achieves IEC 61215 certification for lightweight & flexible HeliaSol® solar film*. Heliatek GmbH. https://www.heliatek.com/en/media/news/detail/heliatek-achieves-iec-61215-certification-for-lightweight-flexible-heliasolr-solar-film/ (accessed 2024-09-25).

(4) Kaienburg, P.; Jungbluth, A.; Habib, I.; Kesava, S. V.; Nyman, M.; Riede, M. K. Assessing the Photovoltaic Quality of Vacuum-Thermal Evaporated Organic Semiconductor Blends. *Advanced Materials* **2022**, *34* (22), 2107584. https://doi.org/10.1002/adma.202107584.

(5) Yang, X.; Loos, J.; Veenstra, S. C.; Verhees, W. J. H.; Wienk, M. M.; Kroon, J. M.; Michels, M. A. J.; Janssen, R. A. J. Nanoscale Morphology of High-Performance Polymer Solar Cells. *Nano Lett.* **2005**, *5* (4), 579–583. https://doi.org/10.1021/nl048120i.

(6) Zhu, L.; Zhang, M.; Zhou, G.; Hao, T.; Xu, J.; Wang, J.; Qiu, C.; Prine, N.; Ali, J.; Feng, W.; Gu, X.; Ma, Z.; Tang, Z.; Zhu, H.; Ying, L.; Zhang, Y.; Liu, F. Efficient Organic Solar Cell with 16.88% Efficiency Enabled by Refined Acceptor Crystallization and Morphology with Improved Charge Transfer and Transport Properties. *Adv. Energy Mater.* **2020**, *10* (18), 1904234. https://doi.org/10.1002/aenm.201904234.

(7) Dong, X.; Jiang, Y.; Sun, L.; Qin, F.; Zhou, X.; Lu, X.; Wang, W.; Zhou, Y. Large-Area Organic Solar Modules with Efficiency Over 14%. *Advanced Functional Materials* **2022**, *32* (15), 2110209. https://doi.org/10.1002/adfm.202110209.

(8) Qin, Y.; Xu, Y.; Peng, Z.; Hou, J.; Ade, H. Low Temperature Aggregation Transitions in N3 and Y6 Acceptors Enable Double-Annealing Method That Yields Hierarchical Morphology and Superior Efficiency in Nonfullerene Organic Solar Cells. *Advanced Functional Materials* **2020**, *30* (46), 2005011. https://doi.org/10.1002/adfm.202005011.

(9) Zhu, W.; Spencer, A. P.; Mukherjee, S.; Alzola, J. M.; Sangwan, V. K.; Amsterdam, S. H.; Swick, S. M.; Jones, L. O.; Heiber, M. C.; Herzing, A. A.; Li, G.; Stern, C. L.; DeLongchamp, D. M.; Kohlstedt, K. L.; Hersam, M. C.; Schatz, G. C.; Wasielewski, M. R.; Chen, L. X.; Facchetti, A.; Marks, T. J. Crystallography, Morphology, Electronic Structure, and Transport in Non-Fullerene/Non-Indacenodithienothiophene Polymer:Y6 Solar Cells. *J. Am. Chem. Soc.* **2020**, *142* (34), 14532–14547. https://doi.org/10.1021/jacs.0c05560.

(10) Zhou, Y.; Taima, T.; Miyadera, T.; Yamanari, T.; Kitamura, M.; Nakatsu, K.; Yoshida, Y. Phase Separation of Co-Evaporated ZnPc:C60 Blend Film for Highly Efficient Organic Photovoltaics. *Appl. Phys. Lett.* **2012**, *100* (23), 233302. https://doi.org/10.1063/1.4726118.

(11) Wang, L.; Guo, S.; Zhou, K.; Ma, W. Control of the Molecular Orientation in Small Molecule-Based Organic Photovoltaics. *Sustainable Energy & Fuels* **2020**, *4* (10), 4934–4955. https://doi.org/10.1039/D0SE00704H.

(12) Bittrich, E.; Domke, J.; Levichkova, M.; Jehnichen, D.; Bittrich, L.; Janke, A.; Formanek, P.; Hübner, R.; Uhlmann, P.; Eichhorn, K.-J.; Forker, R.; Gruenewald, M.; Al-Hussein, M.; Fritz, T.; Walzer, K. Structural Templating of an Organic Solar Cell Absorber by Ellagic Acid To Tune Its Aggregation, Molecular Orientation, and Optical Properties. *ACS Appl. Energy Mater.* **2021**, *4* (12), 14273–14286. https://doi.org/10.1021/acsaem.1c02994.

(13) Kaji, T.; Zhang, M.; Nakao, S.; Iketaki, K.; Yokoyama, K.; Tang, C. W.; Hiramoto, M. Co-Evaporant Induced Crystalline Donor: Acceptor Blends in Organic Solar Cells. *Advanced Materials* **2011**, *23* (29), 3320–3325. https://doi.org/10.1002/adma.201101305.

(14) Kaji, T.; Nakao, S.; Hiramoto, M. Effect of Co-Evaporant Induced Crystallization on Needle Growth of Phthalocyanine Thin Films. *Molecular Crystals and Liquid Crystals* **2013**, *578* (1), 63–67. https://doi.org/10.1080/15421406.2013.804376.

(15) Holzmueller, F.; Wilde, L.; Wölzl, F.; Koerner, C.; Vandewal, K.; Leo, K. Co-Evaporant Induced Crystallization of Zinc Phthalocyanine:C60 Blends for Solar Cells. *Organic Electronics* **2015**, *27*, 133–136. https://doi.org/10.1016/j.orgel.2015.08.031.

(16) Katayama, M.; Kaji, T.; Nakao, S.; Hiramoto, M. Ultra-Thick Organic Pigment Layer Up to 10 Mm Activated by Crystallization in Organic Photovoltaic Cells. *Frontiers in Energy Research* **2020**, *8*.

(17) Ojala, A.; Petersen, A.; Fuchs, A.; Lovrincic, R.; Pölking, C.; Trollmann, J.; Hwang, J.; Lennartz, C.; Reichelt, H.; Höffken, H. W.; Pucci, A.; Erk, P.; Kirchartz, T.; Würthner, F. Merocyanine/C60 Planar Heterojunction Solar Cells: Effect of Dye Orientation on Exciton Dissociation and Solar Cell Performance. *Advanced Functional Materials* **2012**, *22* (1), 86–96. https://doi.org/10.1002/adfm.201101697.

(18) Limbu, S.; Park, K.-B.; Wu, J.; Cha, H.; Yun, S.; Lim, S.-J.; Yan, H.; Luke, J.; Ryu, G.; Heo, C.-J.; Kim, S.; Jin, Y. W.; Durrant, J. R.; Kim, J.-S. Identifying the Molecular Origins of High-Performance in Organic Photodetectors Based on Highly Intermixed Bulk Heterojunction Blends. *ACS Nano* **2021**, 12.

(19) Shahiduzzaman, Md.; Horikawa, T.; Hirayama, T.; Nakano, M.; Karakawa, M.; Takahashi, K.; Nunzi, J.-M.; Taima, T. Switchable Crystal Phase and Orientation of Evaporated Zinc Phthalocyanine Films for Efficient Organic Photovoltaics. *J. Phys. Chem. C* **2020**, *124* (39), 21338–21345. https://doi.org/10.1021/acs.jpcc.0c07010.

(20) Pfuetzner, S.; Meiss, J.; Petrich, A.; Riede, M.; Leo, K. Thick C60:ZnPc Bulk Heterojunction Solar Cells with Improved Performance by Film Deposition on Heated Substrates. *Applied Physics Letters* **2009**, *94* (25), 253303. https://doi.org/10.1063/1.3154554.

(21) Kirchartz, T.; Agostinelli, T.; Campoy-Quiles, M.; Gong, W.; Nelson, J. Understanding the Thickness-Dependent Performance of Organic Bulk Heterojunction Solar Cells: The Influence of Mobility, Lifetime, and Space Charge. *J. Phys. Chem. Lett.* **2012**, *3* (23), 3470–3475. https://doi.org/10.1021/jz301639y.

(22) Firdaus, Y.; Le Corre, V. M.; Khan, J. I.; Kan, Z.; Laquai, F.; Beaujuge, P. M.; Anthopoulos, T. D. Key Parameters Requirements for Non-Fullerene-Based Organic Solar Cells with Power Conversion Efficiency >20%. *Advanced Science* **2019**, *6* (9), 1802028. https://doi.org/10.1002/advs.201802028.

(23) Pivrikas, A.; Juška, G.; Mozer, A. J.; Scharber, M.; Arlauskas, K.; Sariciftci, N. S.; Stubb, H.; Österbacka, R. Bimolecular Recombination Coefficient as a Sensitive Testing Parameter for Low-Mobility Solar-Cell Materials. *Phys. Rev. Lett.* **2005**, *94* (17), 176806. https://doi.org/10.1103/PhysRevLett.94.176806.

(24) Deibel, C. Charge Carrier Dissociation and Recombination in Polymer Solar Cells. *physica status solidi (a)* **2009**, *206* (12), 2731–2736. https://doi.org/10.1002/pssa.200925282.

(25) Sun, K.; Xiao, Z.; Lu, S.; Zajaczkowski, W.; Pisula, W.; Hanssen, E.; White, J. M.; Williamson, R. M.; Subbiah, J.; Ouyang, J.; Holmes, A. B.; Wong, W. W. H.; Jones, D. J. A Molecular Nematic Liquid Crystalline Material for High-Performance Organic Photovoltaics. *Nat Commun* **2015**, *6* (1), 6013. https://doi.org/10.1038/ncomms7013.

(26) Jin, Y.; Chen, Z.; Dong, S.; Zheng, N.; Ying, L.; Jiang, X.-F.; Liu, F.; Huang, F.; Cao, Y. A Novel Naphtho[1,2-c:5,6-C′]Bis([1,2,5]Thiadiazole)-Based Narrow-Bandgap π-Conjugated Polymer with Power Conversion Efficiency Over 10%. *Advanced Materials* **2016**, *28* (44), 9811–9818. https://doi.org/10.1002/adma.201603178.

(27) Schwarz, K. N.; Geraghty, P. B.; Mitchell, V. D.; Khan, S.-U.-Z.; Sandberg, O. J.; Zarrabi, N.; Kudisch, B.; Subbiah, J.; Smith, T. A.; Rand, B. P.; Armin, A.; Scholes, G. D.; Jones, D. J.; Ghiggino, K. P. Reduced Recombination and Capacitor-like Charge Buildup in an Organic Heterojunction. *J. Am. Chem. Soc.* **2020**, *142* (5), 2562–2571. https://doi.org/10.1021/jacs.9b12526.

(28) Bartesaghi, D.; Pérez, I. del C.; Kniepert, J.; Roland, S.; Turbiez, M.; Neher, D.; Koster, L. J. A. Competition between Recombination and Extraction of Free Charges Determines the Fill Factor of Organic Solar Cells. *Nat Commun* **2015**, *6* (1), 7083. https://doi.org/10.1038/ncomms8083.

(29) Stephen, M.; Genevičius, K.; Juška, G.; Arlauskas, K.; Hiorns, R. C. Charge Transport and Its Characterization Using Photo-CELIV in Bulk Heterojunction Solar Cells. *Polymer International* **2017**, *66* (1), 13–25. https://doi.org/10.1002/pi.5274.

(30) Wu, J.; Lee, J.; Chin, Y.-C.; Yao, H.; Cha, H.; Luke, J.; Hou, J.; Kim, J.-S.; Durrant, J. R. Exceptionally Low Charge Trapping Enables Highly Efficient Organic Bulk Heterojunction Solar Cells. *Energy Environ. Sci.* **2020**, *13* (8), 2422–2430. https://doi.org/10.1039/D0EE01338B.

(31) Wu, J.; Luke, J.; Lee, H. K. H.; Shakya Tuladhar, P.; Cha, H.; Jang, S.-Y.; Tsoi, W. C.; Heeney, M.; Kang, H.; Lee, K.; Kirchartz, T.; Kim, J.-S.; Durrant, J. R. Tail State Limited Photocurrent Collection of Thick Photoactive Layers in Organic Solar Cells. *Nature Communications* **2019**, *10* (1), 5159. https://doi.org/10.1038/s41467-019-12951-7.

(32) Hosseini, S. M.; Wilken, S.; Sun, B.; Huang, F.; Jeong, S. Y.; Woo, H. Y.; Coropceanu, V.; Shoaee, S. Relationship between Energetic Disorder and Reduced Recombination of Free Carriers in Organic Solar Cells. *Advanced Energy Materials n/a* (n/a), 2203576. https://doi.org/10.1002/aenm.202203576.

(33) Heiber, M. C.; Okubo, T.; Ko, S.-J.; Luginbuhl, B. R.; Ran, N. A.; Wang, M.; Wang, H.; Uddin, M. A.; Woo, H. Y.; Bazan, G. C.; Nguyen, T.-Q. Measuring the Competition between Bimolecular Charge Recombination and Charge Transport in Organic Solar Cells under Operating Conditions. *Energy Environ. Sci.* **2018**, *11* (10), 3019–3032. https://doi.org/10.1039/C8EE01559G.

(34) Kaienburg, P.; Rau, U.; Kirchartz, T. Extracting Information about the Electronic Quality of Organic Solar-Cell Absorbers from Fill Factor and Thickness. *Phys. Rev. Appl.* **2016**, *6* (2), 024001. https://doi.org/10.1103/PhysRevApplied.6.024001.

(35) Levichkova, M.; Wynands, D.; Levin, A. A.; Walzer, K.; Hildebrandt, D.; Pfeiffer, M.; Janonis, V.; Pranaitis, M.; Kažukauskas, V.; Leo, K.; Riede, M. Dicyanovinyl Sexithiophene as Donor Material in Organic Planar Heterojunction Solar Cells: Morphological, Optical, and Electrical Properties. *Organic Electronics* **2011**, *12* (12), 2243–2252. https://doi.org/10.1016/j.orgel.2011.09.022.

(36) Sánchez-Díaz, A.; Burtone, L.; Riede, M.; Palomares, E. Measurements of Efficiency Losses in Blend and Bilayer-Type Zinc Phthalocyanine/C60 High-Vacuum-Processed Organic Solar Cells. *J. Phys. Chem. C* **2012**, *116* (31), 16384–16390. https://doi.org/10.1021/jp3054422.

(37) Saladina, M.; Wöpke, C.; Göhler, C.; Ramirez, I.; Gerdes, O.; Liu, C.; Li, N.; Heumüller, T.; Brabec, C. J.; Walzer, K.; Pfeiffer, M.; Deibel, C. Power-Law Density of States in Organic Solar Cells Revealed by the Open-Circuit Voltage Dependence of the Ideality Factor. arXiv October 20, 2022. http://arxiv.org/abs/2210.11208 (accessed 2023-02-15).

(38) Kaienburg, P.; Bristow, H.; Jungbluth, A.; Habib, I.; McCulloch, I.; Beljonne, D.; Riede, M. Vacuum-Deposited Donors for Low-Voltage-Loss Nonfullerene Organic Solar Cells. *ACS Appl. Mater. Interfaces* **2023**, *15* (26), 31684–31691. https://doi.org/10.1021/acsami.3c04282.

(39) Yuan, J.; Zhang, Y.; Zhou, L.; Zhang, G.; Yip, H.-L.; Lau, T.-K.; Lu, X.; Zhu, C.; Peng, H.; Johnson, P. A.; Leclerc, M.; Cao, Y.; Ulanski, J.; Li, Y.; Zou, Y. Single-Junction Organic Solar Cell with over 15% Efficiency Using Fused-Ring Acceptor with Electron-Deficient Core. *Joule* **2019**. https://doi.org/10.1016/j.joule.2019.01.004.

(40) Pacalaj, R. A.; Dong, Y.; Ramirez, I.; MacKenzie, R.; Hosseini, S. M.; Bittrich, E.; Heger, J. E.; Kaienburg, P.; Mukherjee, S.; Wu, J.; Riede, M.; Ade, H.; Müller-Buschbaum, P.; Pfeiffer, M.; Durrant, J. From Generation to Collection – Impact of Deposition Temperature on Charge Carrier Dynamics of High-Performance Vacuum-Processed Organic Solar Cells. ChemRxiv August 14, 2024. https://doi.org/10.26434/chemrxiv-2024-zsf3n.

(41) Griffith, O. L.; Liu, X.; Amonoo, J. A.; Djurovich, P. I.; Thompson, M. E.; Green, P. F.; Forrest, S. R. Charge Transport and Exciton Dissociation in Organic Solar Cells Consisting of Dipolar Donors Mixed with ${\mathrm{C}}_{70}$. *Phys. Rev. B* **2015**, *92* (8), 085404. https://doi.org/10.1103/PhysRevB.92.085404.

(42) Jiang, X.; Grott, S.; Körstgens, V.; Wienhold, K. S.; Li, Z.; Zhang, J.; Everett, C. R.; Schwartzkopf, M.; Roth, S. V.; Müller-Buschbaum, P. Film Formation Kinetics of Polymer Donor and Nonfullerene Acceptor Active Layers During Printing Out of 1,2,4-

Trimethylbenzene in Ambient Conditions. *Solar RRL* **2023**, *7* (6), 2201077. https://doi.org/10.1002/solr.202201077.

(43) Schünemann, C.; Wynands, D.; Eichhorn, K.-J.; Stamm, M.; Leo, K.; Riede, M. Evaluation and Control of the Orientation of Small Molecules for Strongly Absorbing Organic Thin Films. *J. Phys. Chem. C* **2013**, *117* (22), 11600–11609. https://doi.org/10.1021/jp400604j.

(44) Heger, J. E.; Chen, W.; Yin, S.; Li, N.; Körstgens, V.; Brett, C. J.; Ohm, W.; Roth, S. V.; Müller-Buschbaum, P. Low-Temperature and Water-Based Biotemplating of Nanostructured Foam-Like Titania Films Using ß-Lactoglobulin. *Advanced Functional Materials* **2022**, *32* (20), 2113080. https://doi.org/10.1002/adfm.202113080.

(45) Peng, Z.; Ye, L.; Ade, H. Understanding, Quantifying, and Controlling the Molecular Ordering of Semiconducting Polymers: From Novices to Experts and Amorphous to Perfect Crystals. *Materials Horizons* **2022**, *9* (2), 577–606. https://doi.org/10.1039/D0MH00837K.

(46) Reus, M. A.; Reb, L. K.; Weinzierl, A. F.; Weindl, C. L.; Guo, R.; Xiao, T.; Schwartzkopf, M.; Chumakov, A.; Roth, S. V.; Müller-Buschbaum, P. Time-Resolved Orientation and Phase Analysis of Lead Halide Perovskite Film Annealing Probed by In Situ GIWAXS. *Advanced Optical Materials* **2022**, *10* (14), 2102722. https://doi.org/10.1002/adom.202102722.

(47) Collins, B. A.; Gann, E. Resonant Soft X-Ray Scattering in Polymer Science. *Journal of Polymer Science* **2022**, *60* (7), 1199–1243. https://doi.org/10.1002/pol.20210414.

(48) Collins, B. A.; Li, Z.; Tumbleston, J. R.; Gann, E.; McNeill, C. R.; Ade, H. Absolute Measurement of Domain Composition and Nanoscale Size Distribution Explains Performance in PTB7:PC71BM Solar Cells. *Advanced Energy Materials* **2013**, *3* (1), 65–74. https://doi.org/10.1002/aenm.201200377.

(49) Meerheim, R.; Körner, C.; Leo, K. Highly Efficient Organic Multi-Junction Solar Cells with a Thiophene Based Donor Material. *Applied Physics Letters* **2014**, *105* (6), 063306. https://doi.org/10.1063/1.4893012.

(50) Wynands, D.; Levichkova, M.; Riede, M.; Pfeiffer, M.; Baeuerle, P.; Rentenberger, R.; Denner, P.; Leo, K. Correlation between Morphology and Performance of Low Bandgap Oligothiophene:C60 Mixed Heterojunctions in Organic Solar Cells. *Journal of Applied Physics* **2010**, *107* (1), 014517. https://doi.org/10.1063/1.3271407.

(51) Cha, H.; Zheng, Y.; Dong, Y.; Lee, H. H.; Wu, J.; Bristow, H.; Zhang, J.; Lee, H. K. H.; Tsoi, W. C.; Bakulin, A. A.; McCulloch, I.; Durrant, J. R. Exciton and Charge Carrier Dynamics in Highly Crystalline PTQ10:IDIC Organic Solar Cells. *Advanced Energy Materials* **2020**, *10* (38), 2001149. https://doi.org/10.1002/aenm.202001149.

(52) Xiao, B.; Calado, P.; MacKenzie, R. C. I.; Kirchartz, T.; Yan, J.; Nelson, J. Relationship between Fill Factor and Light Intensity in Solar Cells Based on Organic Disordered Semiconductors: The Role of Tail States. *Phys. Rev. Applied* **2020**, *14* (2), 024034. https://doi.org/10.1103/PhysRevApplied.14.024034.

(53) Shuttle, C. G.; Maurano, A.; Hamilton, R.; O'Regan, B.; de Mello, J. C.; Durrant, J. R. Charge Extraction Analysis of Charge Carrier Densities in a Polythiophene/Fullerene

Solar Cell: Analysis of the Origin of the Device Dark Current. *Appl. Phys. Lett.* **2008**, *93* (18), 183501. https://doi.org/10.1063/1.3006316.

(54) Shuttle, C. G.; O'Regan, B.; Ballantyne, A. M.; Nelson, J.; Bradley, D. D. C.; de Mello, J.; Durrant, J. R. Experimental Determination of the Rate Law for Charge Carrier Decay in a Polythiophene: Fullerene Solar Cell. *Appl. Phys. Lett.* **2008**, *92* (9), 093311. https://doi.org/10.1063/1.2891871.

(55) Foertig, A.; Wagenpfahl, A.; Gerbich, T.; Cheyns, D.; Dyakonov, V.; Deibel, C. Nongeminate Recombination in Planar and Bulk Heterojunction Organic Solar Cells. *Advanced Energy Materials* **2012**, *2* (12), 1483–1489. https://doi.org/10.1002/aenm.201200718.

(56) Rauh, D.; Deibel, C.; Dyakonov, V. Charge Density Dependent Nongeminate Recombination in Organic Bulk Heterojunction Solar Cells. *Advanced Functional Materials* **2012**, *22* (16), 3371–3377. https://doi.org/10.1002/adfm.201103118.

(57) Kirchartz, T.; Nelson, J. Meaning of Reaction Orders in Polymer:Fullerene Solar Cells. *Physical Review B* **2012**, *86* (16). https://doi.org/10.1103/PhysRevB.86.165201.

(58) Perdigón-Toro, L.; Phuong, L. Q.; Eller, F.; Freychet, G.; Saglamkaya, E.; Khan, J. I.; Wei, Q.; Zeiske, S.; Kroh, D.; Wedler, S.; Köhler, A.; Armin, A.; Laquai, F.; Herzig, E. M.; Zou, Y.; Shoaee, S.; Neher, D. Understanding the Role of Order in Y-Series Non-Fullerene Solar Cells to Realize High Open-Circuit Voltages. *Advanced Energy Materials* **2022**, *12* (12), 2103422. https://doi.org/10.1002/aenm.202103422.

(59) Vollbrecht, J.; Brus, V. V.; Ko, S.-J.; Lee, J.; Karki, A.; Cao, D. X.; Cho, K.; Bazan, G. C.; Nguyen, T.-Q. Quantifying the Nongeminate Recombination Dynamics in Nonfullerene Bulk Heterojunction Organic Solar Cells. *Advanced Energy Materials* **2019**, *9* (32), 1901438. https://doi.org/10.1002/aenm.201901438.

(60) Shuttle, C. G.; Hamilton, R.; Nelson, J.; O'Regan, B. C.; Durrant, J. R. Measurement of Charge-Density Dependence of Carrier Mobility in an Organic Semiconductor Blend. *Advanced Functional Materials* **2010**, *20* (5), 698–702. https://doi.org/10.1002/adfm.200901734.

(61) Röhr, J. A.; Kirchartz, T.; Nelson, J. On the Correct Interpretation of the Low Voltage Regime in Intrinsic Single-Carrier Devices. *J. Phys.: Condens. Matter* **2017**, *29* (20), 205901. https://doi.org/10.1088/1361-648X/aa66cc.

(62) Röhr, J. A.; Moia, D.; Haque, S. A.; Kirchartz, T.; Nelson, J. Exploring the Validity and Limitations of the Mott–Gurney Law for Charge-Carrier Mobility Determination of Semiconducting Thin-Films. *J. Phys.: Condens. Matter* **2018**, *30* (10), 105901. https://doi.org/10.1088/1361-648X/aaabad.

(63) Street, R. A. Localized State Distribution and Its Effect on Recombination in Organic Solar Cells. *Phys. Rev. B* **2011**, *84* (7), 075208. https://doi.org/10.1103/PhysRevB.84.075208.

(64) MacKenzie, R. C. I.; Shuttle, C. G.; Chabinyc, M. L.; Nelson, J. Extracting Microscopic Device Parameters from Transient Photocurrent Measurements of P3HT:PCBM Solar Cells. *Advanced Energy Materials* **2012**, *2* (6), 662–669. https://doi.org/10.1002/aenm.201100709.

(65) MacKenzie, R. C. I.; Shuttle, C. G.; Dibb, G. F.; Treat, N.; von Hauff, E.; Robb, M. J.; Hawker, C. J.; Chabinyc, M. L.; Nelson, J. Interpreting the Density of States Extracted from Organic Solar Cells Using Transient Photocurrent Measurements. *J. Phys. Chem. C* **2013**, *117* (24), 12407–12414. https://doi.org/10.1021/jp4010828.

(66) Bernardo, B.; Cheyns, D.; Verreet, B.; Schaller, R. D.; Rand, B. P.; Giebink, N. C. Delocalization and Dielectric Screening of Charge Transfer States in Organic Photovoltaic Cells. *Nat Commun* **2014**, *5*, 3245. https://doi.org/10.1038/ncomms4245.

(67) Tscheuschner, S.; Bässler, H.; Huber, K.; Köhler, A. A Combined Theoretical and Experimental Study of Dissociation of Charge Transfer States at the Donor–Acceptor Interface of Organic Solar Cells. *J. Phys. Chem. B* **2015**, *119* (32), 10359–10371. https://doi.org/10.1021/acs.jpcb.5b05138.

(68) Shoaee, S.; Eng, M. P.; Espíldora, E.; Delgado, J. L.; Campo, B.; Martín, N.; Vanderzande, D.; Durrant, J. R. Influence of Nanoscale Phase Separation on Geminate versus Bimolecular Recombination in P3HT:Fullerene Blend Films. *Energy Environ. Sci.* **2010**, *3* (7), 971–976. https://doi.org/10.1039/C003394D.

(69) Dimitrov, S. D.; Azzouzi, M.; Wu, J.; Yao, J.; Dong, Y.; Tuladhar, P. S.; Schroeder, B. C.; Bittner, E. R.; McCulloch, I.; Nelson, J.; Durrant, J. R. Spectroscopic Investigation of the Effect of Microstructure and Energetic Offset on the Nature of Interfacial Charge Transfer States in Polymer: Fullerene Blends. *J. Am. Chem. Soc.* **2019**, *141* (11), 4634–4643. https://doi.org/10.1021/jacs.8b11484.

(70) Yao, J.; Kirchartz, T.; Vezie, M. S.; Faist, M. A.; Gong, W.; He, Z.; Wu, H.; Troughton, J.; Watson, T.; Bryant, D.; Nelson, J. Quantifying Losses in Open-Circuit Voltage in Solution-Processable Solar Cells. *Phys. Rev. Appl.* **2015**, *4* (1), 014020. https://doi.org/10.1103/PhysRevApplied.4.014020.

(71) Zhou, Z.; Xu, S.; Song, J.; Jin, Y.; Yue, Q.; Qian, Y.; Liu, F.; Zhang, F.; Zhu, X. High-Efficiency Small-Molecule Ternary Solar Cells with a Hierarchical Morphology Enabled by Synergizing Fullerene and Non-Fullerene Acceptors. *Nat Energy* **2018**, *3* (11), 952–959. https://doi.org/10.1038/s41560-018-0234-9.

(72) Burke, T. M.; Sweetnam, S.; Vandewal, K.; McGehee, M. D. Beyond Langevin Recombination: How Equilibrium Between Free Carriers and Charge Transfer States Determines the Open-Circuit Voltage of Organic Solar Cells. *Advanced Energy Materials* **2015**, *5* (11). https://doi.org/10.1002/aenm.201500123.

(73) Heiber, M. C.; Baumbach, C.; Dyakonov, V.; Deibel, C. Encounter-Limited Charge-Carrier Recombination in Phase-Separated Organic Semiconductor Blends. *Phys. Rev. Lett.* **2015**, *114* (13), 136602. https://doi.org/10.1103/PhysRevLett.114.136602.

(74) Kaienburg, P.; Jungbluth, A.; Habib, I.; Kesava, S. V.; Nyman, M.; Riede, M. K. Assessing the Photovoltaic Quality of Vacuum-Thermal Evaporated Organic Semiconductor Blends. *Advanced Materials n/a* (n/a), 2107584. https://doi.org/10.1002/adma.202107584.

(75) Hofacker, A.; Neher, D. Dispersive and Steady-State Recombination in Organic Disordered Semiconductors. *Phys. Rev. B* **2017**, *96* (24), 245204. https://doi.org/10.1103/PhysRevB.96.245204.

(76) Kiermasch, D.; Baumann, A.; Fischer, M.; Dyakonov, V.; Tvingstedt, K. Revisiting Lifetimes from Transient Electrical Characterization of Thin Film Solar Cells; a Capacitive Concern Evaluated for Silicon, Organic and Perovskite Devices. *Energy & Environmental Science* **2018**, *11* (3), 629–640. https://doi.org/10.1039/C7EE03155F.

(77) Clarke, T. M.; Jamieson, F. C.; Durrant, J. R. Transient Absorption Studies of Bimolecular Recombination Dynamics in Polythiophene/Fullerene Blend Films. *J. Phys. Chem. C* **2009**, *113* (49), 20934–20941. https://doi.org/10.1021/jp909442s.

(78) Maurano, A.; Shuttle, C. G.; Hamilton, R.; Ballantyne, A. M.; Nelson, J.; Zhang, W.; Heeney, M.; Durrant, J. R. Transient Optoelectronic Analysis of Charge Carrier Losses in a Selenophene/Fullerene Blend Solar Cell. *J. Phys. Chem. C* **2011**, *115* (13), 5947–5957. https://doi.org/10.1021/jp109697w.

(79) Melianas, A.; Pranculis, V.; Spoltore, D.; Benduhn, J.; Inganäs, O.; Gulbinas, V.; Vandewal, K.; Kemerink, M. Charge Transport in Pure and Mixed Phases in Organic Solar Cells. *Advanced Energy Materials* **2017**, *7* (20), 1700888. https://doi.org/10.1002/aenm.201700888.

(80) Khan, S.-U.-Z.; Bertrandie, J.; Gui, M.; Sharma, A.; Alsufyani, W.; Gorenflot, J. F.; Laquai, F.; Baran, D.; Rand, B. P. Quantifying the Effect of Energetic Disorder on Organic Solar Cell Energy Loss. *Joule* **2022**. https://doi.org/10.1016/j.joule.2022.10.012.

(81) Fitzner, R.; Mena-Osteritz, E.; Mishra, A.; Schulz, G.; Reinold, E.; Weil, M.; Körner, C.; Ziehlke, H.; Elschner, C.; Leo, K.; Riede, M.; Pfeiffer, M.; Uhrich, C.; Bäuerle, P. Correlation of π-Conjugated Oligomer Structure with Film Morphology and Organic Solar Cell Performance. *J. Am. Chem. Soc.* **2012**, *134* (27), 11064–11067. https://doi.org/10.1021/ja302320c.

(82) Meredith, P.; Armin, A. Scaling of next Generation Solution Processed Organic and Perovskite Solar Cells. *Nat Commun* **2018**, *9* (1), 5261. https://doi.org/10.1038/s41467-018-05514-9.

(83) Meerheim, R.; Körner, C.; Oesen, B.; Leo, K. 10.4% Efficient Triple Organic Solar Cells Containing near Infrared Absorbers. *Appl. Phys. Lett.* **2016**, *108* (10), 103302. https://doi.org/10.1063/1.4943653.

(84) Cui, Y.; Xu, Y.; Yao, H.; Bi, P.; Hong, L.; Zhang, J.; Zu, Y.; Zhang, T.; Qin, J.; Ren, J.; Chen, Z.; He, C.; Hao, X.; Wei, Z.; Hou, J. Single-Junction Organic Photovoltaic Cell with 19% Efficiency. *Advanced Materials* **2021**, *33* (41), 2102420. https://doi.org/10.1002/adma.202102420.

(85) Sun, R.; Wu, Y.; Yang, X.; Gao, Y.; Chen, Z.; Li, K.; Qiao, J.; Wang, T.; Guo, J.; Liu, C.; Hao, X.; Zhu, H.; Min, J. Single-Junction Organic Solar Cells with 19.17% Efficiency Enabled by Introducing One Asymmetric Guest Acceptor. *Advanced Materials* **2022**, *34* (26), 2110147. https://doi.org/10.1002/adma.202110147.

(86) Zhu, L.; Zhang, M.; Xu, J.; Li, C.; Yan, J.; Zhou, G.; Zhong, W.; Hao, T.; Song, J.; Xue, X.; Zhou, Z.; Zeng, R.; Zhu, H.; Chen, C.-C.; MacKenzie, R. C. I.; Zou, Y.; Nelson, J.; Zhang, Y.; Sun, Y.; Liu, F. Single-Junction Organic Solar Cells with over 19% Efficiency Enabled by a Refined Double-Fibril Network Morphology. *Nat. Mater.* **2022**, *21* (6), 656–663. https://doi.org/10.1038/s41563-022-01244-y.

(87) Li, T.; Meyer, T.; Ma, Z.; Benduhn, J.; Körner, C.; Zeika, O.; Vandewal, K.; Leo, K. Small Molecule Near-Infrared Boron Dipyrromethene Donors for Organic Tandem Solar Cells. *J. Am. Chem. Soc.* **2017**, *139* (39), 13636–13639. https://doi.org/10.1021/jacs.7b07887.

(88) Bailey-Salzman, R. F.; Rand, B. P.; Forrest, S. R. Near-Infrared Sensitive Small Molecule Organic Photovoltaic Cells Based on Chloroaluminum Phthalocyanine. *Applied Physics Letters* **2007**, *91* (1), 013508. https://doi.org/10.1063/1.2752992.

(89) Vasseur, K.; Rand, B. P.; Cheyns, D.; Froyen, L.; Heremans, P. Structural Evolution of Evaporated Lead Phthalocyanine Thin Films for Near-Infrared Sensitive Solar Cells. *Chem. Mater.* **2011**, *23* (3), 886–895. https://doi.org/10.1021/cm102329v.

(90) Mueller, T.; Gresser, R.; Leo, K.; Riede, M. Organic Solar Cells Based on a Novel Infrared Absorbing Aza-Bodipy Dye. *Solar Energy Materials and Solar Cells* **2012**, *99*, 176–181. https://doi.org/10.1016/j.solmat.2011.11.006.

(91) Kraner, S.; Widmer, J.; Benduhn, J.; Hieckmann, E.; Jägeler-Hoheisel, T.; Ullbrich, S.; Schütze, D.; Sebastian Radke, K.; Cuniberti, G.; Ortmann, F.; Lorenz-Rothe, M.; Meerheim, R.; Spoltore, D.; Vandewal, K.; Koerner, C.; Leo, K. Influence of Side Groups on the Performance of Infrared Absorbing Aza-BODIPY Organic Solar Cells. *physica status solidi (a)* **2015**, *212* (12), 2747–2753. https://doi.org/10.1002/pssa.201532385.

(92) Li, T.; Benduhn, J.; Qiao, Z.; Liu, Y.; Li, Y.; Shivhare, R.; Jaiser, F.; Wang, P.; Ma, J.; Zeika, O.; Neher, D.; Mannsfeld, S. C. B.; Ma, Z.; Vandewal, K.; Leo, K. Effect of H- and J-Aggregation on the Photophysical and Voltage Loss of Boron Dipyrromethene Small Molecules in Vacuum-Deposited Organic Solar Cells. *J. Phys. Chem. Lett.* **2019**, *10* (11), 2684–2691. https://doi.org/10.1021/acs.jpclett.9b01222.

(93) Lin, L.-Y.; Chen, Y.-H.; Huang, Z.-Y.; Lin, H.-W.; Chou, S.-H.; Lin, F.; Chen, C.-W.; Liu, Y.-H.; Wong, K.-T. A Low-Energy-Gap Organic Dye for High-Performance Small-Molecule Organic Solar Cells. *J. Am. Chem. Soc.* **2011**, *133* (40), 15822–15825. https://doi.org/10.1021/ja205126t.

(94) Chen, Y.-H.; Lin, L.-Y.; Lu, C.-W.; Lin, F.; Huang, Z.-Y.; Lin, H.-W.; Wang, P.-H.; Liu, Y.-H.; Wong, K.-T.; Wen, J.; Miller, D. J.; Darling, S. B. Vacuum-Deposited Small-Molecule Organic Solar Cells with High Power Conversion Efficiencies by Judicious Molecular Design and Device Optimization. *J. Am. Chem. Soc.* **2012**, *134* (33), 13616–13623. https://doi.org/10.1021/ja301872s.

(95) Perdigón-Toro, L.; Zhang, H.; Markina, A.; Yuan, J.; Hosseini, S. M.; Wolff, C. M.; Zuo, G.; Stolterfoht, M.; Zou, Y.; Gao, F.; Andrienko, D.; Shoaee, S.; Neher, D. Barrierless Free Charge Generation in the High-Performance PM6:Y6 Bulk Heterojunction Non-Fullerene Solar Cell. *Advanced Materials* **2020**, *32* (9), 1906763. https://doi.org/10.1002/adma.201906763.

(96) Uhrich, C.; Wynands, D.; Olthof, S.; Riede, M. K.; Leo, K.; Sonntag, S.; Maennig, B.; Pfeiffer, M. Origin of Open Circuit Voltage in Planar and Bulk Heterojunction Organic Thin-Film Photovoltaics Depending on Doped Transport Layers. *Journal of Applied Physics* **2008**, *104* (4), 043107. https://doi.org/10.1063/1.2973199.

(97) Tress, W.; Leo, K.; Riede, M. Influence of Hole-Transport Layers and Donor Materials on Open-Circuit Voltage and Shape of I–V Curves of Organic Solar Cells. *Advanced*

Functional Materials **2011**, *21* (11), 2140–2149. https://doi.org/10.1002/adfm.201002669.

(98) Poelking, C.; Tietze, M.; Elschner, C.; Olthof, S.; Hertel, D.; Baumeier, B.; Würthner, F.; Meerholz, K.; Leo, K.; Andrienko, D. Impact of Mesoscale Order on Open-Circuit Voltage in Organic Solar Cells. *Nature Mater* **2015**, *14* (4), 434–439. https://doi.org/10.1038/nmat4167.

(99) Ngongang Ndjawa, G. O.; Graham, K. R.; Li, R.; Conron, S. M.; Erwin, P.; Chou, K. W.; Burkhard, G. F.; Zhao, K.; Hoke, E. T.; Thompson, M. E.; McGehee, M. D.; Amassian, A. Impact of Molecular Orientation and Spontaneous Interfacial Mixing on the Performance of Organic Solar Cells. *Chem. Mater.* **2015**, *27* (16), 5597–5604. https://doi.org/10.1021/acs.chemmater.5b01845.

(100) Poelking, C.; Andrienko, D. Design Rules for Organic Donor–Acceptor Heterojunctions: Pathway for Charge Splitting and Detrapping. *J. Am. Chem. Soc.* **2015**, *137* (19), 6320–6326. https://doi.org/10.1021/jacs.5b02130.

(101) Cha, H.; Fish, G.; Luke, J.; Alraddadi, A.; Lee, H. H.; Zhang, W.; Dong, Y.; Limbu, S.; Wadsworth, A.; Maria, I. P.; Francàs, L.; Sou, H. L.; Du, T.; Kim, J.-S.; McLachlan, M. A.; McCulloch, I.; Durrant, J. R. Suppression of Recombination Losses in Polymer:Nonfullerene Acceptor Organic Solar Cells Due to Aggregation Dependence of Acceptor Electron Affinity. *Advanced Energy Materials* **2019**, *9* (27), 1901254. https://doi.org/10.1002/aenm.201901254.

(102) Schwarze, M.; Schellhammer, K. S.; Ortstein, K.; Benduhn, J.; Gaul, C.; Hinderhofer, A.; Perdigón Toro, L.; Scholz, R.; Kublitski, J.; Roland, S.; Lau, M.; Poelking, C.; Andrienko, D.; Cuniberti, G.; Schreiber, F.; Neher, D.; Vandewal, K.; Ortmann, F.; Leo, K. Impact of Molecular Quadrupole Moments on the Energy Levels at Organic Heterojunctions. *Nat Commun* **2019**, *10* (1), 2466. https://doi.org/10.1038/s41467-019-10435-2.

(103) Natsuda, S.; Saito, T.; Shirouchi, R.; Sakamoto, Y.; Takeyama, T.; Tamai, Y.; Ohkita, H. Cascaded Energy Landscape as a Key Driver for Slow yet Efficient Charge Separation with Small Energy Offset in Organic Solar Cells. *Energy & Environmental Science* **2022**, *15* (4), 1545–1555. https://doi.org/10.1039/D1EE03565G.

(104) Rand, B. P.; Cheyns, D.; Vasseur, K.; Giebink, N. C.; Mothy, S.; Yi, Y.; Coropceanu, V.; Beljonne, D.; Cornil, J.; Brédas, J.-L.; Genoe, J. The Impact of Molecular Orientation on the Photovoltaic Properties of a Phthalocyanine/Fullerene Heterojunction. *Advanced Functional Materials* **2012**, *22* (14), 2987–2995. https://doi.org/10.1002/adfm.201200512.

(105) Hörmann, U.; Lorch, C.; Hinderhofer, A.; Gerlach, A.; Gruber, M.; Kraus, J.; Sykora, B.; Grob, S.; Linderl, T.; Wilke, A.; Opitz, A.; Hansson, R.; Anselmo, A. S.; Ozawa, Y.; Nakayama, Y.; Ishii, H.; Koch, N.; Moons, E.; Schreiber, F.; Brütting, W. Voc from a Morphology Point of View: The Influence of Molecular Orientation on the Open Circuit Voltage of Organic Planar Heterojunction Solar Cells. *J. Phys. Chem. C* **2014**, *118* (46), 26462–26470. https://doi.org/10.1021/jp506180k.

(106) Nakano, K.; Tajima, K. Organic Planar Heterojunctions: From Models for Interfaces in Bulk Heterojunctions to High-Performance Solar Cells. *Advanced Materials* **2017**, *29* (25), 1603269. https://doi.org/10.1002/adma.201603269.

(107) Credgington, D.; Durrant, J. R. Insights from Transient Optoelectronic Analyses on the Open-Circuit Voltage of Organic Solar Cells. *J. Phys. Chem. Lett.* **2012**, *3* (11), 1465–1478. https://doi.org/10.1021/jz300293q.

(108) Vandewal, K.; Widmer, J.; Heumueller, T.; Brabec, C. J.; McGehee, M. D.; Leo, K.; Riede, M.; Salleo, A. Increased Open-Circuit Voltage of Organic Solar Cells by Reduced Donor-Acceptor Interface Area. *Adv. Mater.* **2014**, *26* (23), 3839–3843. https://doi.org/10.1002/adma.201400114.

(109) Khan, S.-U.-Z.; Rand, B. P. Influence of Disorder and State Filling on Charge-Transfer-State Absorption and Emission Spectra. *Phys. Rev. Appl.* **2021**, *16* (4), 044026. https://doi.org/10.1103/PhysRevApplied.16.044026.

(110) Jungbluth, A.; Kaienburg, P.; Riede, M. Charge Transfer State Characterization and Voltage Losses of Organic Solar Cells. *J. Phys. Mater.* **2022**, *5* (2), 024002. https://doi.org/10.1088/2515-7639/ac44d9.

(111) Almora, O.; Cabrera, C. I.; Garcia-Cerrillo, J.; Kirchartz, T.; Rau, U.; Brabec, C. J. Quantifying the Absorption Onset in the Quantum Efficiency of Emerging Photovoltaic Devices. *Advanced Energy Materials* **2021**, *11* (16), 2100022. https://doi.org/10.1002/aenm.202100022.

(112) Vohra, V.; Kawashima, K.; Kakara, T.; Koganezawa, T.; Osaka, I.; Takimiya, K.; Murata, H. Efficient Inverted Polymer Solar Cells Employing Favourable Molecular Orientation. *Nature Photon* **2015**, *9* (6), 403–408. https://doi.org/10.1038/nphoton.2015.84.

(113) Zhao, J.; Li, Y.; Yang, G.; Jiang, K.; Lin, H.; Ade, H.; Ma, W.; Yan, H. Efficient Organic Solar Cells Processed from Hydrocarbon Solvents. *Nat Energy* **2016**, *1* (2), 1–7. https://doi.org/10.1038/nenergy.2015.27.

(114) Cui, Y.; Yao, H.; Zhang, J.; Zhang, T.; Wang, Y.; Hong, L.; Xian, K.; Xu, B.; Zhang, S.; Peng, J.; Wei, Z.; Gao, F.; Hou, J. Over 16% Efficiency Organic Photovoltaic Cells Enabled by a Chlorinated Acceptor with Increased Open-Circuit Voltages. *Nat Commun* **2019**, *10* (1), 2515. https://doi.org/10.1038/s41467-019-10351-5.

(115) Liu, Q.; Jiang, Y.; Jin, K.; Qin, J.; Xu, J.; Li, W.; Xiong, J.; Liu, J.; Xiao, Z.; Sun, K.; Yang, S.; Zhang, X.; Ding, L. 18% Efficiency Organic Solar Cells. *Science Bulletin* **2020**, *65* (4), 272–275. https://doi.org/10.1016/j.scib.2020.01.001.

(116) Nakano, K.; Chen, Y.; Tajima, K. Quantifying Charge Carrier Density in Organic Solar Cells by Differential Charging Techniques. *AIP Advances* **2019**, *9* (12), 125205. https://doi.org/10.1063/1.5122709.

(117) Credgington, D.; Kim, Y.; Labram, J.; Anthopoulos, T. D.; Durrant, J. R. Analysis of Recombination Losses in a Pentacene/C_{60} Organic Bilayer Solar Cell. *The Journal of Physical Chemistry Letters* **2011**, *2* (21), 2759–2763. https://doi.org/10.1021/jz201338d.

(118) Credgington, D.; Liu, S.-W.; Nelson, J.; Durrant, J. R. In Situ Measurement of Energy Level Shifts and Recombination Rates in Subphthalocyanine/C_{60} Bilayer Solar Cells. *The*

Journal of Physical Chemistry C **2014**, *118* (40), 22858–22864. https://doi.org/10.1021/jp505297u.

(119) Sandberg, O. J.; Tvingstedt, K.; Meredith, P.; Armin, A. Theoretical Perspective on Transient Photovoltage and Charge Extraction Techniques. *J. Phys. Chem. C* **2019**, *123* (23), 14261–14271. https://doi.org/10.1021/acs.jpcc.9b03133.

(120) Vandewal, K.; Tvingstedt, K.; Gadisa, A.; Inganäs, O.; Manca, J. V. Relating the Open-Circuit Voltage to Interface Molecular Properties of Donor:Acceptor Bulk Heterojunction Solar Cells. *Phys. Rev. B* **2010**, *81* (12), 125204. https://doi.org/10.1103/PhysRevB.81.125204.

(121) Vandewal, K.; Tvingstedt, K.; Manca, J. V.; Inganäs, O. Charge-Transfer States and Upper Limit of the Open-Circuit Voltage in Polymer:Fullerene Organic Solar Cells. *IEEE Journal of Selected Topics in Quantum Electronics* **2010**, *16* (6), 1676–1684. https://doi.org/10.1109/JSTQE.2010.2043061.

(122) Cheyns, D.; Poortmans, J.; Heremans, P.; Deibel, C.; Verlaak, S.; Rand, B. P.; Genoe, J. Analytical Model for the Open-Circuit Voltage and Its Associated Resistance in Organic Planar Heterojunction Solar Cells. *Phys. Rev. B* **2008**, *77* (16), 165332. https://doi.org/10.1103/PhysRevB.77.165332.

(123) Linderl, T.; Zechel, T.; Hofmann, A.; Sato, T.; Shimizu, K.; Ishii, H.; Brütting, W. Crystalline versus Amorphous Donor-Acceptor Blends: Influence of Layer Morphology on the Charge-Transfer Density of States. *Phys. Rev. Applied* **2020**, *13* (2), 024061. https://doi.org/10.1103/PhysRevApplied.13.024061.

(124) Yan, J.; Rezasoltani, E.; Azzouzi, M.; Eisner, F.; Nelson, J. Influence of Static Disorder of Charge Transfer State on Voltage Loss in Organic Photovoltaics. *Nat Commun* **2021**, *12* (1), 3642. https://doi.org/10.1038/s41467-021-23975-3.

(125) Vandewal, K.; Benduhn, J.; C. Nikolis, V. How to Determine Optical Gaps and Voltage Losses in Organic Photovoltaic Materials. *Sustainable Energy & Fuels* **2018**, *2* (3), 538–544. https://doi.org/10.1039/C7SE00601B.

(126) Kahle, F.-J.; Rudnick, A.; Bässler, H.; Köhler, A. How to Interpret Absorption and Fluorescence Spectra of Charge Transfer States in an Organic Solar Cell. *Materials Horizons* **2018**, *5* (5), 837–848. https://doi.org/10.1039/C8MH00564H.

(127) Melianas, A.; Felekidis, N.; Puttisong, Y.; Meskers, S. C. J.; Inganäs, O.; Chen, W. M.; Kemerink, M. Nonequilibrium Site Distribution Governs Charge-Transfer Electroluminescence at Disordered Organic Heterointerfaces. *Proceedings of the National Academy of Sciences* **2019**, *116* (47), 23416–23425. https://doi.org/10.1073/pnas.1908776116.

(128) Gong, W.; Faist, M. A.; Ekins-Daukes, N. J.; Xu, Z.; Bradley, D. D. C.; Nelson, J.; Kirchartz, T. Influence of Energetic Disorder on Electroluminescence Emission in Polymer:Fullerene Solar Cells. *Phys. Rev. B* **2012**, *86* (2), 024201. https://doi.org/10.1103/PhysRevB.86.024201.

(129) Shuttle, C. G.; O'Regan, B.; Ballantyne, A. M.; Nelson, J.; Bradley, D. D. C.; Durrant, J. R. Bimolecular Recombination Losses in Polythiophene: Fullerene Solar Cells. *Phys. Rev. B* **2008**, *78* (11), 113201. https://doi.org/10.1103/PhysRevB.78.113201.

5

BLENDS, BILAYERS, SINGLE COMPONENT: SOLUTION-PROCESSED DEVICES

5. Blends, Bilayers, Single Component: Solution-Processed Devices

5.1. Introduction

While the previous chapter focused on the limitations of scalable VP-OSC solutions, this chapter will revolve around solution-processed organic solar cells (SP-OSC) and the study of their fundamental material properties in single component, planar heterojunction and bulk heterojunction architecture.

SP-OSCs based on polymers and non-fullerene acceptors continue to break efficiency records on a laboratory scale. Several studies have reported single-junction bulk heterojunction efficiencies beyond 19 %[1–4] and recently also the threshold of 20 % was broken using a monolithic double-junction device architecture[5]. This is coming close of the theoretical efficiency limit of 20 – 25 % set by the high non-radiative voltage losses in OSCs.[6] The introduction of the Y6-family[7] with its distinct A-D-A'-D-A structure and their efficient charge generation at low energy offsets[8] and low energetic disorder[9–11] was key to these achievements.

While materials innovation (the distinct A-D-A'-D-A core structure) formed the basis of the recent record performances, further meticulous empirical optimisation of the molecular structure (solubilising side chain length/position, halide substitutions),[12–15] D/A ratio (including ternary or even quaternary blends),[2–4,16–19] deposition parameters (solvent choice, solvent temperature, spin-coating speed etc.)[20,21] and post deposition treatments (thermal or solvent vapour annealing)[22,23] was necessary to incrementally push the record efficiency past 19 % for lab-scale devices. At the same time, the highest certified module efficiencies have stagnated partially due to issues in replicating these achievements using up-scalable techniques while reproducing the optimal BHJ morphology.[24,25]

Also, the stability of high-performing solution-processed BHJs remains a challenge in the field. Particularly the effect of the solubilising sidechains on the miscibility and aggregation behaviour of the donor and acceptor poses a challenge in solution-processing that is less critical in evaporated small molecules.[25] Optimised morphologies often rely on kinetically trapping a thermodynamically unfavourable blend morphology during film drying.[26,27] For the Y6-family, with increasing alkyl-side chain length, higher performances are achievable while the glass transition temperature of the Y6-derivatives is reduced which increases the acceptor diffusion rate. This is leading to over-aggregation of the acceptor phase and a loss of

percolation pathways as well as unfavourable vertical phase separation (acceptor diffusion towards the anode) in BHJ cells.[14] Efforts to improve stability (e.g., third components to kinetically stabilise the BHJ morphology[14]) and to improve the BHJ reproducibility are key to take them from the lab- to large-scale real-world applications.

While SP-OSCs based on BHJs continue to break lab efficiency records, research trying to understand the success of novel NFA materials has uncovered additional properties explaining their success. Particularly the high absorbance[28] and high exciton diffusion length demonstrated for a range of NFAs including IT-4F and Y6[29,30] as well as reports about charge generation in neat films of Y6[31,32] and other NFAs[33,34] raise the potential for new pseudo-planar,[35–41] planar heterojunction,[42–44] or single component[32] device architectures for organic solar cell or photodetector applications (OPV and OPD, respectively). Such device architectures could help address issues related to the reproducibility and stability associated with solution-processed bulk heterojunctions.[45,46]

Sequentially coated pseudo-planar heterojunctions achieve high performances due to a balance of an intermixed layer enabling efficient charge generation framed by pure donor and acceptor layers enabling efficient charge extraction. Thereby, the effect of unfavourable vertical diffusion of acceptor molecules causing device instability can be avoided. The sequential deposition also simplifies the optimisation process needed for BHJs and offers a route to upscaling via roll-to-roll techniques.[46]

Planar heterojunctions with a sharp interface cannot easily be produced from solution processing. Ramsdale *et al.* demonstrated the fabrication of sharp bilayers of two polymers by a lift-off technique.[47] More recently, also sharp NFA-polymer bilayer devices in an inverted architecture have been demonstrated by transferring a polymer film formed on water onto the acceptor layer.[43,48,49] Industrially, Swedish company Epishine has demonstrated the feasibility the deposition of bilayers by depositing the respective electrodes and interlayers on the top and bottom flexible substrate followed by solution-coated active layers on both sides. Upon laminating the two substrates together, this essentially forms a bilayer that may subsequently be cured using thermal annealing processes. Note that Epishine applies a BHJ to each substrate but in principle D/A bilayers may be feasible. More information about their process is available on www.epishine.com.

While PHJs typically show a reduced current generation efficiency compared to pseudo-planar heterojunctions, the more controlled interface makes them suitable systems to study the energetics at the D/A interface and their effect on charge generation and recombination[44,50] as well as potentially reducing voltage losses as demonstrated in **Subchapter 4.3**. The remainder of this chapter will be split into four subchapters corresponding to separate – yet related studies – on NFA based planar vs bulk heterojunction as well as single component devices to study fundamental properties. These are intended to give an overview of the limitations of planar heterojunctions in different material systems and elucidate their distinct advantages and differing device physics. My focus will be on the application of optoelectronic techniques to investigate the device performance with additional data from (transient) optical measurements carried out by collaborators.

Subchapter 5.2 is based on the publication "Organic Planar Heterojunction Solar Cells and Photodetectors Tailored to the Exciton Diffusion Length Scale of a Non-Fullerene Acceptor" by Tack Ho Lee *et al.*[51] It focuses on planar and bulk heterojunctions made of PM6 and IT-4F. By tuning the thickness of the acceptor layer to the exciton diffusion length of IT-4F, high photocurrent can be realised. Together with the measured low dark current and increased V_{OC}, this makes the bilayer devices suitable candidates for OPD and OPV applications. By combining transient optoelectronic measurements with measurements of the device emission spectra, I elucidate the origin of the improved photovoltage.

Subchapter 5.3 contains results published in "Molecular orientation-dependent energetic shifts in solution-processed non-fullerene acceptors and their impact on organic photovoltaic performance" by Yuang Fu *et al.*[52] It addresses orientation dependent energetic shifts in Y6 layers prepared from different solvents. Planar heterojunction devices produced with such Y6 bottom layers and PM6 top layers exhibit changes in the current generation and more than 100 mV shift in their V_{OC}. By comparing the charge carrier built-up and recombination in the different planar heterojunctions, the connection between energetic shifts and V_{OC} is studied. Finally, the findings are applied also to BHJs prepared from different solvents that show similar albeit weakened trends compared to the bilayers. Interestingly, PM6/Y6 PHJs do not show and increase in voltage compared to their BHJ counterparts. This will be briefly discussed in relation with results from **Subchapter 5.2**, **Subchapter 5.3** and **Subchapter 4.3** by comparing PHJs and BHJs made up of different active layer components. Specifically,

the relation between non-geminate recombination kinetics and the observed voltage trends is discussed.

Subchapter 5.4 presents some findings of the publication "The State-of-the-Art Solution-Processed Single Component Organic Photodetectors Achieved by Strong Quenching of Intermolecular Emissive State and High Quadrupole Moment in Non-Fullerene Acceptors" by Song Yi Park *et al.*[33] and addresses the topic of charge generation in neat NFA layers that is touched upon in previous sections. Here, the mechanism of free charge generation is discussed in more detail for a range of NFAs including IT-4F and Y6. Furthermore, non-geminate recombination in neat layers is addressed that has been previously proposed to be the limiting factor in Y6 single component devices.[32]

5.2. Planar Heterojunctions Tailored to the Exciton Diffusion Length of IT-4F

5.2.1. Background

The fluorinated ITIC derivative IT-4F has been shown to produce high efficiency BHJs paired with PM6 (PCE > 14 %).[53,54] Several factors related to the fluorination explain its improved performance compared to ITIC and other ITIC derivatives including a highly ordered morphology and its lower bandgap yielding additional current generation in the infrared part of the solar spectrum. More recently, IT-4F has also been shown to possess an improved chemical stability[55] as well as a long exciton diffusion length[29]. These factors make it a suitable candidate for OPV and OPD applications. As for other BHJ organic solar cells, the voltage losses relative to the absorption onset still constitute a major loss mechanism. Voltage losses have previously been demonstrated to scale with the interfacial area.[56] Planar heterojunctions may therefore be a suitable pathway to reduce non-geminate recombination and therefore voltage losses in systems with suitably long exciton diffusion lengths enabling efficient charge generation in optically thick bilayers.

Therefore, in this study,[51] the exciton diffusion length of IT-4F was determined from the exciton-exciton annihilation rates in neat acceptor films measured by ultra-fast transient absorption spectroscopy (TAS) by Yifan Dong and Tack-Ho Lee. They measured the intrinsic exciton lifetime of IT-4F by observing the exciton decay in films of IT-4F diluted in polystyrene that are expected to show reduced exciton-exciton annihilation. Additionally, these results were confirmed by low fluence time-correlated single photon counting (TCSPC) photoluminescence measurements. A value of 40 nm was determined for the exciton diffusion length of IT-4F in line with previous reports.[29,30] Based on this result, PHJ devices with varying IT-4F thickness (40, 60, 70 nm) were produced by Tack-Ho Lee using the aforementioned polymer film transfer method in an inverted architecture. This is technologically favourable to standard structure bilayers that had previously been demonstrated by spin-coating the acceptor on top of the polymer layer using orthogonal solvents.[42,45] Indeed, for an IT-4F thickness of 40 nm, a steep increase in the generated photocurrent was observed. This is well explained by the transfer matrix simulations of the absorption profile carried out by the author of this thesis together with the exciton diffusion length determined from optical measurements. The 40 nm PHJ resulted in the highest *PCE* of 5.4% and excellent OPD performance thanks to a low dark current compared to the BHJ reference. Besides the

decreased J_{SC} and *FF*, all PHJs show an improved V_{OC} relative to the BHJ. After presenting optical results on the J_{SC} trends, the origin of the decreased *FF* and improved V_{OC} is investigated through light intensity dependent *JV*-measurements, device emission spectra and non-geminate recombination kinetics. These results will be discussed in more detail in the following.

5.2.2. Contributions

The majority of the results presented in this section were previously published[51] and are shown here recompiled with additional data for comparison. Tack Ho Lee prepared the devices studied herein and carried out the optical spectroscopy measurements together with Yifan Dong (TCSPC, TAS) and Weidong Xu (PL, EL). Song Yi Park provided additional PL measurements and gave support in the device preparation (single component devices). The results discussed here mainly focus on the light intensity dependent *JV*- and transient optoelectronic measurements as well as the analysis of the emission spectra carried out by the author of this thesis. If not otherwise declared, the measurements were performed by the author of this thesis.

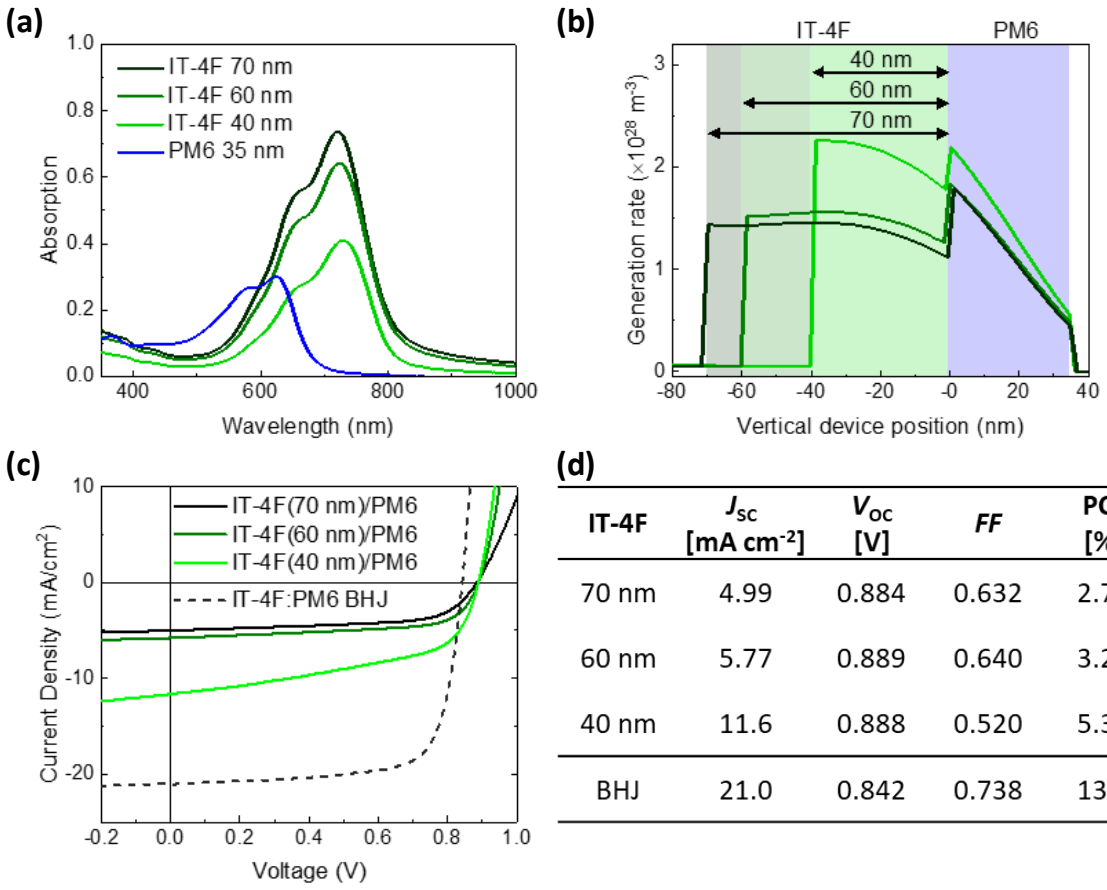
5.2.3. Device Structure and Performance

As described above, the exciton diffusion length of IT-4F was determined to be about 40 nm. Details of the experimental procedure can be found in the publication.[51] Based on this devices with the following structure were prepared: ITO / ZnO / IT-4F (40 nm, 60 nm, 70 nm) / PM6 (35 nm) / MoO_x / Ag.

Figure 5.2.1 shows the absorption spectra of the neat PM6 and IT-4F films as well as the optical transfer matrix modelling of the absorption profile. Optical constants of IT-4F and PM6 (*n*, *k*) were obtained from Kerremans *et al.* and the absorption profile was calculated using the OghmaNano simulation software.[28]

The *JV*-curves of the PHJ devices as well as that of the BHJ reference device are shown in **Figure 5.2.1 I**. **Figure 5.2.1 (d)** lists the corresponding *JV*-parameters. Relative to the BHJ, all PHJs show an increased V_{OC} (40 – 50 mV) but reduced *FF* and J_{SC} resulting in an overall decrease in the performance. The highest PHJ performance is achieved for the 40 nm IT-4F layer due to the enhancement in J_{SC} while the *FF* decreased significantly compared to the thicker PHJ devices. Observations about the current generation efficiency and how this relates to J_{SC} and *FF* will be discussed in **Section 5.2.4** and **5.2.5**, respectively. The trend

regarding the V_{OC} is in line with the findings presented in **Subchapter 4.3** and will be further analysed in **Section 5.2.6** with a focus on the highest performing 40 nm IT-4F PHJ.



(d)

IT-4F	J_{SC} [mA cm^{-2}]	V_{OC} [V]	*FF*	PCE [%]
70 nm	4.99	0.884	0.632	2.78
60 nm	5.77	0.889	0.640	3.29
40 nm	11.6	0.888	0.520	5.38
BHJ	21.0	0.842	0.738	13.0

Figure 5.2.1. (a) Absorption spectra of neat films used for the preparation of PHJ solar cells. **(b)** Transfer matrix modelling of the exciton generation rate under 1 sun illumination for different IT-4F thicknesses. Note that in the used inverted architecture the device is illuminated from the left-hand side. **(c)** JV-curves of the PHJs and BHJ reference. **(d)** Corresponding JV-parameters. Absorption spectra were measured by Tack-Ho Lee.

5.2.4. Hole Transfer Kinetics and the Short Circuit Current Density

Turning to the differences in the J_{SC}, the increase observed for the 40 nm PHJ is in line with what would be expected based on the established exciton diffusion length. Also, the optical modelling shows a significant increase of the exciton generation within the diffusion length from the interface. This is in line with the slightly increased PL quenching in the thinnest PHJ (≈ 80%, compared with > 95% for the BHJ) as shown in the original publication.[51]

Previous studies involving wide-gap polymer:NFA heterojunctions highlighted the efficient energy transfer or ultrafast electron transfer following polymer excitation.[43,57–59] Therefore, the focus in the discussion of the J_{SC} trends will be on the hole transfer as the main charge

generation pathway. Tracking the hole transfer by means of transient absorption spectroscopy for the bilayers and the bulk heterojunction reveals two distinct time scales of hole transfer in the 40 nm PHJ (**Figure 5.2.2 (a)**).

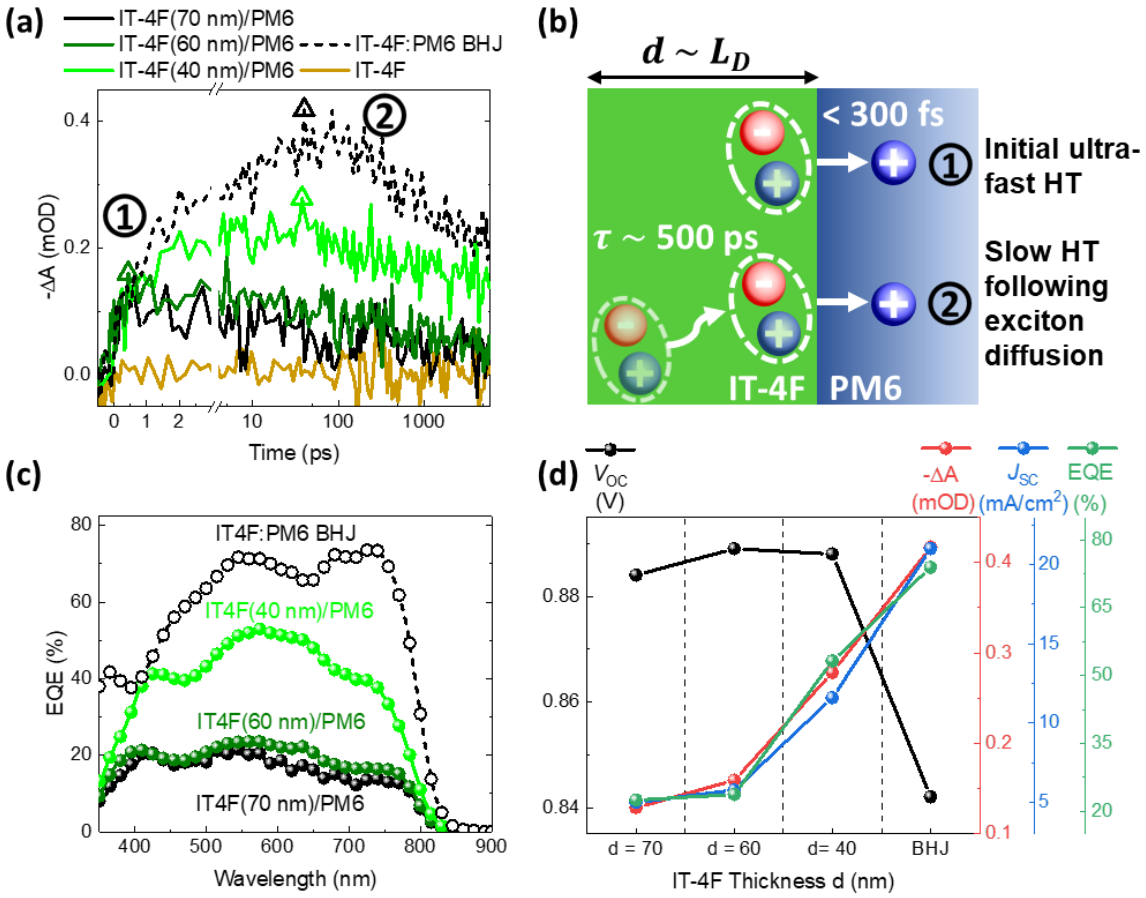


Figure 5.2.2. (a) PM6 ground state bleach (GSB) signal (pump: 775 nm, probe: 560-570 nm) of neat IT-4F, IT-4F/PM6 bilayer and BHJ films. The probe wavelength was chosen to avoid overlap with IT-4F GSB signals. **(b)** Schematic illustration of the hole transfer (HT) process in the IT-4F/PM6 bilayer. **(c)** EQE spectra of the PHJ and BHJ devices. **(d)** Comparison of the trends of the maximum change in absorption (ΔA), EQE and J_{SC} as well as the trend in V_{OC} for the PHJ and BHJ devices. TAS and EQE measurements carried out by Tack Ho Lee.

All PHJ films as well as the BHJ exhibit a fast initial rise of the ground state bleach (GSB) signal on the PM6. This is assigned to ultrafast hole transfer from excitons generated near the charge generating interface occurring within 300 fs. In the 60 nm and 70 nm bilayers, the signal is weaker in line with the reduced absorption in the vicinity of the interface and decays following the initial fast rise. The PM6 GSB signal in the 40 nm bilayer and BHJ continues to rise over several tens of picoseconds. This behaviour may be assigned to additional hole transfer occurring from excitons generated away from the D/A interface but within the exciton diffusion length. **Figure 5.2.2 (b)** schematically illustrates this concept. The maximum of

the GSB peak in TAS measurements (marked by triangles in **Figure 5.2.2 (a)**) correlates well with the measured EQE of the PHJ and BHJ devices (**Figure 5.2.2 (c)**). **Figure 5.2.2 (d)** summarises the trend in J_{SC}, GSB peak (maximum ΔA) and EQE to highlight this correlation.

Note that further decreasing the thickness of the IT-4F layer to 20 nm led to a reduction in EQE, J_{SC} and overall PCE due to the limited absorption (see Supporting Information of the publication).[51] The following discussion will therefore focus on the highest performing 40 nm IT-4F/PM6 device.

5.2.5. Field Dependence of Photocurrent and the Fill Factor

As shown above, all PHJs show a reduced *FF* compared to the BHJ device. The *JV*-curve of the 40 nm PHJ shows a curious inflection point in the forward bias region below the maximum power point that (see **Figure 5.2.3 (a)**) contributes to the additional decrease in *FF* compared to the thicker PHJs. While it is present in the thick PHJ devices, too, it becomes particularly prominent in the 40 nm PHJ at high light intensities (increasing V_{OC}) as shown in the *JV*-curves normalised by the light intensity in **Figure 5.2.3 (a)**. For comparison also the normalised *JV*-curves of the BHJ and the neat IT-4F device (see **Section 5.4** and data from Park *et al.*[33] for details). Neither of the devices exhibit similar *JV*-curve shapes. It should be noted that in the literature, devices utilising thinner IT4F layers (30 nm) show a lowered *FF* but no inflection point as shown here.[45] No inflection point is observed for the 20 nm IT-4F layer mentioned above that resulted in a *FF* of 0.51 – well below the value for the 60 nm and 70 nm PHJs. Investigating the origin of this inflection point and the *FF* reduction in the highest performing PHJs could therefor further boost the achievable PCE of bilayer devices.

Inflection points and S-kinks are often encountered in organic solar cells due to charge extraction issues e.g. misaligned contact layers resulting in extraction barriers[60,61] or imbalanced mobilities (ratio > 100) in PHJs[62]. However, in both cases, typically an inflection point is observed around V_{OC}. Given that the same interlayers are used for the PHJ as for the BHJ, this is unlikely the origin of the *JV*-shape. SCLC measurements on neat films of PM6[63] and IT4F[64] also show a similar magnitude (~ 10^{-4} $cm^2V^{-1}s^{-1}$) of the respective hole and electron mobility. It should, however, be noted that the cited study was conducted on bilayer systems with lower generation current densities at the planar heterojunction. Consequently, firstly the dependence of the *JV*-shape on the generation current is investigated here (**Figure 5.2.3 (a)**) and complimented thereafter with the investigation of field-dependent generation (in **Figure**

5.2.3 **(c)** and **(d)**) that has been inferred from PL quenching measurements and the recombination kinetics under open circuit conditions (**Section 5.2.5**).

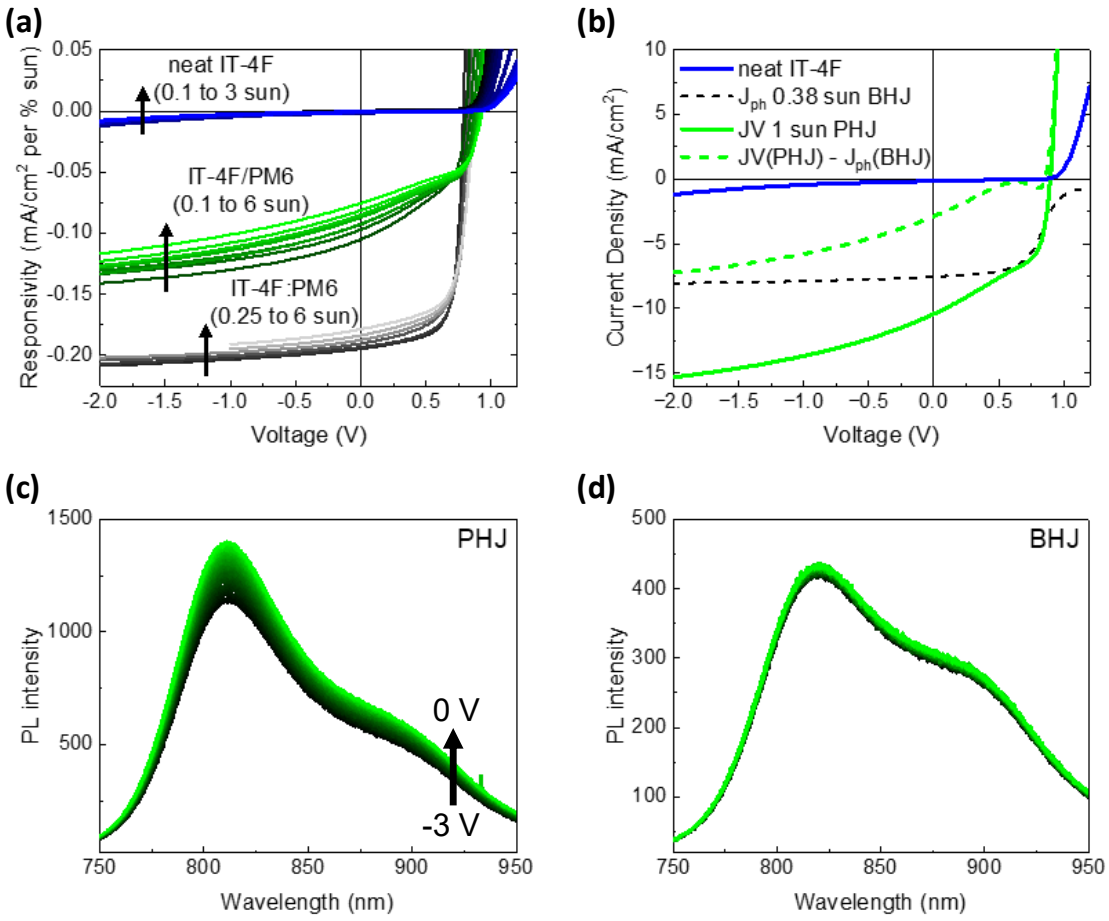


Figure 5.2.3. (a) Light intensity dependent JV-curves of neat IT-4F, 40 nm PHJ and BHJ devices divided by the light intensity in % sun. The data of the neat film is taken from **Section 6.4**. **(b)** JV-curve of the neat IT-4F and 40 nm PHJ device at 1 sun. Additionally shown are the photocurrent of the BHJ device at 0.38 sun equivalent illumination. Subtracting this from the PHJ JV-curve yields the green dashed line. This represents a hypothetical scenario to explain the observed inflection point and field dependence of the JV-curve. **(c), (d)** Field dependent photoluminescence spectra of the 40 nm PHJ and the BHJ, respectively, recorded at an externally biased varying from -3 to 0 V. PL measurements carried out by Tack Ho Lee and Weidong Xu.

The PHJ shows a strongly light Int"nsit' dependent responsivity in the reverse bias region. The intensity dependence (shift upwards) would suggest that this is in part due to non-geminate losses. Interestingly, the responsivity around MPP shows only small variation compared to the typical behaviour of the BHJ where the responsivity loss at MPP is indicative of non-geminate recombination losses during transport to the electrodes. However, in PHJs the majority of non-geminate recombination events is expected to occur directly at the charge generating interface and even the lowest light intensity results in a large gradient of the *JV*-curve,

especially in the power generating quadrant. This may therefore indicate the presence of different charge generation and/or non-geminate recombination mechanisms dominating the different voltage regions.

Firstly, different generation pathways additively contributing to the photocurrent are considered: (1) showing a strong field dependence and carrier density dependence that vanishes towards MPP and (2) relatively independent of the bias and scales proportionally with light intensity causing the emergence of the inflection point at high light intensity. The latter may be compared to the charge generation in the BHJ with an expected similar field dependence. This is illustrated in **Figure 5.2.3 (b)**. It shows the PHJ *JV*-curve at 1 sun as a sum of the BHJ photocurrent at 0.38 sun equivalent light intensity (2) as well as the strongly field-dependent difference between the two (1). At -2 V, this proposed field dependent generation pathway generates approximately 7.5 mA/cm^2. The origin of (1) could stem from different molecular orientations and CT state properties at the D/A interface compared to the BHJ leading to an increased field-dependence compared to the BHJ.[65] In the cited study, the magnitude of this effect is generally smaller than established herein for the same material combination at much lower photocurrent. Another possible origin is direct generation of charges in the neat IT-4F film prior to quenching at the D/A interface. The field dependent PL data in **Figure 5.2.3 (c)** and **(d)** demonstrates the existence of a field dependent exciton quenching pathway in the PHJ. Upon application of an external reverse bias (0 to -3 V) the PHJ shows about 20 % PL quenching. As expected, BHJs exhibit only a small amount of PL quenching at reverse bias. Charge generation was also observed at reverse bias in neat IT-4F devices. The resulting *JV*-curves are shown in **Figure 5.2.3 (b)** for comparison. While the neat IT-4F device can generate photocurrents of a similar magnitude as the hypothetical field-dependent mechanism in the PHJ, this is only achieved at higher reverse bias of -5 V and consequently higher field across the thinner IT-4F layer (as will be shown in **Subchapter 5.4**). This highlights that the majority of charges are generated at the D/A interface over the voltage range studied herein.

To summarize, the exact origin of the field dependent *JV*-curve and the inflection point is difficult to determine. Direct exciton splitting away from the D/A interface in IT-4F (or potentially PM6) may account for some of the additional generation. However, the data of the neat IT-4F device as well as the PL quenching efficiency below 20% seem to suggest that this cannot account for the observed field-dependence of the *JV*-curve. The comparison with the

thicker PHJs, that possess the same interfacial properties, shows a stronger dependence on bias in thin PHJs (also when adjusted for the device thickness) as shown in the supporting information of the original publication. It therefore seems more likely related to charge carrier density dependent effects on the charge transport away from the interface and recombination as also evidenced by the strong light intensity dependence of the responsivity. These effects would be pronounced in the PHJs with the highest generation current, potentially setting an intrinsic trade-off between J_{SC} and *FF* at limited interfaces. Future studies should elucidate this further by employing drift diffusion simulations to better understand the charge carrier distribution and non-geminate recombination in the vicinity of the planar interface. Time-delayed collection field experiments could also aid in distinguishing between geminate and non-geminate recombination experimentally. The non-geminate recombination kinetics at open circuit are analysed in more detail below.

5.2.6. Non-Geminate Recombination Kinetics and Open Circuit Voltage

Following the observations of the light intensity dependence of the *FF*, **Figure 5.2.4 (a)** shows the light intensity dependence of the J_{SC} and V_{OC}. As already indicated by the light intensity dependent normalised *JV*-curves presented above, the PHJ shows a sublinear light intensity dependence of the J_{SC} with a fitted power law exponent of 0.90 compared to 0.97 for the BHJ. Given that the above results suggest – as expected – that the vast majority of charges are generated at the D/A interface, the reduced responsivity stems from larger non-geminate losses due to charge accumulation at the interface modulated by bias and/or light intensity.

In line with this, the PHJ also shows a slight reduction in the light ideality factor determined from V_{OC} vs light intensity. The PHJ and BHJ show ideality factors of 1.1 and 1.2, respectively, and a V_{OC} difference of around 40 mV at around 1 sun equivalent light intensity (**Figure 5.2.4 (b)**). This suggests as in the case of the evaporated PHJ and BHJ devices that the ideality is dominated by bimolecular recombination in the active layer. The absorption onset determined from the EQE spectra shows a small blueshift of about 10 meV for the PHJ device which is also mirrored in a small blueshift in the PL emission shown in **Figure 5.2.3 (c)** and **(d)**. These observations do not explain the full extend of the voltage increase.

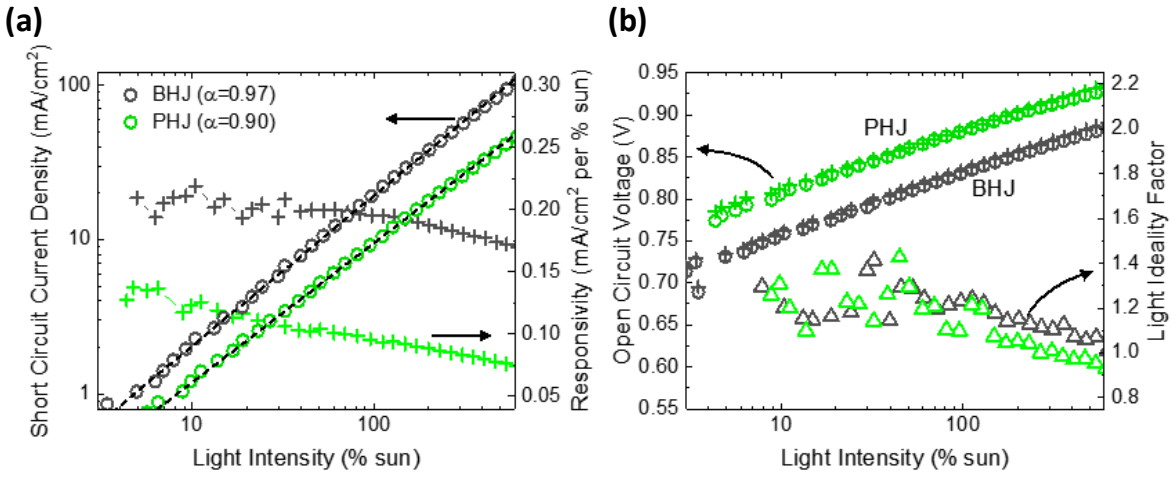


Figure 5.2.4. (a) J_{SC} and responsivity at short circuit versus the light intensity in units of sun equivalent illumination density. The dashed lines are power law fits over the range shown here. Fitted exponents α for BHJ and PHJ are shown in brackets. **(b)** V_{OC} and light ideality factor versus the light intensity. Circles are measured values and crosses show the values of V_{OC} reconstructed from optoelectronic measurements to validate the experimental results.

In order to assess the effect of charge accumulation on the recombination kinetics and hence on V_{OC} and on the field dependence of the *JV*-curve, the charge carrier density and lifetime are measured as discussed before. The accurate V_{OC} reconstruction shown in **Figure 5.2.4 (b)** again demonstrates that the measured values are accurate spatially averaged measures of charge density and lifetime. The good agreement between the differential capacitance and charge extraction measurements also seems to indicate a negligible contribution of field-dependent generation between short-circuit and open-circuit conditions (DC uses the current transient at short-circuit combined with the voltage perturbation at open-circuit).

In close analogy with the observations made for the evaporated PHJs and BHJs, a lower charge carrier density is accumulated in the PHJ (**Figure 5.2.5 (a)**) leading to an increase in charge carrier lifetime (**Figure 5.2.5 (b)**) at the equivalent V_{OC}. This is related to the charge carrier density at the D/A interface where recombination occurs. In the PHJ the limited interface requires a lower charge carrier density to sustain the same potential difference across the interface. The charge carrier density exhibits a smaller slope parameter in the PHJ, while the slopes of the lifetime are comparable. As a result, when plotting the charge carrier lifetime versus the charge carrier density the lifetimes converge towards higher charge carrier density (**Figure 5.2.5 (c)**). **Figure 5.2.5 (d)** additionally shows the lifetime as a function of generation current (calculated by assuming the sub-linear behaviour of the J_{SC} is due to non-geminate losses). This may give additional weight to the charge density directly at the charge

generating interface from where charges diffuse into the bulk of the neat materials at open circuit.

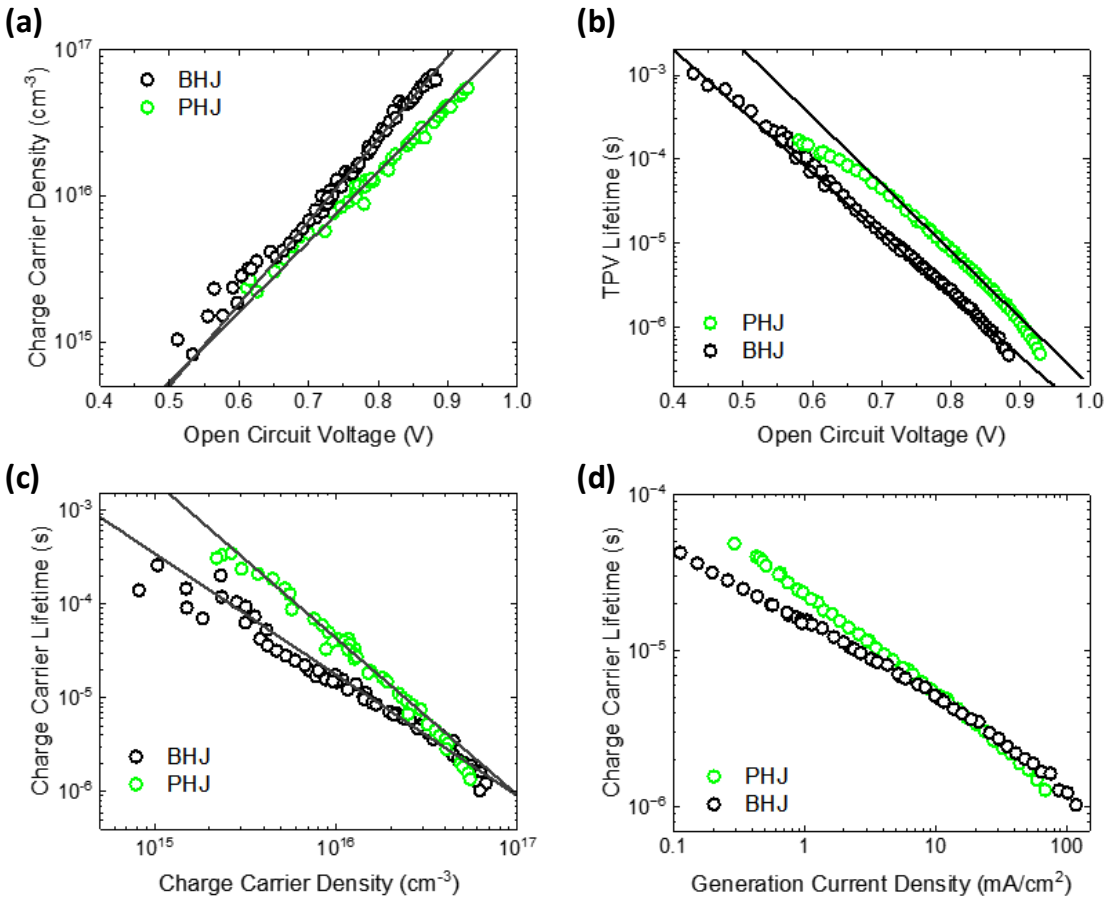


Figure 5.2.5. (a), (b) Charge carrier density and TPV lifetime versus the open circuit voltage. **(c)** Charge carrier lifetime versus charge carrier density. **(d)** Charge carrier lifetime versus generation current density. The generation current density was calculated from the J_{SC} data assuming that any deviation from a power law exponent of 1 is caused by non-geminate recombination.

Despite the lower interfacial area in the PHJ, the charge carrier lifetimes become comparable above a charge carrier density of 3×10^{16} cm^{-3} (> 2 sun equivalent light intensity in the PHJ). This may indicate that at low generation current densities, the charge carriers are more evenly distributed in the PHJ, reducing the charge carrier density at the interface, and thereby enabling longer charge carrier lifetimes. Increasing the light intensity and therefore the highly localised charge generation at the D/A interface leads to an increasing charge carrier density relative to the spatial average leading to an increase of the apparent recombination rate (δ = 2.7). Meanwhile the BHJ exhibits approximately second order kinetics throughout (δ = 2.3, deviations from second order may stem from accumulation of charges in tailstates)[9]. In accordance with this, the lifetime plotted versus the generation current density highlights the

non-uniform charge carrier density distribution in the PHJ and the role of the density at the interface.

These findings are in qualitative agreement with the findings in **Subchapter 4.3** and highlight that the charge carrier lifetimes determined from TPV are not representative of an intrinsic charge carrier lifetime but rather that of a spatially averaged lifetime including a component due to transport to the interface that slows down the effective lifetime. Other methods such as transient photocharge measurements[66] may mitigate experimental limitations such as the effect of the spatial distribution of charge carriers on the photovoltage deflection measured in TPV but will still only yield spatially averaged charge carrier kinetics without knowledge about the spatial distribution of charge carriers in the devices. To relate the observed charge carrier kinetics to the interfacial recombination properties, electroluminescence measurements were carried out by Tack-Ho Lee and Weidong Xu.

5.2.7. Electroluminescence and Photoluminescence Emission Spectra

Figure 5.2.6 **(a)** shows the electroluminescence emission spectra of the PHJ and BHJ devices at an injection current density of about 19 mA/cm^2. The spectra differ significantly which may be a result of excitonic emission dominating the PHJ spectra in line also with the increased emission yield shown in **Figure 5.2.6** **(b)** for varying injection current densities.

To further analyse the electroluminescence spectra, a comparison with the PL spectra shown in **Figure 5.2.3** **(a)** and **(b)** as well as the PL emission of neat IT-4F is necessary. **Figure 5.2.6** **(c)** and **(d)** show the device EL and PL emission in a side-by-side comparison also with the neat IT-4F film PL. The emission spectrum of the PHJ resembles that of the device PL emission with a main 0-0 peak around 810 nm (1.531 eV) and a secondary 0-1 peak around 900 nm (1.377 eV) that is more pronounced in the EL. In contrast to that, the BHJ's EL emission is dominated by a peak centred around 910 nm (1.362 eV) that is roughly equivalent to the secondary peak of the PL emission. It also shows additional shoulders to either side that roughly coincide with the 0-0 and 0-2 peaks of the vibronic progression.[67]

Both devices show an increase of emission in the low energy part of the EL spectrum. This may be expected as charge injection is expected to occur into the lowest lying energetic states. Over the range shown herein that was limited by the use of a silicon detector, even at the lowest injection current density excitonic emission features present in the PL also dominate the EL measurements and no CT feature can clearly be resolved in BHJ and PHJ.

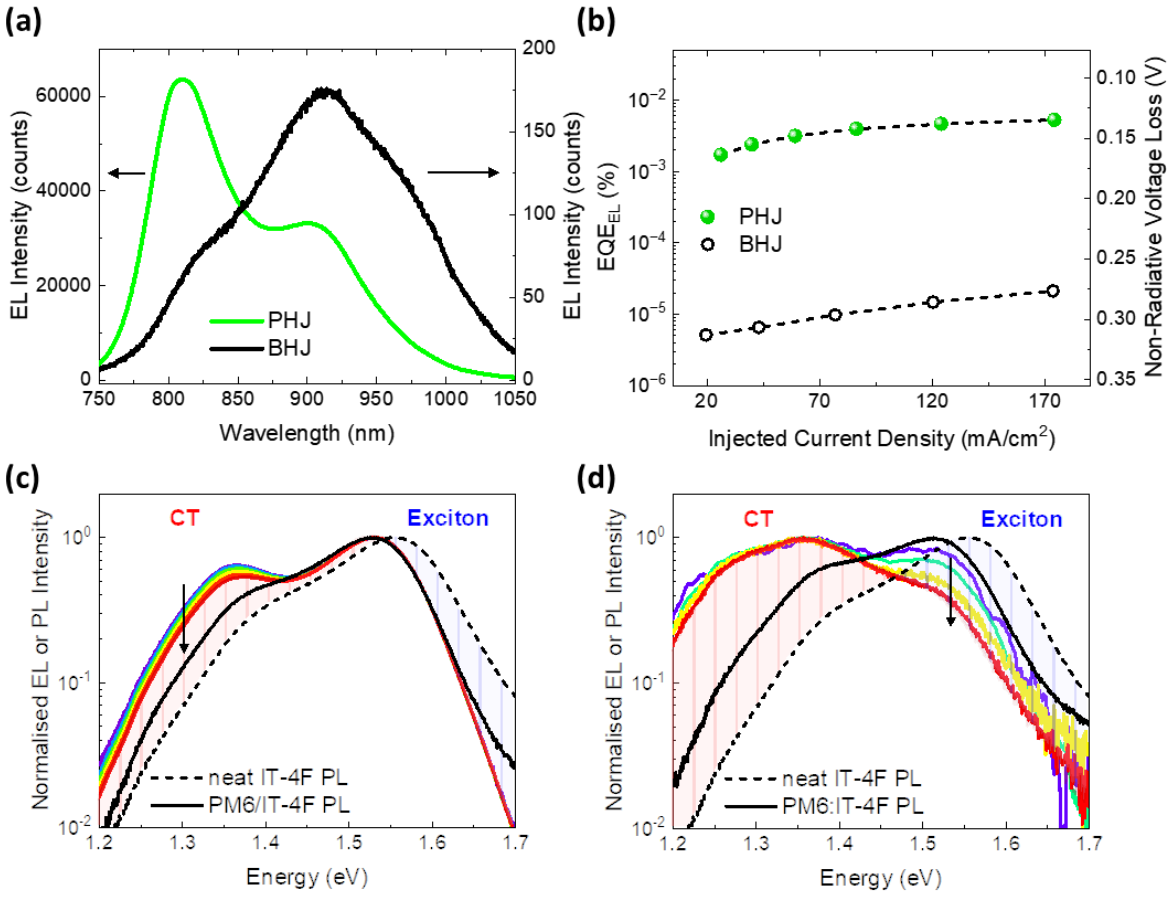


Figure 5.2.6. (a) Electroluminescence spectra of the BHJ and PHJ at an injection current density of 19 mA/cm^2. **(b)** Quantum yield of the electroluminescent emission versus the injected current density. **(c), (d)** Normalised PL and EL spectra of the PHJ and BHJ, respectively, for a range of injected current densities from ~19 to 180 mA/cm^2. The coloured lines are the EL spectra and the arrows indicate increasing current density. Additionally shown is the PL of neat IT-4F films. EL and PL measurements carried out by Tack Ho Lee and Weidong Xu.

The BHJ shows an increased emission intensity in the low energy tail which may originate from CT state emission. The increase in the low energy emission due to emission of increasing CT character in the BHJ device is in line with the increased interfacial area of such states and the role in reducing V_{OC}. The close resemblance of the PHJ EL with the excitonic emission demonstrates the reduction in the radiative recombination through CT character states and a significant hole injection into the acceptor layer. This results in the high emission quantum yield shown in **Figure 5.2.6 (b)** that is two orders of magnitude higher than in the BHJ. However, as shown above the increase in radiative recombination due to the higher quantum yield of excitonic emission only leads to a modest increase in V_{OC} below what might have been expected from the calculated non-radiative voltage losses. As previously pointed out for the non-fullerene acceptor Y6, the high emission yield stemming from more emissive excitons

does not increase the V_{OC} since the majority of recombination events still proceeds through interfacial CT states.[68] This is demonstrated by the short charge carrier lifetimes on a similar order as the BHJ at for an increasing charge accumulation at the interface.

5.2.8. Conclusion

The long exciton diffusion length of IT-4F enables high photocurrent generation in comparatively thick planar heterojunction devices using a 40 nm IT-4F layer. While thicker acceptor layers limit the fraction of excitons diffusing to the D/A interface, thinner acceptor layers result in a loss of absorption thereby limiting the photocurrent. The overall maximum PHJ performance still lacks behind BHJ equivalents due to the – still – limited generation current as well as the low *FF*. The latter is assigned to a small increase in the field-dependence of generation[65] as well as additional non-geminate losses as deduced from the sublinear dependence of the J_{SC} on light intensity. The smaller, well-defined interface of the PHJ devices leads to an increase in the V_{OC} that is related in part to a small shift in the photovoltaic gap and an increased charge carrier lifetime at equivalent interfacial QFLS approximated by the V_{OC}. This is a direct result of the spatial separation of holes and electrons in across the planar heterojunction. In order to further study the effect of the charge carrier density profile and its role in yielding an increase in V_{OC} as well as to further investigate potential intrinsic *FF* limitations arising from the high generation density per unit D/A interface, drift-diffusion simulations should be employed. While the change in voltage losses reported herein can be explained by kinetic considerations and does not require explicit determination of the CT state properties in BHJ and PHJ devices, electroluminescence measurements at lower injection current density and extending to 1 eV by using an InGaAs detector could enable a further investigation of the properties of the CT state on the voltage losses and the field-dependence of generation. Interfacial engineering has already been shown to produce favourable interface properties in PHJs prepared by a film transfer method.[45] Without the need of fine-tuning the active layer morphology and with their increased stability, IT-4F-based PHJ devices may offer an interesting approach for real world OPV or OPD applications. The dark current and detectivity are further investigated in the original publication.[51] Whether there is a fundamental trade-off between device fill factor and high generation current at the limited interface of planar heterojunctions should be addressed in future publications.

5.3. Orientation-Dependent Electrostatic Effects in PM6/Y6 Planar and Bulk Heterojunctions

5.3.1. Background

In addition to OPD and OPV applications, planar heterojunctions are also of academic interest to study physical phenomena at a well-defined interface without additional effects due to morphological or conformational changes.[69] The energy levels at the donor/acceptor interface are a key factor determining the efficiency of free charge generation[70,71] and the magnitude of voltage losses[72–74] in organic solar cells and are highly dependent on morphology and molecular orientation. When pairing wide-gap donor polymers with narrow-gap NFAs, the HOMO-HOMO offset (ΔE_{HOMO}) is the lower of the two offsets and hole-transfer the limiting charge generation step.[59] ΔE_{HOMO} also controls the upper limit of the V_{OC}. Accurately determining ΔE_{HOMO} is therefore key to determine trade-offs between the upper voltage limit and charge generation and assess performance limits of organic solar cells.

While the energy levels of isolated molecules are solely affected by their molecular structure, in reality also inductive[75–77] and electrostatic effects[8,71,78–80], that are dependent on the molecular packing, affect the energy levels of the donor and acceptor component. The former can often be observed by a change in the optical gap upon aggregation, while the latter results in an energetic shift of the HOMO and LUMO level.[75,81] Electrostatic effects may be caused by intrinsic molecular dipole moments[82–84] or dipoles formed at an interface due to ground state charge transfer between a donor and an acceptor[50]. More recently, it was argued that the molecular symmetry and typical packing structures cancel molecular dipoles within films and that the electrostatic interactions on relevant length scales are dominated by the molecular quadrupole moment.[71,80,85]

The dominating molecular quadrupole moment is directed in the π-stacking (Q_π) direction of small molecules and therefore the effect is highly orientation dependent.[71] Dong *et al.* demonstrated the changing orientation of α–6T molecules can create an energetic offset at the boundary between differently oriented domains of 0.4 eV which enabled charge generation in a homojunction of the material.[86] Such orientation-dependent shifts have been demonstrated in a range of highly symmetric evaporated materials such as pentacene,[87,88] SubPc,[89] and various derivatives of ZnPc[71,90] but have proven more difficult to demonstrate experimentally in solution-processed materials.

Also Y6 has a large quadrupole moment in the π-stacking direction that has been linked to the observation of barrierless charge generation in blends with PM6.[8] Simulations predict a downwards bending of the energy levels of Y6 when moving from the interface into the bulk of the material resulting in a driving force for charge generation despite the absence of a significant ΔE_{HOMO} at the interface.[91] These observations were further extended for a range of materials suggesting that such bending is necessary to generate charges efficiently at minimal offset.[59] As pointed out by Eisner and Nelson, this comes at the expense of additional voltage losses as the upper limit of the V_{OC} is now lowered by the amount of the band bending.[92]

As discussed above, inductive and electrostatic effects are highly dependent on morphology and molecular orientation. Direct determination of donor and acceptor energetic levels in blends is difficult to achieve.[93] The energetic levels of neat films determined by photoelectron spectroscopy techniques such as ambient photoelectron spectroscopy (APS)[94] may only serve as a rough guide to the energy levels of the blend. APS measurements on the blend, on the other hand, are dominated by the shallower of the two HOMO levels. Planar heterojunction systems offer an elegant way to assess the interfacial energetics prior to deposition of the top layer without affecting the morphology of the bottom layer.

Previous studies had shown the strong impact of solvent choice (chloroform (CF) versus chlorobenzene (CB)) on the orientation of Y6 molecules in blends.[20] When depositing neat Y6 films from CB or CF, an astonishing orientation dependent shift of the material energetics was found and reported here for the first time in a solution processed system.[52] APS and Kelvin probe measurements were combined to determine the HOMO and Fermi levels, respectively. This is complemented by simulations. By using the film transfer method to make PHJ OSCs, the effect of the energetic changes on the performance in working devices was studied. Transient optical and optoelectronic measurements were carried out to elucidate the generation efficiency and open circuit voltage changes, respectively. Finally, the observed effects were extrapolated to BHJs produced from the same solvents.

5.3.2. Contributions

The results discussed herein will largely focus on the observations regarding the non-geminate recombination kinetics and V_{OC}. A more in-depth discussion of the effect on charge generation as well as additional background for the energetic measurements is given in the original publication.[52] The results shown here are based on devices prepared by Tack-Ho Lee and

Chiara Labanti. Energetic measurements were carried out by Yuang Fu with additional support by Yi-Chun Chin who also provided the simulations of the molecular quadrupole moments. Tack-Ho Lee and Yifan Dong measured and analysed the transient optical results. Daiki Minami provided the molecular dynamics simulations.

5.3.3. Orientation Dependent Energetic Shift in Neat Acceptor Films

By choosing solvents with different boiling points, the molecular orientation of Y6 in spin-coated films can effectively be altered. In this study low boiling point chloroform (CF) and high boiling point chlorobenzene (CB) were used resulting in a face-on and mixed orientation of the Y6 molecules, respectively. This was confirmed by GIWAXS measurements revealing an increased polar angle distribution of the π- π-stacking peak of in Y6 CB films. Atomic force microscopy additionally confirms an increases surface roughness in Y6 CB. These results are discussed in more detail in the original publication[52] and are in line with previous morphological studies.[20,21,95] **Figure 5.3.1** **(a)** schematically depicts the metastable face-on orientation adopted in Y6 CF and the mixed-orientation in Y6 CB films. The results are further supported by the reduced absorbance at similar film thickness in the Y6 CB film. This points to a more random orientation of the optical transition dipole moment (**Figure 5.3.1** **(b)**). The slightly lower optical gap of Y6 CB (1.38 vs 1.41 eV) may be explained by stronger delocalisation effects in more tightly aggregated Y6 molecules as previously suggested.[20]

The energy of the HOMO and Fermi level (E_f) were measured for the two films by APS and Kelvin probe, respectively.[9,55,86,96] **Figure 5.3.1** **I** shows the measured energy levels of as-cast films that were used for the further experiments. A large downward shift of 210 meV from -5.62 eV to -5.83 eV was observed when moving from Y6 CF to Y6 CB. The gap between E_{HOMO} and E_F was slightly reduced from 1.15 eV to 1.13 eV for Y6 CF and Y6 CB, respectively, in line with the observed small changes in the optical gap. Based on these results, a shift of E_{LUMO} similar to that of E_{HOMO} is expected. The publication further shows the photoemission spectra as well as the results for thermally annealed films. Due to the probing depth of the APS measurement of the order of 5 – 10 nm[94], the measured values of E_{HOMO} should reflect the energy levels in the bulk of the Y6 layers.

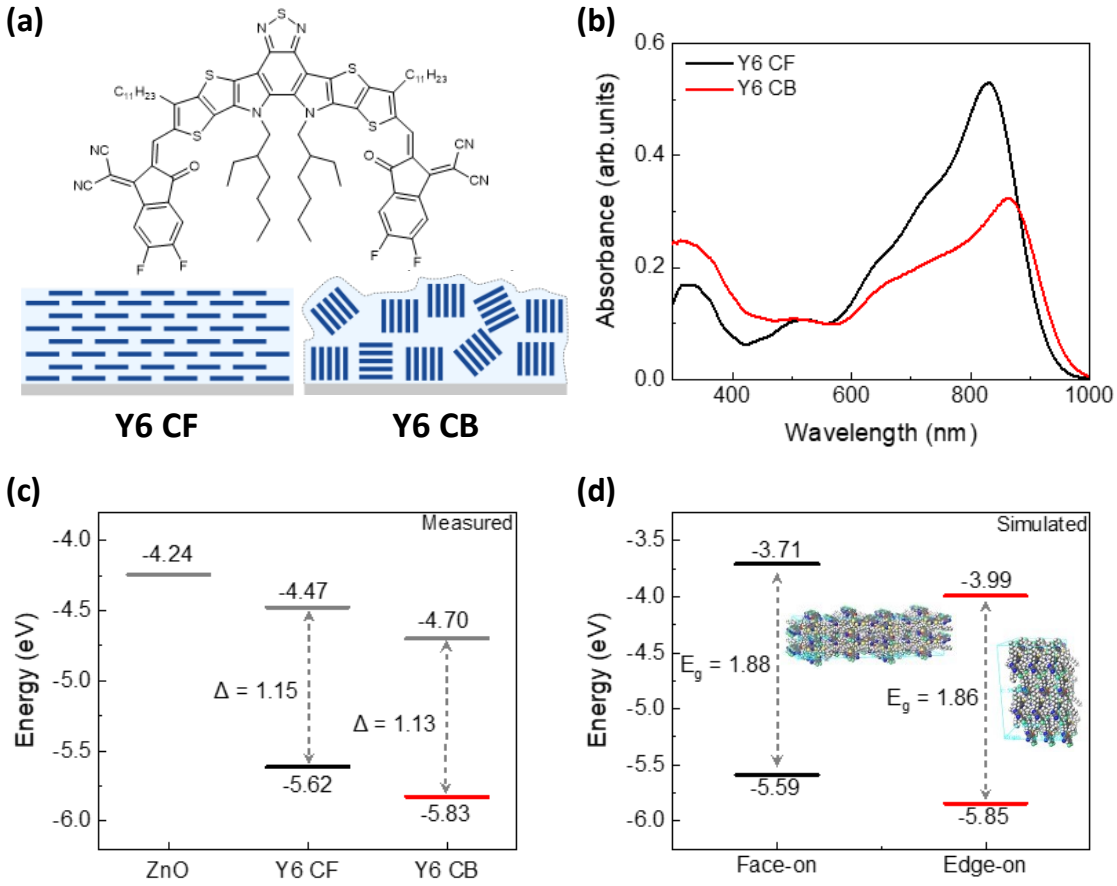


Figure 5.3.1. (a) Chemical structure of Y6 and schematic representation of the Y6 orientation and packing in films spin-coated from CF or CB. **(b)** Absorption spectra of the Y6 films deposited from CF and CB. **(c)** Fermi and HOMO energy level measurements as determined from Kelvin probe and APS measurements, respectively. **(d)** Simulated HOMO and LUMO energy levels obtained from molecular dynamics simulations of face-on and edge-on oriented Y6 clusters with alternate and eclipsed packing structure, respectively. Absorption spectra were measured by Yuang Fu. Measured and simulated energetics provided by Yuang Fu and Daiki Minami, respectively.

The measurements discussed here are the first direct observation of such a large shift of E_{HOMO} in solution-processed acceptor materials. Previous measurements on very regularly packing evaporated α–6T had shown orientation dependent HOMO level shifts of a similar magnitude that could be assigned to quadrupole mediated electrostatic interactions.[86] To further support the above experimental observations and their assignment to the effect of the stronger effect of the molecular quadrupole moment shifting the E_{HOMO} downwards in Y6 CB, density functional theory (DFT) simulations were carried out by Yi-Chun Chin demonstrating a large positive Q_π of 192 ea_0^2. Complimenting the DFT (b3lyp/6-31 G**) results with molecular dynamics (MD) simulations by Daiki Minami, shows that taking charge-quadrupole electrostatic interactions into account can leads to a predicted HOMO level shift of 260 meV

when switching from a face-on to a fully edge-on orientation (**Figure 5.3.1 (d)**). Additionally, a small decrease of the bandgap is predicted for the edge-on case (1.88 eV to 1.86 eV). The observed trends for pure face-on and edge-on simulations are in remarkably good agreement with the experimental results. Strong intermolecular electronic coupling in Y6 compared with other NFAs had previously been demonstrated by MD simulations.[97] Carrying out the simulations for differently oriented dimers (without taking charge-quadrupole interactions into account) resulted in negligible changes in the HOMO/LUMO energy levels. This further supports the assignment of the observed shift to the occurrence of strong molecular orientation dependent charge-quadrupole interactions. As this effect is expected to be diminished at the boundary of the Y6 phases, an upwards bend banding may be expected there in line with the positive Q_π value of Y6.[71]

5.3.4. Bilayers and Planar Heterojunction Devices

Having established the origin of the energy level shift in the Y6 layers produced from CB and CF, bilayers were produced by Tack-Ho Lee through the polymer film transfer technique discussed before. To investigate whether the underlying acceptor layer also affects the energetics of the polymer film transferred onto it, a thin 5 nm PM6 film was deposited on top of the CF and CB films. Fine tuning of the polymer film thickness is possible by changing the concentration of the PM6 solution in the organic solvent from which the film is formed on top of water. Besides affecting the E_{HOMO} of Y6, the orientational changes were subsequently shown to also affect the HOMO levels of the thin 5 nm PM6 layer deposited on top of the Y6 CF and Y6 CB layers, respectively, as shown in **Figure 5.3.2 (a)**. Interestingly, the shift experienced by the PM6 diminishes for layer thicknesses larger than 5 nm which demonstrates the short range of such effects[52] also in line with previous reports in evaporated systems.[71] Based on these results, a downwards band bending of the PM6 electronic levels towards the Y6 interface is expected. Y6 CF shows a larger effect on the thin PM6 layer, downshifting the HOMO level by about 100 meV. This may be explained by the better alignment of the Q_π moment perpendicular to the interface while the CB with its more mixed morphology shows a smaller effect. Markina *et al.* computationally demonstrated similar effects at rough versus planar interfaces.[91] Significant effects caused by vacuum level shifts due to integer charge transfer were ruled out as described in the Supporting Information of the publication.[52]

Following this, PHJ devices were fabricated by Tack-Ho Lee with the structure ITO/ZnO/Y6 (40 nm)/PM6 (30 nm)/MoO_x/Ag. The effect of the changing material energetics and

interfacial band bending affects the charge generation efficiency of the PHJ devices. The absorbance and EQE spectra of the bilayer films and the corresponding devices are shown in **Figure 5.3.2 (b)**. They suggest that for the Y6 CB device the internal quantum efficiency of charge generation is reduced in the PM6 region of absorption and increased in the Y6 region of absorption. While the latter may be a result of the observed band bending effects affecting both generation as well as non-geminate recombination (see **Figure 5.3.2 (d)** light intensity dependence of the responsivity), the former may result from the reduction of electron or energy transfer efficiency following PM6 excitation due to the changing orientation and orbital wavefunction overlap at the interface between PM6 and Y6 CB. Note that the exciton lifetime of Y6 CB determined by time-correlated single photon counting experiments is decreased contrary to what maybe expected from the improved generation efficiency in Y6 CB bilayer devices (see supporting information of the publication). These observations are discussed in more detail in the publication drawing on results from TAS and PL quenching measurements.[52]

The *JV*-curves of the PHJ devices are shown in **Figure 5.3.2 I**. Relative to the CB device, the CF device shows an improvement of all *JV*-parameters. The J_{SC} is increased from 4.95 to 6.21 mA/cm^2 in part due to the differences in charge generation described above as well as additional limitations of non-geminate losses discussed below. Light induced surface photovoltage (SPV) measurements of the neat acceptor layers suggest that both Y6 layers may produce a small number of charges with the more aggregated Y6 CB film showing an increased SPV signal. However, this is not expected to contribute significantly to the charge generation over the region of interest. Such contributions will be discussed further in **Subchapter 5.4**. *FF* shows an improvement from 0.578 to 0.699. This change seems to be mainly due to an increased slope around V_{OC} while the field dependence around J_{SC} appears to be similar for both devices. Finally, the most striking influence of the material energetics is the shift in the device V_{OC} by 110 mV from 0.75 V to 0.86 V for the CB and CF PHJ, respectively. Compared to the total difference of ΔE_{HOMO} of 260 meV (when taking the PM6 interfacial shift into account) between the two devices, this is unexpectedly small. The device PCE is consequently improved from 2.13% to 3.73%. A comparison with the corresponding BHJ performances will be provided later.

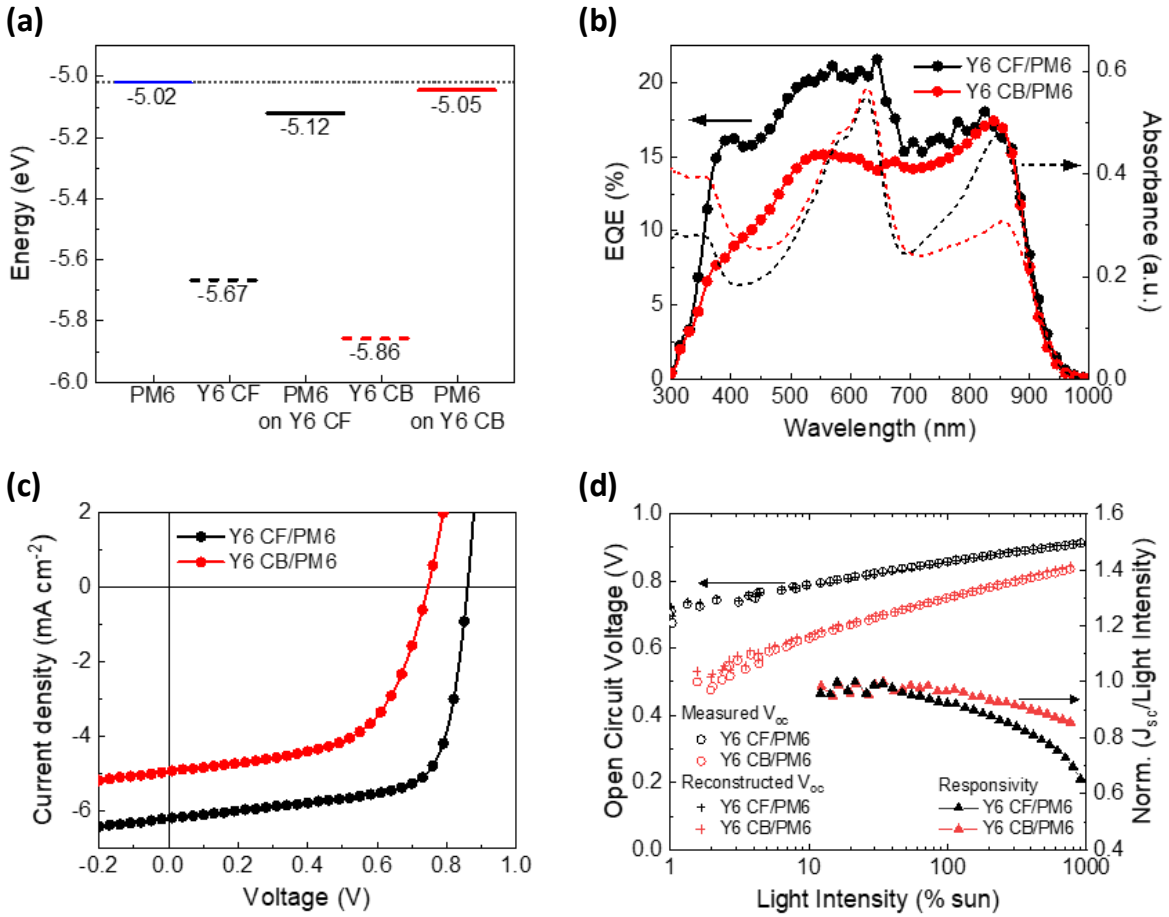


Figure 5.3.2. (a) HOMO energy level of neat PM6 compared to thin layers of PM6 deposited on top of Y6 CF and Y6 CB. Additionally, the HOMO energy level of the Y6 layers deposited from both solvents following thermal annealing are shown. This is consistent with the processing conditions used for the preparation of the PHJ devices. **(b)** EQE and absorption spectra of the full PHJ devices and bilayers, respectively. **(c)** JV-curve of the PHJ devices. **(d)** Light intensity dependence of the V_{OC} and normalised responsivity. The latter was calculated by dividing the J_{SC} by the corresponding light intensity. The crosses signify the values of the reconstructed V_{OC} determined from the transient optoelectronic measurements discussed later. Energetic and EQE measurements carried out by Yuang Fu and Tack-Ho Lee, respectively.

Figure 5.3.2 **(d)** shows the light intensity dependence of the V_{OC} and the normalised responsivity (calculated by dividing the J_{SC} by the corresponding light intensity) for both PHJs. The CB PHJ shows a lower V_{OC} over the entire light intensity range and a significantly increased ideality of approximately 1.5 compared to an ideality factor of close to 1 for the CF PHJ. This may be a result of the non-geminate recombination having a strong monomolecular contribution. Turning to the responsivity, the CB device shows reduced current losses at increasing light intensity in line with a reduced contribution of non-geminate recombination at higher generation rates. Possible explanations for the observations will be discussed in the next section.

5.3.5. Planar Heterojunction: Charge Carrier Kinetics

In order to investigate the effect of electrostatically induced energy level shifts on the non-geminate recombination kinetics as well as the V_{OC} change transient optoelectronic (differential capacitance and transient photovoltage) analyses were carried out. A particular focus will be set on explaining the discrepancy between the energetic shift and that of the V_{OC}, given that typically a linear dependency of these quantities is expected.[98] In line with the results of the evaporated PHJ, the Y6 PHJs studied here show an additional light intensity independent capacitive contribution in charge extraction experiments. This results in discrepancies with the results obtained from differential capacitance measurements. All charge carrier density results quoted from here on are therefore derived from the DC measurements that correctly predict V_{OC} (as shown in **Figure 5.3.2 (d)**) and loss current.

Figure 5.3.3 (a) depicts the differential capacitance results for the two bilayer systems together with exponential fits to the active layer capacitance. As expected from the similar device thickness, both devices show almost identical geometric capacitance values. It is apparent that the CF PHJ's effective electronic bandgap is shifted by about 220 mV when assessed at an equivalent value of the differential capacitance. This is in good agreement with the measured shift of the HOMO level observed in the Y6 films. At equivalent light intensity (and approximately equivalent generation current), the CB device supports significantly more charge. If as the DC results suggest, a similar shape of the DoS is assumed, this means that the Fermi level in Y6 CB is closer to the LUMO energy band edge compared to the CF device. Consequently, the difference in photovoltage at equivalent light intensity is expected to be less than the observed energetic shift.

Such additional charge accumulation is equivalent with an increase in the lifetime of the spatially averaged charge carrier density. **Figure 5.3.3 (b)** shows the obtained charge carrier lifetime versus the charge density per unit area. The data was plotted here per unit area since a uniform charge carrier distribution cannot be assumed in PHJs as previously discussed. The CB PHJ shows a strongly increased lifetime with a similar recombination order (similar slope of τ vs n). Such an increased lifetime is further supported by TAS measurements by performed by Tack-Ho Lee and Yifan Dong in the publication.

Assessed at equivalent values of the charge carrier density, the CB device shows a 50-fold increase in lifetime. The change in charge carrier kinetics can be converted into a gain in potential by utilising the following equation:

$$\Delta V_{oc}^{kinetic} = -\frac{n_{id}kT}{q}\ln\left(\frac{J_{BI}^{CF}}{J_{BI}}\cdot\frac{J_{gen}^{CB}}{J_{gen}^{CF}}\right)$$

where n_{id} is the ideality factor, kT is the thermal energy, q is the elementary charge, J_{BI} and J_{gen} denote the non-geminate loss current $\left(\frac{J_{BI}^{CB}}{J_{BI}^{CF}} = \frac{1}{50}\right)$ and generation current (approximated as J_{SC}), respectively. A kinetic V_{OC} loss of 110 mV for the CF device relative to CB was calculated, which in addition to the 220 mV change of the effective electronic gap determined from differential capacitance measurements takes the difference in V_{OC} to 110 mV. This is in excellent agreement with the experimentally observed difference! Also, the demonstrated V_{OC} reconstruction indicates that the charge carrier density and lifetime data shown here accurately describe the spatially averaged charge carrier kinetics.

The observations made here are fully consistent with earlier observations regarding voltage shifts and charge carrier kinetics in SubPC/C_{60} planar heterojunctions.[99] An increase in the energetic gap was found to be partially counteracted by kinetic contributions in two PHJs deposited from different evaporation sources. Alterations in the evaporation process had been shown to lead to differences in the SubPC orientation and subsequent energetic changes.[89]

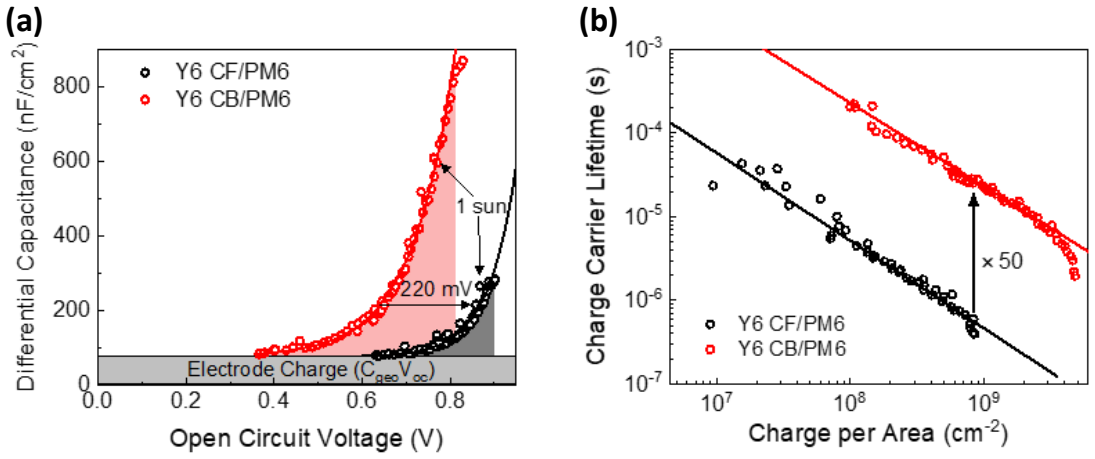


Figure 5.3.3. (a) Differential capacitance of the PHJ devices with exponential fits of the chemical capacitance. The shaded area under the exponential signifies the active layer charge. At the bottom also the charge stored on the electrodes is shown. **(b)** Charge carrier lifetime versus the charge per unit cell area.

5.3.6. Interpretation of Non-Geminate Recombination Analysis

The change in charge carrier lifetime is assigned to a change in the charge carrier distribution in the PHJs due to interfacial band bending rather than a change in the fundamental lifetime of interfacial states at the D/A interface resulting in changes to the radiative/non-radiative voltage losses. In the following, the case for this will be argued:

In PM6:Y6 solar cells, it is notoriously difficult to assess the properties of interfacial CT states through emission or absorption measurements due to the spectral overlap with the excitonic states.[8,68] Especially in bilayers where it has been shown extensively in this thesis that the emission is dominated by the excitonic emission even in larger-offset systems, this would be the case. Therefore, correlation of the voltage losses to changes in CT state properties is difficult here.

However, experimental and theoretical studies may be helpful in ruling out intrinsic CT state lifetime changes as the origin of the recombination related voltage loss. Firstly, assuming that the bulk energetics translate to changing interfacial energetics – without any interfacial band bending present – the recombination loss due to non-radiative CT state recombination would be expected to be higher for the CB according to the energy gap law.[6,100] This contradicts our observations. As previously shown, the density of interfacial states may directly influence the recombination losses. This has also been demonstrated experimentally and theoretically elsewhere.[6,56,101] However, the surface roughness and hence the density of interfacial states is increased in the case of CB resulting in a predicted increase of the recombination rate and voltage losses. Due to the face-on orientation with respect to the interface the electronic coupling between interfacial Y6 and PM6 units would be expected to improve for the CF devices. Several studies show that this is predicted to result in a decrease in recombination related non-radiative voltage losses.[6,102,103] Again, this is contradicting the observations made here. CT state disorder has also been linked to increasing non-radiative recombination[104,105] yet would be expected to increase at the interface of Y6 CB and PM6. Without further knowledge of the properties of the interfacial states, it seems unlikely that their intrinsic lifetime changes by a factor of 50 while also explaining the observed energetic changes.

Instead, the observed changes in the non-geminate recombination kinetics may be consistently explained by invoking the diminishing strength of charge-quadrupole interactions towards the D/A interface in the Y6 film that is predicted to result in an upward

band bending.[71] The strength of this gradient is additionally influenced by the interfacial roughness.[79,91] In the case of CB the stronger electrostatic effects, that are stabilising the HOMO in the bulk of the material, are expected to lead to an increase in the interfacial band bending towards the interface as the strength of the electrostatic interaction diminishes. This is expected to occur over just a few nanometres.[71] Therefore, this would result in a driving force for charge carriers away from the interface, lowering the interfacial recombination rate at equivalent spatially averaged charge carrier densities. This causes a larger number of accumulated charges that can be observed in the differential capacitance measurements. In the case of CB Y6/PM6, the absence of band bending in the PM6 layer at the interface as demonstrated by the APS measurements on various thickness PM6 top layers could further result in a surplus of holes accumulating at the interface. Plausibly this could explain the higher ideality factor in the case of CB Y6/PM6 as recombination is limited by the smaller electron density at the interface. It would also account for the CB PHJ maintaining a higher responsivity at high light intensities due to the efficient spatial separation upon generation at the limited interface. To further support the interpretation of charge accumulation in the bilayer devices, additional evidence from Surface Photovoltage (SPV) measurements is discussed in the original publication. Ultimately, future investigations on bilayers should confirm the above-described effects through drift-diffusion simulations that were beyond the scope of this study.

Figure 5.3.4 schematically illustrates the energy level bending at the interface due to the differences in charge-quadrupole interactions in the two bilayer devices. In the following section, the study will be extended to blend devices deposited from the same solvent systems.

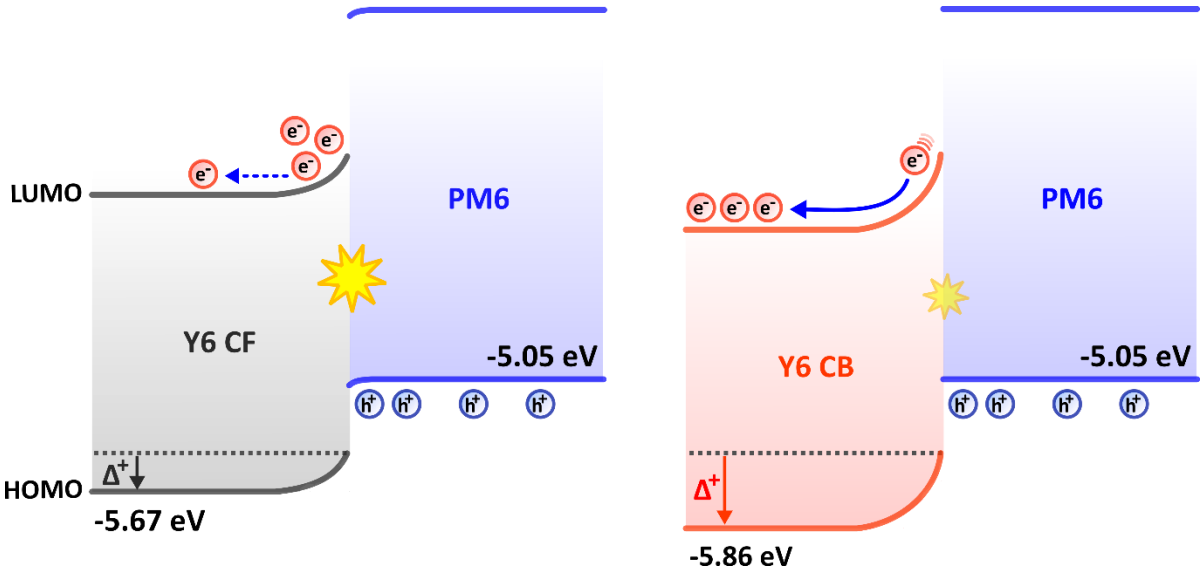


Figure 5.3.4. Schematic representation of the effect of the charge-quadrupole interactions on the band bending at the Y6/PM6 interface. The additional band bending in the Y6 CB layer leads to additional charge accumulation away from the interface which slows down the effective non-geminate recombination rate thereby partially compensating for the energetic penalty on the V_{OC}. Image obtained from the original publication.[52]

5.3.7. Effect of Acceptor Quadrupole on Blend Energetics

The question remains whether the effects observed in PHJ solar cells are relevant to high-performing BHJ solar cells comprised of PM6:Y6 – the "fruit fly" of current high performing systems based on its material derivatives. To this end, PM6:Y6 BHJ films spin-coated from CB and CF were studied here.

As previously mentioned, determining the energetics of the respective components in blend films is difficult to achieve through APS measurements as the spectra are dominated by the shallower of the two HOMO levels. APS spectra carried out on blends therefore only reveal shifts in the polymer HOMO. Neat PM6 films spin-coated from CB or CF showed no appreciable shift in their HOMO levels and no changes in the optical gap. Note that PM6 itself possesses a negligible quadrupole moment.[52] Interestingly, when comparing the APS spectra of neat PM6 spin-coated from CB and CF with the corresponding PM6:Y6 blends deposited using the same solvent, the CF blend exhibited a HOMO level shift while the CB blend remained unchanged. The observed downward shift in the CF blend is of a similar magnitude (87 meV) compared to that observed for a thin layer of PM6 on top of Y6 CF that was discussed above. This would suggest that the CF blend maintains a similar interfacial orientation as the PHJ in line with previous results of preferential face-on orientation of both PM6 and Y6 in blend films coated from CF.[20,21,23] In contrast to that, blends deposited from CB or o-xylene as

another representative higher boiling point solvent resulted in a predominantly edge-on orientation.[20,93] The increased film roughness of the CB BHJ films in AFM measurements (see original publication) also suggest larger domain sizes in line with an interpretation of a more intermixed/edge-on morphology comprised of tightly packed large crystalline phases. This edge-on or mixed orientation in the blend did not affect the measured PM6 HOMO. As a result, also in the BHJ blends a smaller HOMO level offset and hence larger effective electronic bandgap may be expected for the CF compared to the CB BHJ.

Before assessing how these observations translate to the photovoltaic properties of BHJ devices, it is worth noting that the effect of the electrostatic interaction between donor polymer and NFA acceptor quadrupole has been studied for a range of other materials in the framework of this study. **Figure 5.3.5 (a)** shows the calculated Q_π moment of selected representative NFAs of the ITIC family together with IDIC and Y6. All NFAs possess a positive quadrupole moment in line with the molecular A-D-A or A-D-A'-D-A structure they possess. In **Figure 5.3.5 (b)** and **(c)**, the change of the polymer HOMO level upon blending with the NFAs is shown for PM6 and the related PBDB-T. There is a clear correlation between the Q_π and ΔE_{HOMO} for both polymers. Notably, IT-4F with its large quadrupole moment leads to a large downward shift in the PM6 HOMO level. Outliers from the overall trend may be explained by variations in the blend microstructure that have been shown to also affect the PM6:Y6 CB and CF films differently.

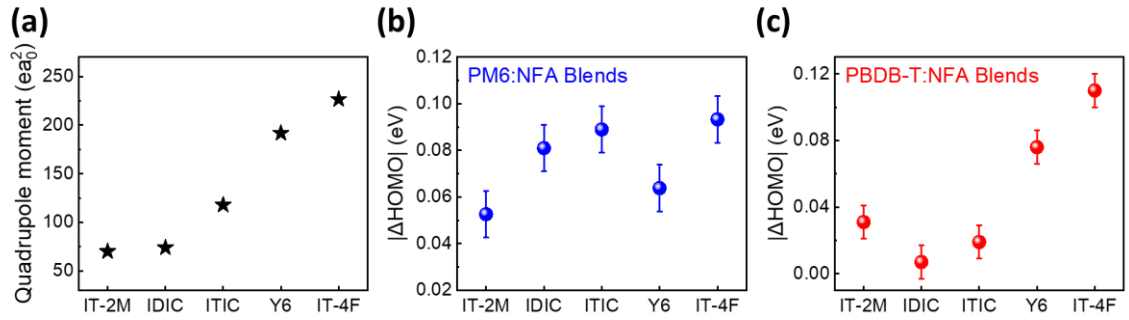


Figure 5.3.5. (a) Molecular quadrupole moment Q_π in π-π-stacking direction for a range of NFAs including ITIC and its derivatives IT-2M and IT-4F, IDIC and Y6. The values were calculated by DFT simulation for isolated molecules. **(b), (c)** Change in polymer HOMO level ΔE_{HOMO} upon blending with the NFAs for PM6 and PBDB-T, respectively. Calculated quadrupole moments provided by Yi-Chun Chin. Energetics measured by Chiara Labanti.

5.3.8. Bulk Heterojunction Device Characterisation

After having established that the relative orientation of the PM6 and Y6 components also affects the energetics in the blend, BHJ devices deposited from CF and CB were prepared and studied analogously to the bilayer devices. **Figure 5.3.6 (a)** shows the *JV*-curves of the BHJ devices with inverted structure (ITO/ZnO/PM6:Y6 (~100 nm)/MoO_3/Ag) produced by Tack-Ho Lee. The CF BHJ shows the superior performance with all *JV*-parameters increasing. Most notably the J_{SC} is improved to 25.5 mA/cm² versus 20.2 mA/cm² for the CB BHJ and the V_{OC} is improved to 0.85 V compared to 0.80 V. Both characteristics accurately reproduce the trends observed by Zhu *et al.* for the same solvent systems[20] and are similar to those observed for a CF/CN vs o-xylene comparison[93]. CN (chloronaphtalene) was used as a solvent additive.

The change in the J_{sc} is mainly due to an increase in the EQE caused by the higher absorption of the CF device in the polymer and acceptor region of absorption (**Figure 5.3.6 (b)**). This may support the above hypothesis of a generally more face-on orientation of the CF blend components resulting in a more in-plane orientation of the transition dipole moment. Additionally, the CF BHJ maintains a higher responsivity at high light intensity (**Figure 5.3.6 (d)**) that is likely related to better charge collection under short circuit conditions. This is supported by the higher effective mobility determined by the charge extraction at short circuit method (**Figure 5.3.6 (c)**). The relative change of the mobility is in good agreement with that found by Zhu *et al.*[20] This improvement in the mobility also explains the increase in *FF*.

Note, that while the trends in extraction time as determined from current transients are the same for BHJs and PHJs alike, the trends in the light intensity dependence of the responsivity reverse for the different device architectures as shown in **Figure 5.3.6 (d)**. While the main limitation of the short-circuit current density in BHJs is the non-geminate loss of carriers while drifting through the disordered blend to the electrodes, the limit to the collection efficiency at short circuit in PHJs is set by the escape time from the planar D/A interface where the non-geminate recombination occurs (or the re-dissociation probability at the interface). The former is primarily limited by the transport properties of the bulk. The latter is dependent on the local mobility and additionally any pronounced bending effects occurring at the well-defined planar interface. Therefore, the responsivity at high light intensity of the CB PHJ benefits from the stronger shift in HOMO level, while the CB BHJ suffers from the reduced mobility of the blend relative to the CF devices.

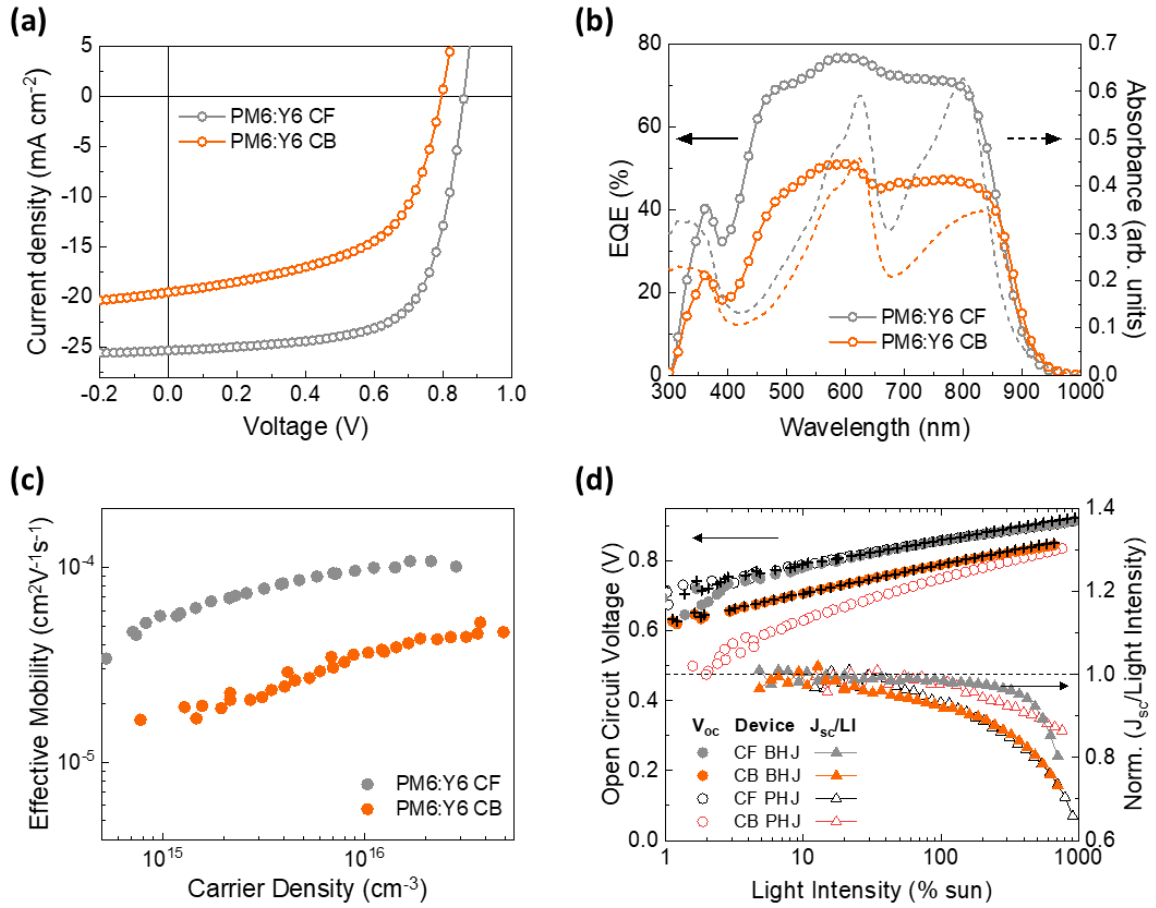


Figure 5.3.6. (a) JV-curves of the BHJ devices deposited from CB and CF. **(b)** EQE and absorption spectra of BHJ devices and films, respectively. Note that the films were of a similar thickness. **(c)** Effective mobility determined from charge extraction at short circuit measurements as previously described.[106] **(d)** V_{OC} and normalised responsivity calculated from the J_{SC} normalised by the light intensity versus the light intensity in units of sun equivalent illumination levels. The crosses show the reconstructed V_{OC} from lifetime and charge carrier density measurements. EQE and absorption measurements by Tack-Ho Lee.

Interestingly, the V_{OC} of neither CF nor CB PHJs benefits from the limited device interface as previously shown for the evaporated bilayer systems as well as the IT-4F/PM6 system (**Subchapters 4.3** and **5.2**, respectively). In the case of the CF BHJ, the V_{OC} and ideality factor is almost indistinguishable from the PHJ as shown in **Figure 5.3.6 (d)**. The CB BHJ shows an improvement of about 50 mV at 1 sun relative to its PHJ equivalent. Its ideality factor is significantly reduced. Both BHJs show a n_{id} of about 1.

The higher V_{OC} of the CF BHJ is in line with what is expected from the downward shift of the PM6 HOMO level in the CF blend that should lead to a reduced offset with the bulk HOMO of the Y6 phase. Additionally, the EQE reveals a slight widening of the photovoltaic gap dominated by the Y6 absorption. To assess the effect this has on the effective electronic gap

and the non-geminate recombination losses of V_{OC}, DC and TPV measurements were carried out.

5.3.9. Bulk Heterojunction: Charge Carrier Kinetics

Figure 5.3.7 **(a)** shows the charge carrier density of the BHJ solar cells versus the V_{OC}. It reveals a shift in the effective electronic bandgap of roughly 90 mV assessed at 1 sun equivalent light intensity. At equivalent light intensity, the charge carrier density accumulated is roughly doubled in the CB BHJ which may be a result of the increasing disorder (40.6 vs 32.1 meV) as well as a reduction in the recombination flux. The smaller difference in the effective electronic gap compared to that of the PHJs is expected due to the disruption of the acceptor phases in blend films that reduces the effect of the electrostatic interactions. Additionally, the smaller respective phases (compared to the 35 nm Y6 layers in the PHJ) would be expected to lead to a more spatially homogeneous charge distribution throughout the BHJ films. Overall, the nature of the complex interface, the additional contribution of morphological disorder, the small shift in the photovoltaic gap and the difficulty in directly assessing the energetic levels in the blend complicate the direct assignment of the changing effective electronic gap to the influence of the electrostatic charge-quadrupole interaction.

The charge carrier lifetimes measured for the BHJs is shown in **Figure 5.3.7** **(b)**. In line with the more homogeneous charge carrier distribution in the BHJ films, the lifetime gain of the CB BHJ is reduced compared to the PHJ case. Still, a 7-fold increase of the charge carrier lifetime at equivalent charge carrier densities results in a kinetic gain of about 40 mV. Together with the shift in the effective electronic bandgap this fully explains the experimentally determined V_{OC} shift of about 50 mV. The reconstructed V_{OC} from lifetime and charge carrier density measurements is shown in **Figure 5.3.6** **(d)**.

Figure 5.3.7 **(a)** also shows the spatially averaged values of the charge carrier density determined for the PHJ devices. The decreasing charge carrier density in the CF PHJ relative to the CF BHJ is in line with an interpretation of a very uneven charge carrier distribution i.e. an increased charge carrier density close to the interface.

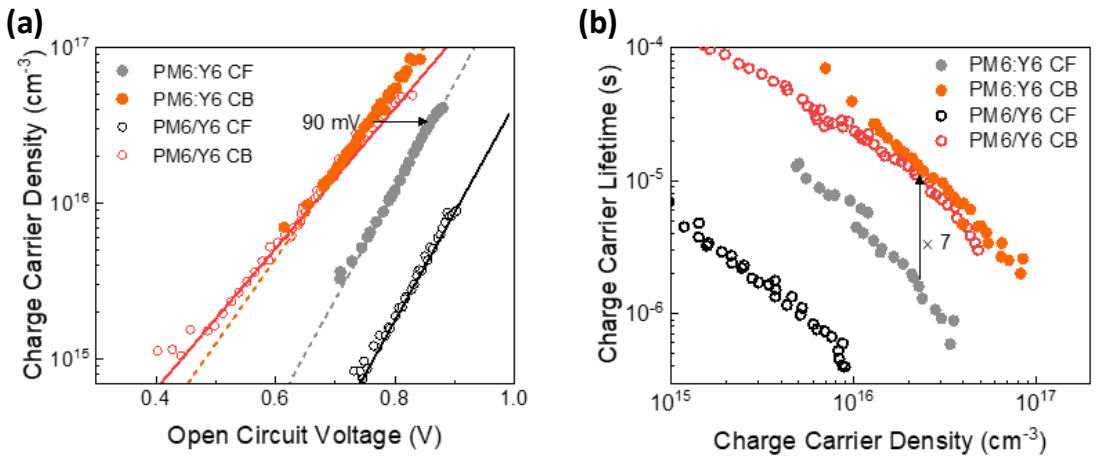


Figure 5.3.7. (a) Charge carrier density versus V_{OC} for the BHJ devices. Additionally, the charge carrier density for the PHJs is shown which was calculated by spatially averaging over the entire active layer. The values were collected for up to a 6 sun equivalent illumination using DC. For CF the CE results are shown that were in generally good agreement with DC but yielded less outliers during the collection. The arrow corresponds to the potential shift at the 1 sun point of the CF BHJ. **(b)** Charge carrier lifetime versus the spatially averaged charge carrier density for the BHJ and PHJ devices.

The Increase In the spatially averaged charge carrier density roughly scales with the Increase in generation current (6.2 vs 25.5 mA/cm^2) in line with a localisation of the charge carrier population around the interface. The comparison of the lifetime plotted against the charge carrier density should be interpreted accordingly as originating from the highly uneven charge carrier distribution in the CF PHJ that results in similar lifetimes at vastly difference spatially averaged charge carrier densities. While such differences likely occur in the CB PHJ and BHJ devices, the lifetime dependence on the carrier density is quite similar for the PHJ and BHJ. Together with the increased generation and decreasing effect of electrostatic HOMO level stabilisation in the BHJ, this may explain the increased V_{OC}. The more uniform charge carrier distribution of opposite carriers with respect to the D/A interface may also explain the lowered ideality factor ($n_{id} \approx 1$) indicative of a second order recombination process compared to the PHJ ($n_{id} \approx 1.5$). The latter had been assigned in the above section to the reduced electron density at the interface as a result of the interfacial energetics giving an increased weight to the electron density in the recombination rate equation.

To summarise: a direct transfer of the conclusions drawn from the bilayer results to the case of blend devices is not straightforward as the complex nature of the BHJ means it is affected by different phenomena. Other previously mentioned studies, show similar trends in the open circuit voltage for CF vs CB and CF/CN vs o-xylene.[20,93] Both analysed the radiative and non-radiative contribution and found with small variations that the change in non-radiative

recombination as determined from EQE_{EL} contributed most to the voltage differences. Other studies related changes in the open circuit voltage and non-geminate recombination kinetics of PM6:Y6 or related derivatives to the disorder and degree of phase separation.[11,107] Furthermore, bandgap narrowing in pure acceptor phases relative to mixed domains (due to aggregation dependent inductive effects) has been proposed to enable efficient generation and would affect V_{OC}.[77] The correlation of the polymer HOMO level shift with the Q_π of the chosen acceptor in blend systems together with the results obtained from planar heterojunctions highlight that charge-quadrupole electrostatic effects should be taken into account when explaining morphology dependent voltage losses. To further study the changing energetics in blend systems, the use of spectroelectrochemical methods should be considered in the future.[93]

5.3.10. Comparison of Planar versus Bulk Heterojunction Systems

A striking difference between the Y6 planar heterojunction produced from either solvent with the previously shown results for the DCV-V-Fu-Ind-Fu-V/C_{60} (**Subchapter 4.3**) and PM6/IT-4F (**Subchapter 5.2**) PHJs is the lack of a voltage gain compared to their BHJ counterparts. As a reminder, the other two systems demonstrated an increase in V_{OC} relative to the BHJ of around 40 – 50 mV. When compared with the BHJs of a similar photovoltaic gap (D:A ratio 2:1 DCV-V-Fu-Ind-Fu-V:C_{60} BHJ, not 1:2) a reduction in the spatially averaged charge carrier density at equivalent values of V_{OC} was shown – in line with the smaller interface requiring a lower total charge at the interface to support the same Fermi-level-splitting. If the interfacial energetics may be assumed to be the same for the PHJ and BHJ, the V_{OC} may be understood as a measure of the charge density at the interface (for suitably chosen transport layers).[108,109] Another consequence of this is the apparent longer charge carrier lifetime at equivalent V_{OC} for the D/C_{60} and PM6/IT-4F PHJs since the charges accumulating away from the interface act essentially as a charge reservoir and do not directly partake in the interfacial non-geminate recombination.

The same observation regarding the spatially averaged charge carrier density was made for the Y6 CF case while the CB PHJ shows a similar spatially averaged charge carrier density to the CB BHJ. This may be explained by pronounced HOMO level deepening in the PHJ case causing additional charge accumulation in line also with the reduced V_{OC}. Interestingly, the lifetime of the devices at equivalent V_{OC} values does not change in the case of Y6 as shown in **Figure 5.3.8**. While the prolonged charge carrier lifetime due to the reduced interface and

charge accumulation away from the interface leads to the apparent shift of the lifetime versus the V_{OC} for the D/C_{60} and PM6/IT-4F, no such shift is observed for either of the Y6 devices. All Y6 devices show a similar dependence of the measured lifetime on the V_{OC} (and approximately the interfacial charge carrier density) regardless of the total accumulated charge carrier density. The lifetime data points are merely shifted along this function dependent on the range of the V_{OC} accessible (for the studied light intensity values of 5 to 600 % sun equivalent illumination) which is determined by the magnitude of the HOMO level shift. No full explanation is given here for this observation, yet it seems that it is a direct result of the low interfacial HOMO level offset and the energy level shift towards the interface affecting the charge carrier accumulation at the interface and their equilibrium with interfacial CT states mediating non-geminate recombination. To this end, the observation of fast recombination despite the apparent barrier by electrostatic effects has previously been raised as a curious property in PM6:Y6 solar cells.[8,107]

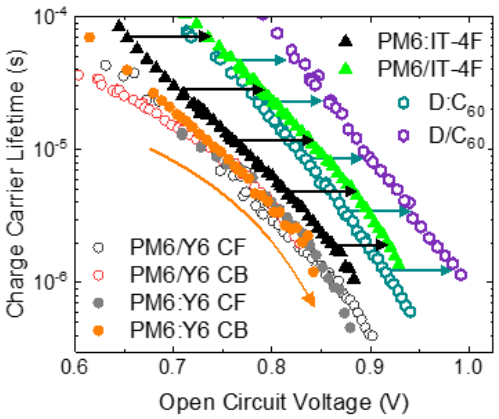


Figure 5.3.8. Charge carrier lifetime determined from transient photovoltage measurements for different material systems in planar and bulk heterojunction configuration. The arrows indicate an apparent shift along the voltage axis when moving from BHJ to PHJ architecture in PM6:IT-4F and DCV-V-Fu-Ind-Fu-V:C_{60} (abbreviated as D:C_{60} in the legend). While the arrow for Y6 devices signifies a shift along a similar functional dependence on the V_{OC} for different solvents and device architectures (PHJ vs BHJ and CB vs CF).

Finally, also the comparatively low photocurrent of the planar Y6 heterojunctions particularly when compared to PM6/IT-4F is noteworthy. Based on the previously determined exciton diffusion length in excess of 30 nm[29,30] and the high absorption coefficient[28] this is surprising. Other bilayer systems containing Y6 with different charge generating interfaces have produced similarly low photocurrents.[65,110–112] Note that the high photocurrents achieved by sequentially deposited pseudo-bilayers may result from partial mixing of the phases at the

interface.[39,40,113,114] The *FF* on the other hand is highly improved compared to the IT-4F planar heterojunctions which may result from fast spatial separation of charges due to the electrostatic effects discussed and the lower generated current density at the interface.

5.3.11. Conclusion

In this study, the effect of the electrostatic charge-quadrupole interaction on the energetics of Y6 films was investigated. Changing the molecular orientation and packing density by using different solvents led to the observation of a downward HOMO level shift of more than 200 meV for more aggregated mixed-orientation acceptor films relative to those with a predominantly face-on orientation. Meanwhile the bandgap remained largely unchanged. This is the first report of such strong orientation-dependent energetic shifts in solution processed films. To study the effect of the electrostatic phenomenon on the charge generation and recombination at a donor-acceptor interface, well defined bilayer films and devices were produced by polymer film transfer onto the acceptor layer. The material energetics correlated well with the effective electronic gap determined from the charge carrier built-up in devices. However, the effect of the narrowing of the electronic gap on V_{OC} was partially offset by the reduced recombination rate caused by an effective barrier to charge non-geminate recombination. Similar albeit weakened trends were observed for bulk heterojunction devices. Here the clear correlation with the material energetics is more difficult than in the planar heterojunction devices because of the complexity of the microstructure and interface. While electrostatic effects such as the charge-quadrupole interaction lead to efficient charge generation in low offset donor/acceptor combinations and can effectively reduce the non-geminate recombination rate, they also set an upper limit to the V_{OC} through the narrowing of the electronic gap as previously discussed by Eisner and Nelson.[92] However, taking this effect into account is crucial to optimise interfacial energetics and further increase organic solar cell performance.

If there is a fundamental energetic driving force required in heterojunctions to facilitate charge generation – be it energetic offsets at the interface or electrostatic band bending effects – what if charges could be generated in a homojunction of a neat material through different generation mechanisms?

5.4. Charge Generation in Neat Non-Fullerene Acceptors

5.4.1. Background

While light absorption in inorganic or hybrid organic-inorganic semiconductors leads to direct free charge generation,[115–118] the weak dielectric screening in organic semiconductors results in the formation of bound excitons upon absorption.[119,120] Some studies have demonstrated a small fraction of (often highly-field dependent) free charge generation in small molecules, homopolymers, or "push-pull" polymers/small molecules (made up of donating and accepting groups).[121–126] Additionally, charge generation has been shown in a homojunction made up of differently oriented small-molecule domains[86] but the energetic offsets at the domain edges essentially makes this a heterojunction. Therefore, all high performance OSCs still rely on the original planar and later bulk heterojunctions that enabled the first efficient OSCs by providing an energetic driving force for exciton separation[127–129] – despite the unavoidable voltage losses caused by employing the heterojunction.[6,92,100]

After the concept of planar or pseudo-heterojunctions has been revived, enabled by the high exciton diffusion lengths of high performing NFAs, also the observation of highly efficient charge generation has been reported in neat layers of Y6[32] raising the possibility of single component OSCs. Have we come full circle, from homojunction to bulk heterojunction and back to homojunction OSCs, through the recent progress in NFA materials innovation?

Price *et al.* indeed argued that under 1 sun conditions 60 to 90% of excitons in neat Y6 films form charges rather than "intra-moiety" charge transfer like states and that they decay bimolecularly rather than geminately. The poor photovoltaic performance was assigned to the poor collection efficiency caused by poor ambipolar transport and fast non-geminate recombination.[32] More modest claims about free charge generation have been made elsewhere relying mainly on the observation of PL quantum yield measurements upon variation of light intensity,[32] temperature,[31] or bias[112]. As previously raised herein, also the bias dependent PL quenching in IT-4F based devices[51] as well as the surface photovoltage measurements on neat Y6 films[52] indicate the occurrence of free charge generation in neat films.

Following these results, single component layers of various NFAs including Y6,[7] IT-4F,[53] IDIC,[130] and IDFBR[131] were studied by Park *et al.*[33] with some results presented in this thesis. The aim was to elucidate the efficiency of free charge generation and the potential for single component organic solar cells or photodetectors (OPD). Particularly for OPDs, that are often

operated under reverse bias to aid extraction and hence the photo-response, single-component systems with their narrower absorption compared to blends are of interest.[132] Indeed, for all studied NFAs significant photocurrent values could be measured under reverse bias conditions. Particularly IT-4F and Y6 showed significant EQE values of up to 50% at -5 V – a roughly 40-fold improvement compared to 0 V for Y6. For all devices, the increase of the EQE correlated well with the increasing PL quenching efficiency for increasing reverse bias. This indicates that the origin of the increased photocurrent is the bias assisted quenching of emissive states (i.e., field-dependent generation) rather than improved extraction. To further support this, the light intensity dependence of the extracted photocurrent is measured at different biases. By combining charge extraction and small-perturbation transient photocurrent measurements, an attempt is made at giving a rough estimate of the bimolecular recombination coefficient under device operating conditions in Y6 single component layers. While the discussion herein will focus on the optoelectronic results obtained for Y6 to elucidate whether single component devices are generation or extraction limited, the paper by Park *et al.* additionally presents the OPD performance, optical spectroscopy results and quantum chemical calculations to explain the observed trends in the charge generation efficiency and its bias dependence in the different NFA materials. A brief overview will be given towards the end of this chapter.

5.4.2. Contributions

The results discussed herein were mainly obtained as part of the study published by Park *et al.* and contain figures adapted from the publication.[33] Song Yi Park and Chiara Labanti fabricated the devices and carried out PL and EQE measurements. Transient optical measurements were performed by Tack Ho Lee and Yifan Dong. Yi-Chun Chin provided the measurements of the acceptor energy levels and calculations of the electrostatic potential and molecular quadrupole moments. The focus of this chapter will be the optoelectronic characterisation, carried out by the author of this thesis, to assess the extraction efficiency in Y6 single component devices. See Park *et al.* for additional data regarding the other NFAs, additional characterisation and details about the methods.[33]

5.4.3. Materials and Absorption Spectra

The four NFAs were chosen as representative materials for different types of molecular structures: twisted (O-IDFBR),[133] planar (IDIC, IT-4F),[134,135] and curved (Y6)[7]. **Figure 5.4.1 (a)** shows the molecular structure of the NFAs.

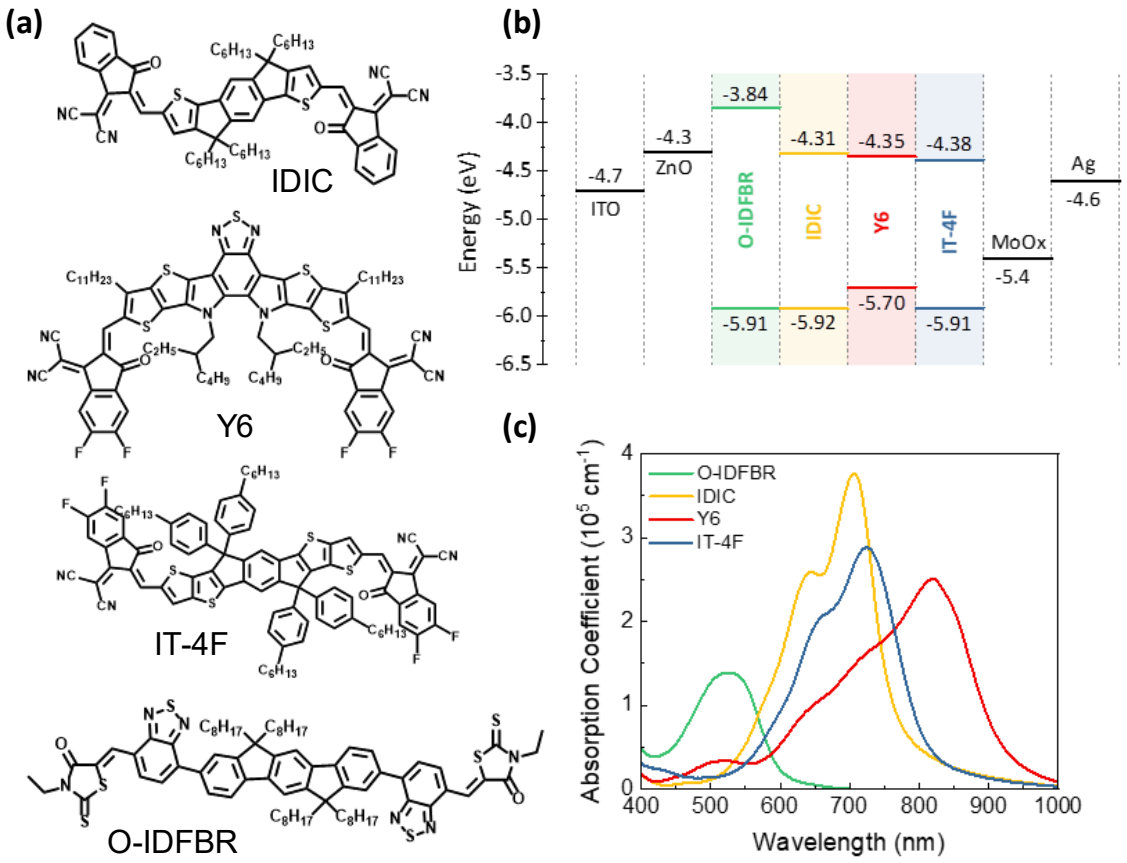


Figure 5.4.1. (a) Molecular structures of the four NFA materials used: IDIC, Y6, IT-4F, O-IDFBR. **(b)** Energy badn diagram of the single component devices. HOMO levels of the NFAs were determined by APS. LUMO levels were calculated by adding the optical gap to the measured HOMO level. **(c)** Absorption coefficient as a funtion of wavelength of the neat NFA films. Energy level measurements carried out by Yi-Chun Chin. Absorption spectra measured by Chiara Labanti.

Devices were produced by Song Yi Park with the structure ITO/ZnO/NFA (~40 nm)/MoO_3-/Ag. The corresponding energy levels are shown in **Figure 5.4.1 (b)** and were determined by Yi-Chun Chin. HOMO energy levels were measured directly by APS and the LUMO was determined from the optical gap. **Figure 5.4.1 (c)** shows the absorption spectra of the different NFAs and demonstrates their suitability for narrow-band photodetection in different wavelength regions. Despite the differences in the absorption coefficients, all four NFAs show a sufficiently high (> 10^{-5} cm^{-1}) value for photodetector applications.

5.4.4. Bias Dependent Photocurrent and Photoluminescence Quenching

To investigate the mechanism of charge generation in the single component devices (and their potential applicability as photodetectors), bias dependent EQE measurements are carried out. The bias dependent EQE spectra of Y6 are shown in **Figure 5.4.2 (a)** (see Park *et al.* for the

spectra of the other NFAs).[33] Figure 5.4.2 **(b)** shows the peak value of the EQE versus the applied bias for all four NFAs.

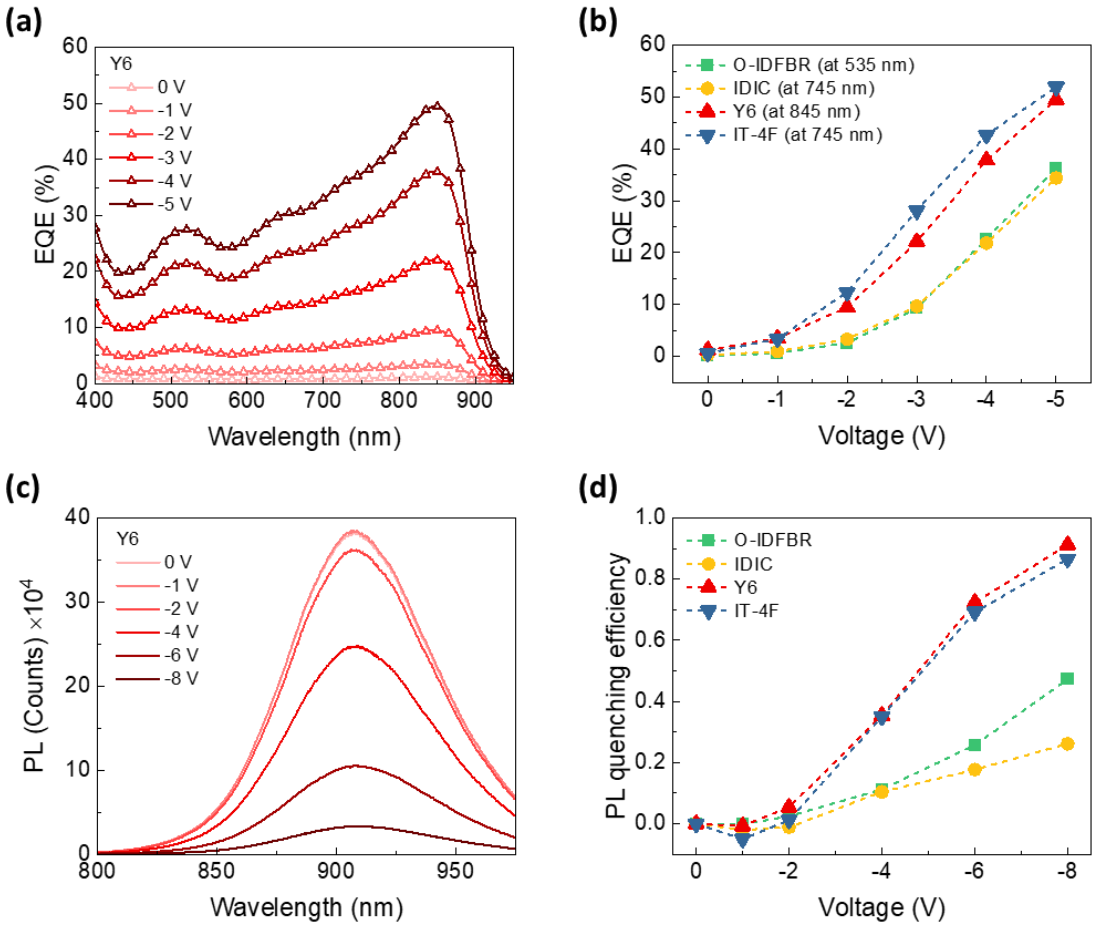


Figure 5.4.2. (a) Bias-dependent EQE spectra of a Y6 single component device. **(b)** Peak value of the EQE spectra versus the applied bias for O-IDFBR, IDIC, IT-4F and Y6. The legend shows the wavelength at which the EQE spectra reach their maximum. **(c)** Bias-dependent PL spectra of a Y6 single component device. **(d)** PL quenching efficiency as a function of bias for all four NFAs. The calculation of the PLQE is described in the text. Measurements carried out by Song Yi Park and Chiara Labanti.

The electric field across the acceptor layer is expected to be comparable based on the similar active layer thickness for all four NFAs (48 – 60 nm). At their EQE peak, IT-4F and Y6 reach a value of ≈ 50% at -5 V while IDIC and O-IDFBR are limited to about 35%. Besides the maximum achievable value of the EQE at -5 V which may additionally be influenced by lower absorption (in the case of O-IDFBR), a striking feature is the earlier onset of the EQE increase at -2 V in the case of IT-4F and Y6. The data indicates that significant charge generation occurs also in other NFA materials (besides the previously mentioned IT-4F and Y6) such as IDIC and O-IDFBR but only when a significant electric field is applied. Furthermore, the data shows

that at 0 V or forward bias, no significant photocurrent is extracted, making the single component devices unsuitable for photovoltaic applications.

To further study the origin of the enhancement of the EQE in the different materials, bias-dependent PL measurements were carried out (see **Figure 5.4.2 I** for the Y6 results). By calculating the photoluminescence quenching efficiency (defined as PLQE(V) = (PL_{0V} – PL(V))/PL_{0V}, where PL_{0V} and PL(V) are the PL intensity at zero bias and the applied voltage, respectively) the EQE can be related to the bias dependent quenching of the emissive states in the NFAs. The results shown in **Figure 5.4.2 (d)** show a very good agreement with the bias-dependence of the EQE peaks depicted in **Figure 5.4.2 (b)**. IDIC and O-IDFBR show the lowest PLQE (< 30% and < 50%, respectively) while IT-4F and Y6 achieve PLQEs of around 90% at -8 V. Also, the onset of the PLQE beyond -2 V coincides well with the EQE onset discussed above. This suggests that the origin of the enhanced photocurrent at reverse bias is the bias-dependent splitting of emissive states to form free charges in contrast to previous hypotheses about charge generation being efficient at forward bias while collection limits the photo-response.

5.4.5. Light Intensity Dependence of the Photo-Response

Light intensity dependent *JV*-curves were measured to investigate any limitations posed by non-geminate recombination on the collection efficiency. The measurements were carried out using white light LEDs that were linearly powered down. To access low light intensities two additional neutral density filters were used. The light intensity of the LEDs was calibrated to the 1 sun current density determined from the integrated EQE at -5 V. Note that this introduces an error if significant non-geminate recombination occurs at 1 sun light intensity compared to the EQE measurement typically carried out at much lower light intensity. As will be discussed below, this error is small and the data is suitable to assess limitations based on the collection efficiency. **Figure 5.4.3 (a)** shows more than 50 normalised *JV*-curves collected at logarithmically spaced light intensity values ranging from 0.028 to 655 mW/cm^2 (sun equivalent power). It demonstrated that an appreciable photocurrent can only be extracted at reverse bias. The profile of the normalised extracted photocurrent shows remarkably little dependence on the light intensity. Any differences observed stem from the normalisation of *JV*-curves and the high noise at low light intensities. **Figure 5.4.3 (b)** shows the total extracted current density measured at -5 and -1 V as well as the photocurrent (J_{ph}) corrected for the dark current. The values were extracted from the measured *JV*-curves. At -5

V, the dark current becomes significant below 0.5 % sun (or 0.5 mW/cm²). **Figure 5.4.3** **(c)** and **(d)** show the corrected J_{ph} and the responsivity calculated from J_{ph} at various biases as a function of the incident light intensity.

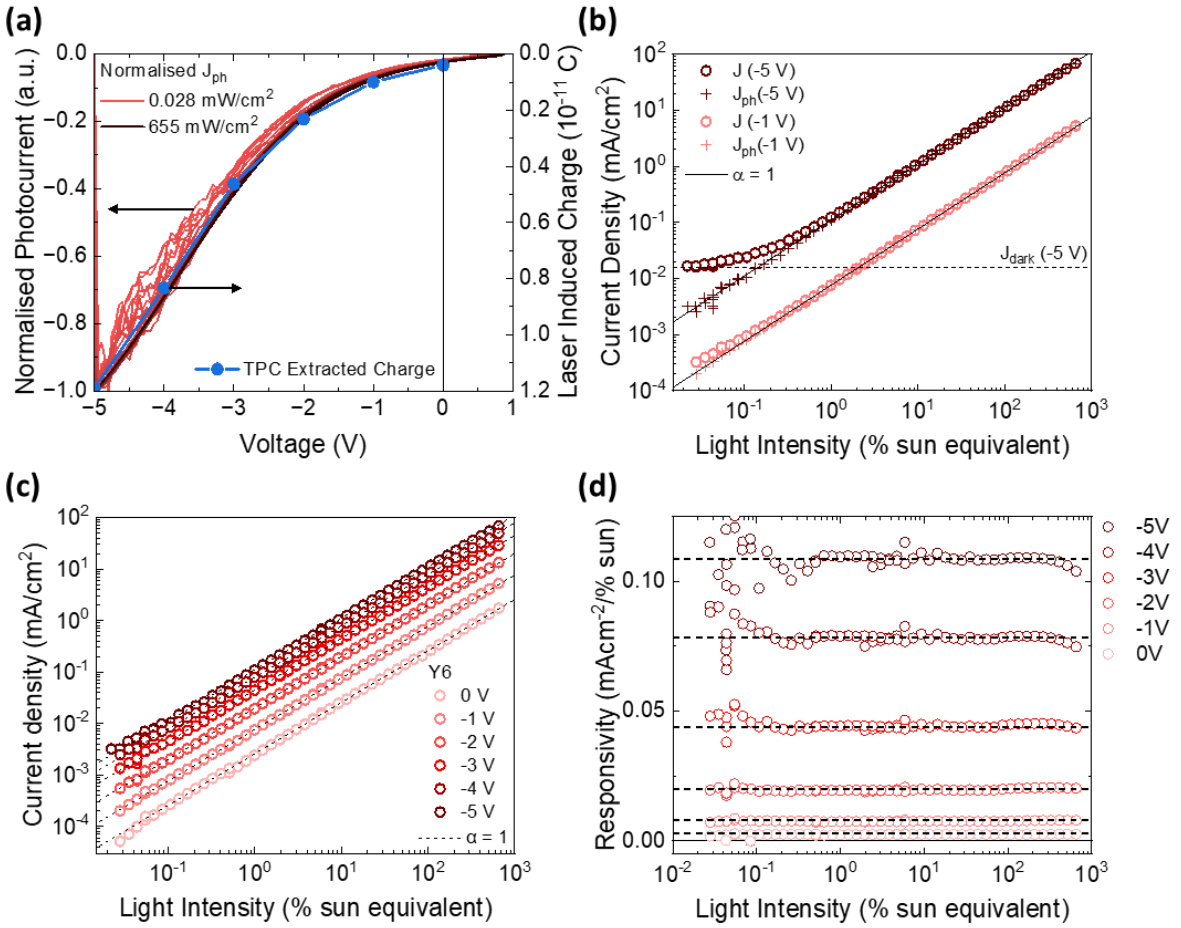


Figure 5.4.3. **(a)** Normalised photocurrent of Y6 versus applied bias at 56 light intensity levels logarithmically spaced from 0.028 to 655 mW/cm² (equivalent to % sun intensity). The LED light intensity was calibrated to reproduce the integrated EQE at 1 sun AM1.5 illumination at -5 V reverse bias. On the right axis, the laser induced charge extracted in transient photocurrent measurements. **(b)** Total extracted current and corrected photocurrent of Y6 at -5 and -1 V illustrating the lower bound of the linear dynamic range at high reverse bias where the dark current increases. The measurements were obtained from the JV-curves. **(c)** Corrected photocurrent of Y6 versus light intensity at short circuit and reverse bias conditions. **(d)** Responsivity calculated from the corrected photocurrent divided by the light intensity in mW/cm² (or % sun equivalent). Not that small discontinuities arise where neutral density filters were inserted (around 8% sun) to access light intensity levels otherwise inaccessible with the LED setup due to the unreliable low power output.

At all biases, even at 0 V, the photocurrent shows a high proportionality with respect to the light intensity. Only beyond 1 sun equivalent illumination at high reverse bias, the responsivity shows a slight reduction. This is in line with the onset of significant bimolecular losses as the increasing light intensity and negative bias result in a significant charge carrier density in the

active layer. However, up to one sun irrespective of the bias, no bimolecular limitation was discernible. Interestingly, the same was true for the other NFAs.[33] There the generally lower charge generation efficiency (IDIC and O-IDFBR) also resulted in a reduced carrier density which lowers the bimolecular recombination rate. Note that these results do not rule out a first-order trap assisted recombination pathway to result in significant non-geminate recombination during collections since the recombination rate would scale linearly with the light intensity.[136]

The light intensity independent responsivity suggests that poor charge collection can be ruled out as the origin of low extracted photocurrent at short circuit (and forward bias) – surprisingly, given that there is no heterojunction present to spatially separate charges and efficiently extract them through their respective phases. This is astonishing and contradicts previous studies that hypothesised extraction to be the limiting factor.[31,32] The findings furthermore support the assignment of the bias dependence of the photocurrent to a field-dependent generation mechanism. In the following, an attempt is made to quantify the bimolecular recombination coefficient under operating conditions from a combination of charge extraction and transient photocurrent measurements.

5.4.6. Determination of the Bimolecular Recombination Coefficient

Due to the poor photovoltaic performance as well as the expected high capacity of the devices, the determination of non-geminate recombination rates from charge extraction and transient photovoltage measurements seems unfeasible. Instead, an attempt is made here to give an estimate of the bimolecular recombination rate constant based on the reduction of the laser induced charge extracted in transient photocurrent measurements as a function of the LED bias light. As the LED bias light intensity is increased, the background charge carrier density causes additional recombination of the laser induced charge with the background charge carrier density.

Firstly, encouraged by the good collection properties at reverse bias conditions charge extraction measurements were carried out. The devices are kept under constant bias and LED light illumination. Upon switching the LED lights off, the extracted charge carrier density in the device is integrated to determine the steady state charge carrier density for a given light and electrical bias condition. **Figure 5.4.4** **(a)** and **(b)** show the extracted charge carrier density as a function of light intensity and the steady-state extracted photocurrent,

respectively. The charge carrier density shows a sub-linear dependence on the light intensity in line with a slightly charge carrier density dependent mobility.[106]

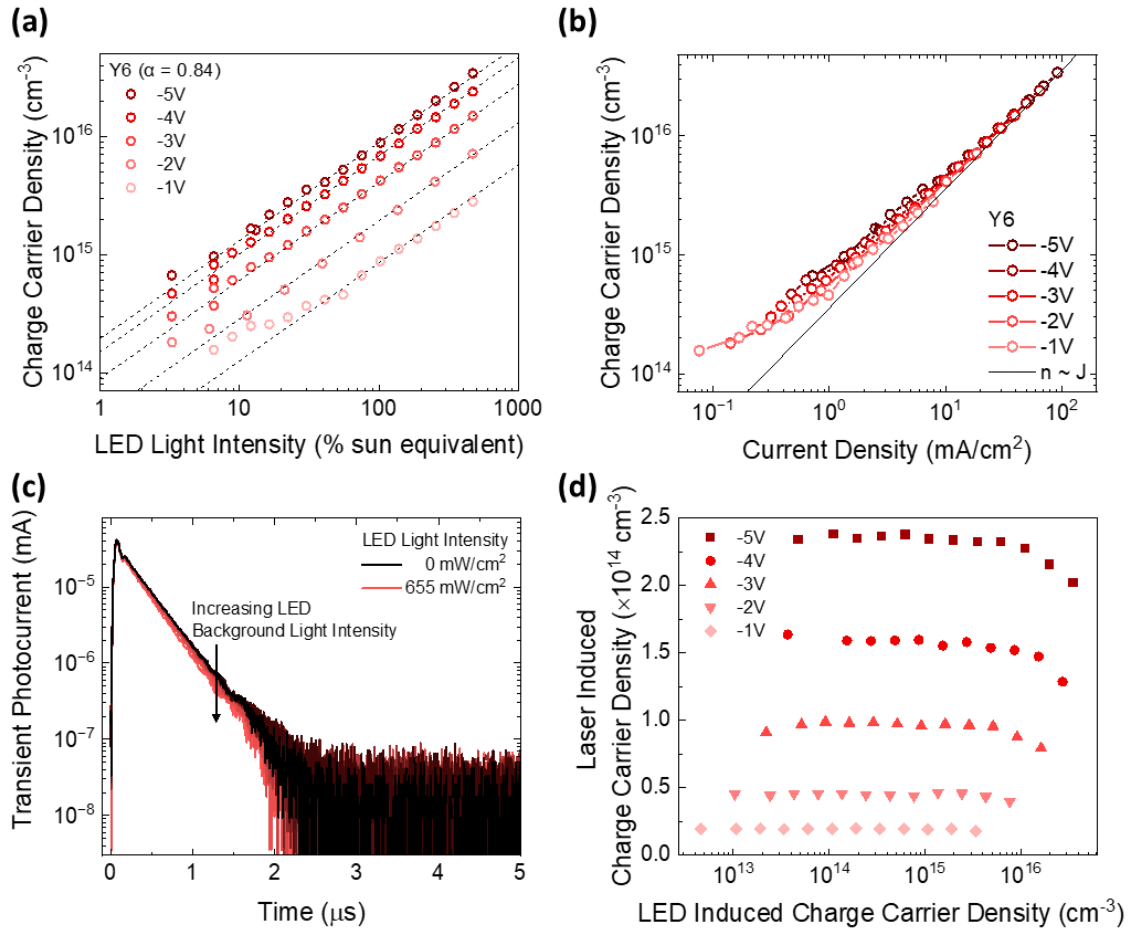


Figure 5.4.4. (a), (b) Extracted charge carrier density versus the LED background light intensity and the steady-state current density, respectively. Dashed lines in **(a)** are fits with a power law exponent of 0.84. The solid line in **(b)** signifies proportionality between the charge carrier density and extracted current density. **(c)** Photocurrent transients recorded with varying background light intensity recorded at -5 V. **(d)** Extracted charge induced by small perturbation laser pulses versus the background charge carrier density induced by LED illumination for different bias conditions.

By comparing the two graphs it becomes evident that the increase in extracted charge carrier density with bias is a result of the increased charge generation rather than extraction issues. As shown in **Figure 5.4.4 (b)**, when plotting against the steady-state photocurrent the data collected at different biases converges towards higher light intensity. The measurements were used to calculate a lower bound of the effective mobility of around 10^{-5} $cmV^{-1}s^{-1}$.[33] This is in line with the relatively high ambipolar mobility that has previously been demonstrated for Y6.[29,112,137]

Following that, laser induced small-perturbation transient photocurrent (TPC) measurements were carried out at different electrical and LED light bias conditions. As shown in **Figure 5.4.3 (a)**, the charge collected in TPC measurements as a function of bias matches well with the generation profile of the steady-state photocurrent measurements. **Figure 5.4.4 (c)** shows the variation of the photocurrent transients with varying the background light intensity as measured at -5 V. It illustrates the recombination losses occurring at high LED light bias between the laser induced charge and the steady-state background charge. The extraction time of the transients was limited by the RC-time constant of the device (**Figure 5.4.4 (c)** and **Figure 5.4.5 (a)**). **Figure 5.4.4 (d)** shows the corresponding laser induced charge determined from integration of the photocurrent transients. The charge carrier density on the x-axis was interpolated from the previously carried out charge extraction measurements.

The measurements show that the small-perturbation charge is highly bias-dependent while no effect of the background carrier density is observed until the emergence of bimolecular losses at high background light intensity – similar to the responsivity in steady-state measurements. This contradicts the previously proposed equilibrium between thermalised charges at steady-state and charge generation.[32] A simple kinetic model was devised to fit this and calculate the bimolecular recombination coefficient. The excess bimolecular recombination upon the small laser perturbation can be calculated by subtracting the steady-state recombination rate from the total recombination rate:

$$\frac{dn}{dt}(excess) = k_2 \cdot \left(\left(n + \Delta n \cdot \exp\left(\frac{t}{RC}\right)\right)^2 - n^2\right)$$

where n is the steady-state carrier density, k_2 is the bimolecular recombination coefficient, Δn is the laser induced charge carrier density that decays approximately with the RC time constant that can be determined from the TPC transients. Integration yields the excess recombined charge carrier density Δn_{rec}:

$$\Delta n_{rec} = k_2 \cdot RC \cdot \left(2n \cdot \Delta n + \frac{\Delta n^2}{2}\right)$$

The RC time constant was experimentally determined to be about 0.3 µs. The extracted laser induced charge Δn as a function of the background charge is then given by:

$$\Delta n(n) = \Delta n(0) - k_2 \cdot RC \cdot \left(2n \cdot \Delta n + \frac{\Delta n^2}{2}\right)$$

This was fitted to the experimental data (**Figure 5.4.5 (b)**) to yield a range of $0.7 - 3 \times 10^{-11}$ cm^3s^{-1}. The range may be attributed to the slightly varying extraction times (**Figure 5.4.5 (a)**). Values obtained by this method are presenting a lower bound as they are collected at reverse bias with potentially highly non-uniform charge carrier distribution.

The low bimolecular recombination coefficient as well as the high charge carrier density are both surprisingly similar to the values reported for BHJs containing Y6 (TPV/CE resulted in values of $k_2 = 2 \times 10^{-11}$ cm^3s^{-1} and $n = 5 \times 10^{16}$ cm^{-3} at 6 sun V_{OC} as shown in **Subchapter 4.2**) despite the lack of a heterojunction to spatially separate holes and electrons. These observations further support our conclusion of bias assisted charge generation to be the key determinant of performance for single component Y6 devices studied herein.

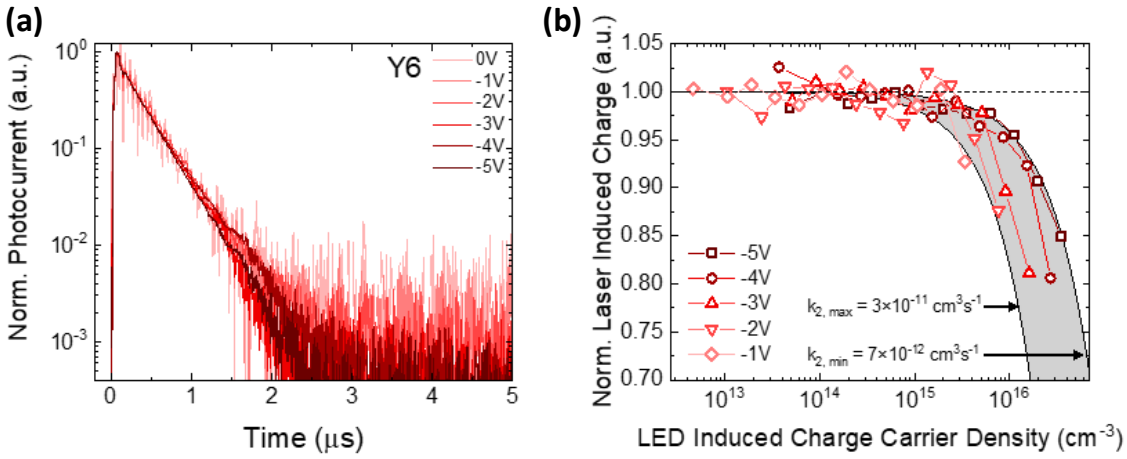


Figure 5.4.5. (a) Photocurrent transients without background illumination at different biases. **(b)** Normalised laser induced charge versus the LED induced steady-state charge carrier density. The grey area signifies the range of values of k_2 encompassing the measurements at all bias conditions.

Despite the uncertainties of the method, these results suggest that the bimolecular recombination rate is about three orders of magnitude slower than previously assumed in device models explaining the poor performance of Y6 single junctions with their poor charge collection.[32] Also other studies suggested that charge collection may be aided by interlayers that would reduce non-geminate losses due to the supposed high recombination coefficient.[112] Given that charge transfer state formation has previously been demonstrated at these inorganic interlayers for a range of acceptor materials,[111] it seems more likely that the

interlayer formed a charge generating heterojunction with Y6 to provide the driving force for exciton separation.

5.4.7. Photophysical Experiments to Elucidate Differences in Charge Generation

In the publication, exemplary photophysical studies on Y6 and O-IDFBR solutions and films address the origin of the differences in charge generation between the different NFAs. A striking feature of Y6 is the strong red shift and reduction in PLQY for solutions with increasing concentration and even more so for solid films. Such shifts are not observed for the more amorphous O-IDTBR in solution and film samples. The observations suggest strong intermolecular interactions between Y6 molecules. This is further supported with quantum chemical simulations that suggest that the lowest energy excited state in Y6 has significant charge transfer character as previously suggested elsewhere to be the precursor of charge generation in PM6:Y6 blends.[126] Delocalisation has also theoretically and experimentally been shown to aid charge generation.[138,139]

The Increased photogeneration efficiency at reverse bias of IT-4F and Y6 may therefore be related to their strong intermolecular interaction,[139] compared to the twisted O-IDFBR structure,[133] aiding the formation of charge transfer excitons that separate to free charges aided by an external bias. Additionally, the higher charge generation efficiency also correlates well with the molecular quadrupole moment and electrostatic potential difference between different molecular moieties in IT-4F and Y6. A more in-depth discussion of these observations can be found in the publication.

Particularly, at no externally applied bias an additional contribution to charge generation may stem from energetic offsets at differently oriented grain boundaries mediated by the molecular quadrupole moment of the acceptor material. In **Subchapter 5.3**, SPV results suggesting such trends for CF and CB deposited films of Y6 alluded to this. Devices built here from neat CF and CB films indeed show small differences in the EQE depending on the morphology of the film (see **Figure 5.4.6**)

However, the overall very low EQE at zero bias suggests that this is not a major charge generation pathway as has been reported previously for well-defined α-6T films.[86] While such grain boundaries and orientation dependent energetics may play a role also at reverse bias,

the majority of the free charge generation seems to be intrinsic without the need of such offsets.

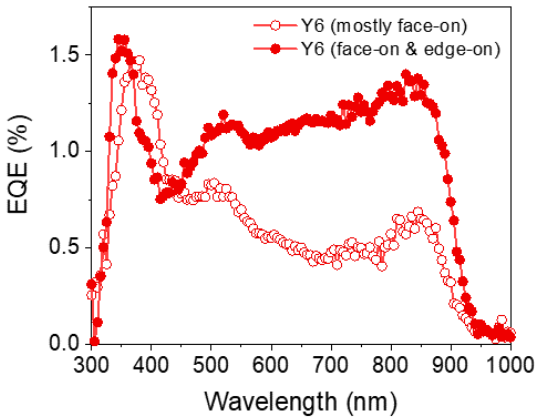


Figure 5.4.6. External quantum efficiency spectrum of devices prepared from chloroform and chlorobenzene resulting in a mostly face-on and mixed orientation, respectively. EQE measurements performed by Song Yi Park.

5.4.8. Conclusion

In conclusion, surprisingly high charge generation efficiency has been demonstrated for representative neat NFA (Y6, IT-4F, IDIC, O-IDFBR) devices when a reverse bias is applied while only miniscule photocurrents could be measured at no applied bias or forward bias. The origin of the large photocurrent when an electric field is applied is the bias dependent quenching of the emissive species in the NFAs as demonstrated by bias-dependent PL measurements. For all four devices, the photocurrent was highly linear with increasing light intensity which demonstrates low collection losses under reverse bias conditions. Focusing on Y6, where free charge generation had previously been proposed to be highly efficient even at no applied bias, additional measurements regarding the charge collection efficiency and the bimolecular recombination rate underline that the bias dependence of the extracted photocurrent arises from electric field dependent generation, not extraction. The observed charge carrier density and bimolecular recombination coefficient in neat Y6 are surprisingly similar to those established for PM6:Y6 BHJs (albeit at different bias conditions). Differences in the charge generation efficiency have been analysed in more detail in the publication by Park *et al.* and point towards the strong intermolecular interaction in IT-4F and Y6 to be the key reason for their high charge generation yield at reverse bias.[33] While these observations make single-junctions unlikely contenders for OSC applications, their high reverse bias responsivity raises the prospect of OPD applications.

5.5. Concluding Remarks: Bulk versus Planar Heterojunctions

Throughout this thesis, different planar and bulk heterojunction systems were compared directly: DCV-V-Fu-Ind-Fu-V/C_{60}, PM6/IT-4F and PM6/Y6. The motivating factors for the use of bilayers are either of a practical nature (reproducibility without the need to optimise the blend morphology, the higher morphological stability) or considerations regarding their potential to reduce non-geminate recombination related voltage losses. The overall performance, however, typically lags behind that of their BHJ equivalents, especially for typically studied high-performance materials that can be optimised to form a favourable blend morphology – meaning that materials that do not form a favourable morphology when blended may benefit from a PHJ architecture but are generally of less interest for applications.

In the systems studied herein, PHJ devices were shown to suffer from a range of issues compared to their BHJ counterparts. Firstly, in **Subchapter 4.3** evaporated DCV-V-Fu-Ind-Fu-V/C_{60} clearly showed a limitation of current generation due to the low exciton diffusion length. When increasing the donor layer thickness from 5 to 15 nm, only a small additional J_{SC} was measured at the expense of a large reduction in *FF* (potentially due to field-dependent generation of charges in the neat donor phase). This made the PHJ a potential candidate for use as a sub-cell in a multi-junction stack where the requirements for current generation are reduced while the voltage is added up across the monolithic sub-cells. Here, the benefit may be the reduced voltage loss of the PHJ that was established due to the reduction of interfacial area essentially lowering the ratio of interfacial CT states to S1 states that was shown to affect V_{OC}.[6,56]

Similarly, PM6/IT-4F showed an increased V_{OC} compared to its BHJ counterpart with qualitatively similar observations regarding the non-geminate recombination related voltage losses. Additionally, IT-4F benefits from its significantly larger exciton diffusion length of around 40 nm. Tuning the active layer thickness according to the exciton diffusion length (much thicker than typically evaporated PHJs) resulted in large improvement of J_{SC}. Still, the BHJs J_{SC} remains unmatched. The PHJ also resulted in a reduced *FF* which was tentatively assigned to a combination of field-dependent generation at the junction and in the neat IT-4F layer prior to reaching the interface as well as strongly light intensity dependent non-geminate effects due to the large generation current density at the limited planar interface. The latter may result in a fundamental trade-off between high charge generation at the small interface and instant non-geminate recombination of the generated carriers due to a high local carrier

density. As with other suboptimal OSCs, it turns out that the PM6/IT-4F planar heterojunction may benefit from its lower dark current when used as an OPD. Trade-offs between the generation at the limited interface and fast non-geminate recombination reducing the fill factor in PHJs with high photocurrent should eb further investigated!

Finally, PHJs produced from Y6 layers with different molecular orientation and morphology were produced. Also Y6 has previously been shown to have a long exciton diffusion length,[29,30] however, the achieved J_{SC} from IT-4F devices could not be matched. This result is in line with other previous reports of bilayer devices utilising Y6, none of which show significantly improved photocurrents despite layer thicknesses of up to 35 nm (in line with the exciton diffusion length).[65,110–112] As a consequence of that, the focus here was put on the observed energetic shifts for films deposited from different solvents and its effect on the V_{OC} that is a result of the strong electrostatic interactions in aggregated Y6 films. The large shift of more than 200 meV in the acceptor HOMO level partially translates to the trends in V_{OC} with the difference being explained by changes in the non-geminate recombination kinetics. The lowered HOMO level shows a reduced non-geminate recombination rate by a factor of 50. This is the result of the energetic offset and interfacial band bending that effectively drives the charges away from the interface. Similar albeit less pronounced trends were observed for the BHJ devices. Interestingly, potentially due to the interfacial band bending effects, the PHJs did not yield an improvement of the photovoltage relative to the BHJs as previously observed for the other PHJ systems. The increased band bending at the interface did however result in an improved linearity of the current density at high light intensities in line with fast non-geminate recombination being the limiting factor to high fill factor and current density in high current density planar devices.

Finally, while neat generation in single component NFA devices was demonstrated in the final chapter, the low charge generation yield at forward bias make them unlikely contenders for OSC application. At reverse bias, a high charge generation efficiency was achieved, especially in IT-4F and Y6 devices. This is in line with the formation of charge transfer excitons enabled by the strong intermolecular interaction in these materials. These delocalised states had previously been suggested to be precursors to charge generation in blend films.[126] In neat films, the application of a reverse bias may provide the driving force to separate these states and generate free charges. Charge collection was not found to be the limiting factor behind their poor OSC performance but again, a poor OSC may make a promising OPD.

The results presented herein show that PHJ systems can be promising for OSC applications, especially for multi-junction systems with reduced J_{SC} requirements. Key to furthering this potential for evaporated materials is the extension of their exciton diffusion length through morphological or structural improvements. IT-4F demonstrates that high photocurrent generation is possible given an increased exciton diffusion length. The *FF* limitations in high photocurrent planar heterojunctions that have also been observed elsewhere[45] should be further addressed in the future. Generally, pseudo-planar heterojunctions may be the more promising approach to high efficiency systems with a more reproducible deposition method and favourable vertical phase separation.[21,39] Case studies like that on Y6 demonstrate that bilayer systems are interesting subjects to elucidate fundamental effects of solar cell operation with well-defined domains and interfaces. Especially, when the effects partially translate to BHJs. Hybrid inorganic-organic[111,112] or evaporated donor-Y6[110] solar cells are potentially also of interest for multi-junction applications if the origin of the relatively low photocurrent can be elucidated.

References

(1) Cui, Y.; Xu, Y.; Yao, H.; Bi, P.; Hong, L.; Zhang, J.; Zu, Y.; Zhang, T.; Qin, J.; Ren, J.; Chen, Z.; He, C.; Hao, X.; Wei, Z.; Hou, J. Single-Junction Organic Photovoltaic Cell with 19% Efficiency. *Advanced Materials* **2021**, *33* (41), 2102420. https://doi.org/10.1002/adma.202102420.

(2) Sun, R.; Wu, Y.; Yang, X.; Gao, Y.; Chen, Z.; Li, K.; Qiao, J.; Wang, T.; Guo, J.; Liu, C.; Hao, X.; Zhu, H.; Min, J. Single-Junction Organic Solar Cells with 19.17% Efficiency Enabled by Introducing One Asymmetric Guest Acceptor. *Advanced Materials* **2022**, *34* (26), 2110147. https://doi.org/10.1002/adma.202110147.

(3) Zhu, L.; Zhang, M.; Xu, J.; Li, C.; Yan, J.; Zhou, G.; Zhong, W.; Hao, T.; Song, J.; Xue, X.; Zhou, Z.; Zeng, R.; Zhu, H.; Chen, C.-C.; MacKenzie, R. C. I.; Zou, Y.; Nelson, J.; Zhang, Y.; Sun, Y.; Liu, F. Single-Junction Organic Solar Cells with over 19% Efficiency Enabled by a Refined Double-Fibril Network Morphology. *Nat. Mater.* **2022**, *21* (6), 656–663. https://doi.org/10.1038/s41563-022-01244-y.

(4) Zhan, L.; Li, S.; Li, Y.; Sun, R.; Min, J.; Chen, Y.; Fang, J.; Ma, C.-Q.; Zhou, G.; Zhu, H.; Zuo, L.; Qiu, H.; Yin, S.; Chen, H. Manipulating Charge Transfer and Transport via Intermediary Electron Acceptor Channels Enables 19.3% Efficiency Organic Photovoltaics. *Advanced Energy Materials* **2022**, *12* (39), 2201076. https://doi.org/10.1002/aenm.202201076.

(5) Zheng, Z.; Wang, J.; Bi, P.; Ren, J.; Wang, Y.; Yang, Y.; Liu, X.; Zhang, S.; Hou, J. Tandem Organic Solar Cell with 20.2% Efficiency. *Joule* **2022**, *6* (1), 171–184. https://doi.org/10.1016/j.joule.2021.12.017.

(6) Azzouzi, M.; Yan, J.; Kirchartz, T.; Liu, K.; Wang, J.; Wu, H.; Nelson, J. Nonradiative Energy Losses in Bulk-Heterojunction Organic Photovoltaics. *Phys. Rev. X* **2018**, *8* (3), 031055. https://doi.org/10.1103/PhysRevX.8.031055.

(7) Yuan, J.; Zhang, Y.; Zhou, L.; Zhang, G.; Yip, H.-L.; Lau, T.-K.; Lu, X.; Zhu, C.; Peng, H.; Johnson, P. A.; Leclerc, M.; Cao, Y.; Ulanski, J.; Li, Y.; Zou, Y. Single-Junction Organic Solar Cell with over 15% Efficiency Using Fused-Ring Acceptor with Electron-Deficient Core. *Joule* **2019**. https://doi.org/10.1016/j.joule.2019.01.004.

(8) Perdigón-Toro, L.; Zhang, H.; Markina, A.; Yuan, J.; Hosseini, S. M.; Wolff, C. M.; Zuo, G.; Stolterfoht, M.; Zou, Y.; Gao, F.; Andrienko, D.; Shoaee, S.; Neher, D. Barrierless Free Charge Generation in the High-Performance PM6:Y6 Bulk Heterojunction Non-Fullerene Solar Cell. *Advanced Materials* **2020**, *32* (9), 1906763. https://doi.org/10.1002/adma.201906763.

(9) Wu, J.; Lee, J.; Chin, Y.-C.; Yao, H.; Cha, H.; Luke, J.; Hou, J.; Kim, J.-S.; Durrant, J. R. Exceptionally Low Charge Trapping Enables Highly Efficient Organic Bulk Heterojunction Solar Cells. *Energy Environ. Sci.* **2020**, *13* (8), 2422–2430. https://doi.org/10.1039/D0EE01338B.

(10) Ma, L.; Zhang, S.; Yao, H.; Xu, Y.; Wang, J.; Zu, Y.; Hou, J. High-Efficiency Nonfullerene Organic Solar Cells Enabled by 1000 Nm Thick Active Layers with a Low Trap-State Density. *ACS Appl. Mater. Interfaces* **2020**, *12* (16), 18777–18784. https://doi.org/10.1021/acsami.0c05172.

(11) Perdigón-Toro, L.; Phuong, L. Q.; Eller, F.; Freychet, G.; Saglamkaya, E.; Khan, J. I.; Wei, Q.; Zeiske, S.; Kroh, D.; Wedler, S.; Köhler, A.; Armin, A.; Laquai, F.; Herzig, E. M.; Zou, Y.; Shoaee, S.; Neher, D. Understanding the Role of Order in Y-Series Non-Fullerene Solar Cells to Realize High Open-Circuit Voltages. *Advanced Energy Materials* **2022**, *12* (12), 2103422. https://doi.org/10.1002/aenm.202103422.

(12) Jiang, K.; Wei, Q.; Lai, J. Y. L.; Peng, Z.; Kim, H. K.; Yuan, J.; Ye, L.; Ade, H.; Zou, Y.; Yan, H. Alkyl Chain Tuning of Small Molecule Acceptors for Efficient Organic Solar Cells. *Joule* **2019**, *3* (12), 3020–3033. https://doi.org/10.1016/j.joule.2019.09.010.

(13) Cui, Y.; Yao, H.; Zhang, J.; Xian, K.; Zhang, T.; Hong, L.; Wang, Y.; Xu, Y.; Ma, K.; An, C.; He, C.; Wei, Z.; Gao, F.; Hou, J. Single-Junction Organic Photovoltaic Cells with Approaching 18% Efficiency. *Advanced Materials* **2020**, *32* (19), 1908205. https://doi.org/10.1002/adma.201908205.

(14) Qin, Y.; Balar, N.; Peng, Z.; Gadisa, A.; Angunawela, I.; Bagui, A.; Kashani, S.; Hou, J.; Ade, H. The Performance-Stability Conundrum of BTP-Based Organic Solar Cells. *Joule* **2021**, *5* (8), 2129–2147. https://doi.org/10.1016/j.joule.2021.06.006.

(15) Cui, Y.; Yao, H.; Zhang, J.; Zhang, T.; Wang, Y.; Hong, L.; Xian, K.; Xu, B.; Zhang, S.; Peng, J.; Wei, Z.; Gao, F.; Hou, J. Over 16% Efficiency Organic Photovoltaic Cells Enabled by a Chlorinated Acceptor with Increased Open-Circuit Voltages. *Nat Commun* **2019**, *10* (1), 2515. https://doi.org/10.1038/s41467-019-10351-5.

(16) Song, J.; Li, C.; Zhu, L.; Guo, J.; Xu, J.; Zhang, X.; Weng, K.; Zhang, K.; Min, J.; Hao, X.; Zhang, Y.; Liu, F.; Sun, Y. Ternary Organic Solar Cells with Efficiency >16.5% Based on Two Compatible Nonfullerene Acceptors. *Advanced Materials* **2019**, *31* (52), 1905645. https://doi.org/10.1002/adma.201905645.

(17) Zhang, Y.; Cai, G.; Li, Y.; Zhang, Z.; Li, T.; Zuo, X.; Lu, X.; Lin, Y. An Electron Acceptor Analogue for Lowering Trap Density in Organic Solar Cells. *Advanced Materials* **2021**, *33* (14), 2008134. https://doi.org/10.1002/adma.202008134.

(18) Zhang, M.; Zhu, L.; Zhou, G.; Hao, T.; Qiu, C.; Zhao, Z.; Hu, Q.; Larson, B. W.; Zhu, H.; Ma, Z.; Tang, Z.; Feng, W.; Zhang, Y.; Russell, T. P.; Liu, F. Single-Layered Organic Photovoltaics with Double Cascading Charge Transport Pathways: 18% Efficiencies. *Nat Commun* **2021**, *12* (1), 309. https://doi.org/10.1038/s41467-020-20580-8.

(19) Arunagiri, L.; Peng, Z.; Zou, X.; Yu, H.; Zhang, G.; Wang, Z.; Lin Lai, J. Y.; Zhang, J.; Zheng, Y.; Cui, C.; Huang, F.; Zou, Y.; Wong, K. S.; Chow, P. C. Y.; Ade, H.; Yan, H. Selective Hole and Electron Transport in Efficient Quaternary Blend Organic Solar Cells. *Joule* **2020**, *4* (8), 1790–1805. https://doi.org/10.1016/j.joule.2020.06.014.

(20) Zhu, L.; Zhang, M.; Zhou, G.; Hao, T.; Xu, J.; Wang, J.; Qiu, C.; Prine, N.; Ali, J.; Feng, W.; Gu, X.; Ma, Z.; Tang, Z.; Zhu, H.; Ying, L.; Zhang, Y.; Liu, F. Efficient Organic Solar Cell with 16.88% Efficiency Enabled by Refined Acceptor Crystallization and Morphology with Improved Charge Transfer and Transport Properties. *Adv. Energy Mater.* **2020**, *10* (18), 1904234. https://doi.org/10.1002/aenm.201904234.

(21) Dong, X.; Jiang, Y.; Sun, L.; Qin, F.; Zhou, X.; Lu, X.; Wang, W.; Zhou, Y. Large-Area Organic Solar Modules with Efficiency Over 14%. *Advanced Functional Materials* **2022**, *32* (15), 2110209. https://doi.org/10.1002/adfm.202110209.

(22) Qin, Y.; Xu, Y.; Peng, Z.; Hou, J.; Ade, H. Low Temperature Aggregation Transitions in N3 and Y6 Acceptors Enable Double-Annealing Method That Yields Hierarchical Morphology and Superior Efficiency in Nonfullerene Organic Solar Cells. *Advanced Functional Materials* **2020**, *30* (46), 2005011. https://doi.org/10.1002/adfm.202005011.

(23) Zhu, W.; Spencer, A. P.; Mukherjee, S.; Alzola, J. M.; Sangwan, V. K.; Amsterdam, S. H.; Swick, S. M.; Jones, L. O.; Heiber, M. C.; Herzing, A. A.; Li, G.; Stern, C. L.; DeLongchamp, D. M.; Kohlstedt, K. L.; Hersam, M. C.; Schatz, G. C.; Wasielewski, M. R.; Chen, L. X.; Facchetti, A.; Marks, T. J. Crystallography, Morphology, Electronic Structure, and Transport in Non-Fullerene/Non-Indacenodithienothiophene Polymer:Y6 Solar Cells. *J. Am. Chem. Soc.* **2020**, *142* (34), 14532–14547. https://doi.org/10.1021/jacs.0c05560.

(24) Lucera, L.; Kubis, P.; Fecher, F. W.; Bronnbauer, C.; Turbiez, M.; Forberich, K.; Ameri, T.; Egelhaaf, H.-J.; Brabec, C. J. Guidelines for Closing the Efficiency Gap between Hero Solar Cells and Roll-To-Roll Printed Modules. *Energy Technology* **2015**, *3* (4), 373–384. https://doi.org/10.1002/ente.201402192.

(25) Riede, M.; Spoltore, D.; Leo, K. Organic Solar Cells—The Path to Commercial Success. *Advanced Energy Materials* **2021**, *11* (1), 2002653. https://doi.org/10.1002/aenm.202002653.

(26) Ye, L.; Li, S.; Liu, X.; Zhang, S.; Ghasemi, M.; Xiong, Y.; Hou, J.; Ade, H. Quenching to the Percolation Threshold in Organic Solar Cells. *Joule* **2019**, *3* (2), 443–458. https://doi.org/10.1016/j.joule.2018.11.006.

(27) Ghasemi, M.; Hu, H.; Peng, Z.; Rech, J. J.; Angunawela, I.; Carpenter, J. H.; Stuard, S. J.; Wadsworth, A.; McCulloch, I.; You, W.; Ade, H. Delineation of Thermodynamic and Kinetic Factors That Control Stability in Non-Fullerene Organic Solar Cells. *Joule* **2019**, *3* (5), 1328–1348. https://doi.org/10.1016/j.joule.2019.03.020.

(28) Kerremans, R.; Kaiser, C.; Li, W.; Zarrabi, N.; Meredith, P.; Armin, A. The Optical Constants of Solution-Processed Semiconductors—New Challenges with Perovskites and Non-Fullerene Acceptors. *Advanced Optical Materials* **2020**, *8* (16), 2000319. https://doi.org/10.1002/adom.202000319.

(29) Firdaus, Y.; Le Corre, V. M.; Karuthedath, S.; Liu, W.; Markina, A.; Huang, W.; Chattopadhyay, S.; Nahid, M. M.; Nugraha, M. I.; Lin, Y.; Seitkhan, A.; Basu, A.; Zhang, W.; McCulloch, I.; Ade, H.; Labram, J.; Laquai, F.; Andrienko, D.; Koster, L. J. A.; Anthopoulos, T. D. Long-Range Exciton Diffusion in Molecular Non-Fullerene Acceptors. *Nat Commun* **2020**, *11* (1), 5220. https://doi.org/10.1038/s41467-020-19029-9.

(30) Riley, D. B.; Sandberg, O. J.; Li, W.; Meredith, P.; Armin, A. Quasi-Steady-State Measurement of Exciton Diffusion Lengths in Organic Semiconductors. *Phys. Rev. Appl.* **2022**, *17* (2), 024076. https://doi.org/10.1103/PhysRevApplied.17.024076.

(31) Zhu, L.; Zhang, J.; Guo, Y.; Yang, C.; Yi, Y.; Wei, Z. Small Exciton Binding Energies Enabling Direct Charge Photogeneration Towards Low-Driving-Force Organic Solar Cells. *Angewandte Chemie International Edition* **2021**, *60* (28), 15348–15353. https://doi.org/10.1002/anie.202105156.

(32) Price, M. B.; Hume, P. A.; Ilina, A.; Wagner, I.; Tamming, R. R.; Thorn, K. E.; Jiao, W.; Goldingay, A.; Conaghan, P. J.; Lakhwani, G.; Davis, N. J. L. K.; Wang, Y.; Xue, P.; Lu, H.; Chen, K.; Zhan, X.; Hodgkiss, J. M. Free Charge Photogeneration in a Single Component High Photovoltaic Efficiency Organic Semiconductor. *Nat Commun* **2022**, *13* (1), 2827. https://doi.org/10.1038/s41467-022-30127-8.

(33) Park, S. Y.; Labanti, C.; Pacalaj, R. A.; Lee, T. H.; Dong, Y.; Chin, Y.-C.; Luke, J.; Ryu, G.; Minami, D.; Yun, S.; Park, J.-I.; Fang, F.; Park, K.-B.; Durrant, J. R.; Kim, J.-S. The State-of-the-Art Solution-Processed Single Component Organic Photodetectors Achieved by Strong Quenching of Intermolecular Emissive State and High Quadrupole Moment in Non-Fullerene Acceptors. *Advanced Materials* **2023**, *35* (49), 2306655. https://doi.org/10.1002/adma.202306655.

(34) Sharma, A.; Gasparini, N.; Markina, A.; Karuthedath, S.; Gorenflot, J.; Xu, H.; Han, J.; Balawi, A.; Liu, W.; Bryant, D.; Bertrandie, J.; Troughton, J.; Paleti, S. H. K.; Bristow, H.; Laquai, F.; Andrienko, D.; Baran, D. Semitransparent Organic Photovoltaics Utilizing Intrinsic Charge Generation in Non-Fullerene Acceptors. *Advanced Materials n/a* (n/a), 2305367. https://doi.org/10.1002/adma.202305367.

(35) Cui, Y.; Zhang, S.; Liang, N.; Kong, J.; Yang, C.; Yao, H.; Ma, L.; Hou, J. Toward Efficient Polymer Solar Cells Processed by a Solution-Processed Layer-By-Layer Approach. *Advanced Materials* **2018**, *30* (34), 1802499. https://doi.org/10.1002/adma.201802499.

(36) Sun, R.; Guo, J.; Sun, C.; Wang, T.; Luo, Z.; Zhang, Z.; Jiao, X.; Tang, W.; Yang, C.; Li, Y.; Min, J. A Universal Layer-by-Layer Solution-Processing Approach for Efficient Non-Fullerene Organic Solar Cells. *Energy Environ. Sci.* **2019**, *12* (1), 384–395. https://doi.org/10.1039/C8EE02560F.

(37) Zhang, J.; Futscher, M. H.; Lami, V.; Kosasih, F. U.; Cho, C.; Gu, Q.; Sadhanala, A.; Pearson, A. J.; Kan, B.; Divitini, G.; Wan, X.; Credgington, D.; Greenham, N. C.; Chen, Y.; Ducati, C.; Ehrler, B.; Vaynzof, Y.; Friend, R. H.; Bakulin, A. A. Sequentially Deposited versus Conventional Nonfullerene Organic Solar Cells: Interfacial Trap States, Vertical Stratification, and Exciton Dissociation. *Advanced Energy Materials* **2019**, *9* (47), 1902145. https://doi.org/10.1002/aenm.201902145.

(38) Zhang, J.; Kan, B.; Pearson, A. J.; Parnell, A. J.; Cooper, J. F. K.; Liu, X.-K.; Conaghan, P. J.; Hopper, T. R.; Wu, Y.; Wan, X.; Gao, F.; Greenham, N. C.; Bakulin, A. A.; Chen, Y.; Friend, R. H. Efficient Non-Fullerene Organic Solar Cells Employing Sequentially Deposited Donor–Acceptor Layers. *J. Mater. Chem. A* **2018**, *6* (37), 18225–18233. https://doi.org/10.1039/C8TA06860G.

(39) Wang, X.; Zhang, L.; Hu, L.; Xie, Z.; Mao, H.; Tan, L.; Zhang, Y.; Chen, Y. High-Efficiency (16.93%) Pseudo-Planar Heterojunction Organic Solar Cells Enabled by Binary Additives Strategy. *Advanced Functional Materials* **2021**, *31* (33), 2102291. https://doi.org/10.1002/adfm.202102291.

(40) Jiang, K.; Zhang, J.; Peng, Z.; Lin, F.; Wu, S.; Li, Z.; Chen, Y.; Yan, H.; Ade, H.; Zhu, Z.; Jen, A. K.-Y. Pseudo-Bilayer Architecture Enables High-Performance Organic Solar Cells with Enhanced Exciton Diffusion Length. *Nat Commun* **2021**, *12* (1), 468. https://doi.org/10.1038/s41467-020-20791-z.

(41) Park, S. Y.; Labanti, C.; Luke, J.; Chin, Y.-C.; Kim, J.-S. Organic Bilayer Photovoltaics for Efficient Indoor Light Harvesting. *Advanced Energy Materials* **2022**, *12* (3), 2103237. https://doi.org/10.1002/aenm.202103237.

(42) Lee, T. H.; Park, S. Y.; Park, W.-W.; Du, X.; Son, J. H.; Li, N.; Kwon, O.-H.; Woo, H. Y.; Brabec, C. J.; Kim, J. Y. Efficient Exciton Diffusion in Organic Bilayer Heterojunctions with Nonfullerene Small Molecular Acceptors. *ACS Energy Lett.* **2020**, *5* (5), 1628–1635. https://doi.org/10.1021/acsenergylett.0c00564.

(43) Lee, T. H.; Park, W.-W.; Park, S. Y.; Cho, S.; Kwon, O.-H.; Kim, J. Y. Planar Organic Bilayer Heterojunctions Fabricated on Water with Ultrafast Donor-to-Acceptor Charge Transfer. *Solar RRL* **2021**, *5* (8), 2100326. https://doi.org/10.1002/solr.202100326.

(44) Park, S. Y.; Chandrabose, S.; Price, M. B.; Ryu, H. S.; Lee, T. H.; Shin, Y. S.; Wu, Z.; Lee, W.; Chen, K.; Dai, S.; Zhu, J.; Xue, P.; Zhan, X.; Woo, H. Y.; Kim, J. Y.; Hodgkiss, J. M. Photophysical Pathways in Efficient Bilayer Organic Solar Cells: The Importance of Interlayer Energy Transfer. *Nano Energy* **2021**, *84*, 105924. https://doi.org/10.1016/j.nanoen.2021.105924.

(45) Wang, R.; Jiang, Y.; Gruber, W.; He, Y.; Wu, M.; Weitz, P.; Zhang, K.; Lüer, L.; Forberich, K.; Unruh, T.; Spiecker, E.; Deibel, C.; Li, N.; Brabec, C. J. Tailoring the Nature of Interface States in Efficient and Stable Bilayer Organic Solar Cells by a Transfer-Printing Technique. *Advanced Materials Interfaces* n/a (n/a), 2200342. https://doi.org/10.1002/admi.202200342.

(46) Sun, R.; Wu, Q.; Guo, J.; Wang, T.; Wu, Y.; Qiu, B.; Luo, Z.; Yang, W.; Hu, Z.; Guo, J.; Shi, M.; Yang, C.; Huang, F.; Li, Y.; Min, J. A Layer-by-Layer Architecture for Printable Organic Solar Cells Overcoming the Scaling Lag of Module Efficiency. *Joule* **2020**, *4* (2), 407–419. https://doi.org/10.1016/j.joule.2019.12.004.

(47) Ramsdale, C. M.; Barker, J. A.; Arias, A. C.; MacKenzie, J. D.; Friend, R. H.; Greenham, N. C. The Origin of the Open-Circuit Voltage in Polyfluorene-Based Photovoltaic Devices. *Journal of Applied Physics* **2002**, *92* (8), 4266–4270. https://doi.org/10.1063/1.1506385.

(48) Noh, J.; Jeong, S.; Lee, J.-Y. Ultrafast Formation of Air-Processable and High-Quality Polymer Films on an Aqueous Substrate. *Nat Commun* **2016**, *7* (1), 12374. https://doi.org/10.1038/ncomms12374.

(49) Sun, L.; Jiang, X.; Zhou, Y. Efficient Nonfullerene Organic Solar Cells with Active Layers Fabricated by Water Transfer Printing. *Journal of Energy Chemistry* **2019**, *37*, 220–224. https://doi.org/10.1016/j.jechem.2019.04.001.

(50) Li, X.; Zhang, Q.; Yu, J.; Xu, Y.; Zhang, R.; Wang, C.; Zhang, H.; Fabiano, S.; Liu, X.; Hou, J.; Gao, F.; Fahlman, M. Mapping the Energy Level Alignment at Donor/Acceptor Interfaces in Non-Fullerene Organic Solar Cells. *Nat Commun* **2022**, *13* (1), 2046. https://doi.org/10.1038/s41467-022-29702-w.

(51) Lee, T. H.; Dong, Y.; Pacalaj, R. A.; Park, S. Y.; Xu, W.; Kim, J.-S.; Durrant, J. R. Organic Planar Heterojunction Solar Cells and Photodetectors Tailored to the Exciton Diffusion Length Scale of a Non-Fullerene Acceptor. *Advanced Functional Materials* **2022**, *32* (51), 2208001. https://doi.org/10.1002/adfm.202208001.

(52) Fu, Y.; Lee, T. H.; Chin, Y.-C.; Pacalaj, R. A.; Labanti, C.; Park, S. Y.; Dong, Y.; Cho, H. W.; Kim, J. Y.; Minami, D.; Durrant, J. R.; Kim, J.-S. Molecular Orientation-Dependent Energetic Shifts in Solution-Processed Non-Fullerene Acceptors and Their Impact on Organic Photovoltaic Performance. *Nat Commun* **2023**, *14* (1), 1870. https://doi.org/10.1038/s41467-023-37234-0.

(53) Zhao, W.; Li, S.; Yao, H.; Zhang, S.; Zhang, Y.; Yang, B.; Hou, J. Molecular Optimization Enables over 13% Efficiency in Organic Solar Cells. *J. Am. Chem. Soc.* **2017**, *139* (21), 7148–7151. https://doi.org/10.1021/jacs.7b02677.

(54) Lin, Y.; Firdaus, Y.; Nugraha, M. I.; Liu, F.; Karuthedath, S.; Emwas, A.-H.; Zhang, W.; Seitkhan, A.; Neophytou, M.; Faber, H.; Yengel, E.; McCulloch, I.; Tsetseris, L.; Laquai, F.; Anthopoulos, T. D. 17.1% Efficient Single-Junction Organic Solar Cells Enabled by n-Type Doping of the Bulk-Heterojunction. *Advanced Science* **2020**, *7* (7), 1903419. https://doi.org/10.1002/advs.201903419.

(55) Luke, J.; Yang, E. J.; Chin, Y.-C.; Che, Y.; Winkler, L.; Whatling, D.; Labanti, C.; Park, S. Y.; Kim, J.-S. Strong Intermolecular Interactions Induced by High Quadrupole Moments Enable Excellent Photostability of Non-Fullerene Acceptors for Organic Photovoltaics. *Advanced Energy Materials* **2022**, *12* (30), 2201267. https://doi.org/10.1002/aenm.202201267.

(56) Vandewal, K.; Widmer, J.; Heumueller, T.; Brabec, C. J.; McGehee, M. D.; Leo, K.; Riede, M.; Salleo, A. Increased Open-Circuit Voltage of Organic Solar Cells by Reduced Donor-Acceptor Interface Area. *Adv. Mater.* **2014**, *26* (23), 3839–3843. https://doi.org/10.1002/adma.201400114.

(57) Zhong, Y.; Causa', M.; Moore, G. J.; Krauspe, P.; Xiao, B.; Günther, F.; Kublitski, J.; Shivhare, R.; Benduhn, J.; BarOr, E.; Mukherjee, S.; Yallum, K. M.; Réhault, J.; Mannsfeld, S. C. B.; Neher, D.; Richter, L. J.; DeLongchamp, D. M.; Ortmann, F.; Vandewal, K.; Zhou, E.; Banerji, N. Sub-Picosecond Charge-Transfer at near-Zero Driving Force in Polymer:Non-Fullerene Acceptor Blends and Bilayers. *Nature Communications* **2020**, *11* (1), 833. https://doi.org/10.1038/s41467-020-14549-w.

(58) Classen, A.; Chochos, C. L.; Lüer, L.; Gregoriou, V. G.; Wortmann, J.; Osvet, A.; Forberich, K.; McCulloch, I.; Heumüller, T.; Brabec, C. J. The Role of Exciton Lifetime for Charge Generation in Organic Solar Cells at Negligible Energy-Level Offsets. *Nat Energy* **2020**, *5* (9), 711–719. https://doi.org/10.1038/s41560-020-00684-7.

(59) Karuthedath, S.; Gorenflot, J.; Firdaus, Y.; Chaturvedi, N.; De Castro, C. S. P.; Harrison, G. T.; Khan, J. I.; Markina, A.; Balawi, A. H.; Peña, T. A. D.; Liu, W.; Liang, R.-Z.; Sharma, A.; Paleti, S. H. K.; Zhang, W.; Lin, Y.; Alarousu, E.; Anjum, D. H.; Beaujuge, P. M.; De Wolf, S.; McCulloch, I.; Anthopoulos, T. D.; Baran, D.; Andrienko, D.; Laquai, F. Intrinsic Efficiency Limits in Low-Bandgap Non-Fullerene Acceptor Organic Solar Cells. *Nat. Mater.* **2021**, *20* (3), 378–384. https://doi.org/10.1038/s41563-020-00835-x.

(60) Tress, W.; Leo, K.; Riede, M. Influence of Hole-Transport Layers and Donor Materials on Open-Circuit Voltage and Shape of I–V Curves of Organic Solar Cells. *Advanced Functional Materials* **2011**, *21* (11), 2140–2149. https://doi.org/10.1002/adfm.201002669.

(61) Tress, W.; Corvers, S.; Leo, K.; Riede, M. Investigation of Driving Forces for Charge Extraction in Organic Solar Cells: Transient Photocurrent Measurements on Solar Cells Showing S-Shaped Current–Voltage Characteristics. *Advanced Energy Materials* **2013**, *3* (7), 873–880. https://doi.org/10.1002/aenm.201200931.

(62) Tress, W.; Petrich, A.; Hummert, M.; Hein, M.; Leo, K.; Riede, M. Imbalanced Mobilities Causing S-Shaped IV Curves in Planar Heterojunction Organic Solar Cells. *Appl. Phys. Lett.* **2011**, *98* (6), 063301. https://doi.org/10.1063/1.3553764.

(63) Zhang, S.; Qin, Y.; Zhu, J.; Hou, J. Over 14% Efficiency in Polymer Solar Cells Enabled by a Chlorinated Polymer Donor. *Advanced Materials* **2018**, *30* (20), 1800868. https://doi.org/10.1002/adma.201800868.

(64) Benatto, L.; Koehler, M. Effects of Fluorination on Exciton Binding Energy and Charge Transport of π-Conjugated Donor Polymers and the ITIC Molecular Acceptor: A Theoretical Study. *J. Phys. Chem. C* **2019**, *123* (11), 6395–6406. https://doi.org/10.1021/acs.jpcc.8b12261.

(65) Nakano, K.; Kaji, Y.; Tajima, K. Origin of Electric Field-Dependent Charge Generation in Organic Photovoltaics with Planar and Bulk Heterojunctions. *J. Mater. Chem. A* **2023**, *11* (48), 26499–26507. https://doi.org/10.1039/D3TA06835H.

(66) Azzouzi, M.; Calado, P.; Telford, A. M.; Eisner, F.; Hou, X.; Kirchartz, T.; Barnes, P. R. F.; Nelson, J. Overcoming the Limitations of Transient Photovoltage Measurements for Studying Recombination in Organic Solar Cells. *Solar RRL n/a* (n/a), 1900581. https://doi.org/10.1002/solr.201900581.

(67) Wu, H.; Ma, Z.; Li, M.; Lu, H.; Tang, A.; Zhou, E.; Wen, J.; Sun, Y.; Tress, W.; Haugaard Olsen, J. M.; Meloni, S.; Bo, Z.; Tang, Z. Impact of Donor Halogenation on Reorganization Energies and Voltage Losses in Bulk-Heterojunction Solar Cells. *Energy & Environmental Science* **2023**, *16* (3), 1277–1290. https://doi.org/10.1039/D3EE00174A.

(68) Perdigón-Toro, L.; Phuong, L. Q.; Zeiske, S.; Vandewal, K.; Armin, A.; Shoaee, S.; Neher, D. Excitons Dominate the Emission from PM6:Y6 Solar Cells, but This Does Not Help the Open-Circuit Voltage of the Device. *ACS Energy Lett.* **2021**, *6* (2), 557–564. https://doi.org/10.1021/acsenergylett.0c02572.

(69) Nakano, K.; Tajima, K. Organic Planar Heterojunctions: From Models for Interfaces in Bulk Heterojunctions to High-Performance Solar Cells. *Advanced Materials* **2017**, *29* (25), 1603269. https://doi.org/10.1002/adma.201603269.

(70) Clarke, T. M.; Durrant, J. R. Charge Photogeneration in Organic Solar Cells. *Chem. Rev.* **2010**, *110* (11), 6736–6767. https://doi.org/10.1021/cr900271s.

(71) Schwarze, M.; Schellhammer, K. S.; Ortstein, K.; Benduhn, J.; Gaul, C.; Hinderhofer, A.; Perdigón Toro, L.; Scholz, R.; Kublitski, J.; Roland, S.; Lau, M.; Poelking, C.; Andrienko, D.; Cuniberti, G.; Schreiber, F.; Neher, D.; Vandewal, K.; Ortmann, F.; Leo, K. Impact of Molecular Quadrupole Moments on the Energy Levels at Organic Heterojunctions. *Nat Commun* **2019**, *10* (1), 2466. https://doi.org/10.1038/s41467-019-10435-2.

(72) Burke, T. M.; Sweetnam, S.; Vandewal, K.; McGehee, M. D. Beyond Langevin Recombination: How Equilibrium Between Free Carriers and Charge Transfer States

Determines the Open-Circuit Voltage of Organic Solar Cells. *Advanced Energy Materials* **2015**, *5* (11). https://doi.org/10.1002/aenm.201500123.

(73) Chen, X.-K.; Qian, D.; Wang, Y.; Kirchartz, T.; Tress, W.; Yao, H.; Yuan, J.; Hülsbeck, M.; Zhang, M.; Zou, Y.; Sun, Y.; Li, Y.; Hou, J.; Inganäs, O.; Coropceanu, V.; Bredas, J.-L.; Gao, F. A Unified Description of Non-Radiative Voltage Losses in Organic Solar Cells. *Nat Energy* **2021**, *6* (8), 799–806. https://doi.org/10.1038/s41560-021-00843-4.

(74) Eisner, F. D.; Azzouzi, M.; Fei, Z.; Hou, X.; Anthopoulos, T. D.; Dennis, T. J. S.; Heeney, M.; Nelson, J. Hybridization of Local Exciton and Charge-Transfer States Reduces Nonradiative Voltage Losses in Organic Solar Cells. *J. Am. Chem. Soc.* **2019**, *141* (15), 6362–6374. https://doi.org/10.1021/jacs.9b01465.

(75) Li, T.; Benduhn, J.; Qiao, Z.; Liu, Y.; Li, Y.; Shivhare, R.; Jaiser, F.; Wang, P.; Ma, J.; Zeika, O.; Neher, D.; Mannsfeld, S. C. B.; Ma, Z.; Vandewal, K.; Leo, K. Effect of H- and J-Aggregation on the Photophysical and Voltage Loss of Boron Dipyrromethene Small Molecules in Vacuum-Deposited Organic Solar Cells. *J. Phys. Chem. Lett.* **2019**, *10* (11), 2684–2691. https://doi.org/10.1021/acs.jpclett.9b01222.

(76) Cha, H.; Fish, G.; Luke, J.; Alraddadi, A.; Lee, H. H.; Zhang, W.; Dong, Y.; Limbu, S.; Wadsworth, A.; Maria, I. P.; Francàs, L.; Sou, H. L.; Du, T.; Kim, J.-S.; McLachlan, M. A.; McCulloch, I.; Durrant, J. R. Suppression of Recombination Losses in Polymer:Nonfullerene Acceptor Organic Solar Cells Due to Aggregation Dependence of Acceptor Electron Affinity. *Advanced Energy Materials* **2019**, *9* (27), 1901254. https://doi.org/10.1002/aenm.201901254.

(77) Natsuda, S.; Saito, T.; Shirouchi, R.; Sakamoto, Y.; Takeyama, T.; Tamai, Y.; Ohkita, H. Cascaded Energy Landscape as a Key Driver for Slow yet Efficient Charge Separation with Small Energy Offset in Organic Solar Cells. *Energy & Environmental Science* **2022**, *15* (4), 1545–1555. https://doi.org/10.1039/D1EE03565G.

(78) Poelking, C.; Andrienko, D. Design Rules for Organic Donor–Acceptor Heterojunctions: Pathway for Charge Splitting and Detrapping. *J. Am. Chem. Soc.* **2015**, *137* (19), 6320–6326. https://doi.org/10.1021/jacs.5b02130.

(79) Poelking, C.; Benduhn, J.; Spoltore, D.; Schwarze, M.; Roland, S.; Piersimoni, F.; Neher, D.; Leo, K.; Vandewal, K.; Andrienko, D. Open-Circuit Voltage of Organic Solar Cells: Interfacial Roughness Makes the Difference. *Commun Phys* **2022**, *5* (1), 1–7. https://doi.org/10.1038/s42005-022-01084-x.

(80) Poelking, C.; Tietze, M.; Elschner, C.; Olthof, S.; Hertel, D.; Baumeier, B.; Würthner, F.; Meerholz, K.; Leo, K.; Andrienko, D. Impact of Mesoscale Order on Open-Circuit Voltage in Organic Solar Cells. *Nature Mater* **2015**, *14* (4), 434–439. https://doi.org/10.1038/nmat4167.

(81) Liu, A.; Zhao, S.; Rim, S.-B.; Wu, J.; Könemann, M.; Erk, P.; Peumans, P. Control of Electric Field Strength and Orientation at the Donor–Acceptor Interface in Organic Solar Cells. *Advanced Materials* **2008**, *20* (5), 1065–1070. https://doi.org/10.1002/adma.200702554.

(82) Duhm, S.; Heimel, G.; Salzmann, I.; Glowatzki, H.; Johnson, R. L.; Vollmer, A.; Rabe, J. P.; Koch, N. Orientation-Dependent Ionization Energies and Interface Dipoles in

Ordered Molecular Assemblies. *Nature Mater* **2008**, *7* (4), 326–332. https://doi.org/10.1038/nmat2119.

(83) Salzmann, I.; Duhm, S.; Heimel, G.; Oehzelt, M.; Kniprath, R.; Johnson, R. L.; Rabe, J. P.; Koch, N. Tuning the Ionization Energy of Organic Semiconductor Films: The Role of Intramolecular Polar Bonds. *J. Am. Chem. Soc.* **2008**, *130* (39), 12870–12871. https://doi.org/10.1021/ja804793a.

(84) Heimel, G.; Salzmann, I.; Duhm, S.; Rabe, J. P.; Koch, N. Intrinsic Surface Dipoles Control the Energy Levels of Conjugated Polymers. *Advanced Functional Materials* **2009**, *19* (24), 3874–3879. https://doi.org/10.1002/adfm.200901025.

(85) D'Avino, G.; Muccioli, L.; Castet, F.; Poelking, C.; Andrienko, D.; Soos, Z. G.; Cornil, J.; Beljonne, D. Electrostatic Phenomena in Organic Semiconductors: Fundamentals and Implications for Photovoltaics. *J. Phys.: Condens. Matter* **2016**, *28* (43), 433002. https://doi.org/10.1088/0953-8984/28/43/433002.

(86) Dong, Y.; Nikolis, V. C.; Talnack, F.; Chin, Y.-C.; Benduhn, J.; Londi, G.; Kublitski, J.; Zheng, X.; Mannsfeld, S. C. B.; Spoltore, D.; Muccioli, L.; Li, J.; I, X.; Beljonne, D.; Kim, J.-S.; Bakulin, A. A.; D'Avino, G.; Durrant, J. R.; Vandewal, K. Orientation Dependent Molecular Electrostatics Drives Efficient Charge Generation in Homojunction Organic Solar Cells. *Nature Communications* **2020**, *11* (1), 4617. https://doi.org/10.1038/s41467-020-18439-z.

(87) Verlaak, S.; Beljonne, D.; Cheyns, D.; Rolin, C.; Linares, M.; Castet, F.; Cornil, J.; Heremans, P. Electronic Structure and Geminate Pair Energetics at Organic–Organic Interfaces: The Case of Pentacene/C60 Heterojunctions. *Advanced Functional Materials* **2009**, *19* (23), 3809–3814. https://doi.org/10.1002/adfm.200901233.

(88) Yamada, K.; Yanagisawa, S.; Koganezawa, T.; Mase, K.; Sato, N.; Yoshida, H. Impact of the Molecular Quadrupole Moment on Ionization Energy and Electron Affinity of Organic Thin Films: Experimental Determination of Electrostatic Potential and Electronic Polarization Energies. *Phys. Rev. B* **2018**, *97* (24), 245206. https://doi.org/10.1103/PhysRevB.97.245206.

(89) Lin, C.-F.; Liu, S.-W.; Lee, C.-C.; Hunag, J.-C.; Su, W.-C.; Chiu, T.-L.; Chen, C.-T.; Lee, J.-H. Open-Circuit Voltage and Efficiency Improvement of Subphthalocyanine-Based Organic Photovoltaic Device through Deposition Rate Control. *Solar Energy Materials and Solar Cells* **2012**, *103*, 69–75. https://doi.org/10.1016/j.solmat.2012.04.005.

(90) Rand, B. P.; Cheyns, D.; Vasseur, K.; Giebink, N. C.; Mothy, S.; Yi, Y.; Coropceanu, V.; Beljonne, D.; Cornil, J.; Brédas, J.-L.; Genoe, J. The Impact of Molecular Orientation on the Photovoltaic Properties of a Phthalocyanine/Fullerene Heterojunction. *Advanced Functional Materials* **2012**, *22* (14), 2987–2995. https://doi.org/10.1002/adfm.201200512.

(91) Markina, A.; Lin, K.-H.; Liu, W.; Poelking, C.; Firdaus, Y.; Villalva, D. R.; Khan, J. I.; Paleti, S. H. K.; Harrison, G. T.; Gorenflot, J.; Zhang, W.; De Wolf, S.; McCulloch, I.; Anthopoulos, T. D.; Baran, D.; Laquai, F.; Andrienko, D. Chemical Design Rules for Non-Fullerene Acceptors in Organic Solar Cells. *Advanced Energy Materials* **2021**, *11* (44), 2102363. https://doi.org/10.1002/aenm.202102363.

(92) Eisner, F.; Nelson, J. Barrierless Charge Generation at Non-Fullerene Organic Heterojunctions Comes at a Cost. *Joule* **2021**, *5* (6), 1319–1322. https://doi.org/10.1016/j.joule.2021.05.024.

(93) Neusser, D.; Sun, B.; Liang Tan, W.; Thomsen, L.; Schultz, T.; Perdigón-Toro, L.; Koch, N.; Shoaee, S.; R. McNeill, C.; Neher, D.; Ludwigs, S. Spectroelectrochemically Determined Energy Levels of PM6 : Y6 Blends and Their Relevance to Solar Cell Performance. *Journal of Materials Chemistry C* **2022**, *10* (32), 11565–11578. https://doi.org/10.1039/D2TC01918C.

(94) Baikie, I. D.; Grain, A. C.; Sutherland, J.; Law, J. Ambient Pressure Photoemission Spectroscopy of Metal Surfaces. *Applied Surface Science* **2014**, *323*, 45–53. https://doi.org/10.1016/j.apsusc.2014.08.159.

(95) Dong, S.; Jia, T.; Zhang, K.; Jing, J.; Huang, F. Single-Component Non-Halogen Solvent-Processed High-Performance Organic Solar Cell Module with Efficiency over 14%. *Joule* **2020**, *4* (9), 2004–2016. https://doi.org/10.1016/j.joule.2020.07.028.

(96) Labanti, C.; Wu, J.; Shin, J.; Limbu, S.; Yun, S.; Fang, F.; Park, S. Y.; Heo, C.-J.; Lim, Y.; Choi, T.; Kim, H.-J.; Hong, H.; Choi, B.; Park, K.-B.; Durrant, J. R.; Kim, J.-S. Light-Intensity-Dependent Photoresponse Time of Organic Photodetectors and Its Molecular Origin. *Nat Commun* **2022**, *13* (1), 3745. https://doi.org/10.1038/s41467-022-31367-4.

(97) Kupgan, G.; Chen, X. K.; Brédas, J. L. Molecular Packing of Non-Fullerene Acceptors for Organic Solar Cells: Distinctive Local Morphology in Y6 vs. ITIC Derivatives. *Materials Today Advances* **2021**, *11*, 100154. https://doi.org/10.1016/j.mtadv.2021.100154.

(98) Credgington, D.; Durrant, J. R. Insights from Transient Optoelectronic Analyses on the Open-Circuit Voltage of Organic Solar Cells. *J. Phys. Chem. Lett.* **2012**, *3* (11), 1465–1478. https://doi.org/10.1021/jz300293q.

(99) Credgington, D.; Liu, S.-W.; Nelson, J.; Durrant, J. R. In Situ Measurement of Energy Level Shifts and Recombination Rates in Subphthalocyanine/C_{60} Bilayer Solar Cells. *The Journal of Physical Chemistry C* **2014**, *118* (40), 22858–22864. https://doi.org/10.1021/jp505297u.

(100) Benduhn, J.; Tvingstedt, K.; Piersimoni, F.; Ullbrich, S.; Fan, Y.; Tropiano, M.; McGarry, K. A.; Zeika, O.; Riede, M. K.; Douglas, C. J.; Barlow, S.; Marder, S. R.; Neher, D.; Spoltore, D.; Vandewal, K. Intrinsic Non-Radiative Voltage Losses in Fullerene-Based Organic Solar Cells. *Nature Energy* **2017**, *2* (6), nenergy201753. https://doi.org/10.1038/nenergy.2017.53.

(101) Ray, B.; Lundstrom, M. S.; Alam, M. A. Can Morphology Tailoring Improve the Open Circuit Voltage of Organic Solar Cells? *Applied Physics Letters* **2012**, *100* (1), 013307. https://doi.org/10.1063/1.3672221.

(102) Ran, N. A.; Roland, S.; Love, J. A.; Savikhin, V.; Takacs, C. J.; Fu, Y.-T.; Li, H.; Coropceanu, V.; Liu, X.; Brédas, J.-L.; Bazan, G. C.; Toney, M. F.; Neher, D.; Nguyen, T.-Q. Impact of Interfacial Molecular Orientation on Radiative Recombination and Charge Generation Efficiency. *Nat Commun* **2017**, *8* (1), 79. https://doi.org/10.1038/s41467-017-00107-4.

(103) Chen, X.-K.; Ravva, M. K.; Li, H.; Ryno, S. M.; Brédas, J.-L. Effect of Molecular Packing and Charge Delocalization on the Nonradiative Recombination of Charge-Transfer States in Organic Solar Cells. *Advanced Energy Materials* **2016**, *6* (24), 1601325. https://doi.org/10.1002/aenm.201601325.

(104) Khan, S.-U.-Z.; Bertrandie, J.; Gui, M.; Sharma, A.; Alsufyani, W.; Gorenflot, J. F.; Laquai, F.; Baran, D.; Rand, B. P. Quantifying the Effect of Energetic Disorder on Organic Solar Cell Energy Loss. *Joule* **2022**. https://doi.org/10.1016/j.joule.2022.10.012.

(105) Hosseini, S. M.; Wilken, S.; Sun, B.; Huang, F.; Jeong, S. Y.; Woo, H. Y.; Coropceanu, V.; Shoaee, S. Relationship between Energetic Disorder and Reduced Recombination of Free Carriers in Organic Solar Cells. *Advanced Energy Materials n/a* (n/a), 2203576. https://doi.org/10.1002/aenm.202203576.

(106) Shuttle, C. G.; Hamilton, R.; Nelson, J.; O'Regan, B. C.; Durrant, J. R. Measurement of Charge-Density Dependence of Carrier Mobility in an Organic Semiconductor Blend. *Advanced Functional Materials* **2010**, *20* (5), 698–702. https://doi.org/10.1002/adfm.200901734.

(107) Hosseini, S. M.; Tokmoldin, N.; Lee, Y. W.; Zou, Y.; Woo, H. Y.; Neher, D.; Shoaee, S. Putting Order into PM6:Y6 Solar Cells to Reduce the Langevin Recombination in 400 Nm Thick Junction. *Solar RRL* **2020**, *4* (11), 2000498. https://doi.org/10.1002/solr.202000498.

(108) Cheyns, D.; Poortmans, J.; Heremans, P.; Deibel, C.; Verlaak, S.; Rand, B. P.; Genoe, J. Analytical Model for the Open-Circuit Voltage and Its Associated Resistance in Organic Planar Heterojunction Solar Cells. *Phys. Rev. B* **2008**, *77* (16), 165332. https://doi.org/10.1103/PhysRevB.77.165332.

(109) Foertig, A.; Wagenpfahl, A.; Gerbich, T.; Cheyns, D.; Dyakonov, V.; Deibel, C. Nongeminate Recombination in Planar and Bulk Heterojunction Organic Solar Cells. *Advanced Energy Materials* **2012**, *2* (12), 1483–1489. https://doi.org/10.1002/aenm.201200718.

(110) Kaienburg, P.; Bristow, H.; Jungbluth, A.; Habib, I.; McCulloch, I.; Beljonne, D.; Riede, M. Vacuum-Deposited Donors for Low-Voltage-Loss Nonfullerene Organic Solar Cells. *ACS Appl. Mater. Interfaces* **2023**, *15* (26), 31684–31691. https://doi.org/10.1021/acsami.3c04282.

(111) Eisner, F.; Foot, G.; Yan, J.; Azzouzi, M.; Georgiadou, D. G.; Sit, W. Y.; Firdaus, Y.; Zhang, G.; Lin, Y.-H.; Yip, H.-L.; Anthopoulos, T. D.; Nelson, J. Emissive Charge-Transfer States at Hybrid Inorganic/Organic Heterojunctions Enable Low Non-Radiative Recombination and High-Performance Photodetectors. *Advanced Materials* **2022**, *34* (22), 2104654. https://doi.org/10.1002/adma.202104654.

(112) Sağlamkaya, E.; Musiienko, A.; Saeed Shadabroo, M.; Sun, B.; Chandrabose, S.; Shargaieva, O.; M, G. L. G.; Hulst, N. F. van; Shoaee, S. What Is Special about Y6; the Working Mechanism of Neat Y6 Organic Solar Cells. *Materials Horizons* **2023**, *10* (5), 1825–1834. https://doi.org/10.1039/D2MH01411D.

(113) Liu, S.; Zhou, Y.; Liang, Z.; Zhao, B.; Wang, W.; Xue, Z.; Ding, K.; Cong, Z.; Wu, H.; Lu, G.; Gao, C. High-Performance Pseudo-Bilayer Organic Solar Cells Enabled by

Sequential Deposition of D18/Y6 Chloroform Solution. *ACS Appl. Energy Mater.* **2023**, *6* (9), 5047–5057. https://doi.org/10.1021/acsaem.3c00694.

(114) Zhao, Z.; Zhao, J.; Chung, S.; Cho, K.; Xu, W.; Kan, Z. Suppressing Bimolecular Charge Recombination and Energetic Disorder with Planar Heterojunction Active Layer Enables 18.1% Efficiency Binary Organic Solar Cells. *ACS Materials Lett.* **2023**, *5* (6), 1718–1726. https://doi.org/10.1021/acsmaterialslett.3c00236.

(115) Gregg, B. A. Excitonic Solar Cells. *J. Phys. Chem. B* **2003**, *107* (20), 4688–4698. https://doi.org/10.1021/jp022507x.

(116) Stranks, S. D.; Burlakov, V. M.; Leijtens, T.; Ball, J. M.; Goriely, A.; Snaith, H. J. Recombination Kinetics in Organic-Inorganic Perovskites: Excitons, Free Charge, and Subgap States. *Physical Review Applied* **2014**, *2* (3). https://doi.org/10.1103/PhysRevApplied.2.034007.

(117) D'Innocenzo, V.; Grancini, G.; Alcocer, M. J. P.; Kandada, A. R. S.; Stranks, S. D.; Lee, M. M.; Lanzani, G.; Snaith, H. J.; Petrozza, A. Excitons versus Free Charges in Organo-Lead Tri-Halide Perovskites. *Nat Commun* **2014**, *5* (1), 3586. https://doi.org/10.1038/ncomms4586.

(118) Miyata, A.; Mitioglu, A.; Plochocka, P.; Portugall, O.; Wang, J. T.-W.; Stranks, S. D.; Snaith, H. J.; Nicholas, R. J. Direct Measurement of the Exciton Binding Energy and Effective Masses for Charge Carriers in Organic–Inorganic Tri-Halide Perovskites. *Nature Phys* **2015**, *11* (7), 582–587. https://doi.org/10.1038/nphys3357.

(119) Few, S.; M. Frost, J.; Nelson, J. Models of Charge Pair Generation in Organic Solar Cells. *Physical Chemistry Chemical Physics* **2015**, *17* (4), 2311–2325. https://doi.org/10.1039/C4CP03663H.

(120) Chen, S.; Tsang, S.-W.; Lai, T.-H.; Reynolds, J. R.; So, F. Dielectric Effect on the Photovoltage Loss in Organic Photovoltaic Cells. *Adv. Mater.* **2014**, *26* (35), 6125–6131. https://doi.org/10.1002/adma.201401987.

(121) Paquin, F.; Latini, G.; Sakowicz, M.; Karsenti, P.-L.; Wang, L.; Beljonne, D.; Stingelin, N.; Silva, C. Charge Separation in Semicrystalline Polymeric Semiconductors by Photoexcitation: Is the Mechanism Intrinsic or Extrinsic? *Phys. Rev. Lett.* **2011**, *106* (19), 197401. https://doi.org/10.1103/PhysRevLett.106.197401.

(122) Kozlov, O. V.; Luponosov, Y. N.; Solodukhin, A. N.; Flament, B.; Olivier, Y.; Lazzaroni, R.; Cornil, J.; Ponomarenko, S. A.; Pshenichnikov, M. S. Ultrafast Exciton-to-Polaron Conversion in Densely Packed Small Organic Semiconducting Molecules. *Advanced Optical Materials* **2017**, *5* (7), 1700024. https://doi.org/10.1002/adom.201700024.

(123) Chandran, H. T.; Ng, T.-W.; Foo, Y.; Li, H.-W.; Qing, J.; Liu, X.-K.; Chan, C.-Y.; Wong, F.-L.; Zapien, J. A.; Tsang, S.-W.; Lo, M.-F.; Lee, C.-S. Direct Free Carrier Photogeneration in Single Layer and Stacked Organic Photovoltaic Devices. *Advanced Materials* **2017**, *29* (22), 1606909. https://doi.org/10.1002/adma.201606909.

(124) Nikolis, V. C.; Dong, Y.; Kublitski, J.; Benduhn, J.; Zheng, X.; Huang, C.; Yüzer, A. C.; Ince, M.; Spoltore, D.; Durrant, J. R.; Bakulin, A. A.; Vandewal, K. Field Effect versus Driving Force: Charge Generation in Small-Molecule Organic Solar Cells. *Advanced Energy Materials* **2020**, *10* (47), 2002124. https://doi.org/10.1002/aenm.202002124.

(125) Reid, O. G.; Pensack, R. D.; Song, Y.; Scholes, G. D.; Rumbles, G. Charge Photogeneration in Neat Conjugated Polymers. *Chem. Mater.* **2014**, *26* (1), 561–575. https://doi.org/10.1021/cm4027144.

(126) Wang, R.; Zhang, C.; Li, Q.; Zhang, Z.; Wang, X.; Xiao, M. Charge Separation from an Intra-Moiety Intermediate State in the High-Performance PM6:Y6 Organic Photovoltaic Blend. *J. Am. Chem. Soc.* **2020**, *142* (29), 12751–12759. https://doi.org/10.1021/jacs.0c04890.

(127) Tang, C. W. Two-layer Organic Photovoltaic Cell. *Applied Physics Letters* **1986**, *48* (2), 183–185. https://doi.org/10.1063/1.96937.

(128) Halls, J. J. M.; Walsh, C. A.; Greenham, N. C.; Marseglia, E. A.; Friend, R. H.; Moratti, S. C.; Holmes, A. B. Efficient Photodiodes from Interpenetrating Polymer Networks. *Nature* **1995**, *376* (6540), 498–500. https://doi.org/10.1038/376498a0.

(129) Yu, G.; Gao, J.; Hummelen, J. C.; Wudl, F.; Heeger, A. J. Polymer Photovoltaic Cells : Enhanced Efficiencies via a Network of Internal Donor-Acceptor Heterojunctions. *Science* **1995**, *270* (5243), 1789–1791.

(130) Lin, Y.; He, Q.; Zhao, F.; Huo, L.; Mai, J.; Lu, X.; Su, C.-J.; Li, T.; Wang, J.; Zhu, J.; Sun, Y.; Wang, C.; Zhan, X. A Facile Planar Fused-Ring Electron Acceptor for As-Cast Polymer Solar Cells with 8.71% Efficiency. *J. Am. Chem. Soc.* **2016**, *138* (9), 2973–2976. https://doi.org/10.1021/jacs.6b00853.

(131) Holliday, S.; Ashraf, R. S.; Nielsen, C. B.; Kirkus, M.; Röhr, J. A.; Tan, C.-H.; Collado-Fregoso, E.; Knall, A.-C.; Durrant, J. R.; Nelson, J.; McCulloch, I. A Rhodanine Flanked Nonfullerene Acceptor for Solution-Processed Organic Photovoltaics. *J. Am. Chem. Soc.* **2015**, *137* (2), 898–904. https://doi.org/10.1021/ja5110602.

(132) Zhao, Z.; Xu, C.; Niu, L.; Zhang, X.; Zhang, F. Recent Progress on Broadband Organic Photodetectors and Their Applications. *Laser & Photonics Reviews* **2020**, *14* (11), 2000262. https://doi.org/10.1002/lpor.202000262.

(133) Luke, J.; Speller, E. M.; Wadsworth, A.; Wyatt, M. F.; Dimitrov, S.; Lee, H. K. H.; Li, Z.; Tsoi, W. C.; McCulloch, I.; Bagnis, D.; Durrant, J. R.; Kim, J.-S. Twist and Degrade—Impact of Molecular Structure on the Photostability of Nonfullerene Acceptors and Their Photovoltaic Blends. *Advanced Energy Materials* **2019**, *9* (15), 1803755. https://doi.org/10.1002/aenm.201803755.

(134) Cha, H.; Zheng, Y.; Dong, Y.; Lee, H. H.; Wu, J.; Bristow, H.; Zhang, J.; Lee, H. K. H.; Tsoi, W. C.; Bakulin, A. A.; McCulloch, I.; Durrant, J. R. Exciton and Charge Carrier Dynamics in Highly Crystalline PTQ10:IDIC Organic Solar Cells. *Advanced Energy Materials* **2020**, *10* (38), 2001149. https://doi.org/10.1002/aenm.202001149.

(135) Chen, M.; Liu, D.; Li, W.; Gurney, R. S.; Li, D.; Cai, J.; Spooner, E. L. K.; Kilbride, R. C.; McGettrick, J. D.; Watson, T. M.; Li, Z.; Jones, R. A. L.; Lidzey, D. G.; Wang, T. Influences of Non-Fullerene Acceptor Fluorination on Three-Dimensional Morphology and Photovoltaic Properties of Organic Solar Cells. *ACS Appl. Mater. Interfaces* **2019**, *11* (29), 26194–26203. https://doi.org/10.1021/acsami.9b07317.

(136) Zeiske, S.; Li, W.; Meredith, P.; Armin, A.; Sandberg, O. J. Light Intensity Dependence of the Photocurrent in Organic Photovoltaic Devices. *Cell Reports Physical Science* **2022**, *3* (10), 101096. https://doi.org/10.1016/j.xcrp.2022.101096.

(137) Xiao, C.; Li, C.; Liu, F.; Zhang, L.; Li, W. Single-Crystal Field-Effect Transistors Based on a Fused-Ring Electron Acceptor with High Ambipolar Mobilities. *J. Mater. Chem. C* **2020**, *8* (16), 5370–5374. https://doi.org/10.1039/D0TC00587H.

(138) Balzer, D.; M. Smolders, T. J. A.; Blyth, D.; N. Hood, S.; Kassal, I. Delocalised Kinetic Monte Carlo for Simulating Delocalisation-Enhanced Charge and Exciton Transport in Disordered Materials. *Chemical Science* **2021**, *12* (6), 2276–2285. https://doi.org/10.1039/D0SC04116E.

(139) Zhang, G.; Chen, X.-K.; Xiao, J.; Chow, P. C. Y.; Ren, M.; Kupgan, G.; Jiao, X.; Chan, C. C. S.; Du, X.; Xia, R.; Chen, Z.; Yuan, J.; Zhang, Y.; Zhang, S.; Liu, Y.; Zou, Y.; Yan, H.; Wong, K. S.; Coropceanu, V.; Li, N.; Brabec, C. J.; Bredas, J.-L.; Yip, H.-L.; Cao, Y. Delocalization of Exciton and Electron Wavefunction in Non-Fullerene Acceptor Molecules Enables Efficient Organic Solar Cells. *Nat Commun* **2020**, *11* (1), 3943. https://doi.org/10.1038/s41467-020-17867-1.

6

CONCLUSIONS AND OUTLOOK

6.Conclusions and Outlook

The impressive learning curve that silicon PV has undergone makes solar energy a central part to any future mitigation scenario to combat the climate crisis. Ironically, this success has eliminated introduction openers of organic solar cell papers that used to promise low-cost solar energy and cited silicon PV's high prices. Organic solar cells are currently lagging behind silicon in terms of price, performance and stability. Yet they offer a great range of niche applications that should be explored and also offer the lowest carbon footprint of any energy conversion technology bar hydro (according to a lifecycle analysis by TÜV Rheinland). Learning from the successful journey, that the silicon PV story demonstrated, would mean that investment into upscale (enabling a technology push) and a guarantee of protected niche markets (creating a market pull) may be crucial to replicating silicon's success. For the academic community, this may mean focusing on research that brings organic solar cells closer to a commercial product rather than breaking the 20% efficiency barrier with small scale fabrication techniques, and unstable or high-cost materials. Vacuum-deposited organic solar cells currently seem to possess the more viable route to large scale application with proven scalable deposition, high stability and cheaper material synthesis (albeit more expensive processing).

The first results chapter (**Chapter 4**) of this thesis focused on gaining a greater understanding into the loss mechanisms encountered in commercially relevant evaporated organic solar cells. In comparison with solution-processed films the higher energetic disorder and lowered charge collection efficiency pose a major challenge that may be addressed through materials innovation of more rigid materials and better deposition control enabling more phase separated films. The size limit imposed by the evaporation process may result in a fundamental limit in this regard. Partially, the constraints by the collection efficiency may be alleviated by the use of multi-junction systems using thinner sub-cells. Here, the lowered requirements for charge collection and photocurrent put strategies to reduce the voltage losses in fullerene-based vacuum-deposited solar cells in the focus. Planar heterojunctions have been shown to be interesting candidates for this if the exciton diffusion length can be increased to yield slightly higher photocurrent values. The introduction of evaporable non-fullerene acceptors may also help to further reduce voltage losses – the results of **Subchapter 4.2** indicate that the miscibility, interaction energy and crystallinity of evaporated donors and

non-fullerene acceptors should be taken into account when choosing suitable materials to enable high collection efficiencies and fill factors.

The261econdd part of this thesis was dedicated to the study of alternative device architectures such as planar heterojunctions and single component devices for solution-processed devices. These may hold promise for increasing stability and more reproducible manufacturing compared to bulk heterojunctions with their complex morphology and high susceptibility to processing conditions. Interestingly, the Swedish company Epishine demonstrated the commercial viability of bilayer devices with their production method. They deposit the respective electrode materials and interlayers on the top and bottom substrate before depositing D/A blends on both sides and laminating the substrates with the active layer side together. However, performance of sharp bilayers of pure donor and acceptor as well as single component devices was merely enough for a second life as organic photodetectors in the cases studied herein. Beyond their performance, these devices offer great insight into some of the open questions of organic solar cells such as the role of the material energetics near the donor acceptor interface. Future research in bulk heterojunction devices should take these electrostatic effects into account when determining the effective electronic gap of the blend. In terms of performance, pseudo-planar heterojunction as reported in the literature may be the way to go. Crucially, research in the field of solution-processed organic solar cells should focus on understanding high-performing materials better and translating these findings to scalable solutions instead of producing another laboratory scale performance record by blending ever more active layer components with little reproducibility.

Having started my OPV journey at Merck with insights into the industrial side of R&D and inspired by the determination of Heliatek to make organic PV a large scale, environmentally friendly solution for urban applications, this has been my takeaway as we have witnessed impressive performance improvements while commercial partners such as Merck or Armor have dropped out of the race.